Spectroscopic Measurements of Atmospheric Trace Gases on Long-Distance Flights

Barbara Dix

Dissertation
submitted to the
Combined Faculties for the Natural Sciences and for Mathematics
of the Ruperto-Carola University of Heidelberg, Germany
for the degree of
Doctor of Natural Sciences

presented by: Barbara Dix
born in: Landau/Pfalz

oral examination: 19.12.2007

Spectroscopic Measurements of Atmospheric Trace Gases on Long-Distance Flights

Referees: Prof. Dr. Ulrich Platt
Prof. Dr. Thomas Wagner

Zusammenfassung

In dieser Arbeit werden Ergebnisse spektroskopischer Messungen atmosphärischer Spurengase auf Langstreckenflügen vorgestellt. Stickstoffdioxid (NO_2), Bromoxid (BrO), Ozon (O_3), Formaldehyd (HCHO) and salpetrige Säure (HONO) wurden in Streulichtspektren mittels Differentieller Optischer AbsorptionsSpektroskopie (DOAS) detektiert. Das Anliegen dieser Messungen ist die Untersuchung globaler Spurengasverteilungen, wie beispielsweise von BrO, das eine wichtige Rolle in der Ozonchemie einnimmt oder von HONO, welches einen Einfluss auf die Oxidationskapazität der Atmosphäre ausübt. Das DOAS Instrument wurde im Rahmen des CARIBIC Projekts (Civil Aircraft for the Regular Investigation of the atmosphere Based on an Instrument Container) entwickelt. Seit Mai 2005 finden einmal im Monat Messflüge auf einer Lufthansa Passagiermaschine statt. Auf Flügen nach Südamerika und Südost-Asien werden Streulichtspektren aus verschiedenen Blickrichtungen aufgenommen, die Aufschluss über die räumliche Verteilung der Spurengase geben können.

HONO Mischungsverhältnisse von ca. 60 ppt wurden in konvektiven Wolken beobachtet, was die Vermutung nahe legt, dass die HONO-Entstehung auf Blitzaktivität zurückzuführen ist. Über Zentralasien konnten BrO und NO_2 in einem Bereich der oberen Troposphäre gemessen werden, welcher sowohl Tropopausenfalten als auch eine starke Variation der Tropopausenhöhe aufwies. Diese Beobachtungen können einen Beitrag zum Verständnis der Austauschprozesse zwischen Tropo- und Stratosphäre leisten. NO_2- und HCHO-Profile in der Grenzschicht von Guangzhou/China konnten aus Messungen während eines Landeanflugs gewonnen werden. Für die Luftschicht von 0 - 1 km Höhe wurden Mischungsverhältnisse von 4.1 ppb ± 0.9 ppb für NO_2 und 8.2 ppb ± 1.2 ppb für HCHO abgeleitet. Abschließend wird der Informationsgehalt der durchgeführten Messungen diskutiert und es werden Anregungen für die Weiterarbeit gegeben.

Abstract

In this thesis results of spectroscopic measurements of atmospheric trace gases on long-distance flights are presented. Nitrogen dioxide (NO_2), bromine oxide (BrO), ozone (O_3), formaldehyde (HCHO) and nitrous acid (HONO) are detected in scattered light spectra by means of Differential Optical Absorption Spectroscopy. The underlying scientific scope is to gain information on global trace gas distributions, e.g. of BrO, which plays an important role in ozone chemistry or of HONO, which affects the oxidation capacity of the atmosphere. Within the framework of the CARIBIC project (Civil Aircraft for the Regular Investigation of the atmosphere Based on an Instrument Container) a DOAS instrument has been developed. Since May 2005, regular measurement flights are performed once a month onboard a Lufthansa passenger aircraft. During flights to South America and South-East Asia, the DOAS instrument records spectra of UV-visible scattered light from three different viewing directions to derive information on the spatial distribution of trace gases.

HONO mixing ratios in the order of 60 ppt were detected in deep convection clouds, suggesting a lightning induced HONO formation. BrO and NO_2 were observed in the upper troposphere in an area charcterized by tropopause folds and strong variations of the tropopause height. These measurements provide insights into troposphere-stratosphere exchange processes. Boundary layer profiles of NO_2 and HCHO were derived from descent measurements in Guangzhou/China, yielding mixing ratios of 4.1 ppb ± 0.9 ppb for NO_2 and 8.2 ppb ± 1.2 ppb for HCHO. A discussion of the information content of the CARIBIC DOAS measurements and possible fields of further studies are included.

Contents

Chapter 1

Introduction

"Why not make CARIBIC complete - and put a DOAS on board?"

The detection of the ozone hole in 1985 [*Farman et al.* 1985] induced a sudden public awareness of the earth's atmosphere. This observation had not only proved that anthropogenic activities do affect the environment on large scales, but also that the consequences are potentially very harmful to humans. The latter presented most likely a major driving force that led to the *Montreal Protocol on Substances that deplete the Ozone Layer* only two years later. The protocol and its following amendments limit the worldwide production of most ozone depleting compounds, such as CFCs. Yet today, pollution and global climate change, generated by a growing world population and globally rising industries, constitute even greater challenges for policy makers and scientists. Accordingly, environmental sciences have moved more and more in the focus of public interest and gained increasing support during recent years.

At present, atmospheric processes are still far from being entirely understood. For a system as complex and variable as the earth's atmosphere, the need of both short- and long-term observations with sufficient detail is evident. The CARIBIC aircraft project is a very comprehensive approach aimed for detailed long-term observations. The acronym stands for *Civil Aircraft for the Regular Investigation of the atmosphere Based on an Instrument Container* and denotes a successful European effort to put an automated instrument container on board a civil long-distance aircraft of Deutsche Lufthansa. The container comprises more than 20 instruments to regularly monitor atmospheric constituents, e.g. CO, O_3, H_2O, Hg, NO and NO_y, hydro- and halocarbons and aerosol number concentrations. Measurement flights are performed once a month since May 2005 and are planned to continue until 2014.

The current CARIBIC project is a second generation project with extended instrumentation, which includes the integration of a DOAS instrument that was built within the scope of this work. DOAS (*Differential Optical Absorption Spectroscopy*) is a widely used spectroscopic technique for the detection of various trace gases, such as nitrogen dioxide (NO_2), bromine oxide (BrO), ozone (O_3), formaldehyde (HCHO) and nitrous acid (HONO). These trace gases are identified by means of their individual absorption structure. The CARIBIC DOAS instrument records spectra of UV-visible scattered sun light from three different viewing directions (nadir, 10° above and below the horizon) to study the abundance and spatial distribution of these trace gases. It thus adds a remote sensing capability to the instrument container, "completing" the CARIBIC project.

The underlying scientific interest is mainly the observation of trace gases in the free troposphere, particularly of BrO, which plays an important role in global ozone chemistry. After more than two years of regular measurement flights, however, a plentitude of rather unexpected findings provides a much wider scientific scope of the CARIBIC DOAS measurements. For example, the detection of HONO in a deep convection cloud and in a biomass burning plume has led to studies on chemical processes inside clouds. Furthermore, on some flights tropopause folds were encountered, where BrO, NO_2 and O_3 could be observed within. Measurements during ascent and descent of the aircraft provide information on trace gas concentration profiles in the boundary layer. Profiles of NO_2 and HCHO in the boundary layer of Guangzhou/China could be retrieved by applying an inversion technique.

As part of this work, a DOAS instrument was developed within the framework of the CARIBIC project, which is the first time a DOAS instrument is deployed on a civil long-distance aircraft to perform regular measurements. Accordingly, this thesis is structured in two main parts: the first part considers technical aspects of the instrument development and flight performance, while the second part presents selected measurement results. The scope of the latter section is to explore the scientific potential of the CARIBIC DOAS data set and to exemplarily discuss its scientific yield. In conclusion, ideas for a continuous work and synergetic use of the CARIBIC data are provided.

Chapter 2

Atmospheric Dynamics and Chemistry

To understand observed distributions of chemical species in the atmosphere, it is necessary to not only comprehend atmospheric chemistry, but also those aspects of atmospheric dynamics pertaining to transport and dynamical mixing of species. In addition, pressure and temperature affect the reaction rate of many chemical reactions and ambient temperature also defines the phase of certain compounds. This chapter presents therefore a brief overview on atmospheric composition and dynamics. The subsequent section on atmospheric chemistry gives an introduction on the trace gases measured as part of this work and presents relevant chemical reactions of these species.

2.1 Atmospheric dynamics

2.1.1 Atmospheric composition and vertical structure

Composition The atmosphere (Greek: $\alpha\tau\mu\acute{o}\varsigma$, atmós, meaning vapor, haze, and $\sigma\varphi\alpha\iota\rho\alpha$, sphera, meaning sphere) is a layer of gases surrounding the earth, being retained by gravity. A selection of current gaseous constituents is given in Table 2.1.

It is noticeable that among the permanent constituents like nitrogen, oxygen or noble gases, the greenhouse gases carbon dioxide (CO_2) and methane (CH_4) have obtained a prominent position. Apart from the components listed in Table 2.1, there are several other substances of minor abundance, but of major importance for atmospheric chemistry and climate, called trace substances or, when gaseous, trace gases. Apart from O_3, CO_2 and CH_4, the most important are carbon monoxide (CO), halogen species (mostly bromine, chlorine or iodine compounds), compounds of nitrogen and sulphur and (volatile) organic compounds. 99 % of all atmospheric gases are found below 40 km of altitude, which renders this region, i.e. troposphere and stratosphere (see Figure 2.1), the main focus of atmospheric research.

Table 2.1: *Composition of the atmosphere.*

Name	**Formula**	**Relative Abundance** [%]
nitrogen	N_2	77.9
oxygen	O_2	20.95
argon	Ar	0.93
carbon dioxide	CO_2	0.036
neon	Ne	0.0018
helium	He	0.0005
water vapor	H_2O	10^{-4} - 4
methane	CH_4	0.00017
krypton	Kr	0.00011
hydrogen	H_2	0.00005
ozone	O_3	$1 \cdot 10^{-6} - 1 \cdot 10^{-3}$

Another important atmospheric constituent are aerosols. "Aerosol" denotes a suspension of all forms of fine liquid or solid particles floating in the atmosphere with sizes ranging from nm to μm, e.g. droplets of water (clouds/fog) or acid, dust or soot particles[1]. Aerosols are involved in atmospheric chemistry and can serve as cloud condensation nuclei, thus promoting the formation of clouds. Aerosols also interact with radiation by either scattering or absorbing photons (see Sections 4.2.3 and 4.2.4). Due to these properties they affect the radiative budget of the atmosphere. Research on aerosols has gained more attention in recent years, because their impact on earth's climate is still not very well quantified.

Vertical structure The vertical structure of the atmosphere can be defined by the characteristics of the temperature profile. Accordingly, the atmosphere is subdivided into several layers with distinct boundaries, called pauses (see Figure 2.1). In the lowermost layer, the troposphere, the temperature profile is dominated by adiabatic expansion and compression of rising and sinking air masses, driven by solar radiation. During the day the surface is heated, warm air elevates and is cooled by expansion, causing the temperature to decrease by 5 -10° per 1 km altitude and leading to a first temperature minimum, called the tropopause. An additional cooling occurs in the upper troposphere by radiative cooling of water in the infrared wavelength range (IR). The height of the tropopause is determined by the water vapor content of the troposphere, which itself is reigned by surface temperature. So the tropopause altitude ranges between 17 - 18 km in the tropics and between 9 - 13 km at higher latitudes, with the lowest tropopause heights occurring at polar winter latitudes. The above mentioned convective processes also lead to a steady mixing of the troposphere.

---

[1] Often the word "aerosols" is used to denote aerosol *particles*. This linguistic usage is applied in this thesis as well.

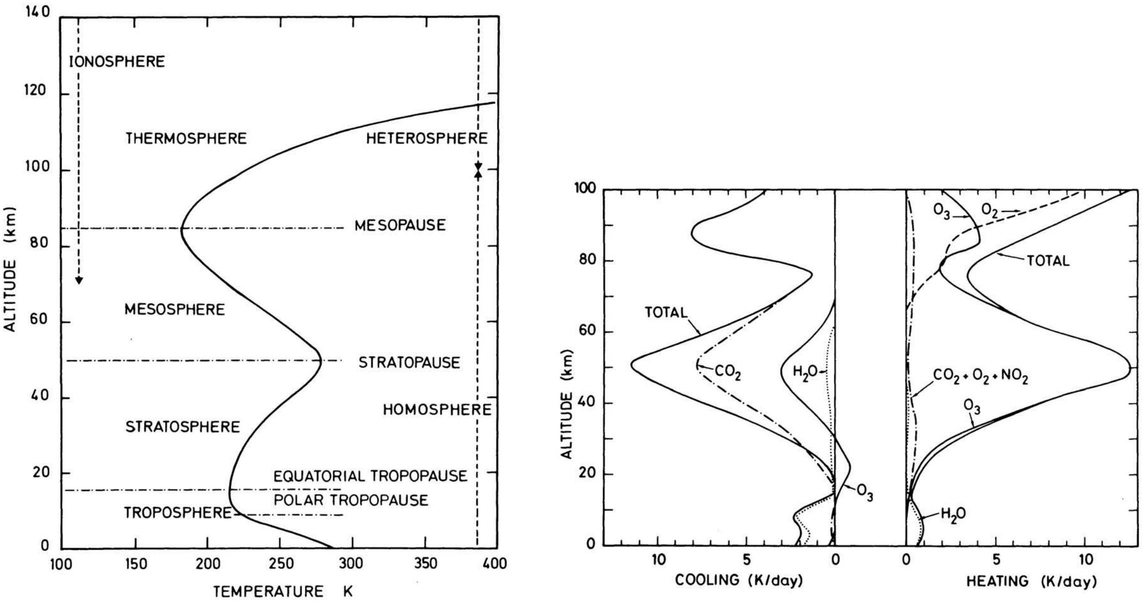

Figure 2.1: *Left panel: thermal structure of atmospheric layers. Adopted from Brasseur and Solomon [1986]. Right panel: Vertical distribution of solar short wave heating rates by* O_3, O_2, NO_2, H_2O, CO_2, *and of terrestrial long wave cooling rates by* CO_2, O_3, *and* H_2O. *Adopted from London [1980].*

In the stratosphere the conditions are vice versa. The heating in the upper stratosphere by absorption of solar radiation by ozone lead to an increase of temperature with altitude and thus to very little convection and mixing.[2] In contrast to the troposphere, the radiative budget of the stratosphere is determined by absorption of solar radiation and emission of thermal IR radiation. Above the stratopause, which is given by a temperature maximum around 50 km altitude, is the mesosphere where temperatures decrease again due to similar processes as in the troposphere. Thereafter, in the thermosphere, the temperature is again strongly increasing caused by absorption of solar UV radiation (mainly by oxygen) up to values of 1200 - 1500 K. The higher atmospheric layers (above 50 km) are called ionosphere, because of the occurrence of ions and free electrons. At altitudes above 100 km, atmospheric constituents start to separate, according to their mass, e.g. above 1000 km there is only hydrogen left, which is why this region is also referred to as heterosphere in contrast to the homosphere below.

---

[2] This fact is also reflected in the names: Greek: $\tau\rho o\pi\eta$, tropé, meaning turn, change and Latin: stratum, meaning blanket.

2.1.2 Global dynamics

2.1.2.1 Dynamics in the troposphere

The troposphere itself can be subdivided into several layers according to their dynamics. The lowermost millimeters form the molecular viscous layer. The name already implies that its dynamics are governed by molecular viscosity while above it is dominated by turbulent diffusion. The next 20 - 200 m form the *Prandtl layer* where surface friction is the strongest force. The transition to the free troposphere above ca. 1000 m, where dynamics are dominated by global circulation patterns, occurs in the *Ekman layer*. Here wind directions change steadily from the ground wind directions to the direction of the geostrophic winds of the free troposphere, i.e. isobaric wind stream caused by an equilibrium state between the forcing of pressure gradients and the Coriolis force. These layers combined form the planetary boundary layer or mixing layer, which is characterized by steady mixing. The planetary boundary layer is particularly interesting when studying the effects of emissions, either natural or anthropogenic, because most sources are ground-based. The global circulation patterns of the free troposphere are then responsible for the long-range transport of emitted trace gases and are briefly discussed in the following.

Global circulation is driven by the strong differences in incoming solar radiation between the tropics and higher latitudes. Even though the radiative forcing provides on average zero net energy input, it produces entropy which drives the circulation. In the tropics, large scale tropospheric circulation is triggered by convective latent heat release, leading to deep vertical motion. This occurs primarily in the zone of the strongest incoming solar radiation, the *Inner Tropical Convergence Zone* (ITCZ). The ITCZ is a narrow band of latitudes, moving back and forth across the equator, following the sun during the course of a seasonal cycle. There the uplift of hot humid air is most powerful. Once the convective air masses reach their level of neutral buoyancy at about 10 - 12 km, they cannot rise much further, start to flow poleward and typically descend at 30 - 35 degrees latitude in both hemispheres, since the poleward flow is constrained by conservation of angular momentum. This region is called the subtropical high pressure belt and is characterized by a downward wind component. The strong convection in the ITCZ leads to a rather low air pressure there, causing air near the ground to flow from higher latitudes towards the equator and simultaneously be deflected to the west by the Coriolis force: the trade winds. They are the dominating wind system in the tropics up to about 30 - 35 degrees of northern and southern latitude. The trade winds blow quite smoothly from northeast on the northern and from southeast on the southern hemisphere and converge in the ITCZ. This whole circulation pattern is referred to as *Hadley cell*. The descending branches of the Hadley circulation are undersaturated in water vapor and undergo adiabatic warming, because the moisture has largely been lost as rain during convection. This accounts for the hot, dry desert regions found in the subtropics and the humid green tropical regions.

Embedded within the Hadley cell are longitudinal circulation cells, which results in a break up of almost any cross-equatorial flow. This explains why there are noticeable inter-hemispheric differences in the distribution of trace gases, e.g. CO_2, despite its long life time. While horizontal tropospheric mixing times range between days and several weeks within one hemisphere, global mixing times are extended to a year or even more.

In the extratropics, meridional circulation is driven by pressure instabilities, caused by the temperature gradient between (sub-)tropical and higher latitudes, with a poleward flow in the upper troposphere and a return flow in the surface layer (west wind drift zone). At the so called polar front cold air masses from high latitudes and warmer air masses from the mid-latitudes collide. This region is characterized by low pressure which increases again towards the poles. At high polar latitudes there are circumpolar east winds up to a height of about 3 km. The winds are caused by cooled air, "falling" downward (catabatic winds) and deflected eastward by the Coriolis force.

2.1.2.2 Dynamics in the stratosphere

While the tropospheric circulation is thermally driven, the radiative equilibrium of the stratosphere (and mesosphere) is dynamically very stable. Apart from zonal flows (i.e. flow along latitude circles), associated with temperature gradients and the Coriolis force, and the meridional circulation resulting from the slight radiative imbalance caused by the annual cycle, there is also a meridional circulation pattern in the stratosphere. This circulation cannot be explained thermally, because persistent meridional motion requires a torque to move air masses across surfaces of constant angular momentum. As there are no external angular momentum sources in the atmosphere, such torques can only arise from angular momentum transfer by atmospheric motion. This transfer is induced by planetary waves and is also referred to as *wave-drag*. Planetary waves are the propagation of a local disturbance in the atmosphere, e.g. caused by topography. Some of these waves reach up into the stratosphere, where they drive the meridional circulation.

In the extra-tropical stratosphere, wave-drag comes mostly from planetary-scale *Rossby waves*. Rossby waves are caused in meridional flows by the rotation of the earth. These waves propagate into the stratosphere and drive a poleward circulation within the stratosphere, which leads to a descending motion in the extratropics and to an ascending motion in the tropics (*Brewer-Dobson circulation*). To be precise, the above discussed tropospheric upward motion in the tropics is not because of "hot air rising", but is rather mechanically driven by stratospheric wave-drag.

The meridional equatorward temperature gradient within the troposphere leads to an eastward zonal flow in both hemispheres. Maximum winds are achieved at the subtropical tropopause, which accounts for the rather famous jet streams. Within the stratosphere, the temperature minimum over the winter pole also leads to eastward flows, parallel to the troposphere, except that in the stratosphere the temperature gradient is concentrated more in sub-polar latitudes, shifting the jet maximum poleward. This leads to the so called *polar vortex*, because the circumpolar flow constitutes a vortex. In the summer hemisphere however, the temperature maximum over the pole leads to a change in wind direction in the stratosphere and the eastward zonal flows become westward winds. This is why there is hardly any meridional mixing in summer, whereas it is rather intense during winter time. Consequences can for example be seen in the global ozone distribution: ozone produced in the tropical stratosphere is transported to higher latitudes during winter while this transport breaks down during summer, causing lower ozone values in high latitudes during fall compared to spring.

The zonal winds of the summer stratosphere also stop Rossby waves from propagating into the stratosphere. So the Brewer-Dobson circulation is mainly a wintertime phenomenon. Moreover it is stronger in the Northern Hemisphere, because the distribution of land masses in the North is such as to generate stronger planetary waves. Since stronger downwelling at the pole implies warmer temperatures due to adiabatic warming, the Arctic winter stratosphere is usually warmer and has a weaker polar vortex than its Antarctic counterpart. In return the Antarctic polar vortex is typically very stable and colder. It confines polar air and provides the conditions for ozone hole chemistry (see 2.2.3). In spring, the vortex breaks down and the zonal wind pattern changes from winter to summer type (final warming). This causes fragments of the vortex to be transported to mid-latitudes, where e.g. ozone poor Antarctic air can reach the stratosphere over Australia and New Zealand.

In a simplified scheme it can be summarized that stratospheric circulation is driven by waves, while the temperature is determined by radiative equilibrium and circulation induced differences to that state. This renders the processes in the stratosphere a complex system of angular momentum and thermodynamical balances. For a detailed discussion see e.g. [*Sheperd* 2003].

2.1.2.3 Stratosphere-troposphere exchange

Of particular interest are the exchange processes between troposphere and stratosphere since all anthropogenic pollutants, except for e.g. exhaust gases of supersonic jets, are emitted into the troposphere and hence enter the stratosphere from there. The low stratospheric water content suggests that the main entry to the stratosphere occurs via the very cold tropical tropopause which acts as a cold trap. This is explained by the ascent of air in the ITCZ which continues through the tropopause into the stratosphere. In the extratropical stratosphere, the air generally descends and, thus, can enter the troposphere. This effect is strongest in the polar vortex and weakest in the summer hemisphere, and is, e.g., the origin of most of the ozone in the free troposphere. Additionally, there is dynamic mixing of stratospheric and tropospheric air by diabatic transport, i.e. transport of air masses with heat exchange. Adiabatic mixing between troposphere and stratosphere is also possible. The characteristic exchange times between lower and middle stratosphere range between some months and two years, while timescales for stratosphere-troposphere exchange are in the order of 15 - 18 months.

Further mechanisms for stratosphere-troposphere exchange are transports along isentrops (surface of constant potential temperature[3]) and tropopause folding events. The dissipation of planetary-scale Rossby waves in the winter time stratosphere is known as "wave breaking" [*Sheperd* 2003]: atmospheric waves grow in amplitude as they propagate upward and the density of the air decreases, which leads to intense mixing on isentropic surfaces. Stratospheric intrusions of air that sinks below the dynamical tropopause (2PVU-isosurface, see Excursion below) are known as tropopause folds. They are directly associated with the strength of the horizontal temperature gradient at the tropopause level. In a tropopause fold, dry and clean stratospheric air, rich of ozone and potential vorticity (see Excursion below), is transported downward to tropospheric levels. Observations of the circulation near folding events reveal that tropospheric air is lifted upward as well. This tropospheric air usually contains larger amounts of water vapor, aerosols and CO as typical stratospheric air. Thus CO is also a good tracer for troposphere-stratosphere transport. In the subtropics, the probability of fold events is particularly high over the Asian continent. And in fact, several tropopause folds have been detected on the Asian routes of the measurement flights of this work.

Excursion: Utilizing potential vorticity as tropopause definition The conservation of vorticity is a fundamental law of atmospheric dynamics. *Vorticity* describes the vortex strength of the circulation of air masses in a horizontal plane. The *Potential Vorticity* (PV)[4] is derived by combining the law of vorticity conservation and that of the conservation of mass. It characterizes the change in the absolute vorticity when an air mass is vertically stretched or compressed. Potential vorticity is typically given in units of PVU, i.e. Potential Vorticity Units. 1 PVU = 10^{-6} K$\cdot$m$^2\cdot$s$^{-1}\cdot$kg^{-1}. The steep gradient of the PV in the tropopause region implies the use of PV as tropopause definition instead of temperature. It is commonly suggested to define the extra tropical tropopause with PV $\approx$ 1.5 PVU, and with 1 PVU $\leq PV \leq$ 5 PVU in the subtropics. Near the equator, this definition fails due to the disappearing Coriolis force, which has a strong impact on the absolute vorticity.

In this work modeled PV values are utilized to determine the flight level either to be in the troposphere or stratosphere (see 5.3.2). Figure 2.2 shows an example of these PV values for a CARIBIC measurement flight from Frankfurt to Guangzhou/China. Plotted are PV and flight altitude in a vertical cross section as a function of time. On this day, the tropopause was highly structured along the flight track and two tropopause folds were within the flight route: One between point 4 and 6, the other between 8 and

---

[3] The potential temperature θ of an air parcel at pressure p and temperature T is the temperature the air parcel would acquire when adiabatically brought to a standard reference pressure p_0, usually 1013 hPa: $\theta = T \cdot (p_0/p)^a$. a depends on the ratio of the specific heat capacities at constant pressure and constant volume. For air, $a = 0.286$ can be used.

[4] The potential vorticity is defined as PV $= \eta/\rho \cdot d\theta/dz$ with the vorticity $\eta = 2\Omega \sin\phi + (\overrightarrow{\nabla} x \overrightarrow{v})_z$ (Ω: angular velocity of the earth rotation, ϕ: latitude, v: velocity of the air parcel), the air density ρ, the potential temperature θ and the altitude z. The potential vorticity is conserved along trajectories of air parcels.

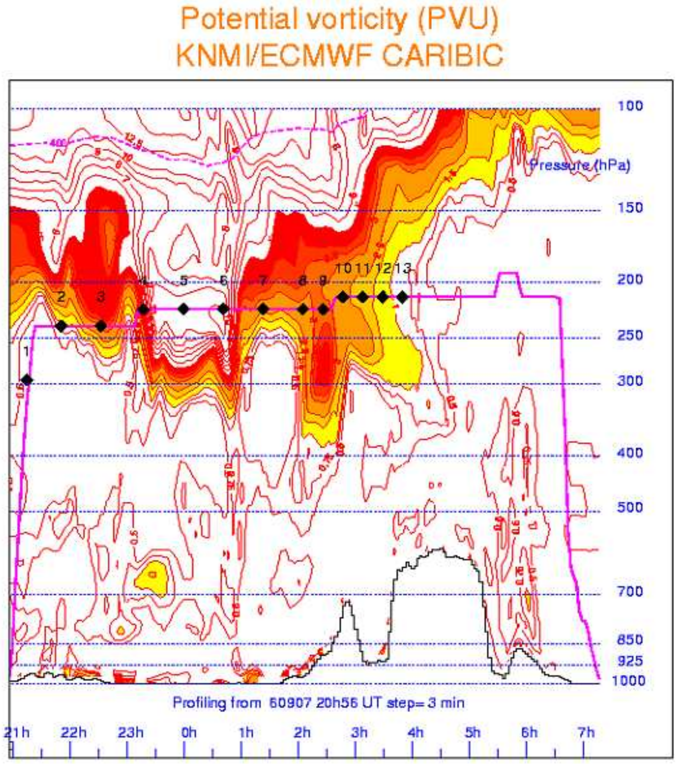

Figure 2.2: *Modeled potential vorticity values for a flight from Frankfurt/Main to Gunagzhou/China on September 8, 2006. The PV values (red contours) are shaded for values from 1 to 5 PVU (from yellow to red), indicating the tropopause. The flight track passes through two tropopause folds at 23h to 1h and from 2h to 4h UT. The black topography line shows the flight track crossing the Tibetan plateau.*

13, with these points denoting place and time of air sampling. The information gained from these plots is helpful for the interpretation of the DOAS measurements, because the height of the tropopause influences the vertical profile of e.g. ozone and nitrogen dioxide and thus also the radiative transfer (see 4.3).

To conclude, dynamical transport is one important variable determining global trace gas distributions. Some of the above discussed dynamical processes are shown in a simplified scheme in Figure 2.3. The selection represents the scientific focus of the CARIBIC aircraft project. This project is the framework of the spectroscopic measurements done in this work and is introduced in Section 5.1. For a more detailed description of atmospheric dynamics it is referred to corresponding literature, e.g. *Roedel* [2000].

While atmospheric dynamics are mainly responsible for the transport and mixing of species, atmospheric chemistry determines production, life times and depletion of atmospheric compounds. The following section gives an introduction to the chemistry of the trace gases measured within this work.

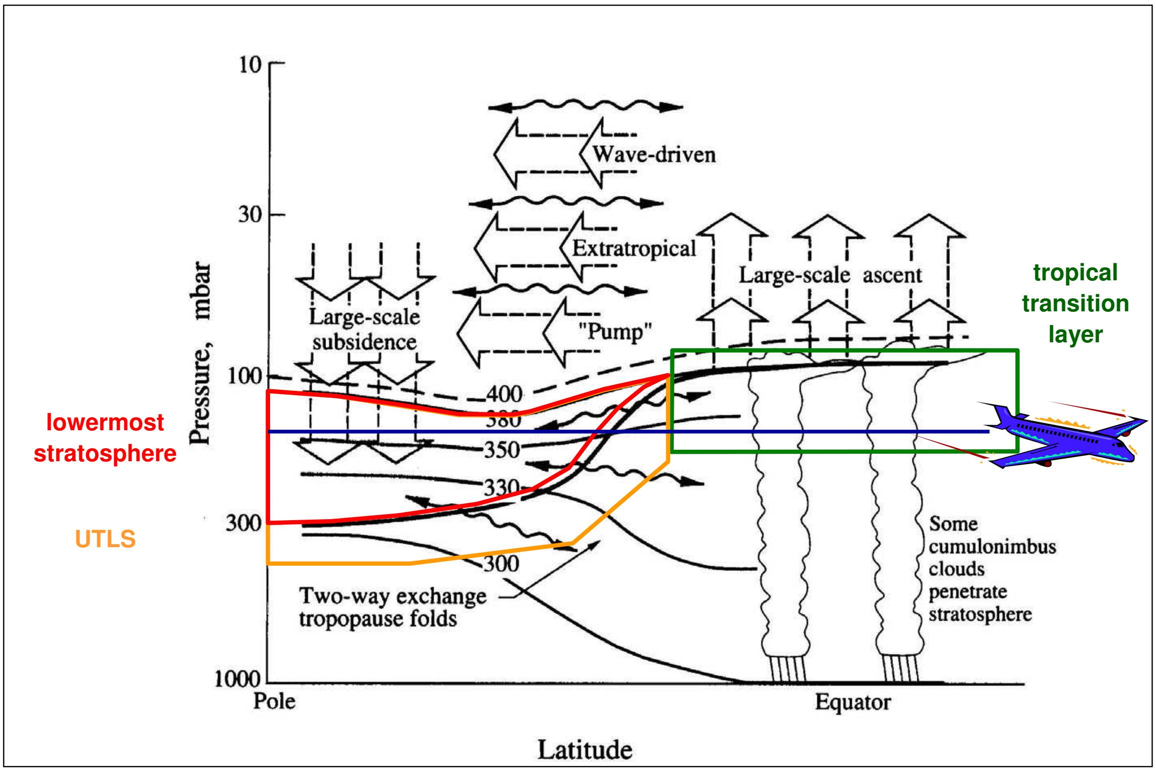

Figure 2.3: *Simplified scheme of global circulation processes shown as latitudinal cross section. Main regions covered by the measurement flights of this work are highlighted. Adapted from Holton et al. [1995].*

2.2 Atmospheric nitrogen oxides and ozone

Human induced changes on atmospheric chemistry are not only seen in the stratosphere (e.g. the ozone hole), but also in the troposphere, e.g. in urban smog episodes due to anthropogenic emissions of nitrogen and sulfur compounds as well as hydrocarbons and other organic compounds. Of these species, many are involved in ozone chemistry and they all affect human health, as they attack the respiratory tract and can possibly cause nausea, headaches or worse health problems. So does ozone, which, in the boundary layer, is a product of specific smog conditions and commonly known as summer smog.

With respect to atmospheric chemistry, the nitrogen compounds nitric oxide (NO) and nitrogen dioxide (NO_2) are among the most important trace gases, as both are radicals and thus highly reactive. NO and NO_2, often referred to as NO_x (see below), are involved in several chemical reactions and catalytic cycles that destroy ozone in the stratosphere, but they can also transfer ozone destructive halogen species into passive reservoir products. In the troposphere, reactions involving NO_x are a key sequence for the formation and destruction of ozone, thus affecting the radiative budget and the oxidation capacity [5] of the atmosphere.

While tropospheric ozone formation is influenced by anthropogenic emissions, stratospheric ozone, which constitutes about 90 % of the global ozone, is naturally formed. Lightning, biomass burning and soil releases constitute natural sources of NO_x, but today more than 50 % of the total emissions are from fossil fuel combustion and biomass burning due to arson. In consequence, tropospheric levels of NO_x have likely doubled over the last hundred years in the northern hemisphere, and exceed natural background levels (~ 10 ppt)[6] by several orders of magnitude in polluted urban air (up to 1 ppm) [*Seinfeld and Pandis* 1997]. The ratio of NO and NO_2, called *Leighton ratio*, is linked with ozone and introduced below. The joining sections give an overview of the most important chemical mechanisms involving nitrogen oxides and ozone chemistry.

2.2.1 The Leighton ratio

NO and NO_2 are rapidly converted into each other in the daytime atmosphere, therefore they are commonly summed up as NO_x ($:= NO + NO_2$).[7] All inorganic nitrogen species are summarized as NO_y.

The partitioning of NO and NO_2 during daytime is determined by:

$$\mathrm{NO} + \mathrm{O_3} \longrightarrow \mathrm{NO_2} + \mathrm{O_2} \tag{2.1a}$$

$$\mathrm{NO_2} + h\nu \longrightarrow \mathrm{NO} + \mathrm{O(^3P)} \qquad \lambda \leq 420\ nm \tag{2.1b}$$

$$\mathrm{O(^3P)} + \mathrm{O_2} + \mathrm{M} \longrightarrow \mathrm{O_3} + \mathrm{M} \tag{2.1c}$$

where M is an inert molecule needed for the conservation of momentum. This partitioning is ozone controlled, which is expressed by the *Leighton ratio L*:

$$L := \frac{[\mathrm{NO}]}{[\mathrm{NO_2}]} = \frac{J(\mathrm{NO_2})}{[\mathrm{O_3}] \cdot k} \tag{2.2}$$

with k denoting the *reaction rate constant*, which is a measure for the speed of the specific reaction. The unit of k depends on the reaction order n: $[k] = \mathrm{molec}^{-(n-1)} \cdot \mathrm{cm}^{(n-1)3} \cdot \mathrm{s}^{-1}$. J, the *photolysis frequency* in s^{-1}, is the analogue to k for photochemical

---

[5] The term *oxidation capacity* denotes the capability of the atmosphere to oxidize or otherwise degrade trace species emitted into it. This ability is crucial for the removal of pollutants and is also referred to as the *self-cleaning* capacity of the atmosphere. Very often the oxidation capacity is associated with the abundance of OH. However, many other oxidants (including O_2 and O_3) can contribute to the oxidation capacity as well.

[6] 1ppt = 1 parts per trillion, i.e 1 trace gas molecule among 1 trillion air molecules. Also used are the abbreviations ppm = parts per million and ppb = parts per billion

[7] Sometimes NO_x denotes NO, NO_2 *and* NO_3. Since NO_3 is not present in the sunlit atmosphere, because it is rapidly destroyed by photolysis, it is not included in NO_x in the following.

reactions.

The Leighton ratio depends on ozone concentration, the NO_2 photolysis rate and temperature. The percentage of NO_x present as NO_2 in equilibrium is defined as:

$$f_{NO2} := \frac{[\mathrm{NO_2}]}{[\mathrm{NO_x}]} = \frac{1}{1+L} \tag{2.3}$$

In the boundary layer, most NO_x is usually present as NO_2 ($f_{NO2} \approx 0.7, L \approx 0.4$). With increasing altitude, the Leighton ratio is shifted towards NO due to the temperature dependency of k_1 and higher NO_2 photolysis frequencies; at 10 km altitude f_{NO2} is about 0.4 (L = 1.5). In practice, however, NO_x and ozone chemistry is also controlled by other species like CO or volatile organic compounds. Therefore it is referred to Section 2.2.4. During night, all NO_x is shifted to NO_2, NO_3 and N_2O_5 (see next section), because no photolysis (reaction (2.1b)) takes place.

Primarily most NO_x is emitted as NO and subsequently transformed to NO_2 by reaction (2.1a). The dominating reactions leading to the formation of NO are described by the *Zeldovich mechanism* [*Zeldovich and Raizer* 1967]: In connection with high temperatures (> 2000° C) that occur in burning processes (e.g., any kind of fossil fuel combustion or biomass burning) or lightning, air molecules (particularly O_2) dissociate:

$$\mathrm{O_2 + M \rightleftharpoons O + O + M} \tag{2.4}$$

NO is subsequently formed in the Zeldovich reactions:

$$\mathrm{O + N_2 \rightleftharpoons NO + N} \tag{2.5a}$$
$$\mathrm{N + O_2 \rightleftharpoons NO + O} \tag{2.5b}$$

The equilibria (2.5) strongly depend on temperature and are shifted to the right side for high temperatures. If the gas is exposed to a rapid cooling process (i.e. faster than the time the system needs to achieve equilibrium), NO is "freezing out". Further sources of nitrogen oxides are microbiological processes in soils [*Yienger and II* 1995]. The transport of tropospheric NO_x to the stratosphere is only of minor importance, as the life time of NO_x is usually shorter than respective transport times.

2.2.2 Stratospheric nitrogen oxides

Nitrous oxide (N_2O) is the most important source of NO_x in the stratosphere. N_2O is emitted in the troposphere, where it is rather inert, in contrary to NO_x, with a lifetime of about 120 years. Tropospheric N_2O sources are both natural and anthropogenic. The major contributions come from oceans and tropical forests (soil), but also from chemical industry: N_2O is a widely used propellant and is found in artificial fertilizers. In consequence, the tropospheric N_2O level has risen with an average annual growth rate of ~ 0.75 ppb [*WMO* 2003] since preindustrial times. After it has been transported to the stratosphere, it is either photolyzed or oxidized to NO. 90 % of N_2O in the stratosphere are removed by photolysis:

$$\mathrm{N_2O} + h\nu \longrightarrow \mathrm{N_2} + \mathrm{O}(^1\mathrm{D}) \qquad \lambda \leq \mathit{298\ nm} \tag{2.6}$$

The remaining N_2O can be oxidized to NO with electronically excited oxygen radicals:

$$\begin{aligned} \mathrm{O}(^1\mathrm{D}) + \mathrm{N_2O} &\longrightarrow 2\,\mathrm{NO} && (58\ \%) && (2.7a)\\ &\longrightarrow \mathrm{N_2} + \mathrm{O_2} && (42\ \%) && (2.7b) \end{aligned}$$

The photolysis of NO and the subsequent reactions of N with NO act as a sink for NO_x in the upper stratosphere with the net reaction:

$$\mathrm{NO} + \mathrm{N} \longrightarrow \mathrm{N_2} + \mathrm{O} \tag{2.8}$$

During the day NO and NO_2 are in a photochemical equilibrium as described by the *Leighton ratio* (see 2.2.1). With the beginning of night, NO is rapidly converted to NO_2 due to missing NO_2 photolysis. NO_2 is then oxidized to NO_3 by O_3:

$$\mathrm{NO_2} + \mathrm{O_3} \longrightarrow \mathrm{NO_3} + \mathrm{O_2} \tag{2.9}$$

NO_3 does not exist during the day, because it photolyzes too rapidly. During night it reacts with NO_2 and builds the night time reservoir species N_2O_5:

$$\mathrm{NO_3} + \mathrm{NO_2} \longrightarrow \mathrm{N_2O_5} \tag{2.10}$$

N_2O_5 reacts back to NO_2 and NO_3 by collisional decomposition or photolysis during day:

$$\begin{aligned} \mathrm{N_2O_5} + \mathrm{M} &\longrightarrow \mathrm{NO_3} + \mathrm{NO_2} + \mathrm{M} && && (2.11a)\\ \mathrm{N_2O_5} + h\nu &\longrightarrow \mathrm{NO_2} + \mathrm{NO} + \mathrm{O_2} && \lambda \leq 1252\ \mathit{nm} && (2.11b) \end{aligned}$$

Once sunlight is present, all NO_3 is destroyed very quickly. Therefore the photolysis of the remaining NO_2 and of N_2O_5 is initiated in the morning. Since the photolysis of NO_2 proceeds some orders of magnitude faster than that of N_2O_5, the observed NO_2

concentration decreases in the morning until a photochemical steady state between NO and NO_2 via reactions (2.1) is established. Accordingly, the NO_2 concentration increases in the evening due to its reduced photolysis and the reaction of NO with O_3. The slow photolysis of N_2O_5 leads to an additional increase of the NO_2 concentration throughout the day. The result of these processes is a "tilted-u-shaped" diurnal variation of the NO_2 concentration.

The only daytime sink for NO_x is the reaction of NO_2 with OH:

$$NO_2 + OH \longrightarrow HNO_3 \tag{2.12}$$

while HNO_3 is usually removed from the atmosphere by precipitation. During long winter nights and especially during polar night, NO_2 is almost completely converted to its reservoir species N_2O_5 and HNO_3 by heterogeneous reactions, i.e. reactions in which the reactants are components of two or more phases (e.g. gaseous and solid or gaseous and liquid). N_2O_5 reacts with particles of *Polar Stratospheric Clouds* (PSCs)[8] in the following reactions:

$$N_2O_5 + HCl \xrightarrow{\text{heterog.}} HNO_3 + ClONO_2 \tag{2.13a}$$

$$N_2O_5 + H_2O \xrightarrow{\text{heterog.}} 2\,HNO_3 \tag{2.13b}$$

These processes lead to a pronounced seasonal variation of NO_x, with a strong concentration decrease during winter (*denoxification*). The strength of this seasonal cycle depends on temperature, duration of night time and is, as seasons themselves are, latitude dependent. Figure 2.4 shows two examples of yearly NO_2 cycles: one for sub-polar regions (Kiruna, North-Sweden), where the seasonal cycle is very pronounced with distinct NO_2 maxima during summer and minima during winter. The second example shows data measured in the Tropics (Paramaribo, Suriname, South America), where no PSCs occur and where the seasonal dependency is thus very weak.[9] The HNO_3 produced in reactions (2.13) remains in the cloud particles until the sedimentation of the PSCs. This can irreversibly remove inorganic nitrogen from the stratosphere (*denitrification*) and leads to stronger ozone depletion in polar spring (see 2.2.3).

An important question of stratospheric nitrogen chemistry is the contribution of individual species to the total NO_y abundance (all inorganic nitrogen spcecies), referred to as *NO_y partitioning.* It is determined by the different life times of the NO_y species. Both the production and destruction of HNO_3, are slow processes so HNO_3 has only a small impact on the diurnal variation of NO_x. The denoxification during polar winter

---

[8] PSCs consist usually of ice or acid particles and exist only in the very cold polar winter stratosphere. They appear often in very nice pearly colors.

[9] The presented data is analyzed by the author of this thesis. The measurements in Paramaribo represent one of the first long term series of atmospheric NO_2 columns in the Tropics.

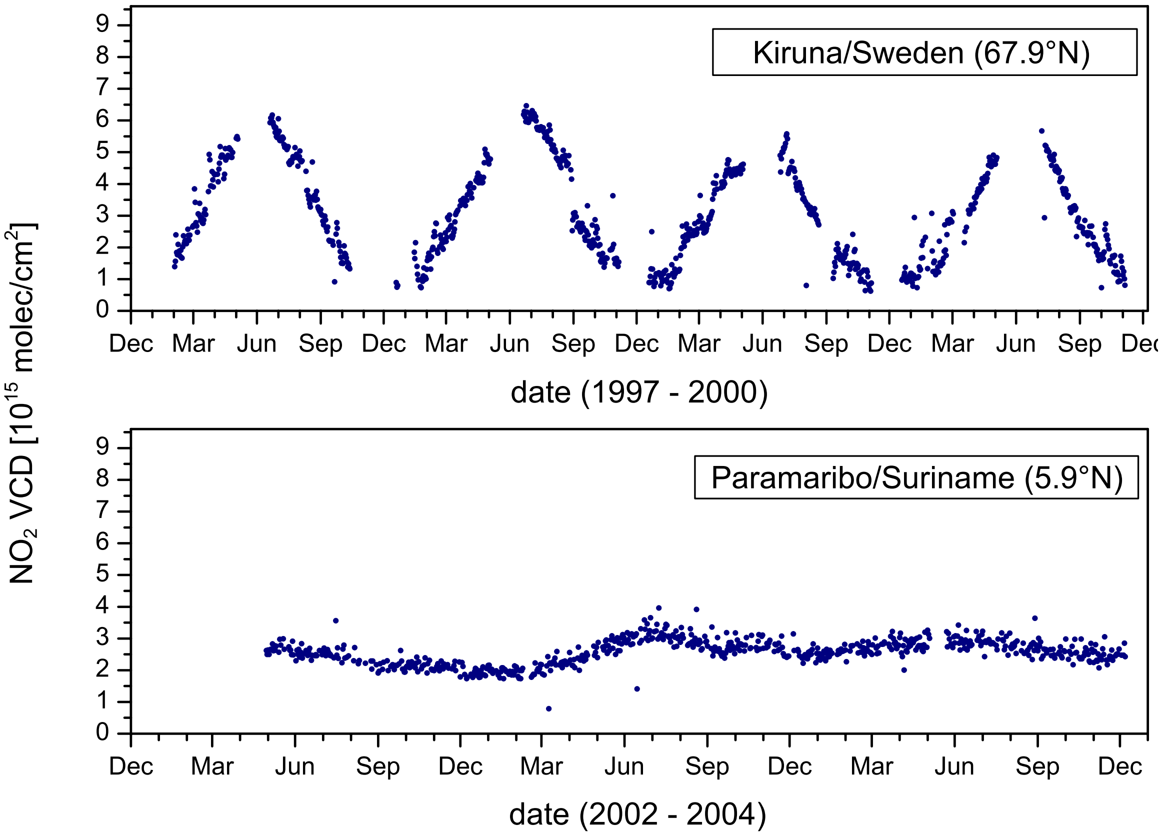

Figure 2.4: *Seasonal variation of* NO_2 *vertical column densities (VCD) from two ground-based DOAS measurements at different latitudes. Top panel:* NO_2 *vertical columns at high latitude, exhibiting a very pronounced seasonal cycle. Bottom Panel:* NO_2 *in the Tropics showing only a weak seasonal signature.*

however renders HNO_3 the by far dominant NO_y species in this time period (see above), being also an important prerequisite for the formation of the ozone hole (see 2.2.3). As N_2O is the major source of stratospheric NO_y, the distribution of NO_y and N_2O are photochemically linked (reactions (2.7a) and (2.6)). This correlation defines NO_y (= standard climatological NO_y) and any deviation is usually a sign of denitrification [*Rinsland et al.* 1996]. Below 30 km altitude, NO_y and N_2O are almost linearly anti-correlated. The slope of this lower stratospheric correlation is controlled by a combination of photochemistry and dynamics. Higher up (30 - 70 km) the correlation is dominated by the increasing destruction of NO_y by reaction (2.8).

2.2.3 Stratospheric ozone

More than 90 % of the total atmospheric ozone is located in the stratosphere, where the ozone profile shows a distinct concentration maximum at 15-30 km altitude. This maximum is often referred to as the ozone layer (see Figure 2.5), where most absorption of the harmful UV radiation takes place.

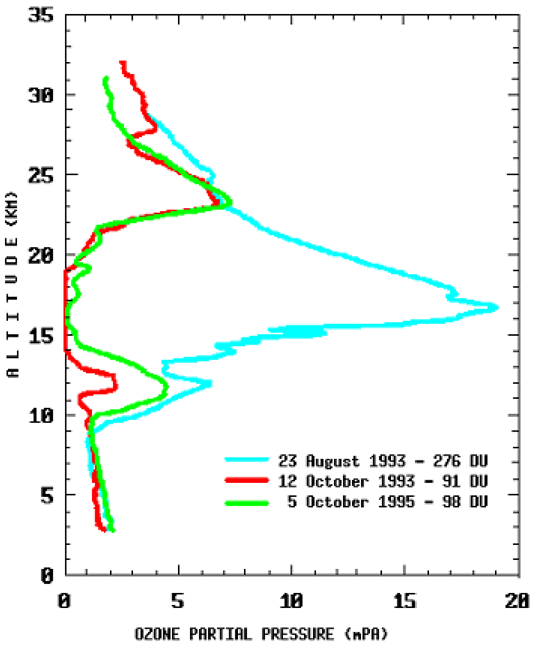

Figure 2.5: *Ozone profiles measured over the South Pole by balloon ozone sondes. Light blue denotes a regular ozone profile, whereas red and green show values for ozone hole periods. The total ozone columns are given in Dobson Units (DU)*[10]*. Adapted from http://www.cpc.noaa.gov.*

In 1930 the first theory on the photochemical formation of ozone in the stratosphere was proposed by *Chapman* [1930], predicting a maximum around 20 km altitude. *Chapman* describes the formation and destruction of ozone in the stratosphere by the so called *odd-oxygen chemistry*. The production of ozone is initiated by the photolysis of molecular oxygen:

$$\mathrm{O_2} + h\nu \longrightarrow 2\,\mathrm{O}(^3\mathrm{P}) \qquad \lambda \leq 242\ nm \tag{2.14a}$$

$$\mathrm{O}(^3\mathrm{P}) + \mathrm{O_2} + \mathrm{M} \longrightarrow \mathrm{O_3} + \mathrm{M} \tag{2.14b}$$

Ozone is formed via the reaction (2.14b) of $\mathrm{O} + \mathrm{O_2}$ with a collision partner M. The ozone destruction proceeds via photolysis with UV radiation:

---

[10] A Dobson Unit is a common measure for vertical ozone columns. The unit is named after G.M.B. Dobson, one of the first scientists to investigate atmospheric ozone. 100 DU is defined to be a layer of pure ozone with 1 mm thickness at standard temperature and pressure.

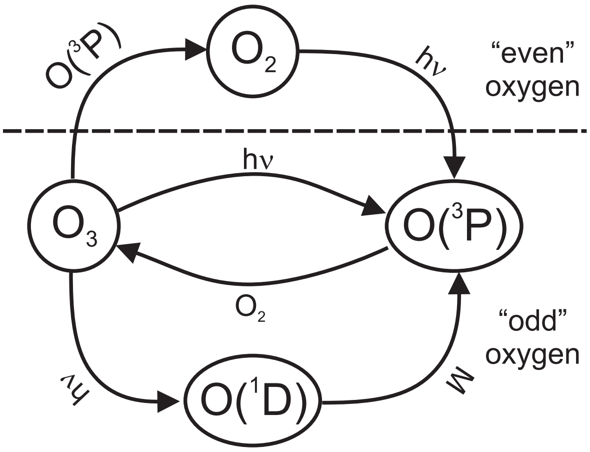

Figure 2.6: *Schematic diagram of the Chapman Cycle.*

$$
\begin{aligned}
O_3 + h\nu &\longrightarrow O_2 + O(^1D) && \lambda \leq 320\ nm && (2.15a)\\
O(^1D) + M &\longrightarrow O(^3P) + M && && (2.15b)\\
O_3 + h\nu &\longrightarrow O_2 + O(^3P) && \lambda \leq 1180\ nm && (2.15c)\\
2\,O(^3P) + M &\longrightarrow O_2 + M && && (2.15d)\\
O(^3P) + O_3 &\longrightarrow 2\,O_2 && && (2.15e)
\end{aligned}
$$

The photolysis of O_2 (2.14a) and thus the O_3 production mainly takes place in the upper stratosphere where radiation at short wavelengths occurs with high intensity. Together with the O_3 photodissociation reactions (2.15a) and (2.15c) an equilibrium builds up. Note that by O_3 photolysis atomic oxygen is produced which reacts back to O_3 in the order of seconds (2.14b). Therefore the timescales on which these reactions occur need to be considered. This leads to the definition of the *odd* and *even* oxygen groups. Species can be transformed within their own group on short timescales while the lifetime of the whole group is rather long. A sketch of the Chapman cycle and its groups is shown in Figure 2.6.

By observations it soon became clear that the Chapman cycle alone cannot explain the measured ozone profiles. Model calculations including only oxygen chemistry overestimated the stratospheric ozone abundance by a factor of two. Therefore additional ozone sinks must exist. In the following years the observed lower ozone levels were subsequently explained by stratospheric chemistry cycles involving species such as hydrogen and nitrogen as well as halogen compounds. These compounds all destroy ozone in catalytic reactions:

$$O_3 + X \longrightarrow O_2 + XO \tag{2.16a}$$

$$O(^3P) + XO \longrightarrow O_2 + X \tag{2.16b}$$

$$\text{net:} \quad O(^3P) + O_3 \longrightarrow O_2 + O_2$$

where the radical groups HO_x, NO_x, ClO_x and BrO_x serve as X or as XO respectively, e.g. in the HO_x cycle X denotes OH and XO stands for HO_2. The HO_x cycle, explained next, denotes the first of numerous catalytic reaction cycles proposed for the destruction of ozone. The contribution of the most important catalytical cycles to the total ozone depletion is shown in Figure 2.7.

The HO_x cycle A set of ozone destroying reaction cycles, involving hydrogen oxides, was first proposed by *Bates and Nicolet* [1950]:

$$O + OH \longrightarrow O_2 + H \tag{2.17a}$$

$$H + O_2 + M \longrightarrow HO_2 + M \tag{2.17b}$$

$$O + HO_2 \longrightarrow O_2 + OH \tag{2.17c}$$

$$\text{net:} \quad 2\,O \longrightarrow O_2$$

$$O + OH \longrightarrow O_2 + H \tag{2.18a}$$

$$H + O_3 + M \longrightarrow OH + O_2 + M \tag{2.18b}$$

$$\text{net:} \quad O + O_3 \longrightarrow 2\,O_2$$

$$O_3 + OH \longrightarrow O_2 + HO_2 \tag{2.19a}$$

$$O + HO_2 \longrightarrow OH + O_2 \tag{2.19b}$$

$$\text{net:} \quad O + O_3 \longrightarrow 2\,O_2$$

OH is produced in the stratosphere by the reaction of water vapor with $O(^1D)$. Since the cold tropopause prevents tropospheric water vapor from entering the stratosphere, water vapor is produced in the stratosphere by the oxidation of methane (CH_4):

$$CH_4 + O(^1D) \longrightarrow OH + CH_3 \tag{2.20a}$$

$$CH_4 + OH \longrightarrow H_2O + CH_3 \tag{2.20b}$$

$$O(^1D) + H_2O \longrightarrow 2\,OH \tag{2.20c}$$

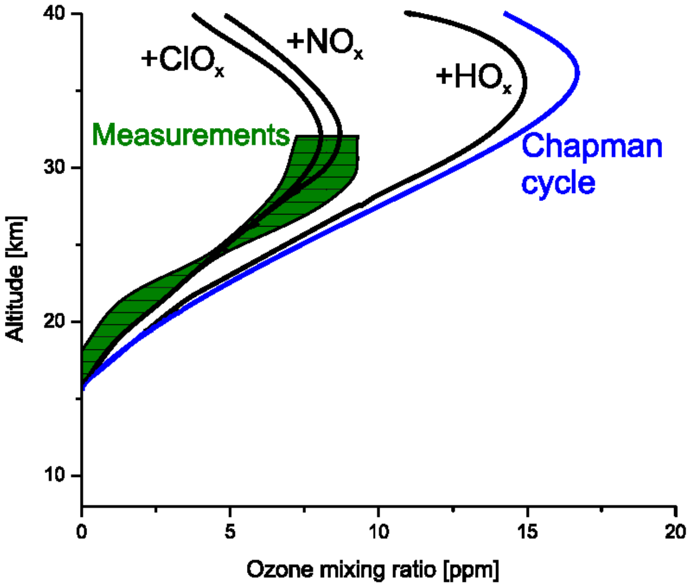

Figure 2.7: *Comparison between observed and modeled stratospheric ozone mixing ratios by taking only the Chapman cycle or additionally HO_x, NO_x and ClO_x chemistry into account. Adapted from Röth [1994].*

The compound responsible for the conversion of ozone to molecular oxygen (OH) is restored after one cycle and therefore remains available for the destruction of ozone unless it is removed by other sinks. This is why catalytic reactions have such a strong impact on the ozone budget even if their concentration is by far smaller than that of ozone. The HO_x cycle is particularly important for the ozone budget in the lower stratosphere (10 - 15 km altitude), where the catalytic cycles (2.17) to (2.19) are responsible for about 80 % of the total ozone loss processes.

The NO_x cycle This cycle involves nitrogen oxides via the following reactions [*Crutzen* 1970; *Johnston* 1971]:

$$O_3 + NO \longrightarrow O_2 + NO_2 \tag{2.21a}$$
$$O + NO_2 \longrightarrow NO + O_2 \tag{2.21b}$$

$$\text{net:} \qquad O + O_3 \longrightarrow 2\,O_2$$

$$\begin{aligned}
O_3 + NO &\longrightarrow O_2 + NO_2 && (2.22a)\\
NO_2 + O_3 + M &\longrightarrow NO_3 + O_2 && (2.22b)\\
NO_3 + h\nu &\longrightarrow NO + O_2 && (2.22c)\\
\hline
\text{net:} \quad 2\,O_3 + h\nu &\longrightarrow 3\,O_2
\end{aligned}$$

The NO_x cycles (2.21) and (2.22) are particularly for the ozone budget in the middle stratosphere (30 - 40 km altitude), where they are responsible for 60 - 70 % of the odd oxygen loss. An anthropogenic influence on the stratospheric NO_x budget is given by the increasing abundance of the source gas N_2O (see 2.2.2), but also by direct emissions of nitrogen oxides in the stratosphere from supersonic aircrafts.

The ClO_x cycle Even in the 1970s it was postulated by *Molina and Rowland* [1974] that the release of industrially produced halocarbons, in particular the chlorofluorocarbons (CFCs) $CFCl_3$ and CF_2Cl_2, could cause severe depletion of stratospheric ozone by reactions involving the photolytical products from CFC radicals Cl and ClO as catalysts. The following catalytic cycles involve also combined chlorine bromine chemistry. For a more detailed bromine chemistry, see Section 2.3.

$$\begin{aligned}
Cl + O_3 &\longrightarrow ClO + O_2 && (2.23a)\\
ClO + O &\longrightarrow Cl + O_2 && (2.23b)\\
\hline
\text{net:} \quad O + O_3 &\longrightarrow 2\,O_2
\end{aligned}$$

$$\begin{aligned}
Cl + O_3 &\longrightarrow ClO + O_2 && (2.24a)\\
Cl + O_3 &\longrightarrow ClO + O_2 && (2.24b)\\
ClO + ClO + M &\longrightarrow Cl_2O_2 + M && (2.24c)\\
Cl_2O_2 + h\nu &\longrightarrow Cl + ClO_2 && (2.24d)\\
ClO_2 + M &\longrightarrow Cl + O_2 + M && (2.24e)\\
\hline
\text{net:} \quad 2\,O_3 &\longrightarrow 3\,O_2
\end{aligned}$$

$$\begin{aligned} Cl + O_3 &\longrightarrow ClO + O_2 && (2.25a)\\ Br + O_3 &\longrightarrow BrO + O_2 && (2.25b)\\ BrO + ClO &\longrightarrow Br + ClO_2 && (2.25c)\\ ClO_2 + M &\longrightarrow Cl + O_2 + M && (2.25d)\\ \hline \text{net:} \quad 2\,O_3 &\longrightarrow 3\,O_2 \end{aligned}$$

Under normal (non - ozone hole, see below) conditions, most of the chlorine in the stratosphere is usually bound in the reservoir species hydrogen chloride (HCl) and chlorine nitrate ($ClONO_2$) formed in the following reactions:

$$\begin{aligned} Cl + CH_4 &\longrightarrow HCl + CH_3 && (2.26a)\\ ClO + NO_2 + M &\longrightarrow ClONO_2 + M && (2.26b) \end{aligned}$$

Only about 10 % of the stratospheric inorganic chlorine is available in its activated forms Cl, ClO and Cl_x for the above introduced reaction cycles. This situation changes significantly during polar winter and is closely related to NO_x: Reaction (2.26b) shows that NO_x does not only lead to ozone depletion via the NO_x cycle, but that NO_x also plays a crucial role in slowing down ozone destruction by transforming other ozone depleting species into their reservoir gases. Besides (2.26b), NO_x is also involved in the HO_x cycle, transforming OH via NO_2 into HNO_3 (equation (2.12)).

In polar winter however, when NO_x is transformed into its reservoir species and when the denoxification process is very pronounced (see 2.2.2), a different chemistry starts to take place: Under the special conditions of the polar winter stratosphere (darkness, temperatures below 190° K and a stable polar vortex, see 2.1.2.2) heterogeneous reactions on the surface of polar stratospheric clouds (PSCs) can transform 30 - 60 % of chlorine into activated forms, e.g. into Cl_2 by:

$$ClONO_2 + HCl \xrightarrow{\text{heterog.}} Cl_2 + HNO_3 \qquad (2.27a)$$

As a result, molecular chlorine can accumulate inside the polar vortex during polar winter, while at the same time sedimentation of HNO_3-containing PSCs takes place and the reservoirs of nitrogen oxides are effectively removed from the polar vortex (denitrification, see 2.2.2). As soon as sunlight is present during polar spring the photolysis of Cl_2

$$Cl_2 + h\nu \longrightarrow Cl + Cl \qquad (2.28a)$$

produces chlorine atoms which can efficiently destroy ozone in the catalytic cycles

(2.23), (2.24) and - if bromine is present - (2.25). During polar spring these processes lead to the stratospheric ozone hole, where, over Antarctica, typically all ozone at about 15 - 20 km altitude is destroyed (see also Figure 2.5). These reactions are particularly efficient, because the formation of $ClONO_2$ by reaction (2.26b) cannot take place due to missing NO_x. The ozone depletion continues until the polar vortex breaks up and NO_x is restored by inflow from mid-latitudes.

In summary, the consideration of all catalytic cycles described above leads to an ozone budget in the stratosphere which is consistent with the observations [*Molina and Rowland* 1974; *Molina and Molina* 1987; *McElroy et al.* 1986].

2.2.4 Tropospheric nitrogen oxides and ozone

In the troposphere, NO_x and ozone chemistry is generally different from the stratosphere: Reactions (2.21) of the NO_x cycle are negligible due to low concentrations of atomic oxygen, and ozone production via reactions (2.14) of the Chapman cycle needs UV light below 242 nm, which is - thanks to stratospheric ozone - not available in the troposphere. While NO_x sources are tropospheric already, it was commonly assumed until the late 1970s that tropospheric ozone has its origin in the stratosphere (e.g. [*Junge* 1963]). Stratospheric ozone was assumed to mix through the tropopause region, exhibiting a gradient towards the earth's surface, which was also thought to be the dominant sink. Today it is believed that only about 10 % of the tropospheric ozone has its origin in the stratosphere. Tropospheric sources of ozone are given by NO_x chemistry and reactions involving methane and other reactive hydrocarbons [*Fishman and Crutzen* 1978], as well as reactions with CO and *Volatile Organic Compounds* (VOCs). The oxidation of these species in the presence of NO_x in most cases results in ozone production. For very high levels of NO_x, however, a further increase of NO_x does not lead to higher ozone production anymore; this phenomenon is called the VOC-limited regime and is described below.

A key sequence for the formation *and* destruction of tropospheric ozone are reactions (2.1) involving NO_x. In areas with elevated NO_x (10 - 30 ppt), nitrogen and hydrogen oxides are able to produce ozone by reactions with CO, methane (CH_4) or higher hydrocarbons and VOCs. The ozone production, e.g. by oxidation of CO is initiated by a reaction with OH:

$$
\begin{aligned}
\mathrm{CO} + \mathrm{OH} &\longrightarrow \mathrm{CO_2} + \mathrm{H} && \text{(2.29a)}\\
\mathrm{H} + \mathrm{O_2} + \mathrm{M} &\longrightarrow \mathrm{HO_2} + \mathrm{M} && \text{(2.29b)}\\
\mathrm{HO_2} + \mathrm{NO} &\longrightarrow \mathrm{OH} + \mathrm{NO_2} && \text{(2.29c)}\\
\mathrm{NO_2} + h\nu &\longrightarrow \mathrm{NO} + \mathrm{O} && \text{(2.29d)}\\
\mathrm{O_2} + \mathrm{O} + \mathrm{M} &\longrightarrow \mathrm{O_3} + \mathrm{M} && \text{(2.29e)}\\
\hline
\text{net:} \quad \mathrm{CO} + 2\,\mathrm{O_2} &\longrightarrow \mathrm{CO_2} + \mathrm{O_3}
\end{aligned}
$$

In the presence of NO the following reaction

$$\mathrm{NO} + \mathrm{HO_2} \longrightarrow \mathrm{NO_2} + \mathrm{OH} \tag{2.30}$$

competes with the ozone *destructive* reaction of NO with O_3 to form NO_2 (reaction (2.1a)). With NO sources being primarily in urban areas, the freshly emitted NO reacts via (2.1a) with already present ozone. So NO_x can also cause ozone loss. In fact, during ozone smog periods ozone concentrations in cities can be lower than in the rural areas around, where neither NO sources nor primarily higher ozone values are found. The plumes of NO_x-rich air are then transported by wind to the countryside. Since sunlight is needed to produce new NO from NO_2 (reaction (2.1b)), ozone smog is a typical problem of long and sunny summer days.

The oxidation of CH_4 and VOCs leading to ozone production is more complex, as several branchings of reaction paths occur. In general, peroxy radicals (RO_2) are produced that can oxidize NO to NO_2 in analogy to (2.30):

$$\mathrm{NO} + \mathrm{RO_2} \longrightarrow \mathrm{NO_2} + \mathrm{RO} \tag{2.31}$$

The peroxy radical family consists of HO_2 and RO_2 with R representing the unreactive organic part of the molecule. Thus the oxidation of CO and VOCs leads to ozone production via (2.1b) and (2.1b), if NO_x levels are high enough to compensate the ozone losses of the HO_x loss cycle (see 2.2.3). This holds true for NO_x concentrations above a 10 - 30 ppt threshold. This threshold typically separates rural areas with a background NO_x concentration of about 10 ppt from urban areas, that exhibit higher concentrations. Below this threshold, CO and hydrocarbons instead lead to destruction of ozone:

$$\begin{aligned}
\mathrm{CO} + \mathrm{OH} &\longrightarrow \mathrm{CO_2} + \mathrm{H} && \text{(2.32a)}\\
\mathrm{H} + \mathrm{O_2} + \mathrm{M} &\longrightarrow \mathrm{HO_2} + \mathrm{M} && \text{(2.32b)}\\
\mathrm{HO_2} + \mathrm{O_3} &\longrightarrow \mathrm{OH} + 2\,\mathrm{O_2} && \text{(2.32c)}\\
\hline
\text{net:} \qquad \mathrm{CO} + \mathrm{O_3} &\longrightarrow \mathrm{CO_2} + \mathrm{O_2}
\end{aligned}$$

To conclude: For NO_x levels above 10 - 30 ppt (i.e. for most regions of the world except for very clean, remote regions), ozone is formed.

For very high NO_x concentrations, however, up to several 100 ppb in heavily polluted urban air, reaction (2.12) removes NO_x from the system and competes with reactions of OH with CO (2.29a) and VOCs. In this case, increasing NO_x emissions can reduce ozone concentrations if not enough VOCs are present for the formation of HO_2 and RO_2. This situation is called the *VOC limited regime*, in contrast to the *NO_x*

limited regime, where ozone increases with increasing NO_x emissions. For a successful strategy against ozone pollution in cities, it is therefore crucial to distinguish between VOC limited and NO_x limited regimes and to focus on the reduction of the limiting pollutants.

Besides the removal of NO_2 by OH producing HNO_3 (equation (2.12)), night time reactions via NO_3 and N_2O_5 and the heterogeneous reactions of N_2O_5 with aerosols as described in Section 2.2.2, are further NO_x sinks. The produced HNO_3 is finally removed from the atmosphere by precipitation, which is apart from H_2SO_4 the important constituent of acid rain, causing severe damage to ecosystems.

In Figure 2.8 a scheme of the coupled tropospheric NO_x and O_3 chemistry is presented, summarizing the above discussed reactions.

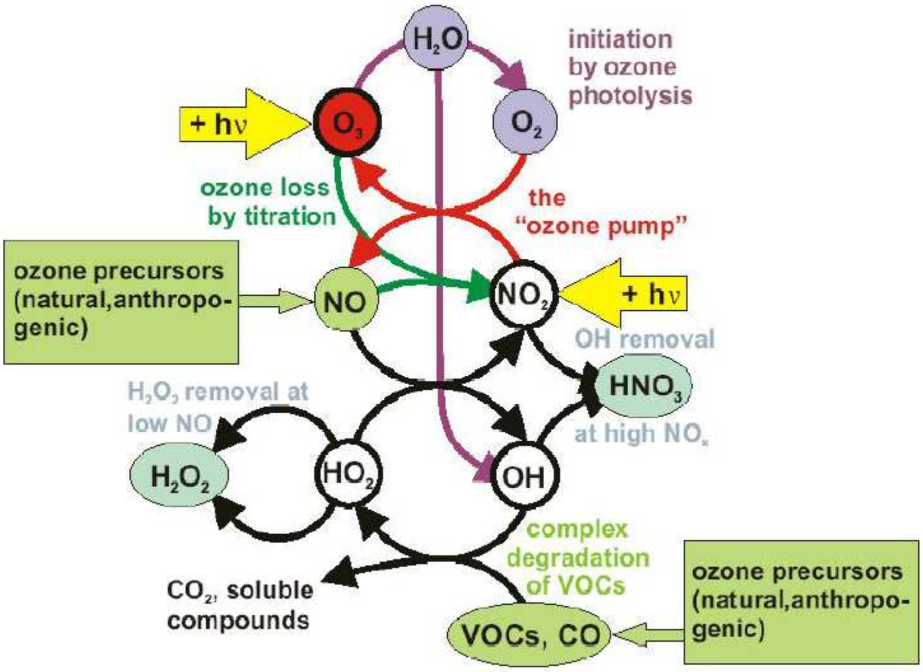

Figure 2.8: *Scheme of tropospheric NO_x and O_3 chemistry. Adapted from Schurath [2003].*

2.3 Atmospheric bromine oxide

Bromine (Br) is found in the seventh group of the periodic table, the halogens, together with Fluorine (F), Chlorine (Cl), Iodine (I) and Astatine (As). Halogens are very reactive, because they lack only one electron before reaching an inert gas configuration. Among the existing five halogens, chlorine, bromine and iodine play important roles in atmospheric chemistry and are associated with stratospheric ozone depletion (see also Section 2.2.3), whereas flour species are much more stable and are thus of minor importance for stratospheric chemistry. Astatine, in contrast, is a solid intermediate in radioactive decay of e.g. Bismuth. From chlorine over bromine to iodine, the respective compounds are less stable and, thus, their ozone destruction potential increases. Chlorine represents a major contribution to ozone destruction due to its significant stratospheric abundances, whereas the atmospheric bromine load is much smaller ($\sim$ 0.6 % of chlorine), but compensated for by being about 50 times more efficient in ozone depletion. Even though iodine is observed in the troposphere, the contribution of iodine species to ozone deletion is still not totally clear as there are no exact measurements of its stratospheric load.

The sources of stratospheric reactive bromine ($BrO_x = Br + BrO$) are about half natural and half anthropogenic. The most important source is methyl bromide (CH_3Br), released by biomass burning as well as by oceans and, with a smaller contribution, coming from agriculture and leaded gasoline. Another important source are halogenated hydrocarbon gases (halons) mostly used in fire extinguishers. Although controlled by the Montreal protocol, their global mean concentration is still slightly increasing, caused by the use of large halon stocks and a continuous production in developing countries. The mean annual growth rate, however, is much smaller than the rates observed in the mid-1990s [*Dorf* 2005]. The overall bromine trend is dominated by anthropogenic emissions, mainly by halons, as they exhibit a sufficiently long lifetime to be transported into the stratosphere. The total stratospheric Br_y load is around 20 ppt, with most of it being present as BrO. There is very likely a bromine influx of around 3 ppt from the troposphere to the stratosphere [*Pfeilsticker et al.* 2000].

Even after the discovery of the stratospheric ozone hole, halogen compounds were not thought to be of importance for tropospheric chemistry. This view changed when sudden ozone losses in the arctic boundary layer were observed, coinciding with high levels of bromine [*Barrie et al.* 1988]. By now, these events have been reported for both, the Arctic (e.g. [*Hausmann and Platt* 1994; *McElroy et al.* 1999; *Hönninger et al.* 2004; *Peters et al.* 2005]) and the Antarctic (e.g. [*Kreher et al.* 1997; *Frieß* 2001; *Frieß et al.* 2004]) boundary layer during polar sunrise, and they are often referred to as *polar tropospheric ozone hole* or *polar Ozone Depletion Event (ODE)*. BrO clouds, i.e. air masses characterized by unusually high BrO concentrations, covering extended areas of several million square kilometers in both hemispheres, are regularly observed during polar spring by satellite observations [*Wagner and Platt* 1998; *Richter et al.* 1998; *Hegels et al.* 1998]. Liberation from sea salt, the sea salt aerosol or the surface of the Arctic sea ice represent sources of the observed BrO. Particularly sea ice surfaces, strongly enriched in sea salt, are of importance: Surface brines (i.e. a liquid layer with high salinity on frozen sea ice) and frost flowers (i.e. fragile ice crystals highly enriched in sea salt on young sea ice) or freshly formed sea ice provide surfaces for heterogeneous bromine release. Long-term observations by the GOME (Global Ozone Monitoring Experiment) satellite instrument indicate that these areas increased by 10% between 1996 and 2001 [*Hollwedel et al.* 2004].

Enhanced BrO in the boundary layer and simultaneous ozone depletion has also been detected at salt lakes e.g. by *Hönninger et al.* [2004] and *Stutz et al.* [2002], at the Dead Sea [*Hebestreit et al.* 1999] and the Caspian Sea [*Wagner et al.* 2001]. Studies by *Van Roozendael et al.* [2000] suggest a free tropospheric background of 1 to 3 ppt BrO, as inferred from to multi-platform observations, and similar findings were published in 2002 [*Van Roozendael et al.* 2002]. BrO levels in the same order were reported for the mid-latitude marine boundary layer by *Leser et al.* [2003] and *Saiz-Lopez and Plane* [2004]. In recent years, high amounts of BrO were found in volcanic plumes [*Bobrowski et al.* 2003; *Bobrowski* 2005].

Bromine radicals in the troposphere are formed by photolysis of dihalogens or other halogen precursor compounds. Since the following reaction paths are found analogous for chlorine and iodine, these three halogen atoms are now represented by X. Upon release, halogen atoms react immediately with O_3 :

$$\mathrm{X} + \mathrm{O_3} \longrightarrow \mathrm{XO} + \mathrm{O_2} \tag{2.33}$$

When the oxides photolyze, O_3 and the halogen radical are reformed and no net reaction occurs. Among the main ozone destruction paths, also reactions involving HO_x occur:

$$\begin{aligned}
\mathrm{X} + \mathrm{O_3} &\longrightarrow \mathrm{XO} + \mathrm{O_2} && \text{(2.34a)}\\
\mathrm{XO} + \mathrm{HO_2} &\longrightarrow \mathrm{HOX} + \mathrm{O_2} && \text{(2.34b)}\\
\mathrm{HOX} + h\nu &\longrightarrow \mathrm{X} + \mathrm{OH} && \text{(2.34c)}\\
\mathrm{OH} + \mathrm{CO} + \mathrm{O_2} &\longrightarrow \mathrm{CO_2} + \mathrm{HO_2} && \text{(2.34d)}\\
\hline
\text{net:} \quad \mathrm{CO} + \mathrm{O_3} &\longrightarrow \mathrm{CO_2} + \mathrm{O_2}
\end{aligned}$$

Thus halogens also affect the oxidation capacity of the atmosphere. When BrO levels are sufficiently high, e.g. during polar spring time, the two branches of the BrO self reaction represent a strong catalytic O_3 destruction cycle:

$$\begin{aligned}
&2\,(\mathrm{BrO} + \mathrm{O_3} \longrightarrow \mathrm{BrO} + \mathrm{O_2}) && && \text{(2.35a)}\\
&\mathrm{BrO} + \mathrm{BrO} \longrightarrow 2\,\mathrm{Br} + \mathrm{O_2} && |\mathrm{BrO} + \mathrm{BrO} \longrightarrow \mathrm{Br_2} + \mathrm{O_2} && \text{(2.35b)}\\
&\qquad |\mathrm{Br_2} + h\nu \longrightarrow 2\,\mathrm{Br} && && \text{(2.35c)}\\
\hline
&\text{net:} \quad 2\,\mathrm{O_3} \longrightarrow 3\,\mathrm{O_2}
\end{aligned}$$

In the troposphere, merely the BrO self reaction and the BrO - HO_2 reaction are of importance, whereas during stratospheric ozone depletion events, ozone destruction is dominated by the ClO self reaction and the BrO - ClO cross reaction. Halogen oxide cross reactions are of importance in the stratosphere as well and might also play a role in tropospheric ozone loss [*von Glasow and Crutzen* 2003]:

$$
\begin{aligned}
\mathrm{X} + \mathrm{O_3} &\longrightarrow \mathrm{XO} + \mathrm{O_2} && \text{(2.36a)}\\
\mathrm{Y} + \mathrm{O_3} &\longrightarrow \mathrm{YO} + \mathrm{O_2} && \text{(2.36b)}\\
\mathrm{XO} + \mathrm{YO} &\longrightarrow \mathrm{X} + \mathrm{Y} + \mathrm{O_2} && \text{(2.36c)}\\
\hline
\text{net:} \quad 2\,\mathrm{O_3} &\longrightarrow 3\,\mathrm{O_2}
\end{aligned}
$$

with Y denoting a second halogen, different from X. In regions with elevated NO_x, the formation of halogen nitrates can be important. Depending on local conditions, these compounds either decompose thermally, photolyze or react with water.

Apart from the effects of halogens on ozone chemistry and on the HO_x budget, there also exist important links between halogen chemistry and the sulfur cycle: Bromine and chlorine are involved in the oxidation of DMS, a volatile sulphur compound mainly produced by phytoplankton, thus reducing the yield of gas phase SO_2. This again leads to a reduced production of new sulfate particles, which serve as cloud condensation nuclei (CCN). Bromine also oxidizes elemental mercury, which leads to the formation of highly toxic bioaccumulative Hg(II), affecting human health as well as ecosystems, in particular in regions enriched with reactive bromine like the polar regions [*Lindberg et al.* 2001; *Platt and Hönninger* 2003; *Simpson and Domine* 2005]. An overview of the most important halgen related processes is provided in Figure 2.9.

2.4 Atmospheric formaldehyde and nitrous acid

Formaldehyde (HCHO) and nitrous acid (HONO) exert both an influence on the oxidizing capacity of the atmosphere, since they are involved in reaction cycles that can lead to the formation of OH.

Formaldehyde is an important high-yield intermediate in the oxidation mechanism of hydrocarbons in the troposphere [*Chance et al.* 2000]. Daytime decomposition reactions of HCHO are associated with the formation of CO and highly reactive odd-hydrogen radicals. The overall net change of HO_x due to hydrocarbon oxidation also depends on available NO_x concentrations, which renders formaldehyde a significant player in the interrelated chemistries of ozone, HO_x and NO_x, driving photochemical smog formation (see also Section 2.2.4).

HCHO is very toxic as it attacks the respiratory tract and can cause cancer. Predominantly, HCHO is generated as a secondary product of the oxidation of (VOCs), which is why it is typically found in urban areas, exhibiting mixing ratios of 1 to 20 ppb, or even more in highly polluted air masses [*Finlayson-Pitts and Pitts, Jr.* 2000]. Further sources are direct emission from fossil fuel combustion and industrial activity. However, formaldehyde has also natural sources as it is subsequently formed

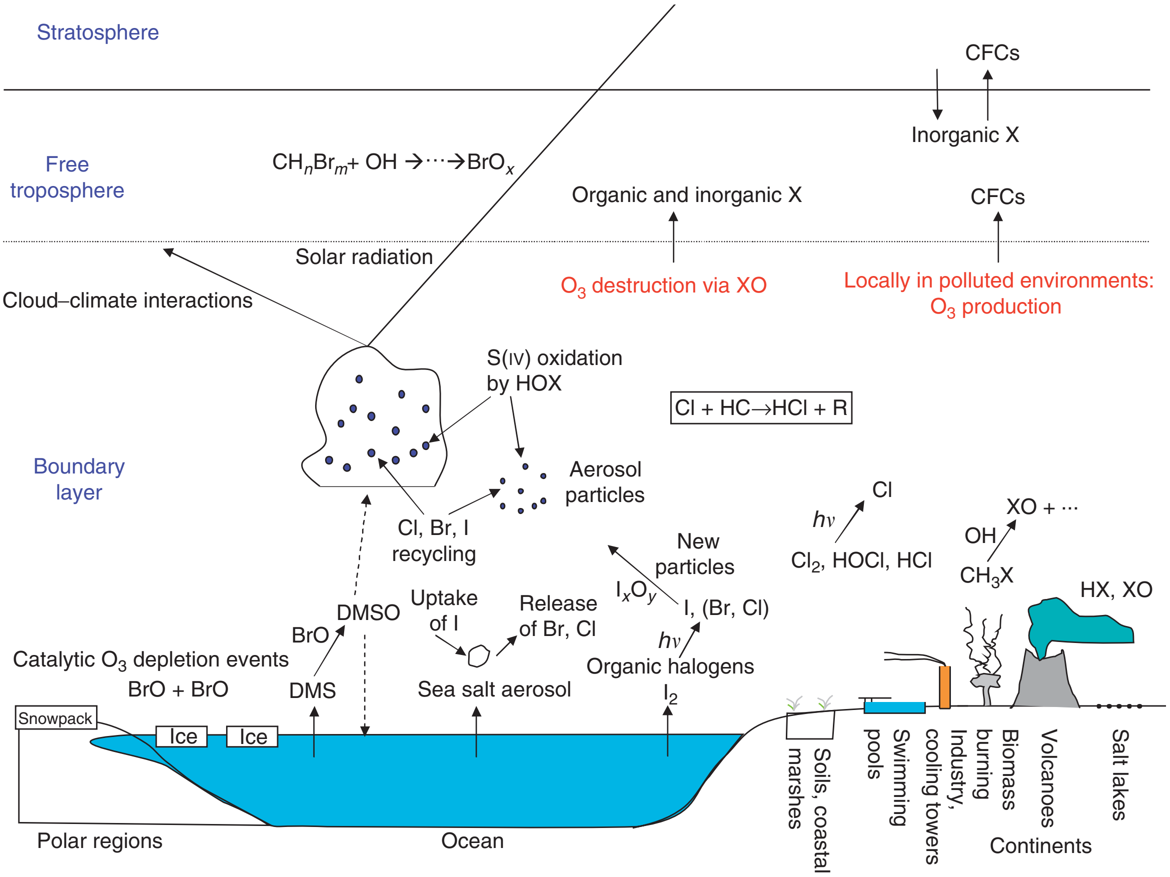

Figure 2.9: *Schematic overview of the most important halogen related processes in the troposphere. Adopted from von Glasow and Crutzen [2003].*

from precursor gases, namely isoprenes, which are emitted by vegetation. This explains HCHO background levels in rural areas (below 0.5 ppb). Accordingly, formaldehyde is also emitted during biomass burning, and secondary HCHO formation can serve as a tracer for biomass burning events.

Apart from these sources, HCHO can also be formed by reactions with methane (CH_4). Since CH_4 has a lifetime of about 9 years and is very abundant in the atmosphere (about 1.7 ppm), it leads to a constant HCHO distribution up to an altitude of about 15 to 20 km [*Finlayson-Pitts and Pitts, Jr.* 2000]. Recent satellite measurements by *Steck et al.* [2007] found zonal mean profiles exhibiting a prominent maximum in the upper tropical stratosphere with values of up to 130 ppt. The authors also observed enhanced formaldehyde values of about 70 ppt in the upper tropical troposphere, which are attributed to biomass burning emission, while in the stratosphere, formaldehyde production and destruction is dominated by photochemical reactions.

In the presence of daylight, formaldehyde is either photolyzed or degraded by reaction with OH:

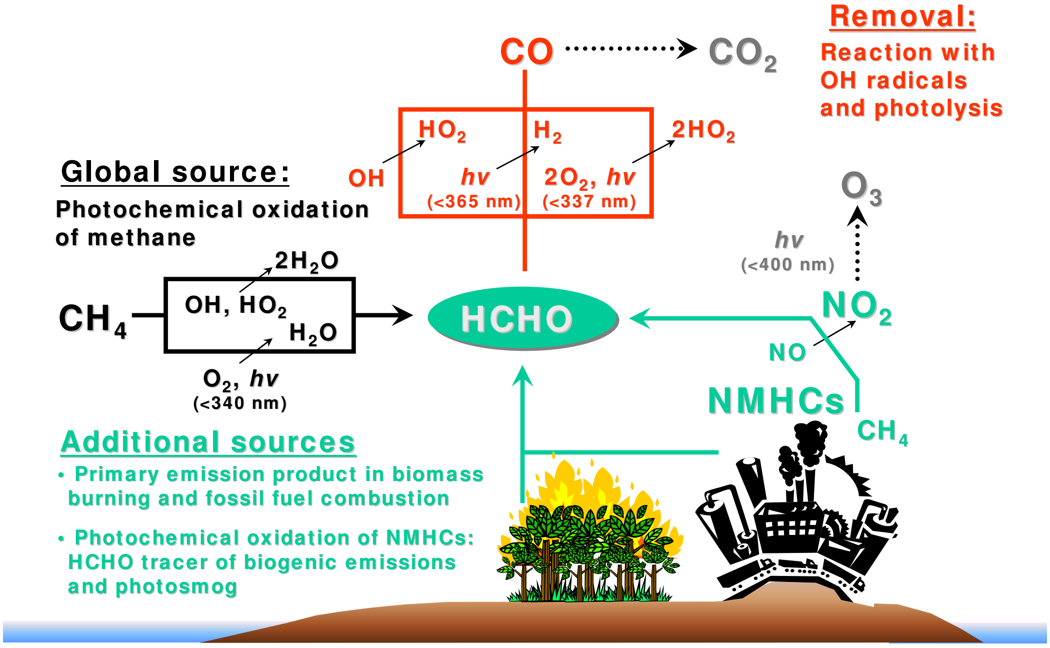

Figure 2.10: *Daylight cycle of formaldehyde in the troposphere. Adapted from Marbach et al. [2007].*

$$HCHO + h\nu \longrightarrow H_2 + CO \qquad \lambda \leq 365\ nm \tag{2.37a}$$
$$HCHO + h\nu \longrightarrow H + HCO \qquad \lambda \leq 337\ nm \tag{2.37b}$$
$$HCHO + OH \longrightarrow H_2O + HCO \tag{2.37c}$$
$$\tag{2.37d}$$

Since HCO reacts rapidly with O_2, resulting in HO_2 and CO, all degradation paths of HOCO lead to CO formation. During daytime, the lifetime of HCHO is relatively short, in the order of several hours [*Logan et al.* 1981; *Hak* 2006]. The overall reaction pathways of HCHO are too numerous to be further discussed here. A brief summary on the above discussed HCHO chemistry is provided in Figure 2.10.

Nitrous acid (HONO) represents a radical source upon photolysis, yielding OH and NO at wavelengths between 300 and 405 nm, whereas other nitrogen compounds generally act as a radical sink. Thus, as formaldehyde, HONO affects the oxidizing capacity of the atmosphere [*Platt et al.* 1980; *Alicke et al.* 2003]. During night time, HONO accumulates in the boundary layer. In the morning, its fast photolysis can represent the most important OH source, as observed by *Volkamer et al.* [2007] in Mexico City.

HONO is regularly detected in polluted cities. A direct emission of HONO by combustion sources has been observed [*Kessler and Platt* 1984; *Winer and Biermann*

1994], but these emissions are too small to explain the measured concentrations of HONO in the atmosphere [*Platt* 1986]. Nitrous acid can be formed by gas phase reactions. One of the most important reactions is the recombination of OH with NO, which can yield significant amounts of HONO:

$$\mathrm{OH} + \mathrm{NO} + \mathrm{M} \longrightarrow \mathrm{HONO} + \mathrm{M} \tag{2.38}$$

Since most OH sources require photolysis of some precursor, this reaction can become the dominating reaction during daylight hours, if sufficient amounts of NO and OH are present. Between the reactants, a steady state can be reached within ten minutes. To explain observed night time concentrations of HONO, other sources must exist, since NO and OH concentrations drop during night [*Geyer et al.* 2003; *Trick* 2004].

Further reactions leading to HONO formation are heterogenous reactions, e.g. on humid surfaces like aerosols or buildings [*Platt* 1986; *Ammann et al.* 1998]. Presently, the heterogeneous formation of HONO is believed to be the dominant HONO source [*Kleffmann et al.* 1998; *Pitts et al.* 1984]. Thereby, reactions of NO_2 with water are of importance:

$$2\,\mathrm{NO_2(gas)} + \mathrm{H_2O(liq)} \xrightarrow{\text{surface}} \mathrm{HONO(gas)} + \mathrm{HNO_3(gas)} \tag{2.39a}$$

$$\mathrm{NO(gas)} + \mathrm{NO_2(gas)} + \mathrm{H_2O(liq)} \xrightarrow{\text{surface}} 2\,\mathrm{HONO(gas)} \tag{2.39b}$$

$$\tag{2.39c}$$

Several other heterogenous reactions are suggested, e.g. reactions with sulfuric acid [*Svensson et al.* 1987] or the reaction of surface adsorbed nitric acid [*Saliba et al.* 2000]. Overall, the heterogeneous formation processes of HONO are still highly debated and yield many open questions. Particularly, the observation of unexpected high values of HONO in unpolluted environments during daytime, e.g by *Acker et al.* [2006] have raised new questions on the formation processes of HONO.

Chapter 3

Absorption Spectroscopy

Spectroscopic studies of the earth's atmosphere date back to the 19th century and have largely contributed to the understanding of atmospheric processes, e.g. they have played an important role in recognizing the importance of atmospheric ozone. Especially after the first total ozone column measurements by Fabry and Buisson in 1920 [*Platt and Stutz* 2008] and by Dobson in 1925 [*Dobson and Harrison* 1926], spectroscopic measurements have become an essential part of atmospheric sciences. Most of these spectroscopic studies were done by analyzing the absorption of light caused by trace substances. Today absorption spectroscopy is a widely used and well established measurement technique. It is based on the wavelength dependent absorption of light and makes use of the fact that each trace gas has a characteristic absorption pattern.

In this chapter the principle of *Differential Optical Absorption Spectroscopy* (DOAS) is described, which is the designated measurement technique of this work. It starts by explaining the DOAS theory and then shows how the DOAS technique is applied in order to derive trace gas concentrations from measured spectra. Furthermore specific corrections are introduced, which are needed when conducting DOAS measurements with scattered sunlight, as done in this work. An introduction on radiative transfer processes is given in the following chapter, because knowledge of these processes is necessary for the interpretation of scattered light DOAS measurements.

3.1 The DOAS technique

DOAS was introduced in 1979 [*Perner and Platt* 1979; *Platt et al.* 1979] to measure atmospheric trace gas concentrations. Since then, the DOAS technique has been widely applied to detect trace gases both in the troposphere and stratosphere [*Platt* 1994; *Solomon et al.* 1987] as well as under simulated atmospheric conditions [*Etzkorn* 1998]. In fact, several important atmospheric trace gases were measured for the first time using DOAS, e.g. OH [*Perner et al.* 1976], HONO [*Perner and Platt* 1979; *Platt and Perner* 1980], NO_3 [*Platt et al.* 1980], BrO [*Hausmann and Platt* 1994], IO [*Alicke et al.* 1999] and glyoxal [*Volkamer et al.* 2005; *Volkamer et al.* 2005] in the troposphere, and OClO and BrO [*Sanders et al.* 1988] in the stratosphere. Apart from the above mentioned trace gases, a large number of other molecules absorbing light in the UV and visible wavelength region can be detected, e.g. NO, NO_2, ClO, O_3, SO_2, OIO, H_2O and HCHO [*Platt* 1978; *Platt* 1994]. Recently DOAS measurements were also accomplished in the infrared spectral region, measuring CO_2 and methane [*Frankenberg et al.* 2005; *Woyde* 2007].

The DOAS method can be utilized in an active (using an artificial light source) or passive (using an extra terrestrial light source, i.e sun or moon) configuration. The latter can be separated in direct light measurements, where the instrument points directly into the sun or moon, and measurements using scattered sunlight as intensity source. The measurements in this thesis are performed with UV-visible scattered sunlight. In either way the DOAS technique has several advantages:

- It is a very sensitive method for the above mentioned trace gases, because they show highly structured absorption cross sections in the UV and visible spectral regions, which makes them easy to be identified. Furthermore, light path lengths of 10-20 km for active applications and up to 1000 km for passive DOAS measurements ensure a very high sensitivity towards very small trace gas concentrations.

- DOAS is especially useful when measuring highly reactive species, such as the free radicals OH, NO_3, halogen oxides (BrO, IO, etc.) or NO_2: The simultaneous determination of the concentration of several trace gases by analyzing the sum of their absorptions in one wavelength interval allows to derive the average chemical composition of the observed air mass at high temporal resolution.

- The passive DOAS instruments using scattered sky light are employed in a great variety of viewing geometries (Multi-Axis technique, see 4.5), which makes these measurements sensitive towards selected atmospheric layers. In addition, very small instruments have been developed for this configuration, which can be deployed on many different platforms like cars, ships, airplanes, balloons or even satellites. Each platform has its unique viewing geometry and specific sensitivity towards different parts of the atmosphere.

3.1.1 The Lambert-Beer Law

To quantify trace gas concentrations, the DOAS method, like many other spectroscopic techniques, makes use of Lambert-Beer's law, which describes the absorption of radiation in matter as follows:

$$I(\lambda, L) = I_0(\lambda) \cdot exp(-\sigma(\lambda) \cdot c \cdot L) \tag{3.1}$$

$I_0(\lambda)$ denotes the initial light intensity at wavelength λ, $I(\lambda)$ is the intensity after the radiation has passed through a homogeneous absorbing layer of length L and $\sigma(\lambda)$ represents the wavelength dependent absorption cross section, which is characteristic for each absorbing species. This absorption principle is the basis of DOAS and is illustrated in Figure 3.1.

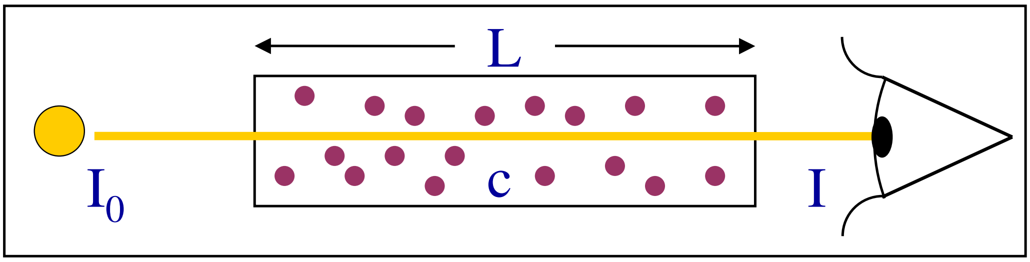

Figure 3.1: *The basic principle of absorption spectroscopy. The observation at the end of the light path is realized by a suitable spectrograph-detector unit.*

For active DOAS applications the initial light intensity $I_0(\lambda)$ and the light path length L can be derived from the instrumental setup. The average trace gas concentration c for one absorber can then be calculated from the measured ratio $I_0(\lambda)/I(\lambda)$ by using Lambert-Beer's law:

$$c = \frac{ln\left(\frac{I_0(\lambda)}{I(\lambda)}\right)}{\sigma(\lambda) \cdot L} = \frac{\tau}{\sigma(\lambda) \cdot L} \tag{3.2}$$

with

$$\tau := ln\left(\frac{I_0(\lambda)}{I(\lambda)}\right) = \sigma(\lambda) \cdot c \cdot L \tag{3.3}$$

being defined as the *Optical Density*.

For passive DOAS measurements, the Law of Lambert-Beer needs to be expanded, because absorption by other trace gases and aerosols as well as scattering by air molecules (Rayleigh scattering, see 4.2.1) and aerosol particles (Mie scattering, see 4.2.3) reduce the initial light intensity $I_0(\lambda)$ additionally. Furthermore $I_0(\lambda)$ and the light path L become unknown entities when measuring scattered light. This leads to the following expression of Lambert-Beer's law:

$$I(\lambda, L) = I_0(\lambda) \cdot exp\Big(- \int_0^L \Big[\sum_i \sigma_i(\lambda) \cdot c_i(l) + \epsilon_R(\lambda, l) + \epsilon_M(\lambda, l)\Big] dl\Big) \tag{3.4}$$

For each trace gas species i the parameter $\sigma_i(\lambda)$ denotes the respective absorption cross section which does not only depend on wavelength λ, but also on pressure and temperature at the position l along the light path of total length L. For simplification the pressure and temperature dependency is neglected here. In practice this dependency is accounted for by using cross sections measured at different atmospheric conditions. The total light path L is represented by the integral over all photon paths, which on average yields the most probable light path L (see also 4.3.1). The Rayleigh extinction and Mie extinction coefficients[1] are described by ϵ_R and ϵ_M. The optical density τ is now written as:

$$\tau = ln\Big(\frac{I_0(\lambda)}{I(\lambda)}\Big) = \sigma(\lambda) \cdot \int_0^L c(l)dl \tag{3.5}$$

with

$$S := \int_0^L c(l)dl \tag{3.6}$$

being defined as the *Slant Column Density* (SCD). The SCD of an absorber is the integrated concentration along a given light path L, often expressed in units of $[\frac{molec}{cm^2}]$.

Solving equation (3.4) when only measuring $I(\lambda, L)$ implies the following problems: The true intensity $I_0(\lambda)$, typically solar radiation, could only be determined in the absence of any absorbing and scattering processes, i.e. in the absence of the whole atmosphere. This is possible for DOAS applications on satellites, which can retrieve a direct sun spectrum, yet for all earth-based passive DOAS measurements it is not.[2] The solution to this is the *differential* absorption spectroscopy, i.e. measuring the difference between the absorption at two different wavelengths, which is explained in the following paragraph.

3.1.2 Differential optical absorption spectroscopy

Differential optical absorption spectroscopy makes use of the fact that Rayleigh and Mie extinction processes show *only* broad band spectral characteristics, i.e. a "slow" variation with wavelength, whereas trace gas absorptions exhibit broad *and* narrow band structures, the latter being "fast" variations with wavelength. The foundation of DOAS is thus to separate broad and narrow band spectral structures in an absorption spectrum in order to isolate the narrow trace gas absorptions (see Figure 3.2). The narrow band part is also called *differential* part of a cross section and it is derived by applying the following separation to the original cross section $\sigma(\lambda)$:

---

[1] Extinction usually denotes the sum of absorption and scattering. When only scattering takes place, extinction can be understood as processes disturbing the original photon direction.

[2] In theory ground-based measurements could utilize a solar spectrum measured in space as $I_0(\lambda)$, but this in practice leads to problems in the analysis procedure (see 3.2.1) and is thus not applied.

$$\sigma(\lambda) = \sigma'(\lambda) + \sigma^b(\lambda) \tag{3.7}$$

with $\sigma^b(\lambda)$ denoting the broad band and $\sigma'(\lambda)$ the narrow band part. Inserting equation (3.7) in equation (3.4) leads to:

$$\begin{aligned} I(\lambda, L) &= I_0(\lambda) \cdot exp\Big(- \int_0^L \Big[\sum_i \sigma_i'(\lambda) \cdot c_i(l) \Big] dl \Big) \cdot \\ & \quad exp\Big(- \int_0^L \Big[\sum_i \sigma_i^b(\lambda) \cdot c_i(l) + \epsilon_R(\lambda, l) + \epsilon_M(\lambda, l) \Big] dl \Big) \end{aligned} \tag{3.8}$$

where the first exponential function describes the effect of the differential absorption structure of a trace species, while the second exponential constitutes all broad band parts, which are the "slowly" varying absorptions as well as the influence of Rayleigh and Mie scattering. When expressing equation (3.8) as:

$$I(\lambda, L) = I_0'(\lambda) \cdot exp\Big(- \int_0^L \Big[\sum_i \sigma_i'(\lambda) \cdot c_i(l) \Big] dl \Big) \tag{3.9}$$

with

$$I_0'(\lambda, L) = I_0(\lambda) \cdot exp\Big(- \int_0^L \Big[\sum_i \sigma_i^b(\lambda) \cdot c_i(l) + \epsilon_R(\lambda, l) + \epsilon_M(\lambda, l) \Big] dl \Big) \tag{3.10}$$

then I_0' can be defined as the intensity in the *absence* of differential absorption and thus Lambert-Beer's law in equation (3.9) is only applied to the narrow band trace gas absorptions.

Likewise a differential optical density τ' can be defined in analogy to equation (3.3):

$$\tau' = ln\Big(\frac{I_0'(\lambda)}{I(\lambda)} \Big) \tag{3.11}$$

This leads to the valuable conclusion, that slant column densities of absorbers can be derived by only observing differential quantities:

$$S = \frac{\tau(\lambda)}{\sigma(\lambda)} = \frac{\tau'(\lambda)}{\sigma'(\lambda)} \tag{3.12}$$

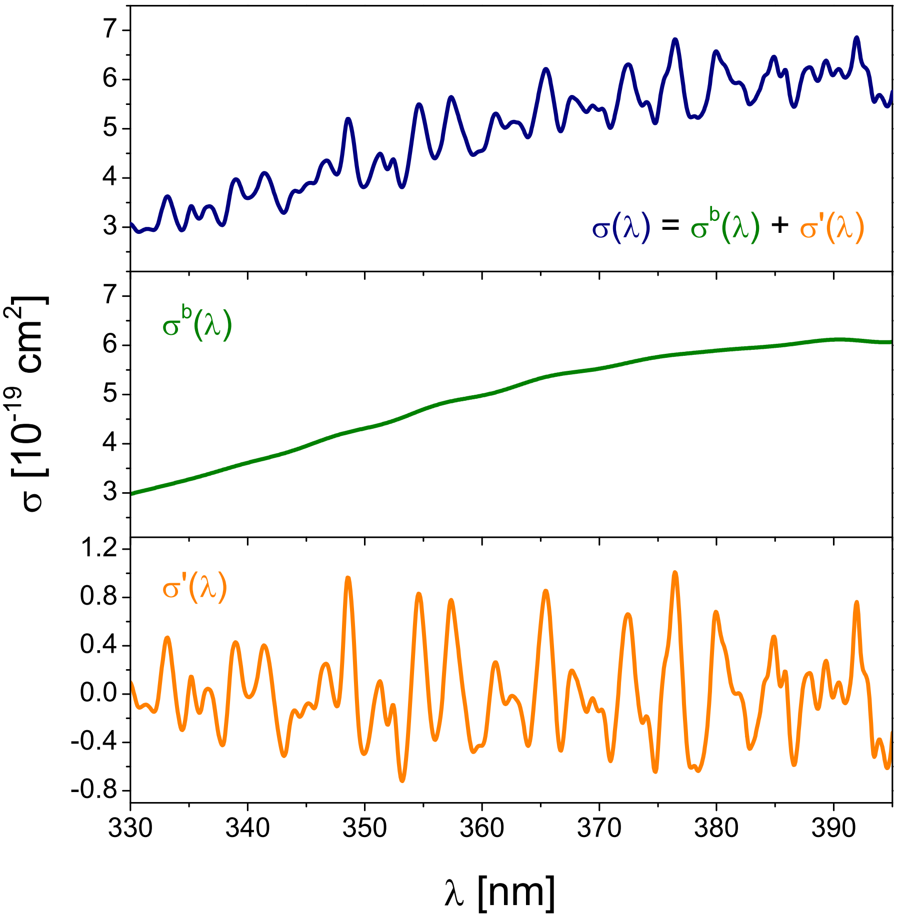

Figure 3.2: *Separation of a NO_2 trace gas cross section into its differential and broad band part. The top panel shows the complete cross section, whereas the middle panel displays the broad band part $\sigma^b(\lambda)$ and the lower panel the narrow band/differential part $\sigma'(\lambda)$.*

Thus the knowledge of the true intensity I_0 is not necessary[3] and the effects of Rayleigh and Mie extinction processes are accounted for.

3.1.3 Spectral retrieval

While the previous section dealt with the theoretical background of the DOAS technique, this section is dedicated to the actual retrieval of trace gas slant column densities from measured spectra. It explains the measurement process and shows how Lambert Beer's law is applied in practice by means of a corresponding fitting process. The following descriptions apply for DOAS measurements in general. There are, however, specific differences when conducting active or passive DOAS measurements. As this work is based on passive measurements, Section 3.2 is dedicated to the specifications of passive DOAS measurements.

---

[3] The quantity that is actually utilized as I_0 is introduced in 3.2.1

3.1.3.1 The measurement principle

The measurement process is illustrated in Figure 3.3. It starts with (a), the absorption process in the atmosphere, assuming that only one absorbing trace gas, in this case formaldehyde (HCHO), is present in the observed air mass.[4] The spectrum $I(\lambda, L)$ shows the resulting high resolution absorption structures of HCHO. The light is then usually focused onto a quartz fiber by a suitable telescope, transmitted to the entrance slit of a grating spectrograph and recorded with a detector system. The spectral resolution of the spectrograph, however, is limited, reducing in consequence the resolution of the dispersed spectrum $I^*(\lambda, L)$. Mathematically this process is a convolution of $I(\lambda, L)$ with the instrument function H of the spectrograph. Figure 3.3(b) shows the spectrum $I^*(\lambda, L)$ after this convolution as it is projected by the spectrograph onto the detector. In the last step, the spectrum is recorded by a multi channel detector, mapped to discrete pixels, and stored as $I^{**}(\lambda, L)$ on a computer for analysis (Figure 3.3(c)). Each pixel n integrates the light from wavelength interval $\lambda(n)$ to $\lambda(n+1)$:

$$I^{**}(n) = \int_{\lambda(n)}^{\lambda(n+1)} I^*(\lambda^{**}, L) d\lambda^{**} \tag{3.13}$$

where the wavelength interval is given by the *wavelength-to-pixel mapping* of the instrument, also referred to as *wavelength calibration* C_N. The spectral width of a pixel $\Delta\lambda(n) = \lambda(n+1)$ - $\lambda(n)$ is constant, if the dispersion of the spectrograph is linear: C_N: $\lambda(n) = \lambda(0) + c \cdot n$. In general, C_N can be approximated by a polynomial:

$$C_N : \lambda(n) = \sum_{k=0}^{q} c_k \cdot n^k \tag{3.14}$$

The wavelength calibration is determined by the parameter c_k and is a specific property of any given instrument. While a change in c_0 causes a spectral shift of the spectrum, changing parameter c_1 results in a linear stretch or squeeze and changing parameters with higher k values cause distortions of higher order.

Determining the wavelength calibration of the respective instrument is an essential part of the spectra preprocessing. The same applies to an electronic offset and dark current correction. Both needs to be done before the actual fitting process can be started. A detailed description of the spectra preprocessing is therefore provided in Section 5.2.3.2.

---

[4] The Figure illustrates an active DOAS set up. When conducting passive DOAS measurements, then the light has traversed the whole atmosphere before it reaches the detector and is therefore not received as parallel light.

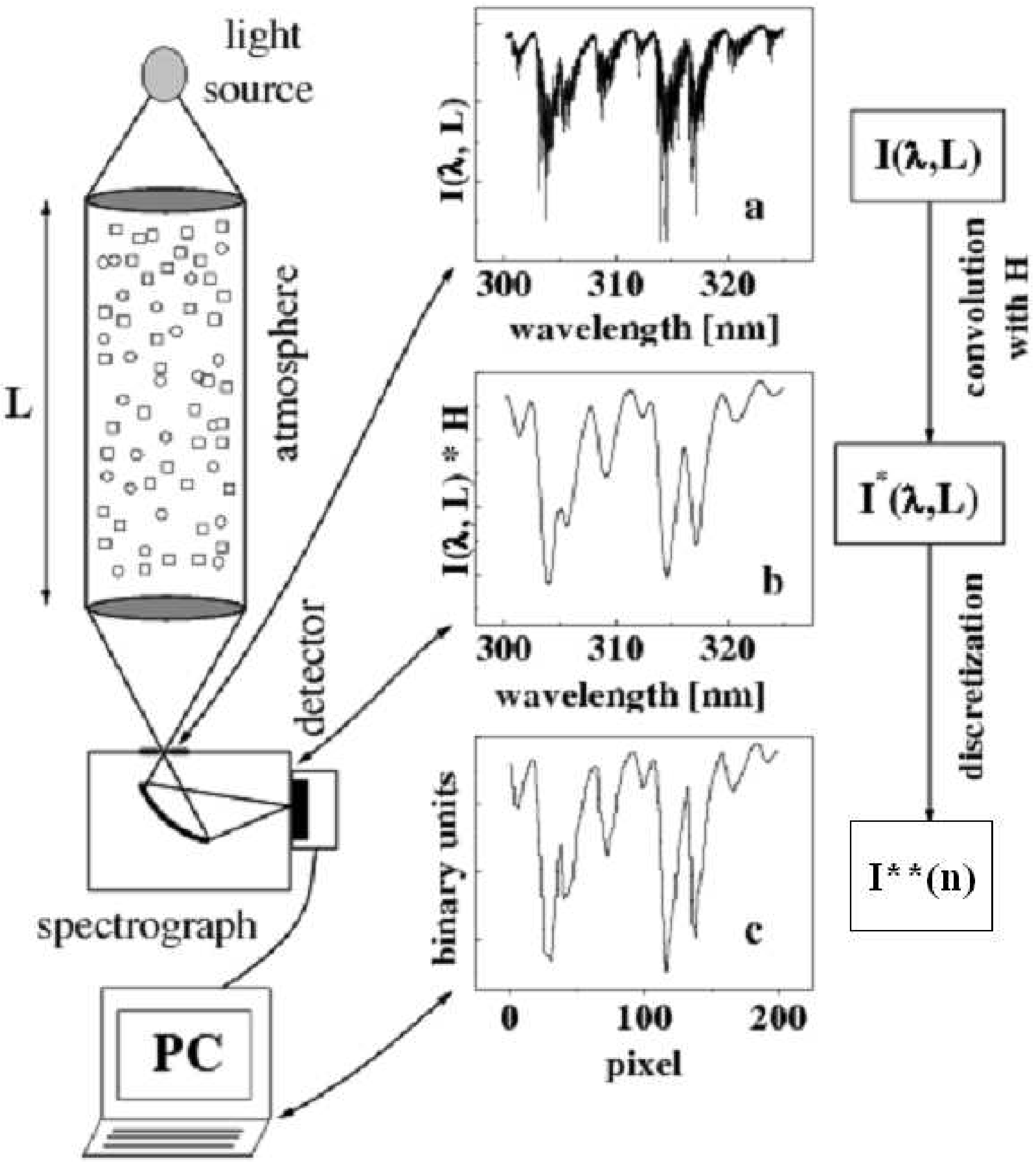

Figure 3.3: *The components of a simplified DOAS setup. Light emitted by an appropriate light source is collected by a telescope and recorded by a spectrograph-detector unit after passing through an air mass. (a): An example absorption spectrum of this light entering the spectrograph, assuming that only formaldehyde (HCHO) as absorbing trace gas has been present in the observed air mass. (b): The same spectrum convoluted with the spectrograph's instrument function H reaches the detector. (c): The spectrum after it has been mapped by the detector to discrete pixels. Then the data is digitalized, stored on a computer and analyzed numerically later. Adapted from Stutz [1996].*

3.1.3.2 The spectral fitting process

It has been shown in Section 3.1.2 that the DOAS method provides a solution of the Lambert-Beer law (equation (3.4)) by separating broad and narrow band features. In practice, this separation is achieved by either high-pass filtering spectra or by approximating all broad band spectral features with a polynomial [*Platt et al.* 1979]. Here, the latter method is utilized. To illustrate this, equation (3.4) can be written as:

$$I(\lambda,L) = I_0(\lambda)\cdot exp\Big(-\int_0^L \Big[\sum_i \sigma_i'(\lambda)\cdot c_i(l)+\sigma_i^b(\lambda)\cdot c_i(l)+\epsilon_R(\lambda,l)+\epsilon_M(\lambda,l)\Big]dl\Big) \quad (3.15)$$

Taking the logarithm leads to:

$$ln(I(\lambda,L)) = ln(I_0(\lambda))-\Big(\int_0^L \Big[\sum_i \underbrace{\sigma_i'(\lambda)\cdot c_i(l)}_{narrow\ band}+\underbrace{\sigma_i^b(\lambda)\cdot c_i(l)+\epsilon_R(\lambda,l)+\epsilon_M(\lambda,l)}_{broad\ band}\Big]dl\Big) \quad (3.16)$$

The broad band features are now simultaneously approximated by the polynomial $P(\lambda) = \sum_{k=0}^{q} p_k \cdot \lambda^k$ of the order q (typically q = 2 - 5), which leads to:

$$\begin{aligned} ln(I(\lambda,L)) &= ln(I_0(\lambda)) - \left(\int_0^L \sum_i \sigma_i'(\lambda)\cdot c_i(l)dl + \sum_{k=0}^{q} p_k\cdot\lambda^k\right) \\ &= ln(I_0(\lambda)) - \sum_i \sigma_i'(\lambda)\cdot\int_0^L c_i(l)dl - \sum_{k=0}^{q} p_k\cdot\lambda^k \\ &= ln(I_0(\lambda)) - \sum_i \sigma_i'(\lambda)\cdot S_i - \sum_{k=0}^{q} p_k\cdot\lambda^k \end{aligned} \quad (3.17)$$

To optimize the retrieval, this equation is typically solved within an appropriate wavelength interval that includes strong differential absorption structures of the trace gases of interest. The SCDs can be derived by applying a least squares fit [*Gomer et al.* 1993; *Stutz and Platt* 1996]. This fitting algorithm uses the *Levenberg-Marquard* method [*Levenberg* 1944; *Marquardt* 1963] which is an iterative combination of a linear part for the retrieval of the trace gas absorptions and a non linear part which accounts for possible spectral shifts between the measured spectrum $I(\lambda, L)$, the reference spectrum $I_0(\lambda)$ and the absorption cross sections $\sigma_i(\lambda)$.

The linear fitting process

Equation (3.17) is solved by modeling $ln(I(\lambda))$ so that χ^2 in the following equation is minimized by a least squares fit. $ln(I(\lambda))$, $ln(I_0(\lambda))$, and the absorption cross sections

$\sigma_i(\lambda)$ are the input parameters, whereas the desired S_i and q_i are the free parameters and output of this fitting process.

$$\chi^2 := \int_{\lambda_1}^{\lambda_2} \left(ln(I(\lambda)) - ln(I_0(\lambda)) + \sum_i \sigma_i'(\lambda) \cdot S_i + \sum_{k=0}^{q} p_k \cdot \lambda^k \right)^2 d\lambda \overset{!}{\rightarrow} min \quad (3.18)$$

Since $I(\lambda, L)$ is sampled on a discrete wavelength grid determined by the pixel size of the detector, the integral over the wavelength in equation (3.18) is replaced by a sum over discrete data points:

$$\chi^2 := \sum_n \left(ln(I(\lambda_n)) - ln(I_0(\lambda_n)) + \sum_i \sigma_i'(\lambda_n) \cdot S_i + \sum_{k=0}^{q} p_k \cdot \lambda_n^k \right)^2 \overset{!}{\rightarrow} min \quad (3.19)$$

In this thesis the intensities $ln(I(\lambda_n))$ and $ln(I_0(\lambda_n))$ are measured, whereas the absorption cross sections σ_i are taken from literature, i.e. cross sections measured in the laboratory with high resolution. These literature cross sections are convoluted with the instrument function H, so that they can be properly fitted to the measured spectra.

In practice, the number of simultaneously fitted absorbers is determined by those trace gases showing sufficiently strong absorption structures to be detected with the DOAS method. The number of trace gases included in the fitting process is typically between 3 and 10. Ideally, for the analysis a wavelength range is chosen where the absorber of interest exhibits strong and characteristic absorption structures, whereas other absorbers show only weak structures in order to minimize correlation effects during the fit process.

The residual R of a fitting process is defined as the difference between the optical density of the measured and the modeled spectrum:

$$R_n = ln(I(\lambda_n)) - ln(I_0(\lambda_n)) + \sum_i \sigma_i'(\lambda_n) \cdot S_i + \sum_{k=0}^{q} p_k \cdot \lambda_n^k \quad (3.20)$$

R_n and χ^2 are therefore a measure for the overall quality of the fit. An ideal measurement and a perfect fit would yield a residual that only consists of noise. In practice several factors can cause higher or systematic residuals, e.g. literature cross sections, which do not properly match the instrument function, wavelength misalignments of the cross sections or of the evaluated spectrum, absorbers not considered in the process or instrumental stray light. Since the above introduced fitting process cannot account for these effects, a non-linear fitting procedure is also included in this DOAS fit.

The non-linear fitting process

The spectral retrieval of trace gases with small optical density is very sensitive to changes in the wavelength calibration. Wavelength shifts in the order of a few percent of a pixel can already cause strong systematic structures in the residual. Changes in the wavelength calibration of the measured spectra can be accounted for by allowing a shift and a squeeze of the spectrum. These are the non-linear terms of the fitting process and are numerically solved by the *Levenberg-Marquard* algorithm. In this part of the fitting process, the wavelength calibration of the spectrum to be analyzed, $I(\lambda_n)$, is varied with respect to the references (I_0 and σ_i) to achieve the best match of the absorption features in the measured spectrum. For that purpose the measured and calibrated spectrum $I(\lambda_n)$ is interpolated on new wavelength grid points:

$$I(\lambda_n) \rightarrow I(\lambda_n') \quad \text{with} \quad \lambda_n' = \lambda_n + s_0 + s_1(\lambda_n - \lambda_c) + s_2(\lambda_n - \lambda_c)^2 \tag{3.21}$$

where $I(\lambda_n')$ is the measured spectrum on the new wavelength grid, $s_0 - s_2$ are the non-linear shift and squeeze parameters and λ_c the center wavelength of the pixel.

The spectral retrieval can also be affected by an artificial offset signal, caused by instrumental stray light due to reflection inside the spectrograph housing or by unstable electronic detector properties (see 5.2.3.2). If this offset signal varies only slowly with wavelength, which can usually be assumed for the above mentioned reasons, then it can be approximated by a polynomial $P_{offs}(\lambda)$. This polynomial, also referred to as intensity offset, is subtracted *before* the logarithm is taken and should not be confused with the polynomial that accounts for the broad band structures in the fitting process. In order to remove an artificial offset signal $I(\lambda)$ is corrected via:

$$I(\lambda) \rightarrow I'(\lambda) = I(\lambda) - P_{offs}(\lambda) \tag{3.22}$$

Again the parameters of $P_{offs}(\lambda)$ are determined by a non-linear algorithm.

3.1.3.3 Error considerations

The linear least-squares fit applied in the analysis procedure will only yield the best possible result when the following assumptions are valid:

1. *The errors of the pixel intensity has a finite variance* [*Albritton et al.* 1976]. Since the error of $I(n)$ is normally dominated by photon noise, the errors are Poisson distributed, therefore this assumption is valid.

2. *The intensity errors of individual pixel are independent* [*Albritton et al.* 1976; *Bevington* 1969]. This is not strictly fulfilled, because the instrument function usually has a width of 6-8 pixels. Thus neighboring pixels are not completely independent.

3. *The systematic error of the pixel intensity is zero* [*Albritton et al.* 1976]. Depending on the instrument, this is not always true. Some detectors show a specific pixel to pixel structure, but which can be measured and corrected (see 5.4.1).

4. *The SCD does not vary within the analyzed wavelength range.* This can be assumed for weak absorbers with a small optical density (even though they exhibit a broad band wavelength dependency caused by Rayleigh scattering). If, however, the examined trace gas is a very strong absorber, like ozone in the UV, then the wavelength dependency of the trace gas cross section needs to be considered particularly: Equation (3.5) shows that the measured optical density τ is modulated with the wavelength dependency of the trace gas cross section $\sigma(\lambda)$. E.g. strong ozone absorptions in the UV alter the light path distribution within the finite wavelength range used for the analysis such, that the light paths *cannot* be assumed to be uniform anymore. For a further discussion and suitable corrections see Section 4.3.

5. *The influence of the spectral resolution of the instrument can be neglected.* This can be assumed for absorbers with an optical density $\ll 1$. The problem arises from the typical spectral resolution of a DOAS instrument, which is in the UV-visible region usually in the range of about a few tenths to several nanometers. Thus the natural line widths of the atmospheric absorptions are not resolved. To account for this, as stated above, the absorption cross sections of the trace gases have to be convoluted with the instrument function $H(\lambda)$ before they are utilized as input files for the fitting process:

$$\sigma^*(\lambda) = H * \sigma(\lambda) = \int \sigma(\lambda') \cdot H(\lambda - \lambda') d\lambda' \tag{3.23}$$

In the actual measurement process, however, this convolution occurs in the spectrograph, where the incoming intensity $I(\lambda)$ is convoluted with the instrument function H as described in Section 3.1.3.1:

$$I^*(\lambda) = H * I(\lambda) = H * [I_0(\lambda) \cdot exp(-\sigma(\lambda) \cdot S)] \tag{3.24}$$

Applying equations (3.5) and (3.6) leads to:

$$\begin{aligned} \tau(\lambda) &= ln\left[\frac{H * I_0(\lambda)}{H * [I_0(\lambda) \cdot exp(-\sigma(\lambda) \cdot S)]}\right] \\ &\neq H * ln\left[\frac{I_0(\lambda)}{I_0(\lambda) \cdot exp(-\sigma(\lambda) \cdot S)}\right] = H * \sigma(\lambda) \cdot S \end{aligned} \tag{3.25}$$

> The convolution and the logarithm or exponential function can not be exchanged. Therefore, fitting convoluted cross sections to the optical density measured by a low resolving instrument is not strictly correct. For optically thin absorbers like atmospheric BrO or HCHO, the exponential function and the logarithm can be approximated by the first two terms of the Taylor expansion. If additionally the spectrum of the light source can be approximated by a constant, then the following can be assumed:
>
> $$\tau(\lambda) \approx H * [\sigma(\lambda) \cdot S] \tag{3.26}$$
>
> This means that for small absorptions the measured optical density is proportional to the SCD. It should be noted, however, that the solar spectrum is highly structured due to absorptions of the sun's atmosphere (*Fraunhofer lines*), which can lead to retrieval errors, because equation (3.26) is then no longer valid. This effect is often referred to as the solar I_0 effect and will be discussed in Section 3.2.2.

When applying a least squares fit, residual structures that are not caused by noise are a common problem in the DOAS analysis. These structures could indicate an unknown absorber or can be caused by the instrument itself and occur very often randomly. Stable residual structures cause systematic errors, which cannot be described by statistical methods. These structures can usually be corrected, once the source of the systematic error is found. If they appear, however, randomly, then they can be quantified by statistical methods, e.g. by an approach based on simple Monte Carlo methods [*Hausmann et al.* 1997; *Hausmann et al.* 1999] or by multiplying the fit errors with the appropriate factor for the respective analysis [*Stutz and Platt* 1996]. In any case such structures have to be considered carefully in order to optimize the spectral fitting procedure and to determine the uncertainty of the derived SCDs. For a detailed discussion on the error estimation of the analyzes of this work see Section 5.4.6.

3.2 Scattered light DOAS: implications and corrections

The passive DOAS measurements of this thesis use scattered sunlight as radiation source. This leads to several implications that need to be considered additionally in the analysis procedure, which are explained now.

3.2.1 The Fraunhofer reference spectrum

All measured sunlight spectra show the typical Fraunhofer lines, which lead to strong variations in the intensity of the solar spectrum. The optical density of the Fraunhofer lines is in the order of two magnitudes higher than the optical densities of the underlaying trace gas absorptions, which can lead to significant evaluation errors, if not properly accounted for. Therefore an accurate correction of the Fraunhofer lines is crucial for a good fitting process. To do so, a *Fraunhofer Reference Spectrum* (FRS) is needed. A solar spectrum measured in space could serve this purpose and could simultaneously be utilized as $I_0(\lambda)$, because it is free of atmospheric absorptions. This spectrum would then need to be convoluted with the instrument function H, like done with the trace gas cross sections. Since, however, most instruments do not have a stable resolution over their whole wavelength range, the measured instrument function H is usually only an approximation of the true mapping characteristics of the spectrograph-detector unit (see Section 5.2.3.2). A convoluted Fraunhofer reference could therefore never account completely for the measured Fraunhofer absorptions and would lead to very high residual structures due to the large optical density of the Fraunhofer lines.

To solve this problem, a spectrum from the measured data set is chosen as Fraunhofer reference spectrum, which then also serves as $I_0(\lambda)$. The criterion for the selection of the FRS is typically that it contains the lowest possible absorption structures of the trace gas of interest within the analyzed time series. Since the measured absorption depends both on the concentration profile of the respective trace gas and on the light path length in this trace gas layer, the selection of the FRS is usually determined by considering these two aspects. The result of the fitting process then only yields the *difference* of the atmospheric absorptions, which also explains occasionally retrieved negative values. The absorption contained in the FRS itself have to be determined independently and are added to derive the total absorption of the measurement. Since the absorption of the FRS can often only be derived with comparably large uncertainties (see 4.3.2), this procedure represents a specific limitation of DOAS measurements using scattered sunlight. In the following "FRS" always denotes a spectrum recorded with the same instrument as utilized for the measurements of the spectra to be evaluated.

3.2.2 The solar I_0 effect

The typical resolution of a DOAS instrument ranges between tenths of a nanometer to several nanometers and cannot resolve the highly structured Fraunhofer lines (see Figure 3.4). This leads to variations in the detected absorption structures when observing scattered sunlight in comparison to the laboratory reference spectra, usually applied the in the fit process, that where recorded with an unstructured light source. Since these errors arise from the spectral structures of the solar I_0 spectrum, it is usually referred to as the *solar* I_0 *effect* [*Platt et al.* 1997; *Richter* 1997].

While for most of the atmospheric absorbers this only leads to negligible effects, in some cases the I_0 effect has to be considered. This is in particular the case when strong atmospheric absorbers like O_3 have to be "removed" to measure the underlying weak absorptions of other trace gases like BrO. The solar I_0 effect can be accounted for by using I_0 corrected cross sections. These can be calculated in the following manner [*Johnston* 1996]: First a high resolution solar spectrum $I_0(\lambda)$ is convoluted with the instrument function H:

$$I_0^*(\lambda) = H * I_0(\lambda) \tag{3.27}$$

In the next step a synthetic absorption spectrum of the chosen trace gas is calculated using a highly resolved cross section, the high resolution solar spectrum and a typical column density (SCD) of the respective trace gas. This synthetic absorption spectrum is then convoluted with the instrument function H:

$$I^*(\lambda) = H * [I_0(\lambda) \cdot exp(-\sigma(\lambda) \cdot S)] \tag{3.28}$$

The I_0-corrected cross section is then derived:

$$\sigma_{I_0}(\lambda, S) = ln\left(\frac{I_0^*(\lambda)}{I^*(\lambda) \cdot S}\right) \tag{3.29}$$

Obviously I_0-corrected cross sections derived this way match the absorptions in the measured atmospheric spectrum only if the SCD in equation (3.28) is the same as found in the atmosphere. For an improved DOAS analysis, an iterative approach could be applied, using the retrieved SCDs of a first fitting process to calculate I_0-corrected cross sections of several absorbers. These could be used for the next DOAS fit and so on. This method is, however, very time consuming and it was found that the calculation for a typical SCD could be utilized for all measured spectra, without causing significant errors. For the DOAS evaluations in this thesis, all NO_2 and O_3 reference spectra are I_0-corrected. For the other trace gases analyzed in this work the effect is neglected since they exhibit either no high resolution spectral features or the absorptions are too weak to change significantly due to the I_0 effect.

3.2.3 The Ring effect

When observing scattered sunlight, the optical density of the Fraunhofer lines is reduced compared to direct sunlight observations [*Grainger and Ring* 1962]. The Fraunhofer lines appear to be "filled in". This effect is called *Ring effect*. It is most likely caused by rotational Raman scattering, i.e. inelastic scattering (see 4.2.2) on air molecules [*Brinkmann* 1968]. As a result of the interaction between an oscillating electric field and a rotating molecule, the photon changes its wavelength. Even though the Ring effect is only in the order of a few per cent, its consideration is essential, since otherwise the Fraunhofer lines can not be perfectly corrected. This would in consequence lead to systematic residual structures too large to still allow the analysis of weak absorbers. Therefore a Ring reference spectrum is calculated and included in the spectral analysis.

The measured intensity, including the elastic Rayleigh and Mie scatter processes, can be written as:

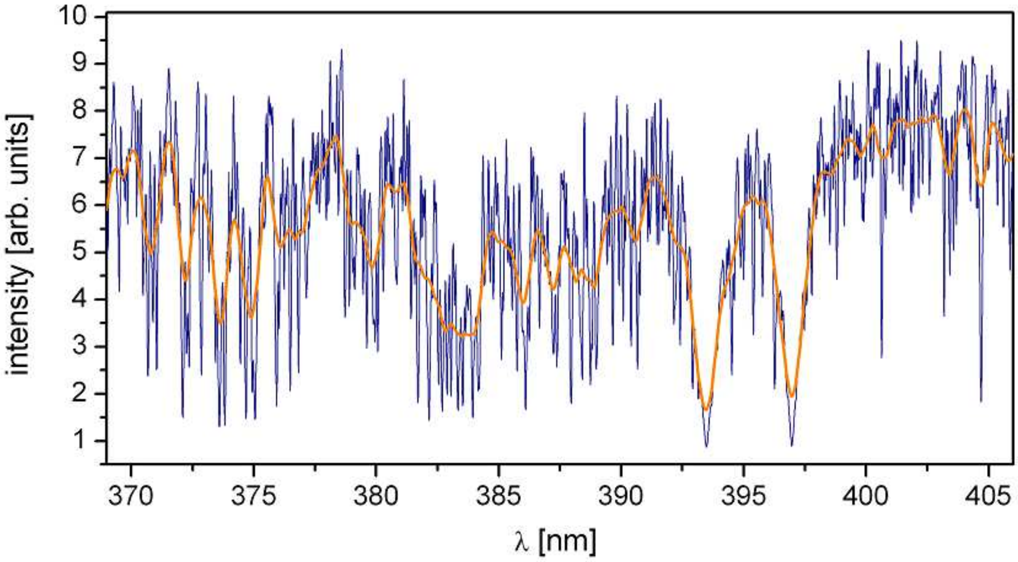

Figure 3.4: *Fraunhofer lines measured with two different spectral resolutions. Blue: a high resolution spectrum retrieved by a Fourier transform spectrograph. Orange: a spectrum with a typical DOAS resolution.*

$$I_{meas} = I_{Rayleigh} + I_{Mie} + I_{Raman} = I_{elastic} + I_{Raman} \tag{3.30}$$

Taking the logarithm leads to:

$$\begin{aligned} ln(I_{meas}) &= ln(I_{elastic} + I_{Raman}) \\ &= ln(I_{elastic}) + ln\Big(1 + \frac{I_{Raman}}{I_{elastic}}\Big) \\ &\approx ln(I_{elastic}) + \frac{I_{Raman}}{I_{elastic}} \end{aligned} \tag{3.31}$$

with

$$I_{Ring} \equiv \frac{I_{Raman}}{I_{elastic}} \tag{3.32}$$

This spectrum is usually referred to as *Ring spectrum* and is included in the fitting routine to account for the Ring effect. There are two different approaches to determine a Ring spectrum:

1. *Measured Ring spectrum:* The polarization of Raman scattered light is very small compared to Rayleigh scattered light. This fact can be used to determine the Ring

spectrum by measuring spectra with different polarization orientations [*Solomon et al.* 1987]. This method, however, has several disadvantages. First, it requires that only Rayleigh and Raman scattering occurs in the atmosphere. In practice, aerosols are usually present. Since scattering on aerosols also has a weak wavelength dependency, the measured Ring spectrum would contain structures caused by Mie scattering. Secondly, the light paths are different for light with different polarization. Therefore the light paths contributing to the measurement can contain different absorptions of atmospheric trace gases. In consequence a measured Ring spectrum can contain an unknown amount of atmospheric absorptions which affects the retrieval of the trace gas absorptions in the fitting process. [*Wagner* 1999].

2. *Modeled Ring spectrum:* Using the known rotational states of oxygen and nitrogen (see 4.2.2), the spectrum of inelastically scattered light can be calculated [*Bussemer* 1993], thus omitting the above mentioned disadvantages. Comparisons between calculated Ring spectra and atmospheric observations in high spectral resolution have shown very good agreement [*Aben et al.* 2001]. Therefore modeled Ring spectra are used for the spectral analysis in this work.

The calculation of the Ring spectrum according to *Chance and Spurr* [1997] consists of a convolution of a high resolution solar spectrum using calculated rotational Raman scattering cross sections and the instrument function H. The high resolution solar spectrum can be replaced by a measured spectrum from the data set to be evaluated (typically the same spectrum as utilized as I_0). This has the advantage that the Ring reference matches better the measured structures. Since the Ring effect can be quite strong, an accurate correction is necessary. Sensitivity studies carried out within this work have shown that a ring reference calculated from a spectrum recorded with the same instrument as the data to be analyzed, and thus omitting the convolution with the instrument function, leads to better fit results with 10 - 15 % smaller residual structures. Accordingly, this method is chosen for the calculation of the Ring references in this work. An exemplary fit result is shown in Figure 3.5. The Ring spectrum retrieved with a high resolution solar spectrum was calculated with the WinDOAS software [*Fayt and Van Roozendael* 2001] and the Ring spectrum derived from a spectrum of the same instrument was retrieved with the DOASIS software [*Kraus* 2006].

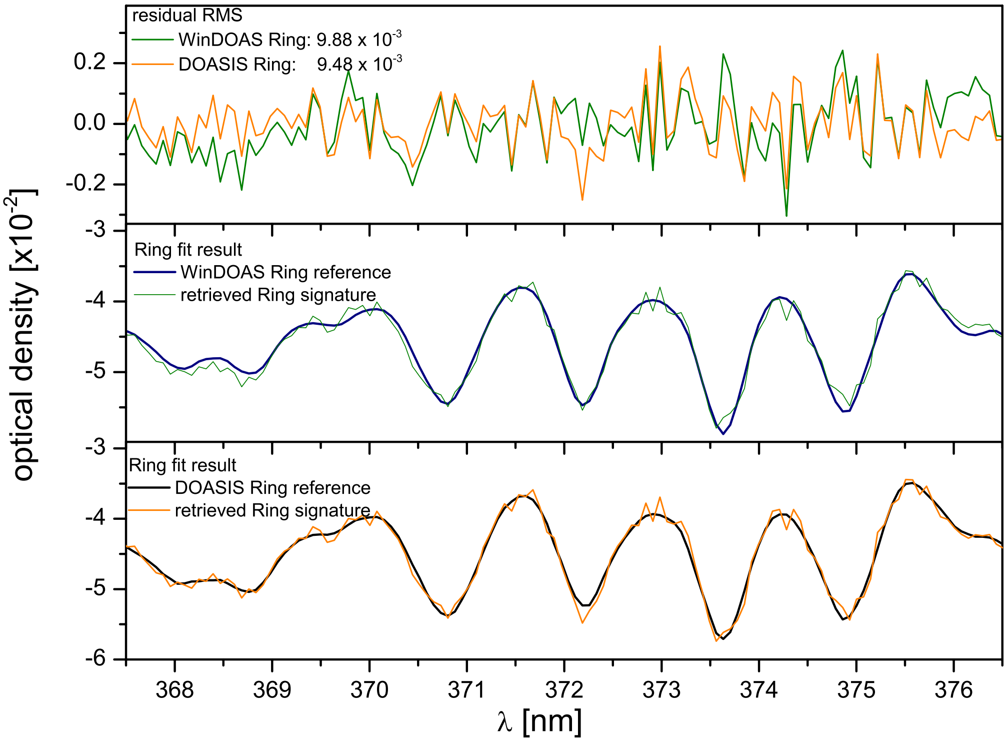

Figure 3.5: *Exemplary Ring fit utilizing different Ring spectra. Top panel: Residual structures and RMS values of a fit with the WinDOAS Ring (green) and of a fit using the DOASIS Ring (orange). Middle panel: Fitted WinDOAS Ring reference (blue) and the retrieved spectral signature including the residual structure (green). Bottom panel: Fitted DOASIS Ring reference (black) and the retrieved spectral signature (orange).*

Chapter 4

Radiative Transfer in the Atmosphere

Radiative transfer describes all processes influencing the propagation of radiation in an absorbing and scattering medium like the atmosphere. The understanding of these processes is a key prerequisite to the interpretation of passive DOAS measurements. As described in Section 3.1.1, the DOAS analysis yields slant column densities (SCDs), which depend on the light path L through the absorbing layer. Absorption by trace gases and scattering, e.g. on air molecules and aerosol particles, alter the light paths contributing to a measurement. In order to convert the measured SCDs into a light path independent quantity, a conversion factor is needed, the so called *Air Mass Factor* (AMF). The AMF quantifies the above mentioned processes, which are summarized in the theory of radiative transfer.

For a better understanding, this section starts with a brief overview on the theory of radiative transfer, before the interaction processes of radiation with matter are explained in more detail. Subsequently the concept of air mass factors is implemented. Since the calculation of AMFs usually requires the use of radiative transfer models, Section 4.4 provides an introduction to the model approach and to the model utilized for the AMF calculations of this thesis (TRACY-II). This chapter concludes with a discussion on specific DOAS viewing geometries (Multi-Axis DOAS) and presents the setup of the airborne Multi-Axis measurements of this work.

4.1 Theory of radiative transfer

The propagation of radiation in the atmosphere is a very complex process, governed by several interaction processes of radiation with matter:

- Absorption, e.g. by trace gases, removes photons from the atmosphere and converts their energy into some other form of energy, e.g. heat.
- Elastic scattering, i.e. Rayleigh and Mie scattering (see 4.2.1 and 4.2.3), is possible in any given direction, changing the propagation direction of the photon.

- Inelastic scattering, i.e. Raman scattering (see 4.2.2), changes the direction of a photon *and* its energy.
- Thermal emission from molecules and aerosols.

These processes are expressed in the *Radiative Transport Equation* (RTE). Understanding the RTE implies the knowledge on the following basic radiometric quantities:

Radiation flux: the radiation flux Φ is defined as the incident radiation energy per time:

$$\Phi = \frac{dE}{dt} \qquad \left[\frac{Ws}{s} = W\right] \tag{4.1}$$

Radiation intensity: the radiation intensity is the radiation flux per solid angle Ω:

$$F = \frac{\Phi}{\Omega} \qquad \left[\frac{W}{sr}\right] \tag{4.2}$$

Radiance: the radiance, also simply called *intensity*, is the radiation intensity, considering a perpendicular propagation of the radiation from the radiation area A_r:

$$I = \frac{\Phi}{\Omega \cdot A_r} \qquad \left[\frac{W}{sr \cdot m^2}\right] \tag{4.3}$$

Irradiance: the irradiance is the radiation flux received perpendicular by an illuminated area A_i:

$$B = \frac{\Phi}{A_i} \qquad \left[\frac{W}{m^2}\right] \tag{4.4}$$

The RTE describes the change of the radiance $I(\lambda)$ while passing through the atmosphere. This radiance is measured by the DOAS instrument at a given time and location. When applying the RTE in the UV-visible spectral range, as done in this work, thermal emission can be neglected and the RTE is given by:

$$\frac{dI(\lambda)}{dl} = \underbrace{-I(\lambda) \cdot [\epsilon_a(\lambda) + \epsilon_s(\lambda)]}_{1} + \underbrace{\epsilon_s(\lambda) \int_0^{\pi} \int_0^{2\pi} I(\lambda, \vartheta, \varphi) \cdot \frac{S(\vartheta, \varphi)}{4\pi} d\varphi \cdot \sin(\vartheta) d\vartheta}_{2} \tag{4.5}$$

with "1" denoting the extinction of radiation by absorption and scattering processes and "2" describing the radiance added to the direction of propagation by scattering.

$S(\vartheta, \varphi)$ is a dimensionless scattering function. Complications in solving the RTE arise from improper knowledge on atmospheric conditions, e.g. the spatial distribution and physical properties of absorbing and scattering species (trace gases, aerosols, cloud particles). Possible approaches to solve the RTE are discussed in Section 4.4, while the following section presents the interaction processes of radiation with matter in more detail.

4.2 Interaction processes of radiation in the atmosphere

Atmospheric extinction of radiation is defined as the sum of absorption and scattering. Apart from the absorption by trace gases, the main processes in the atmosphere are Rayleigh and Raman scattering by air molecules, Mie scattering on aerosols, cloud droplets or ice particles and absorption by aerosols. Scattering by air molecules can either be elastic (Rayleigh scattering) or inelastic (Raman scattering). The latter has already been mentioned in 3.2.3 and leads to the necessary correction of the Ring effect. Scattering on aerosols can also be inelastic, depending on the particle composition and on the wavelength of the interacting light. These important processes, Rayleigh- and Raman scattering as well as scattering (Mie) and absorption by aerosols are now explained in more detail.

4.2.1 Rayleigh scattering

Rayleigh scattering denotes the elastic scattering of light by dielectric particles, which are small compared to the wavelength of the scattered light (e.g. air molecules). The physical process can be described by incident light that induces an oscillating dipole in a polarizable air molecule. The relative intensity of the scattered light is given by the scattering phase function. For unpolarized light, the Rayleigh scattering phase function $\Phi(\theta)$ is given by:

$$\Phi(\cos(\theta)) = \frac{3}{4} \cdot (1 + \cos^2(\theta)) \tag{4.6}$$

with $\theta' = \frac{\pi}{2} - \theta$ being the angle between dipole axis and Poynting vector of the incident light. If the anisotropy of the polarizability is taken into account (see [*Penndorf* 1957]), equation (4.6) changes to:

$$\Phi(\cos(\theta)) = 0.7629 \cdot (0.9324 + \cos^2(\theta)) \tag{4.7}$$

The wavelength dependency of the Rayleigh scattering cross section was first derived by Lord Rayleigh and is very strong:

$$\sigma_R \propto \frac{1}{\lambda^4} \tag{4.8}$$

The blue color of scattered skylight and the sun's red color during sunset and sunrise are due to the strong wavelength dependency of the Rayleigh cross section causing predominantly light of shorter wavelength to be scattered. The "true" color of the sky is actually in the UV, but human eyes are not sensitive for that wavelength range.

4.2.2 Raman scattering

Inelastic scattering of photons by air molecules is called Raman scattering. It can be described as light interacting with an air molecule that changes its excitation state during the scattering process. The photon either transfers part of its energy to the molecule (Stokes lines, $\Delta J = +2$, S-branch) or takes over part of the molecule's excitation energy (Anti-Stokes, $\Delta J = -2$, O-branch). The term rotational Raman scattering (RRS) is used, if only the rotational excitation is affected ($\Delta\nu = 0$), if also the vibrational state changes the term rotational-vibrational Raman scattering (RVRS) is used ($\Delta\nu = \pm 1$). Only discrete amounts of energy given by the difference between the discrete excitation levels can be transferred between the photon and the molecule. The RVRS is one order of magnitude weaker then the RRS, hence only RRS is regarded for the calculation of the Ring spectrum (see 3.2.3). However, when conducting radiative transfer calculations for the retrieval of air mass factors (see Section 4.3), then Raman scattering can be neglected. Details on Raman scattering can be found in literature, e.g. [*Haug* 1996; *Sioris and Evans* 1999].

4.2.3 Mie scattering

Mie scattering occurs when light is scattered by a particle that is comparable in size or larger than the wavelength of the incident light. In the atmosphere these particles are typically aerosols (see also 2.1.1). Their size ranges from about 0.01-10 micrometer in diameter, thus explaining their interference effects with light. Over continents the average aerosol concentrations range from 10^3 (rural areas) to 10^5 (polluted urban areas) particles per cm^{-3}, over oceans from 10^2 to 10^3. In most cases the concentration decreases strongly with altitude [*Roedel* 2000]. Examples of naturally emitted aerosols are sea salt particles, mineral dust or particles emitted by volcanic emissions and biomass burning. Anthropogenic sources originate mostly from fossil fuel combustion and consist of fine dust, nitrates, sulfates, and soot. It can be distinguished between primary and secondary aerosols. Sea salts and mineral dust are examples for primary aerosols because they are directly emitted, whereas secondary aerosols like sulphates or nitrates are produced in the atmosphere by physical or chemical processes involving precursor gases.

There is a great variety of shapes and sizes among aerosols can make the calculation of the scattering phase function very complicated. This problem is addressed by the *Mie theory*, which includes a number of numerical models to calculate scattering phase functions and extinction coefficients (see next section) for given aerosol types and particle size distributions [*Van de Hulst* 1981; *Wiscombe* 1980]. In general the particles are assumed to be spherical. The scattering phase function, determining the direction of the scattered light, depends in general on the ratio between the radius r of the particle and the wavelength λ of the scattered light, expressed in the aerosol size parameter x:

$$x = \frac{2 \cdot \pi \cdot r}{\lambda} \tag{4.9}$$

Figure 4.1 shows Mie scattering phase functions for water droplets of three different aerosol size parameters, x = 1, x = 3, and x = 10, calculated for $\lambda = 550$ nm. With increasing x, the forward direction dominates the scattering process. Besides this strong forward preference of the scattered light, the most important difference to Rayleigh scattering is the much weaker wavelength dependency of the Mie scattering phase function:

$$\sigma_M \propto \frac{1}{\lambda^{\alpha}} \tag{4.10}$$

where α is the *Ångström exponent*, which depends on the aerosol size parameter x introduced above. Small particles ($x \ll 1$) have high values of α, approaching the Rayleigh limit of $\alpha = 4$ as they become smaller. For larger particles α decreases. A typical atmospheric distribution of particles is characterized by $\alpha \approx 1.3$.

Modeling varying size and chemical compositions of atmospheric aerosols is a huge computational effort. Within the Mie theory it is therefore common to reduce this effort by describing bulk scattering properties, e.g. by integrating the single scattering properties of aerosols over their entire size distribution. Thus the overall behavior of ambient aerosols can be approximated. To describe the bulk scattering properties of the aerosol, an *asymmetry coefficient g* between 0 and 1 is often used to parameterize the forward peakedness of the scattering process. A coefficient of 1 means that the scattering direction is solely forward and g = 0 represents isotropic scattering. Most common is the *Henyey-Greenstein parameterization* for the aerosol scattering phase function[*Henyey and Greenstein* 1941], which only depends on g:

$$\Phi(\cos(\theta)) = \frac{(1 - g^2)}{4\pi \cdot (1 + g^2 - 2g \cdot \cos(\theta))^{3/2}} \tag{4.11}$$

while g is the average cosine of the scattering function

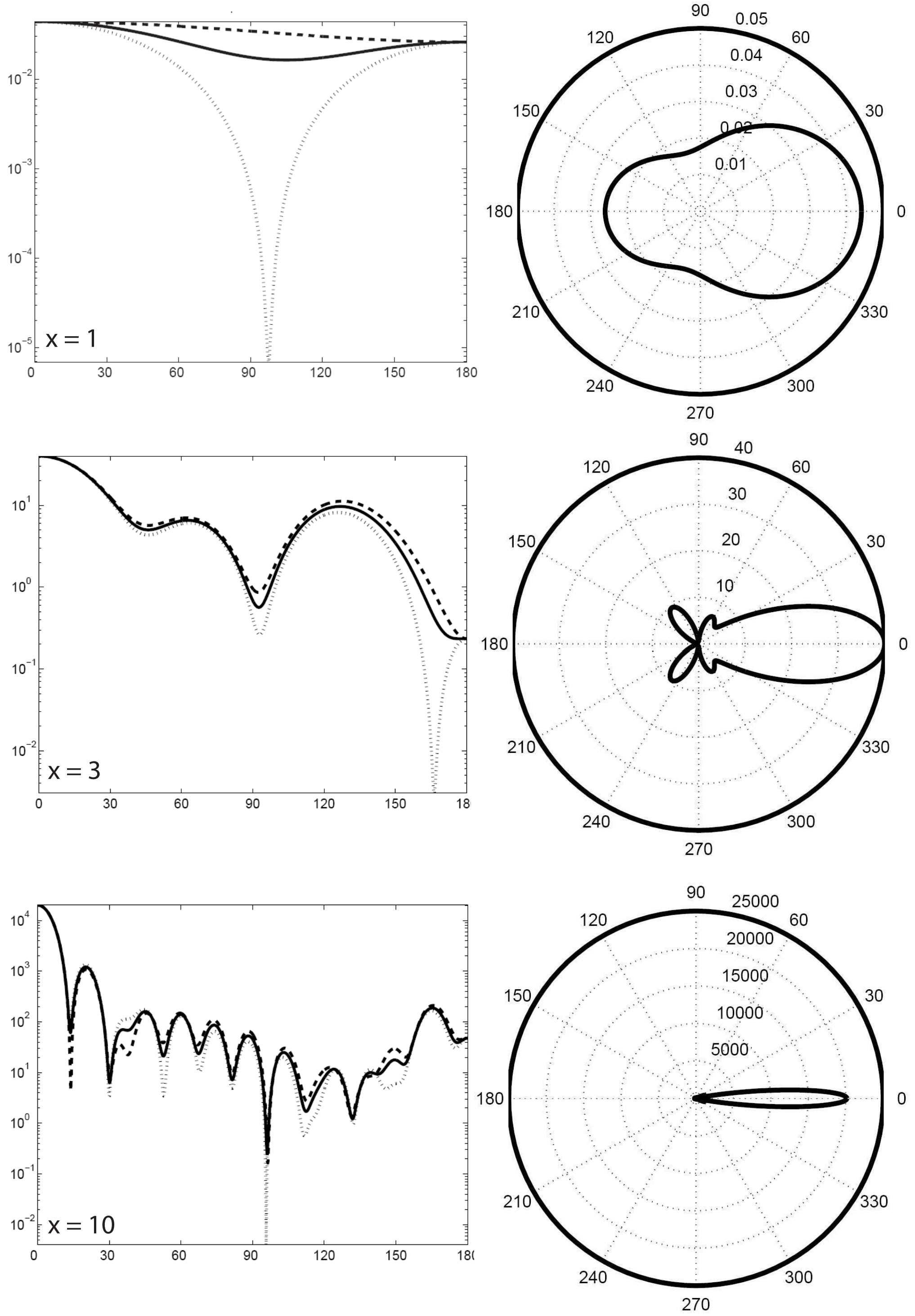

Figure 4.1: *Mie scattering phase functions at 550 nm for water droplets with aerosol size parameters x=1 (top), x=3 (center) and x=10 (bottom). The left column shows the phase functions on a logarithmic scale, the right column polar diagrams of the same phase functions on a linear scale. It becomes apparent that forward scattering dominates with increasing particle size. Adapted from [Sanghavi 2003].*

$$g = \langle \cos(\theta) \rangle \tag{4.12}$$

Typical values for tropospheric aerosol are $g \approx 0.6 - 0.7$. The Henyey-Greenstein parameterization is also applied in the radiative transfer model utilized in this work (see 4.4.1).

4.2.4 Aerosol extinction

Depending on their chemical composition, aerosols do not only scatter, but also absorb light. Therefore, besides their scattering phase functions, they are also characterized by an *extinction coefficient* ϵ_a and a *single scattering albedo* (SSA). The extinction coefficient is a measure of the probability of light extinction due to absorption *and* scattering, while the single scattering albedo denotes the fraction of extinction caused only by scattering. For example a SSA of 1 denotes a "white" aerosol, meaning all light is scattered and SSA = 0 stands for a "black" aerosol where only absorption and no scattering occurs. In accordance to equation (4.10), which defines the wavelength dependent scattering by aerosols, the macroscopic extinction coefficient ϵ_a, i.e. bulk extinction coefficient, can be defined as:

$$\epsilon_a(\alpha) = const \cdot \lambda^{-\alpha} \tag{4.13}$$

with $\alpha = 1.3$. ϵ_a is usually given in units of inverse length, often in [km^{-1}]. To quantify the total aerosol extinction, Lambert-Beer's law can be applied, assuming the aerosol extinction to be the dominant extinction process in the observed atmosphere region:

$$I(\lambda, L) = I_0(\lambda) \cdot exp(-\epsilon_a(\lambda) \cdot L) \tag{4.14}$$

In practice, the effect of the total aerosol extinction can be noticed by a reduction of the visibility. This, and the fact that a human eye can observe intensity differences as small as 2 % (i.e. contrast differences) in the visible wavelength range [*Roedel* 2000], can be utilized to get a first approximation on the total aerosol extinction: It can simply be estimated by the visibility distance L_{vis}:

$$L_{vis} = \frac{3.9}{\epsilon_a} \tag{4.15}$$

To use for example an observation of $L_{vis} = 2$ km for the interpretation of a measurement retrieved at e.g. 360 nm, the extinction coefficient can be calculated via (4.13) and (4.15). Setting $\lambda_{eye} = 500$ nm, a wavelength where the human eye is very sensitive, then ϵ_a (500 nm) = 1.95 km^{-1} and ϵ_a (360 nm) $\approx$ 3 km^{-1}. In a very clean atmosphere, the visibility can be more than 200 km.

4.3 The concept of air mass factors

Air mass factors (AMFs) are required to account for radiative transfer processes influencing the light path distribution and thus the measured slant column densities. AMFs convert the light path dependent slant column densities (SCDs) into a light path independent quantity, the so called *Vertical Column Density* (VCD). The retrieved VCD is then a comparable measure, ideally only determined by the trace gas concentration.

4.3.1 Definition and calculation of air mass factors

The SCD is defined in (3.6) as the integrated trace gas concentration $c(l)$ along the light path:

$$S = \int c(l)dl \tag{4.16}$$

The SCD is usually converted into a VCD, which is defined as the trace gas concentration $c(z)$ integrated along a vertical path through the atmosphere:

$$V := \int c(z)dz \tag{4.17}$$

The VCD only depends on the trace gas concentration profile and is therefore independent of all other factors influencing the light paths. To convert a slant column into a vertical column requires a conversion factor, the air mass factor, which is defined as:

$$A(\lambda, \theta\, \alpha, \phi) := \frac{S(\lambda, \theta\, \alpha, \phi)}{V} \tag{4.18}$$

with θ denoting the *Solar Zenith Angle* (SZA), i.e. the angle between the position of the sun and zenith, α the viewing angle of the detector, also called *(telescope) elevation angle*, i.e. the angle between the detector viewing direction and horizon, and Φ the *relative azimuth angle*, i.e. the angle between the detector viewing direction and the sun in a horizontal plane. The detector viewing direction of a DOAS instrument is usually defined by a telescope system with apertures in the range of $0.5° - 10°$. Thus the viewing direction can be approximated by the line of sight. A DOAS observation geometry for airborne measurements and the respective angles are shown in Figure 4.2. For simplification, the relative azimuth angle Φ is set to 180°.

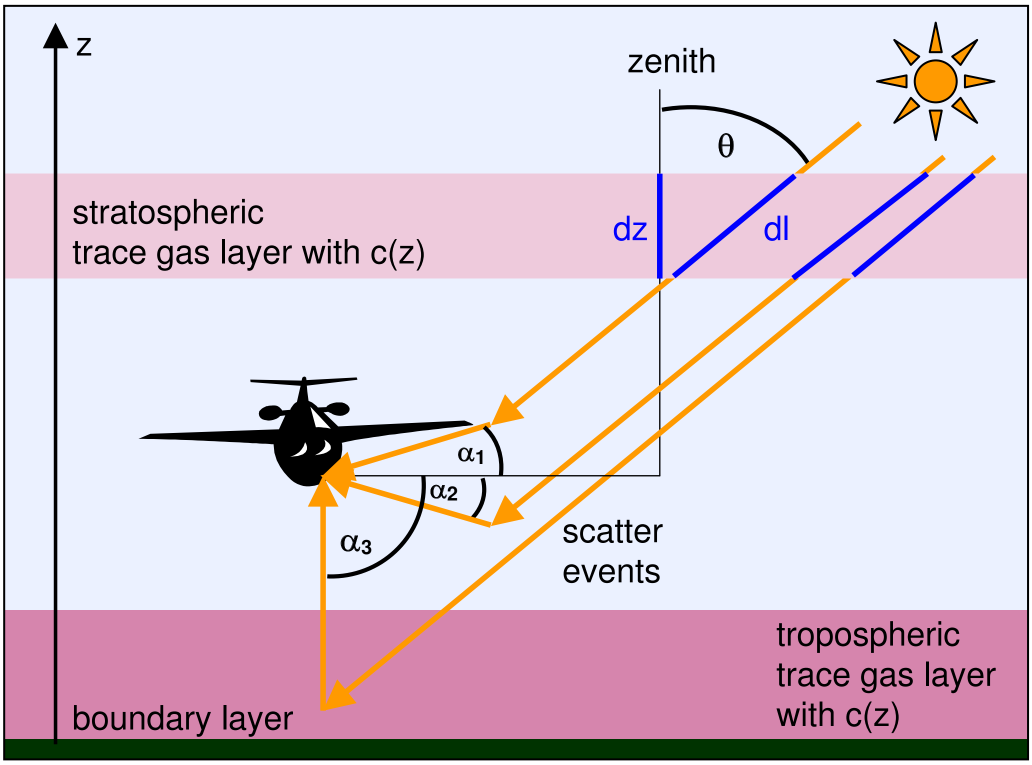

Figure 4.2: *Observation geometry for airborne DOAS measurement with scattered light. Sunlight enters the atmosphere with the solar zenith angle θ. For a single scattering approximation, the measured photons are scattered only once into one of the three detector viewing directions, defined by the respective elevation angles α. The observed stratospheric SCD (integral along dl) is larger than the corresponding VCD (integral along dz).*

The light path distribution and thus the measured SCD is not only determined by the geometry shown in Figure 4.2, but also by the presence of clouds and aerosols, by surface albedo, refraction and for strong absorbers by the trace gas profile $c(z)$. The relation between SCD and VCD can be expressed via the optical density τ (see equation (3.3)), with the solar radiation passing through a concentration field $c(\vec{x})$ and assuming the temperature and pressure dependency of the absorption cross section $\sigma(\lambda)$ to be small:

$$\tau(\lambda) = ln\left(\frac{I_0(\lambda)}{I(\lambda)}\right) = \sigma(\lambda) \cdot \int_0^L c(\vec{x})dl = \sigma(\lambda) \cdot S(\lambda) \tag{4.19}$$

Using equations (4.18) and (4.19) leads to:

$$A(\lambda) = \frac{\tau(\lambda)}{\sigma(\lambda) \cdot V} \tag{4.20}$$

It must be noted that the individual photons contributing to a single SCD measurement have very likely traveled on different light paths through the atmosphere. Therefore equation (4.16) represent only the most probable path defined by the photon statistic of the viewing geometry. Thus also (4.19) is only valid for a well defined light path between the position of the sun and the telescope. In a good approximation this is the case for the situation sketched in Figure 4.2. When neglecting refraction and assuming a plane parallel atmosphere with a horizontally evenly distributed stratospheric trace gas layer $c(z)$, the path integral in equation (4.19) is calculated along a straight line between the sun and the position of the scattering process and thus also through the stratospheric trace gas layer. When no additional absorption is encountered along the path between the scattering process and the detector, which is true for the viewing directions defined by α_1 and α_2 in Figure 4.2, then the line element for a given solar zenith angle θ is dl = dz/cos(θ) with dz being the vertical line element. For the SCD follows:

$$S_{strat}(\theta) = \int c(\vec{x})dl = \int c(z) \cdot \frac{dz}{\cos(\theta)} = \frac{V}{\cos(\theta)} \tag{4.21}$$

and for the AMF:

$$A_{strat}(\theta) = \frac{S_{strat}(\theta)}{V} = \frac{1}{\cos(\theta)} \tag{4.22}$$

In this geometric approximation the air mass factor is only a function of the solar zenith angle θ, which works well for trace gas layers in the stratosphere, as long as the scattering occurs below the trace gas layer. This can be assumed for $\theta \leq 75°$. For higher SZAs, the scattering altitude increases and light paths inside the stratospheric trace gas layers are not comparable anymore. Figure 4.3 shows the difference between geometrical AMFs, calculated with (4.22) for a stratospheric NO_2 layer and the respective AMFs modeled with the radiative transfer model Tracy-II. It can be seen, that the geometric approach is valid for $\theta \leq 75°$.

Likewise a tropospheric AMF can be calculated via AMF$_{trop}$ = 1/sin(θ). Yet this is only valid for a very limited number of viewing geometries and only for cloud and aerosol free scenarios. Furthermore tropospheric air mass factors are very sensitive to surface albedo and multiple scattering [*Perliski and Solomon* 1993]. Thus it is suitable to use a multiple scattering model for the calculation of tropospheric AMFs, as done in this work.

When measuring scattered radiation, the observed intensity is a sum of photons traversing the atmosphere on many *different* light paths (see above), which can also be described as the integrated intensity over all possible light paths reaching the instrument [*Marquard et al.* 2000]. This fact leads to several implications for the calculation of AMFs:

- For strong absorbers the measured optical density τ_{meas} and therefore also the AMF are modulated with the wavelength dependency of the trace gas cross section:

$$\tau_{meas} = \sigma(\lambda) \cdot S(\lambda) = \sigma(\lambda) \cdot V \cdot A(\lambda, \tau_{meas}) \tag{4.23}$$

  Thus the optical density is not a linear function of the cross section. This has important implications for the spectral retrieval, since it is performed over a finite wavelength interval. For weak absorbers, this effect can be neglected, because it can be assumed that the absorption of the measured absorber itself hardly influences the light path distribution. For strong absorber, however, such as ozone in the UV, the light paths are very much influenced by the wavelength dependent ozone absorption itself, leading to typically shorter light paths within the trace gas layer in the wavelength range of strong absorption. From this follows a modulation of the absorption structure which can be compensated by using $\sigma(\lambda) \cdot A(\lambda)$ instead of $\sigma(\lambda)$ as trace gas reference spectrum (*modified DOAS*) [*Diebel et al.* 1995; *Richter* 1997]. Then the analysis yields directly the VCD.

- If a single weak absorber is present in the atmosphere, the light path distribution depends only on scatter processes and refraction. If more than one species absorbs in the considered wavelength interval, which is usually the case, the light paths distribution becomes a function of all involved absorption cross sections and their distribution. Therefore, the air mass factor for a specific trace gas

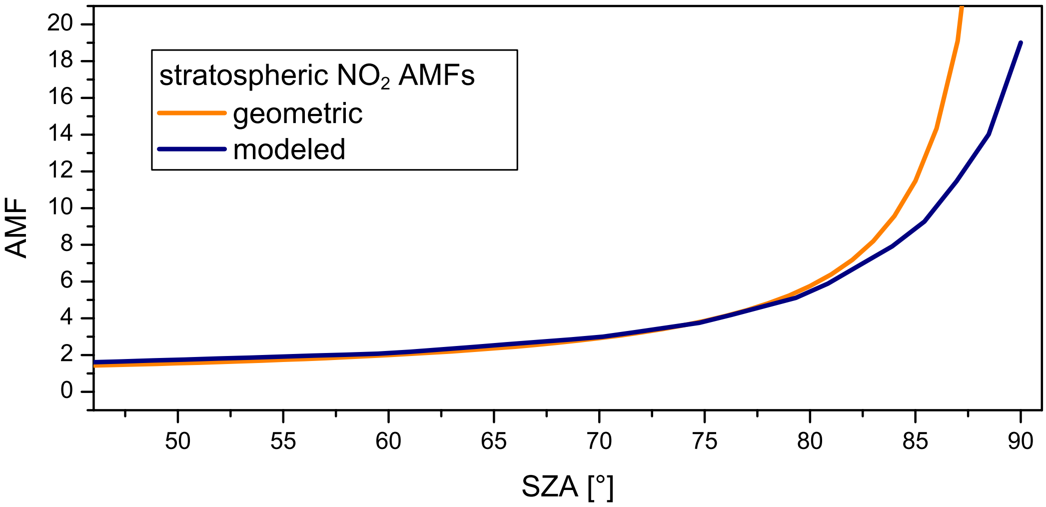

Figure 4.3: *Geometric and modeled AMFs for stratospheric NO_2. Orange: Calculated AMFs for stratospheric NO_2 via $A_{strat} = 1/\cos(\theta)$. Blue: The same AMFs modeled with the radiative transfer model Tracy-II. The increasing error of the geometrical AMFs for $\theta > 75°$ is apparent. For $\theta < 75°$ the difference between both methods is smaller than 5 %.*

depends also on the abundance of all other species absorbing in the given wavelength range. Again, this can be neglected if only weak absorbers are present. But for example the air mass factor for BrO, with absorption bands in the UV, changes significantly with the amount of ozone present, due to the above mentioned reason.

- The concentration of a trace gas can change throughout a day due to photochemistry. For radiative transfer calculations this change is associated with the change in solar zenith angle and referred to as *chemical enhancement*. This fact can be taken into account in the model by using a two dimensional concentration field, which not only depends on altitude, but also on the local solar zenith angle. The concentration field can be determined by photochemical model calculations.

A method to derive the absorption contained in the Fraunhofer reference spectrum $I_0(\lambda)$ (see Section 3.2.1), utilizing the above introduced AMFs, is the Langley plot method, presented in the following.

4.3.2 The Langley Plot

The Fraunhofer reference spectrum $I_0(\lambda)$ itself contains absorption structures (see 3.2.1). Therefore the derived SCDs are from now on referred to as *differential Slant Column Densities* (dSCDs). The dSCD is the difference between the SCD of spectrum $I(\theta, \alpha, \phi)$, measured at solar zenith angle θ, with a telescope elevation angle α and a relative azimuth angle ϕ, and the SCD of the Fraunhofer reference spectrum $I_0(\theta_0, \alpha_0, \phi_0)$:

$$dS(\theta, \alpha, \phi) = S(\theta, \alpha, \phi) - S_{ref}(\theta_0, \alpha_0, \phi_0) \tag{4.24}$$

For a well characterized stratospheric absorber and a clean troposphere, the respective AMFs depend mainly on the solar zenith angle θ. This dependency can be used to convert the dSCD into SCDs by combining equations (4.18) and (4.24):

$$dS(\theta) = V \cdot A(\theta) - S_{ref}(\theta_0) \tag{4.25}$$

The differential slant column density is a linear function of the air mass factor. Equation (4.25) implies that the slant column density of the Fraunhofer reference spectrum, SCD_{ref}, is given by the intercept of the straight line when plotting dSCD(θ) versus AMF(θ), which represents the *Langley Plot*. The slope is the vertical column density. An example for a Langley plot can be found in Section 6.3.2.

The accuracy of the Langley plot method depends on correct AMFs. Apart from the above discussed principle difficulties of the AMF calculations, the lack of knowledge on the atmospheric conditions at the time of measurement is the biggest uncertainty of this method: Clouds, aerosols and other trace gases significantly change the radiative transfer. To model these processes correctly is already a numerical challenge itself, yet the actual problem arises from not knowing and/or not being able to characterize the atmospheric state in such a way that it can serve as input parameters for the radiative transfer model. Thus these circumstances represent a principle limitation of DOAS measurements using scattered sunlight.

4.4 Radiative transfer modeling

The calculation of air mass factors usually requires to simulate the radiative transfer in the atmosphere. In practice this means to solve the radiative transport equation (see 4.1). As it is not possible to analytically solve the RTE without introducing simplification, solutions are often calculated numerically. In general, the numerical approach can be divided in two groups: The RTE is either solved by calculating the resulting radiation field of a given atmospheric state, or by a statistical approach, where individual photon paths are simulated for the desired conditions. The radiation field can then be derived from the photon density. The quality of the latter depends on statistics. The primary output of a radiative transfer model is typically the radiance obtained by a specific detector for a defined atmospheric scenario. The AMFs are calculated in a second step. The radiative transfer model Tracy-II is based on the statistical approach and is introduced now.

4.4.1 The radiative transfer model Tracy-II

TRACY-II (Trace gas RAdiative monte Carlo Ymplementation) is an in-house developed by *Deutschmann and Wagner* [2006] (see also [*Wagner et al.* 2007]. It shares the name and the statistical Monte Carlo method with its predecessor Tracy [*von Friedeburg* 2003], yet it is a complete reimplementation with new features and improvements. In general the Monte Carlo method is utilized to model physical processes with multiple outcomes that occur with a certain probability. The advantage of this approach is that it still yields a reasonable result - with a good statistic, even when analytical solutions are difficult or impossible to find. Furthermore, in contrast to analytical models, no simplifications, e.g. regarding the sphericity of the earth, have to be made.

TRACY-II is based on the backward Monte Carlo method: a photon emerges from a detector in an arbitrary line of sight direction and is followed through the atmosphere along its path until it leaves the top of the atmosphere. Instead, a multitude of photons would need to be simulated before even one photon hit the detector in a forward model, which would be very time consuming. The various possible scattering or absorption events along the path are defined by suitable probability distributions. When, for example, a photon hits an air molecule, a random number is drawn - just like rolling the dices in a casino in Monte Carlo. If the number lies in a certain interval depending on the probability of the process, this process occurs and the photon is, e.g., scattered to a different direction of propagation. When enough light paths are modeled, the contribution of each light path to the intensity measured at the detector is calculated by weighting the sum of the probabilities of all scattering events along the path (local estimation method [*Marchuk et al.* 1980]). The generation of the photon paths is independent of the position of the sun. Instead, at each scattering event the probability that the photon is scattered into the sun is calculated. When setting the sun's position to a specific solar zenith angle, then a forward run of the model calculates the corresponding intensities and air mass factors, using the paths and probabilities generated in the backward run.

There are different methods to calculate AMFs: As introduced in 4.3.1, the total AMF can be calculated for optically thin absorbers, i.e. weak absorbers, by [*Solomon et al.* 1987; *Perliski and Solomon* 1993; *Eskes and Boersma* 2003]:

$$A = \frac{ln\left(\frac{I_0(\lambda)}{I(\lambda)}\right)}{\sigma(\lambda)\cdot V} \tag{4.26}$$

For strong absorbers, however, e.g. for ozone in the UV, the light paths contributing to $I(\lambda)$ are influenced by the ozone absorption itself and differ thus from the light paths contributing to $I_0(\lambda)$. Equation (4.26) is then no longer valid.

Many models, including Tracy-II, use therefore a different approach and calculate so called *Box-AMFs* instead. When the atmosphere is divided along its vertical axis into several layers of height h, called boxes, then the Box-AMF$_i$ (A_i) is the air mass factor for box i under the assumption of a homogeneous trace gas distribution in the box defined by the vertical column density of this box (V_i). The Box-AMF is then defined by:

$$A_i = \frac{d\tau}{\sigma(\lambda)\cdot dV_i} \tag{4.27}$$

According to equation (3.5) and (4.18) this can also be written as:

$$A_i = \frac{dS}{dV_i} \tag{4.28}$$

The Box-AMF denotes how sensitive the measurements are towards changes of the VCD within that box or, in other words, how strongly the measured SCD changes with an alteration of VCD$_i$. Using the derivatives in equations (4.27) and (4.28) ensures that the shortcomings of equation (4.26) for strong absorbers are avoided. Descriptively this can be understood that the derivative causes only minor changes in VCD$_i$, which do not influence the light path distribution, but which as a result yield the sensitivity of the SCD towards these changes.

Box-AMFs derived this way can then also be utilized to solve inversion problems, e.g. to retrieve trace gas profiles from measured SCDs. Yet it must be noted that for strong absorbers the Box-AMFs depend on the trace gas concentration ($A_i = A_i(V_i)$, non-linear inversion problem), whereas for weak absorbers the Box-AMFs are constant (linear inversion problem). When normalized to one, then Box-AMFs are *weighting functions* [*Rodgers* 1976; *Rodgers* 2000], representing the weight of the sensitivity towards different atmospheric layers for a specific viewing geometry. Thus they show where the measurement is most sensitive when the absorber of interest is present in the observed air mass. This information is of interest when looking for the most suitable detector viewing geometry in order to study absorbers with a known or assumed vertical profile.

Total AMFs can easily be calculated from Box-AMFs and the respective trace gas profile as the sum of the Box-AMFs over the whole atmosphere and the corresponding partial trace gas vertical columns (V_i):

$$A = \frac{\sum A_i \cdot V_i}{\sum V_i} \tag{4.29}$$

The sum is carried out from the surface to the top of the atmosphere over all layers i. For weak absorbers, i.e. when the Box-AMFs are independent from the concentration profile, arbitrary trace gas profiles can be used with the same set of Box-AMFs in order to derive total AMFs for different scenarios. For strong absorbers, i.e. when the Box-AMFs do depend on the concentration profile, the same vertical concentration profile as utilized for the calculation of the respective Box-AMFs must be used to derive the total AMF. In principle also 2- and 3-dimensional Box-AMFs can be modeled, yet for this work only 1-D AMFs are calculated.

With Tracy-II the radiative transfer is modeled monochromatically, time independent and unpolarized in a fully spherical and inhomogeneous 3-D atmosphere. Aerosols and cloud scenarios as well as an arbitrary ground level hight can be included. Even two-dimensional terrains attributed with different albedo values can be simulated.

4.4.2 Parameters for radiative transfer modeling

The model atmosphere in Tracy-II is called *lattice*. The lattice dimensions are defined in spherical coordinates (r, φ, θ) with r = 0 representing the earth's surface. A 3-D subinterval of this grid is called *voxel*. The atmosphere itself is characterized by vertical pressure, temperature, humidity and air density files. Trace gases are specified by a vertical concentration profile and their absorption cross section. The surface can be put on any height and even mountains can be simulated. So far there is one albedo value to characterize the ground properties. Aerosol input files consist of a vertical extinction coefficient file, a single scattering albedo and the asymmetry parameter g of the Henyey-Greenstein phase function parameterization being used in Tracy-II (see 4.2.3). Clouds can be simulated by adapting the aerosol input file or by using a drawing tool with which the aerosols extinction coefficient can be "painted" in arbitrary voxels. Each voxel contains constant values, derived by linear interpolated between voxel boundaries, except for pressure and air density profiles, which are interpolated exponentially. This needs to be considered when wanting to model specific profile shapes, e.g. box profiles.

After the model environment is defined, a detector can be put in an arbitrary position inside the lattice. Besides its position, the detector is defined by its viewing direction and field of view. The solar zenith angle is given in absolute numbers whereas the azimuth can either be absolute or relative to the detector. Finally a wavelength must be chosen for which the radiative transfer in this model atmosphere is simulated. Possible output parameters are Box-AMFs, total AMFs, SCDs, optical densities, photon path lengths distributions and normalized radiances. The latter are the modeled radiances (received by the detector) I_d, normalized with respect to the modeled solar irradiance B_s:

$$I_n = \frac{I_d}{B_s} \tag{4.30}$$

The normalized radiance I_n is a number between 0 and $1/\pi$ and has thus the advantage to directly yield how much of the incident light is received by the detector. This can serve as a very sensitive tool to detect errors in the model runs, which might not be detectable if only AMFs were considered, because potential errors of the modeled radiances typically cancel out each other in AMF calculations. Furthermore the modeled normalized radiances are a good tool for comparison exercises. Normalized radiances and Box-AMFs of Tracy-II have been validated in a workshop together with 8 other radiative transfer models of international research groups. The differences between all models were found to be smaller than 5 % [*Wagner et al.* 2007]. Even though Tracy-II is up to now still further being developed, the version utilized for the model runs of this work is consistent with the workshop version of Tracy-II (*T. Deutschmann*, personal communication).

This Tracy-II version, however, does not have a functioning error output yet. If there are no systematic errors, then the error of a Monte Carlo model is dominated by statistics. To quantify this effect, the same arbitrary model scenario was utilized to perform AMF calculations for a different number of photon paths, i.e. trajectories. For each number of modeled trajectories the simulation run was repeated ten times. Figure 4.4 shows the respective results. Plotted are AMFs and root mean square (RMS) values. The latter refer to deviations from the arithmetic mean of each ten model runs. As expected, the retrieved RMS become smaller with an increasing number of modeled photon paths. For 25000 trajectories, maximum deviations in the order of 1-2 % were observed, for 50000 photon paths 1 % respectively. All AMF calculations in this work were performed with either 20000 or 50000 trajectories, hence a total error of 2 % is assumed for all Tracy-II results.

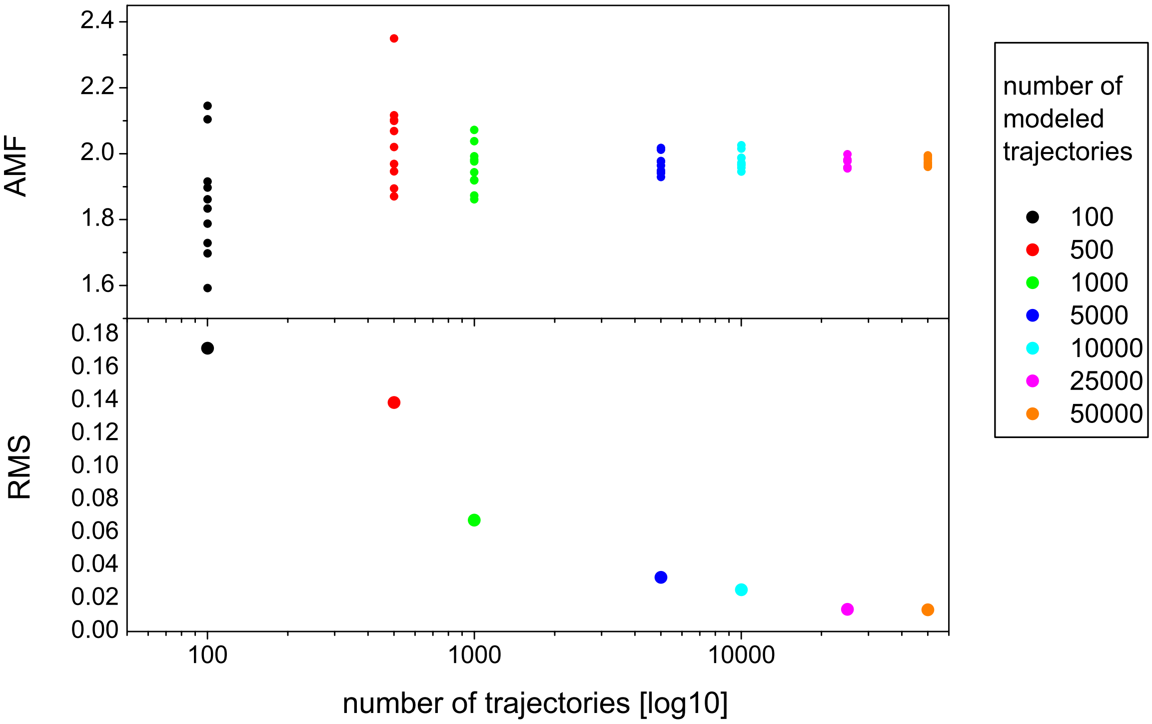

Figure 4.4: *Statistical error of Tracy-II model runs. Top panel: AMF values of the same model scenario, repeated ten times for each selected number of trajectories. Bottom panel: Root mean square (RMS) of deviations from the arithmetic mean of the respective AMF values.*

4.5 Multi-Axis-DOAS

The viewing geometry of the airborne measurements shown in Figure 4.2 is an example for a *Multi-AXis-DOAS* (MAX-DOAS) setup, which is characterized by deploying different viewing geometries within one instrumental setup. MAX-DOAS measurements are an advancement of zenith scattered sunlight DOAS, which marks the beginning of passive DOAS. In the first years of DOAS measurements, there were mainly two instrumental setups: Either active DOAS, using artificial light sources and a defined light path or zenith scattered sunlight DOAS. The latter is characterized by a telescope with a zenith viewing direction. The majority of the measured photons is scattered once into zenith direction before being detected. These measurements are especially interesting for the study of stratospheric absorbers, due to big air mass factors in the mornings and evenings (see 4.3). Even though the sensibility towards the troposphere is much smaller, due to shorter light paths therein, measurements of tropospheric absorbers could also be performed [*Solomon et al.* 1987; *Noxon* 1975]. The advantage of zenith scattered DOAS is that the radiative transfer is comparably simple for single scattering photon paths. As the scientific interest in tropospheric trace gases grew and also multi scattering radiative transfer models became available, a variety of scattered sunlight DOAS applications have been developed, which are summarized as Multi-Axis-DOAS.

MAX-DOAS has been developed by *Sanders et al.* [1993] to measure OClO over Antarctica during twilight. Since the sunset or sunrise horizon is much brighter than zenith at the same time, the authors simply turned the telescope towards the horizon. Incidently they also found that the measured slant columns of tropospheric absorbers were greatly enhanced (e.g. of O_4, see also excursion below), while the retrieved columns of a pure stratospheric absorber (e.g. of NO_2) remained unchanged. From then on off-axis measurement, i.e. pointing the telescope to anywhere but zenith, were widely used to study the troposphere. In the beginning, off-axis retrieval usually meant turning the telescope to selected directions (e.g. [*Miller et al.* 1997]). Today's MAX-DOAS measurements typically do a repeated sequence of different elevation angles (e.g. [*Hönninger* 2002; *Hönninger et al.* 2004; *Van Roozendael et al.* 2003]). When the DOAS instrument is stationary and the measurements are done within a short time interval, then the stratospheric light paths dl (see Figure 4.2) are the same for all telescope elevation angles α and the stratospheric absorptions are canceled out when taking for example the zenith measurement of each elevation sequence as Fraunhofer reference I_0. Thus the measured slant columns are tropospheric columns only. The length of the tropospheric light paths and thus the sensitivity towards the troposphere is determined by the elevation angle α. For a Rayleigh atmosphere the highest sensitivity is usually given for the smallest elevation angle. If however aerosols or clouds are present within the tropospheric trace gas layer, then the light path length differences between the elevation angles become smaller and can even disappear, depending on the specific cloud or aerosol load.

In summary, the MAX-DOAS technique enables passive DOAS measurements to become sensitive for specific atmospheric layers and the separation of tropospheric and stratospheric absorbers is easily possible. Depending on number and settings of the elevation angles, a profile retrieval using inversion methods can be performed (e.g. [*Weidner* 2005; *Dorf* 2005]). Furthermore, with a sufficient number of elevation and azimuth angles and taking also the measured intensity into account, information on aerosol properties and even the aerosol profile itself can be retrieved, using mathematical inversion techniques (e.g. [*Sinreich et al.* 2005; *Wagner et al.* 2004; *Wittrock et al.* 2004; *Frießet al.* 2006]). A lot of these methods make use of the information gained by analyzing the O_4 absorption structures of MAX-DOAS measurements. Therefore, the information content of O_4 is briefly discussed below.

Excursion: The information content of O_4 measurements The oxygen dimer O_4 is a short-lived collision complex of the oxygen molecule. It has a well known, nearly constant atmospheric concentration profile, depending on pressure and temperature. O_4 is most abundant in the lower troposphere, with a scale height[1] of approximately 4 km. Observed O_4 absorptions allow thus to conclude on the atmospheric distribution of photon paths. Aerosols change the photon path distribution in a characteristic way,

---

[1] The scale height denotes the vertical distance over which the number concentration of a trace gas decreases by the factor 1/e.

e.g. by multiple scattering or by absorption, depending on their allocation. Accordingly, from MAX-DOAS O_4 observations, information on the atmospheric aerosol profile and on the length of light paths can be derived as applied in several of the above mention references, e.g. by *Sinreich et al.* [2005], *Wagner et al.* [2004], *Frießet al.* [2006].

Measured SCDs of O_4 cannot be directly linked with O_4, because the equilibrium constant for O_4 and $(O_2)_2$ is not known. Instead, the O_4 SCD is usually referred to the integrated quadratic concentration of O_2 (see also [*Greenblatt et al.* 1990]). Hence, the O_4 SCD includes the equilibrium constant and is given in units of [molec^2/cm^5].

4.6 Airborne Multi-Axis-DOAS

MAX-DOAS instruments are installed on a variety of moving platforms, e.g. ships, cars, balloons or airplanes (e.g. [*Leser et al.* 2003; *Weidner* 2005; *Heue* 2005]), each deploying a specific viewing geometry adjusted to the atmospheric layers of interest. In a simplified scheme, airborne MAX-DOAS measurements offer the possibility of flying above tropospheric and below stratospheric trace gas layers. It is therefore useful to install up and down looking telescopes, the difference of which yields direct information on the troposphere.

The instrumental setup for the airborne MAX-DOAS measurements of this work, however, is very much determined by specifications and requirements of the CARIBIC project (see 5.2). The telescopes could only be installed underneath the aircraft, thus confining the upward viewing direction to 10° above horizon. The telescope elevation angles α_1, α_2, α_3, shown in Figure 4.2, indicate the actual CARIBIC MAX-DOAS elevation angles with α_1 = 10° (above horizon), α_2 = -10° (below horizon) and α_3 = -82° (referred to as *nadir* viewing direction). The deviance of 8° from a "real" nadir viewing direction (-90°) is caused by a slightly tilted mounting of the inlet system at the aircraft (see 5.2.1). With respect to radiative transfer this slight offset can be neglected. In spite of project restrictions, the MAX-DOAS viewing geometry could thus nevertheless be set up to be sensitive towards all atmospheric layers, with an emphasis on the troposphere.

In Figure 4.5 Box-AMFs for the CARIBIC DOAS viewing directions are presented. They are calculated for a flight altitude of 10 km, at a wavelength of 355 nm, which is suitable for most trace gases measured in this work and a solar zenith angle of 30°. It is apparent that the slant looking viewing directions yield the highest sensitivities to atmospheric layers above and below the aircraft. The nadir direction exhibits overall smaller Box-AMFs, yet it provides the highest sensitivity towards the lowermost layers near the ground. The latter is strongly determined by ground albedo. The value of 10 %, chosen for all model runs in this work, is representative for measurements above continents in the UV wavelength range, whereas oceans are characterized by a lower albedo. Oceans, however, do not need to be considered, because flight legs over water

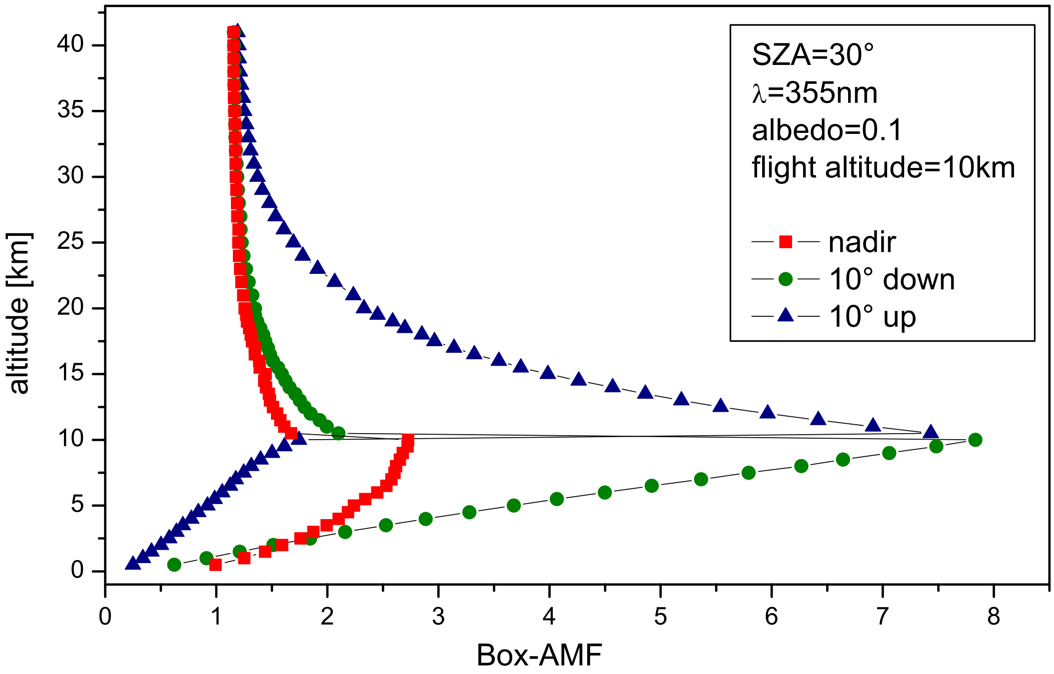

Figure 4.5: *Box-AMFs for the CARIBIC DOAS viewing geometry, calculated for a flight altitude of 10 km.*

are mostly covered at nigh. A description on flight routes of the measurement flights is included in the results chapter of this work.

Chapter 5

Instrumental Setup and Data Analysis

The first part of this work has been the development and assembly of a new DOAS instrument within the framework of the CARIBIC aircraft project. The final instrumental setup emerged from a close cooperation with project partners and in compliance with civil aircraft requirements. Therefore, the project and its specific demands are introduced first. Then the DOAS instrument, its integration into the aircraft and its flight performance are presented. The last section of this chapter is dedicated to the practical aspects of spectra analysis.

5.1 The CARIBIC project

The current CARIBIC project (*Civil Aircraft for the Regular Investigation of the atmosphere Based on an Instrument Container*) is a follow up of the first CARIBIC project, where an airfreight container with automated instruments was operated on a monthly basis on board a Boeing 767-300 ER of LTU International Airways during long-distance flights from 1997 to 2002 [*Brenninkmeijer et al.* 1999]. Subsequently, a more advanced system has been developed, using a larger container with additional equipment, including the DOAS instrument, and an improved inlet system for the sampling of ambient air [*Brenninkmeijer et al.* 2007]. CARIBIC phase 2 has been implemented on a new long-range aircraft type Airbus A340-600[1] of Deutsche Lufthansa. Both the aircraft and the inlet system are shown in Figure 5.1. The first successful measurement flight was accomplished in December 2004. Since May 2005, regular measurement flights are performed once a month and are planned to continue until 2014.

---

[1] The A340-600 is a long range (14 000 km) stretched member (up to 380 passengers) of the A340 family (see *www.airbus.com*).

Figure 5.1: *An Airbus A340-600 of the Lufthansa fleet serves as carrier for the CARIBIC project. The newly developed inlet system (small picture) has been installed permanently at the marked position.*

5.1.1 Scientific aims and motivation

While atmospheric chemistry and climate research is often based on measurement campaigns with a specific focus for a limited period of time, the scientific aim of the CARIBIC project is, in contrast, a detailed long-term observation. So far, monitoring is mostly conducted by ground stations and has been supplemented by satellite observations in recent years. CARIBIC is filling the gap between ground- and space-based research by studying the upper troposphere and lower stratosphere (UTLS) in great detail. The UTLS plays an important role in both dynamical transport and chemical processes, thus affecting the distribution and global budget of trace gases such as ozone or greenhouse gases. The following excursion provides some more information on the UTLS.

Excursion: The importance of the upper troposphere and lower stratosphere (UTLS) The UTLS plays an important role in atmospheric chemistry and climate in terms of troposphere-stratosphere exchange (see Section 2.1.2.3), but also due to the radiative forcing by infrared active species, such as water vapor, ozone and cirrus cloud particles, which are all strong absorbers of outgoing long-wave radiation.

At the same time, the complex UTLS is still one of the less well documented and understood regions of the atmosphere. The main reasons are the extreme dynamical and chemical complexity of the UTLS and the difficulty of regular monitoring at affordable costs. Open scientific questions are for example the individual contribution of processes like tropopause folds or deep convection to the troposphere-stratosphere exchange, or the quantification of the HO_x budget of the UTLS, which is directly linked to the oxidation capacity of the atmosphere (see Section 2.2).

Civil Aircraft regularly fly in the UTLS. Atmospheric monitoring using civil aircraft is thus a logical concept. The advantages are evident: civil aviation offers regular, long-distance, and long-term coverage. Once the initial instrumentation is developed, the flight costs are very moderate compared to specific research aircrafts. Possible disadvantages are that flight routes, instrumental development and changes are subject of close coordination with the airline operating the aircraft. Using civil aircrafts as a measurement platform is not a new idea. In the late sixties and seventies CO and O_3 distributions were determined using instruments inside the plane to analyze air from the cabin's ventilation system. (In those days ozone was not removed from the cabin air supply.) More projects followed, e.g. GASP by NASA, MOZAIC and its successor IAGOS, the JAL project by Japan airlines, measuring e.g. CO, CO_2, O_3, H_2O, and NO_y. For details see *Brenninkmeijer et al.* [2007]. In November 1997, the CARIBIC project phase 1 started regular flights and has been succeeded by CARIBIC phase 2 in May 2005.

The old CARIBIC data set has so far provided a basis for e.g. studies on aerosols, tropospheric O_3 and CO correlations as well as on isotopic composition of CO. 360 air samples of condensable gases (CO_2, N_2O, hydrocarbons, etc.) have been archived for laboratory analysis. In summary, a considerable amount of systematic and up to now unavailable data set has been obtained, which is still subject of scientific investigations. CARIBIC phase 2 follows that concept with extended instrumentation. The UTLS at mid- to high latitudes coincides with the 10 to 12 km cruising altitude of the aircraft, while in the tropics the free troposphere is probed, due to the higher tropopause there. So far, measurement flights were headed to South America or South-East Asia. With these destinations, more than half of the flight time is spent in mid-latitudes and thus in the UTLS. Although long-range aircraft spent most time cruising, vertical profiles during ascent and descent can also be obtained.

5.1.2 Instrumentation and requirements

The CARIBIC project relies on a fully automated airfreight container equipped with in-situ instruments (except for the DOAS and a video camera) and sampling devices for more than 60 different trace gases and aerosol properties. The basic measurement principle is to have an inlet system on the outside of the aircraft to sample ambient air, which is either analyzed in-situ or stored in the instrument container inside the aircraft. The connection between inlet and instruments is accomplished by appropriate tubing that is specified to avoid surface reactions with the sampled trace species. Applying this principle to the DOAS measurements leads accordingly to the installation of the following components: telescopes mounted in the inlet system and spectrograph-detector units inside the airplane to record sepctra of UV-visible scattered sun light. The connection of both is realized by three glass fibre cables, transmitting light from the telescopes to the instrument. The inlet system, shown in the embedded picture of Figure 5.1, is mounted permanently at the marked position at the bottom of the airplane.

For the inlet system strict regulations had to be fulfilled concerning its impact on aerodynamics, on the integrity of the aircraft hull, the absence of vibrations, its behavior at icing conditions and general stability. During the development phase of the new inlet system the possible effects on the aircraft were calculated extensively. The resulting inlet was a compromise of minimizing the disturbance and still being able to sample air totally outside the aircraft's boundary layer. Thereafter the inlet parts were manufactured and the inlet assembled in three weeks of time at Lufthansa Technik in Hamburg. A photograph of the inlet system in shown in the left panel of Figure 5.1.2. Apart from sampling tubes and the camera, three entrance holes for the DOAS telescopes can be seen. On the right panel of the same Figure, a schematic drawing of the inlet is presented. There, the position of the telescope block (see also Section 5.2.1), which houses three miniaturized telescope units can be seen.

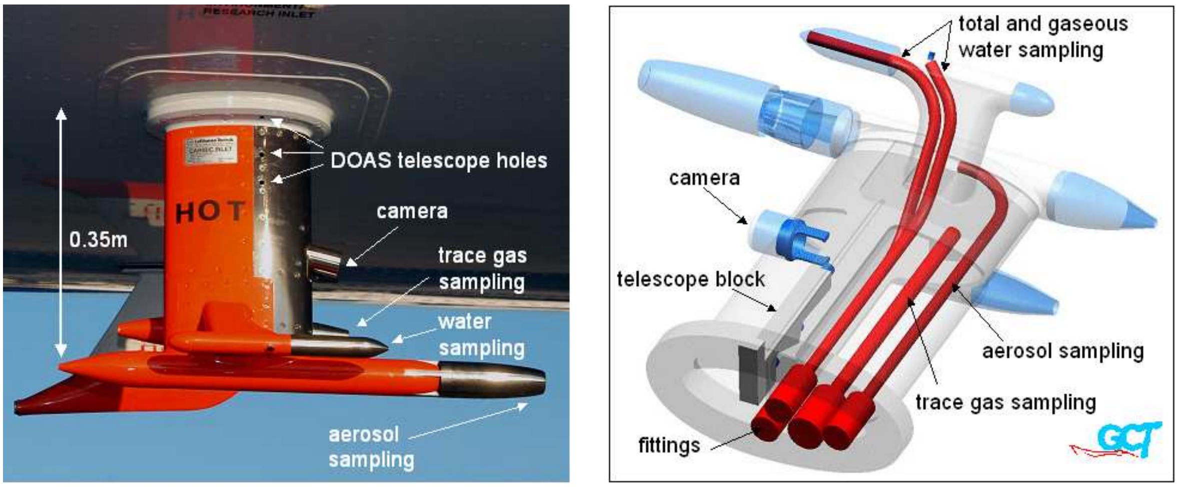

Figure 5.2: *The CARIBIC inlet system. Left panel: A photograph of the inlet system showing sampling tubes, the camera and three DOAS telescope entrance holes. Right panel: A sketch of the inlet system, showing the position of the DOAS telescope block and of the sampling tubes inside the inlet. "Fittings" denotes airtight connections through the hull of the aircraft. Adapted from Garner CAD Technik.*

The integration of the CARIBIC system required several modifications of the aircraft. Most important were the structural changes to the hull around the mounting position of the inlet system, because that meant actually "cutting a hole" in the hull, followed by the installation of the air tubings and cables. One of the biggest challenges was to plan the installation of the DOAS glass fibre cables, because they cannot be taken apart, as can be done with other tubing.[2] Therefore the mounting of the inlet system was very much planned focused on the installation of the glass fibre cables. Also needed were a container connector interface, a control panel in the cockpit, and modifications to electrical hardware, electronics and software.

Ideally, the inlet system should be positioned directly beneath the container, because short tubing minimizes contamination and loss of gases and aerosol particles. However the aircraft's structure demanded a position about 2 m away from the instrument container. The container position itself is determined by practical reasons: It is located in the aft of the front cargo compartment, so that the instrument container is the first container to be loaded before departure and the last to be off loaded upon arrival. Therefore, it does not need to be moved at destination airports. For the respective positions, see Figure 5.3.

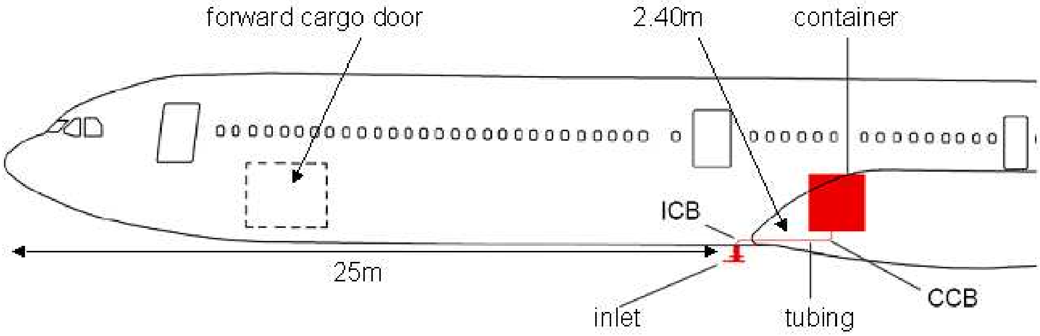

Figure 5.3: *The position of the instrument container and inlet system. ICB denotes "Inlet Connector Bracket" whereas CCB stands for "Container Connector Bracket". The first represents the airtight connection between the inlet sampling tubes and the connection tubes inside the airplane, while the latter houses all the necessary fittings for the connection of the container instruments to the sampling tubes. The distance between ICB and CCB is 2.40 m. Adopted from Brenninkmeijer et al. [2007].*

Even though the container instruments do not directly interfere with the aircraft structure, they nevertheless have to fulfill a multitude of requirements to meet the operational safety standards of civil aviation. There are mechanical requirements for the container and its instruments (e.g. loads on equipment, racks and container as a whole during acceleration/crash conditions), electrical requirements (bonding, fuses etc.), and requirements concerning combustible materials. Furthermore, specifications

---

[2] In principle, there are adapters for glass fibre cables, but they were tried to be omitted as they cause intensity loss.

with respect to the control of equipment (computer controlled switching on and off of instruments) and concerning the absence of conducted or radiated electromagnetic energy have to be met. Above all, to aim for small and light-weight instruments with little power consumption was always applicable. Although each instrument had to pass an individual radiation test, the container is only certified as a whole unit. Thus, all instruments need to be on board during measurement flights (once a month), which can create difficulties if extensive tests or repairs are necessary. The power supply of the container is controlled from the cockpit and can be switched off at any time in case of emergency. To ensure a controlled power consumption, all instruments are governed by a master computer via ethernet connection, which allows or stops individual measurements. A picture of the instrument container is presented in Figure 5.4. It shows the position of the DOAS instrument and the space for the container connector bracket (CCB). When the container is on board the aircraft, it is directly mounted above the CCB and all connections to the instruments are established. This includes the coupling of the glass fibre cables with the spectrographs, which are otherwise stored in the CCB.

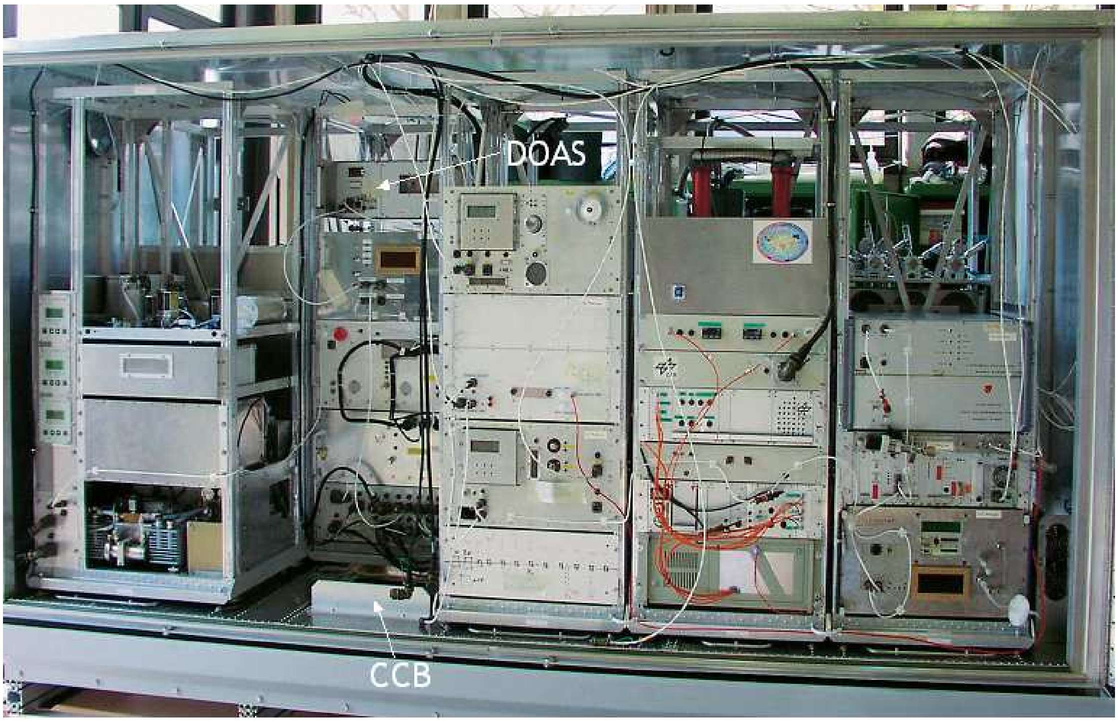

Figure 5.4: *Photograph of the (not yet fully equipped) instrument container. The DOAS instrument is mounted in the rack directly above the container connector bracket (CCB) to minimize the length of the sensitive glass fibre cables.*

Apart from the DOAS instrument, the container comprises detectors for the measurement of ozone, total and gaseous water, NO and NO_y, CO, CO_2, O_2, Hg, and number concentrations of sub-micrometer particles ($>$ 4 nm, $>$12 nm, and $>$ 18 nm diameter). Furthermore, an optical particle counter and a proton transfer mass spectrometer are installed. Aerosol samples are collected for the analysis of elemental composition and particle morphology after each flight as well as 15 air samples being taken in glass containers for laboratory examination of hydrocarbons, halocarbons and greenhouse gases in several laboratories of project partners. Absorption tubes collect oxygenated volatile organic compounds. The video camera at the inlet provides information on clouds and lightning events along the flight track. Data is shared among project participants and has proved to be very helpful for the interpretation of the DOAS measurements. A detailed description of the overall technical setup and instruments as well as related publications is given by *Brenninkmeijer et al.* [2007]. A complete listing of CARIBIC instruments, measured species and participating institutions is provided in the appendix (A.1), whereas references to in-situ data presented in the results chapter of this work are given below. Further information on recent publications and measurement flights as well as a data base of the old CARIBIC project are available at *http://www.caribic-atmospheric.com.*

5.1.3 CARIBIC data references

Data of other CARIBIC participants referred to in this work is taken from 10 s merged files, which combine measurement results of all instruments for each flight, interpolated on a 10 s time grid. Time synchronization is assured by an internal protocol, demanding Δt $<$ 10 s to Master PC time (see Section 5.2.3). Table 5.1 gives an overview of the respective trace substances, measurement techniques and references of data used in this work.

Table 5.1: *Trace substances, measurement techniques and references of CARIBIC data referred to in this work.*

Trace Substance	**Measurement Technique**	**References**
aerosol number concentration	condensation particle counter	M. Hermann, IFT, Leipzig, Germany
CO	VUV fluorescence	F. Slemr, D. Scharffe, MPI-Ch, Mainz, Germany
H_2O total and gaseous	Laser photo acoustic chilled mirror	A. Zahn, IMK-FZ, Karlsruhe, Germany
NO/NO_y	NO: chemiluminescence with O_3 NO_y[3]: chemiluminescence after conversion to NO	H. Ziereis, DLR, Oberpfaffenhofen, Germany
O_3	UV absorption	A. Zahn, IMK-FZ, Karlsruhe, Germany

---

[3] NO_y is the sum of reactive nitrogen compounds that can yield NO, e.g NO, NO_2, NO_3, HNO_3, PAN, PPN, HNO_2, HNO_4, N_2O_5, organic nitrate compounds, aerosol nitrates, but excluding N_2O, CH_3CN, NH_3, HCN.

5.2 DOAS on board CARIBIC

As described above, each CARIBIC instrument has to meet several project requirements. The specifications applicable to the DOAS instrument are summarized in the following:

1. All instrumentation should be light-weight and small, and exhibit a low power consumption. To be small in seize is particularly crucial for the telescope system of the DOAS instrument, because it must be integrated in the inlet system, the design of which was originally supposed to only house trace gas sampling tubes.
2. The instrument needs to pass a radiation test.
3. Measurements must be fully automated, controlled by a master computer via ethernet connection.
4. All parts permanently installed in the aircraft must be maintenance free.

Ad 1: The design of the CARIBIC DOAS instrument employed only the essential parts needed for DOAS measurements: A telescope system, glass fibre cables, a temperature stabilized spectrograph-detector unit and a measurement computer. The telescope system could be realized by three miniaturized telescope units, housed in an 12 x 7 x 1.5 cm aluminum block. The container instrument houses three custom made spectrograph-detector units (Ocean Optics USB2000) (9 x 6 x 3.5 cm, 190 g), power supplied via USB connection. The computer is a 10 x 12 x 2 cm embedded PC solution with a power consumption of 5 V. For the temperature stabilization of the spectrograph-detector units, an electronic temperature controller operates Peltier elements[4], needing a maximum of 60 W when starting to cool in the beginning of a measurement phase. In total, the DOAS container instrument measures 50 x 45 x 18 cm, weighs 16 kg and needs about 75 W at maximum, thus being the most light weight and least power consuming instrument of the whole CARIBIC container. Are more detailed description on the instrumental parts is provided in the following.

Ad 2: The instrument housing was specified by project requirements and is especially designed to retain radiation (ratiopac PRO). Since the electronic parts of the DOAS instrument do not represent big radiation sources anyway, the use of the specified housing was sufficient to pass the electro-magnetic radiation test.

Ad 3: DOAS measurements are typically controlled by a software defining measurement periods and spectra properties. Already existing software could be adapted to ensure fully automated measurements and is described below. Since the DOAS instrument has such a small power consumption, measurements start directly once the CARIBIC container is power supplied. This has the great advantage that spectra during ascent and descent can be recorded, while instruments with larger power

---

[4] A Peltier element is a thermoelectric cooler. Its function is based on the *Peltier-effect*: an electric current induces a temperature difference, as applied here, or vice versa.

consumption are in stand-by during these periods due to safety requirements. Thus, the DOAS instrument does not depend on a master computer command to start its measurements. Communication, however, with the master computer is established via ethernet, sending the instrument status upon request to fulfill project requirements.

Ad 4: The telescope housing is designed to be vacuum tight and to resist strong pressure and temperature differences. This is particularly important, because the inlet system is permanently mounted underneath the aircraft, thus experiencing repeated material stress. The telescope entrance holes are covered during non measurement flights to prevent dirt from covering optical components. The only maintenance regularly done is the cleaning of the telescope prisms before each measurement flight. The glass fibre cables are air tight and are not sensitive to pressure and temperature changes. The end pieces are cleaned before connections to the spectrographs are established.

Besides project requirements, there are also specifications in regard to a reliable instrument performance and spectra quality:

1. Changes in the optical adjustment can affect the spectral retrieval. Therefore a high thermal and mechanical stability is required.
2. Due to limited access to the container instrument, regularly needed maintenance should be kept to a minimum and be avoided where possible.
3. Moving parts should be avoided, as they are particularly susceptible to damage due to vibrations of the aircraft. This is particularly important for all parts permanently mounted in the airplane.
4. Any additional optical components (e.g. mirrors or glass fibre adapters) that lead to intensity losses or could cause interference effects should be avoided.

Ad 1: The utilized USB2000 spectrographs are manufactured by *Ocean Optics* and consist of an integrated spectrograph-detector unit in a closed housing. To ensure thermal stability, the whole unit is temperature stabilized. Unfortunately, occasional strong variations of air temperatures around the instrument container during measurement flights lead to shifts in the wavelength mapping of the spectrographs (see 5.2.3.2). The connection between the glass fibre cables and the spectrographs needs to be reestablished for each measurement flight. Accordingly, the instrumental set up is such to ensure a mechanical reproduction of the position of the glass fibres. So far, no problems were encountered that could be specifically attributed to this mechanical procedure. In general, damage caused by strong vibrations of the aircraft cannot be fully excluded (see also 5.2.4).

Ad 2: The regular maintenance of the DOAS instrument is kept to a minimum. Merely a change of drying agent is necessary about every six month, to prevent moisture from entering the spectrograph-detector units.

Ad 3: This advise has been clearly followed: there are no moving parts in the CARIBIC DOAS instrument.

Ad 4: The glass fibre cables are exposed to high risks: They need to be connected to the instrument before each measurement flight and stowed away afterwards. During loading and unloading of cargo, the glass fibres are exposed to anything or anyone accidently hitting the container. It has also happened that the instrument container was tried to be offloaded in spite of clear labeling and locks. As the glass fibre cables are thus very likely to get damaged, they consist of two individual cables each, which leads to an overall intensity loss in the order of 20-40 %. The connection is placed close to the container connector bracket, so that the part of the glass fibre cables, which is exposed to the highest risk can be exchanged when necessary. The high risk was assumed to justify the loss of intensity, because a complete glass fibre cable cannot be replaced at all, unless the inlet system is removed. Up to now, the glass fibre cables have proved to be quite robust and no repairs were necessary. Otherwise, there are no additional optical components.

5.2.1 The telescope system

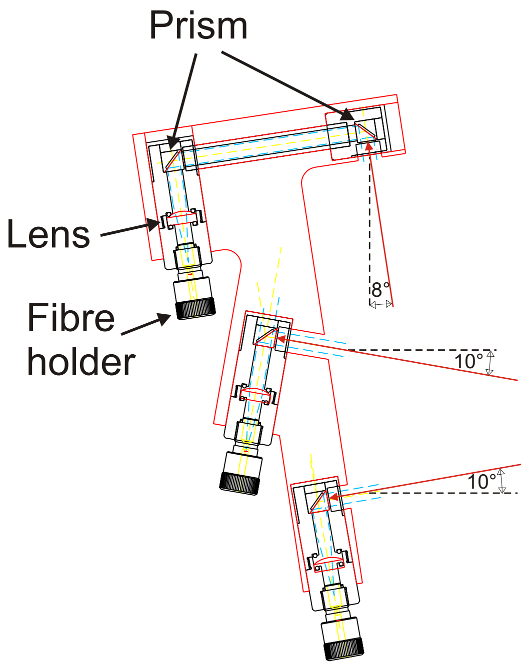

Figure 5.5: *Sketch of the CARIBIC DOAS telescope block. Three telescope units are embedded in a 120 x 70 x 15 mm aluminum block. The viewing directions are indicated by red lines.*

The primary goal of the CARIBIC DOAS measurements is the investigation of the free troposphere. Therefore a telescope system has been developed with two downward looking and one upward looking viewing directions. As described in Section 4.6, the two down looking directions are particularly sensitive to the troposphere, while the upward looking telescope is mainly observing the stratosphere. The telescope system consists of three miniaturized telescope units, embedded in an 120 x 70 x 15 mm aluminum block. Figure 5.5 presents a sketch of the telescope block. Three integrated telescope units serve as entrance optics for the respective viewing directions, i.e. 10° below and above horizon and nadir, which are indicated by red lines. The deviance of 8° from a "real" nadir viewing direction is caused by a slightly tilted mounting of the inlet system at the aircraft (see also Section 4.6). Each telescope unit consists of a quartz glass lens, one or two quartz glass prisms and a filter. Using quartz glass is necessary to enable the transmittance of UV light, whereas the filter (UG5) reduces the intensity of light with wavelengths higher than 400 nm to ensure a good saturation in the desired wavelength range (320 - 400 nm, see Section 5.2.3.2).

Incoming light is reflected by 90°, using 5 x 5 mm prisms, and then focused on the entrance of a glass fibre bundle by a lens with a focal length (f) of 15 mm. The units are vacuum sealed to prevent condensation of water vapor on optical components. During measurement flights, the telescope block is heated by three heating pads (12.5 x 25.4 mm, 15 W, unregulated) to avoid freezing of water on the outside surface of the prisms. The glass fibre cables are connected to the telescopes by 1/16" Swagelok Ultra Torr adapters. These adapters are vacuum tight and are secured with an adhesive that endures strong temperature differences. The seal ring of each Ultra Torr adapter was replaced by a silicone ring, also adapted to a temperature range of -60° to +40° C. The endurance of these rings was tested with dry ice, to ensure they do not brittle upon low temperatures. Finally, the whole telescope unit was tested on impermeability in a 200 mbar environment.

Figure 5.6 shows two photographs of the DOAS telescope block, taken during the assembly of the inlet system. On the left panel, the Ultra Torr adapters for the connection of the glass fibre cables can be seen as well as the red cables belonging to the heating pads. Since the Ultra Torr adapters point downward, the glass fibre cables had first to be conducted downwards and then up again through the inlet system to go inside the aircraft. The complex and somewhat crowded inside of the inlet system forced a final installation of the glass fibre cables in an "8-shaped" position, supported by a copper tube that has been especially manufactured for that purpose. The end of this tube can also be seen in Figure 5.6 (left side). To feed all three glass fibre cables through this tube was a rather delicate task and has been practised beforehand to ensure a smooth procedure upon aircraft installation. The right panel of Figure 5.6 shows a top view of the inlet system and the telescope block. The tight fitting allows the heating pads only to be placed on one side.

The field of view (α)[5] of each telescope is defined by the focal length of the lens, $f = 15$ mm, and the diameter D of the glass fibre entrance. D is calculated from a circular arrangement of 4 individual fibers with a diameter of 210 μm each (see following section). With $D \approx 0.48$ mm, α is given by:

$$\alpha = 2 \arcsin\left(\frac{D}{2f}\right) \approx 1.9^\circ \tag{5.1}$$

Assuming a flight altitude of 10 km, an aircraft velocity of 900 km/h, and a typical CARIBIC DOAS time resolution of 30 s, then the ground pixel covered by the nadir field of view is about 0.33 x 7.5 km.

---

[5] The field of view is commonly referred to as α, which should not be confused with the elevation angle α, introduced in Section 4.3.1.

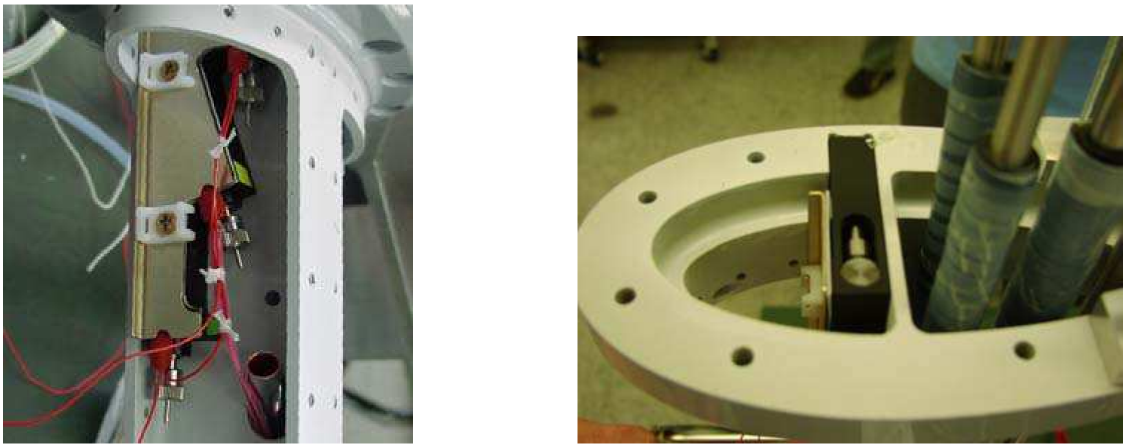

Figure 5.6: *The telescope block during the inlet system assembly. Left side: The telescope system in its final position in the inlet system. The Ultra Torr Adapters for the connection of the glass fibre cables as well as the red cables of the heating pads are visible. Right side: Top view of the inlet system, showing the telescope block and sampling tubes wrapped in heating foil.*

5.2.2 The glass fibre cables

All three utilized glass fibre cables consist of 4 individual quartz glass fibers with a diameter of 210 μm each and a numerical aperture of 0.22. The numerical aperture is adjusted to the specifications of the spectrograph-detector units.[6] There are several reasons to utilize glass fibre bundles instead of a single, thicker fibre: Fibre bundles allow a more flexible arrangement. This was necessary, because the integration of the glass fibre cables in the inlet system required bending the cables with a radius of merely 6 cm. The minimum radius guaranteed by the supplier (Loptek, Berlin) is 6 cm, 5 cm are possibly tolerated. Fibre bundles are also known for largely reducing the polarization sensitivity of grating spectrometers [*Stutz and Platt* 1997]. At the telescope side, the four single fibres of each cable are arranged in a circular geometry to fit the area illuminated by the quartz lens. Likewise, the fibre bundles are linearly aligned at the spectrograph side, where the light enters the 50 μm wide and 1000 μm high spectrometer entrance slit. A sketch of a complete glass fibre cable is presented in Figure 5.7. The geometrical alignment of the fibre bundles is sketched underneath the respective end of the cable.

Inside the inlet system the cables are teflon coated to enable bending with a radius of 6 cm. At the inlet connector bracket (”Druckdose”), all three cables are conducted through an adapter piece and sealed air and pressure tight with an adhesive from Lufthansa Technik. Inside the aircraft the glass fibre cables run underneath the cargo compartment floor panels. Here they are coated with a flexible stainless steel tube for

---

[6] At the time of instrument development, the aperture of the Ocean Optics USB2000 spectrographs - a spectrograph widely used at the Institute of Environmental Physics, Heidelberg - was commonly assumed to be f/2. Later on it was found to be f/4, thus implying that the current instrumental setup over-illuminates the grating, possibly leading to additional stray light inside the spectrograph.

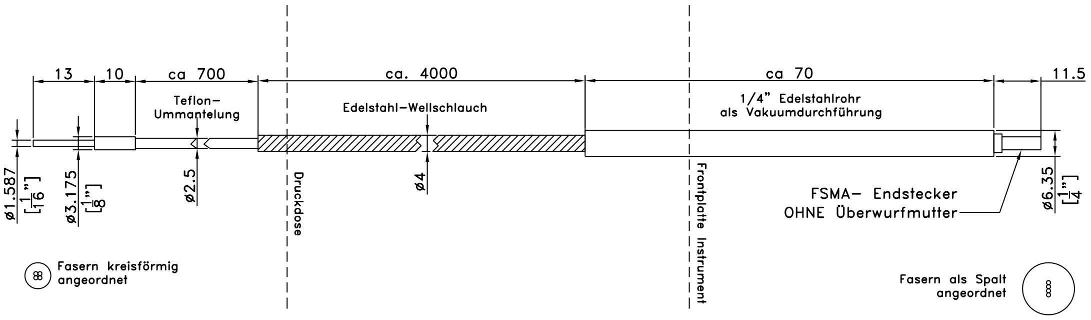

Figure 5.7: *Sketch of a CARIBIC DOAS glass fibre cable with a total length of 6 m. The future position of the inlet connector bracket (Druckdose) as well as that of the front panel of the container instrument upon connection with the spectrographs are indicated by dashed lines.*

better protection.

At the container connector bracket (CCB), the cables enter the cargo compartment of the aircraft. After each measurement flight, the glass fibre cables are stored in the CCB, which is then covered and locked. Since the CCB does not provide much room for storage, the glass fibre cables need to be rolled up with a radius of 14 cm, as shown in Figure 5.8. Since this part of the cables needs to endure a lot of handling, it is additionally coated with a green cloth tube for further protection.

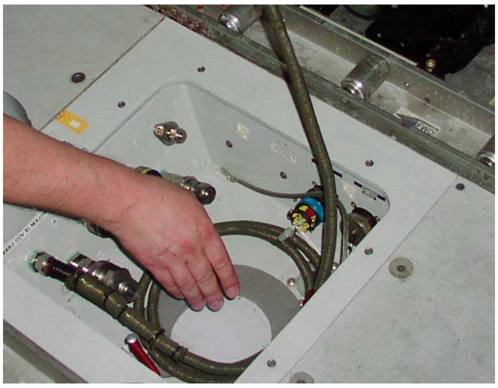

Figure 5.8: *Storage of glass fibre cables in the CCB.*

The FSMA connector at the instrument side of the cables is a commercial standard connection that suits the entrance of the Ocean Optics USB2000 spectrograph. Since this connection needs to be re-established inside the container instrument before each measurement flight, the respective screw nut is omitted. To ensure temperature stability, the Ocean Optics spectrographs are mounted in a separate airtight box inside the container instrument. Thus the coupling of glass fibres and spectrographs needs to be air tight too. This purpose serve the 1/4" stainless steel end pieces of the glass fibre cables, which are the counterpart of 1/4" Swagelok Ultra Torr Adapters mounted at the front panel of the container instrument. In order to reproduce the mechanical alignment of the linearly arranged fibre bundle and the entrance slit of the spectrographs, the cable end pieces and the Ultra Torr adapters are equipped with spanner flats, allowing only a connection in the correct position.

5.2.3 The container instrument

As mentioned above, the components of the DOAS container instrument were kept to minimum requirements. Figure 5.9 provides a block diagram, showing the final setup of the instrument. Several parts are compulsory components: the RS232 ethernet converter is necessary to establish communication between the measurement instrument and the master PC, which is one of the project rquirements (see above). Furthermore, and EMV filter had to be installed and the DC/DC converter had to be supplied by VICOR, as both elements reduce electromagnetic radiation.

All other components are related to the DOAS measurements. The "heart" of the container instrument are three Ocean Optics USB2000 spectrograph-detector units, one for each viewing direction. They are mounted in a separate air tight and temperature stabilized box. The temperature is measured by a PT100 sensor (i.e. a resistance thermometer), which is connected to an electronic temperature controller. The latter operates three Peltier elements inside the spectrograph box. The USB2000 units are connected and power supplied via USB ports of the measurement computer. An USB hub is needed to provide the necessary number of USB connections. The measurement PC is a 96 x 116 mm PC/104 embedded PC solution with a 200 MHz processor (type Geode GX1), providing all features of a full sized PC. It runs on 5 V and a 1 GB flash memory card is utilized as hard disk. Since the measurement program is Windows based, Windows2000 had to be installed, leaving space for data of about 45 flight hours. A typical measurement flight provides about 30 hours of data. Hence, spectra a deleted from the flash memory card before each measurement flight. A possible disadvantage of the miniaturized computer could be that it does not contain an active cooling, yet its operation standard extends to 60°C and so far no problems were encountered.

Photographs of the container instrument in front and top view as well as a picture of the opened spectrograph box are provided on the following pages in Figures 5.10, 5.11, and 5.12.

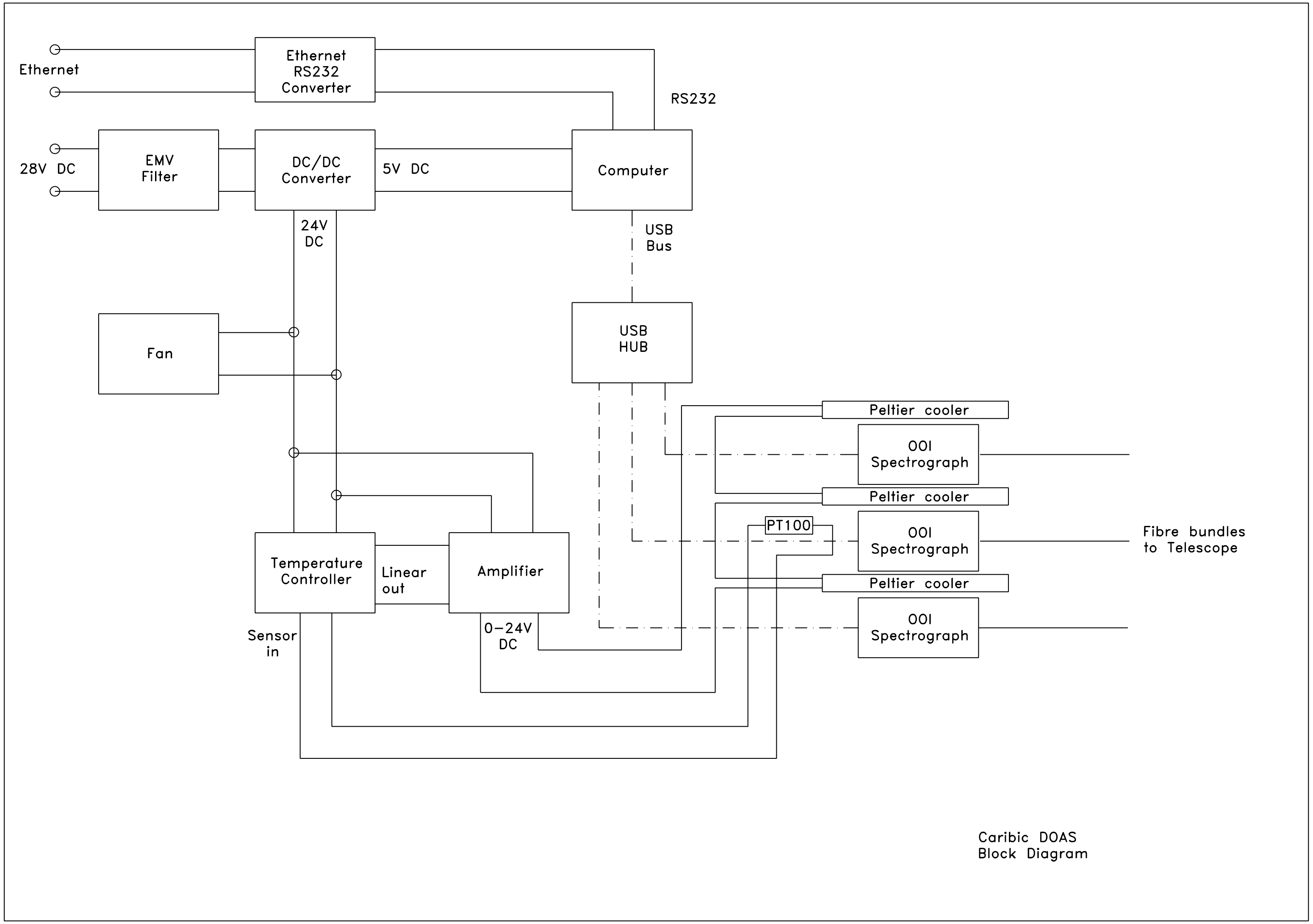

Figure 5.9: *Block diagram of the CARIBIC DOAS container instrument.*

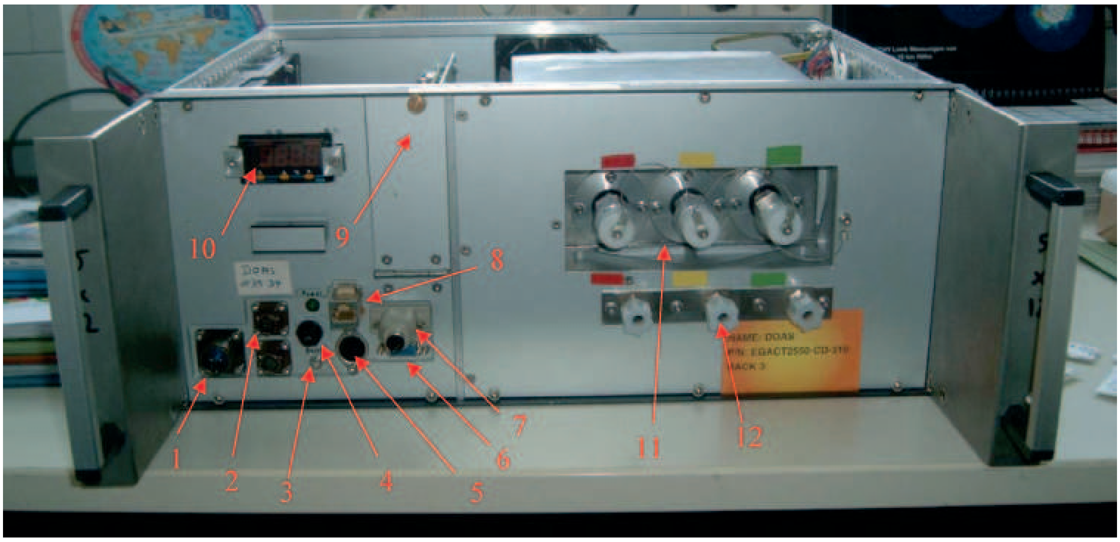

Figure 5.10: *Front view of the container instrument.*

The numbering of the front view denotes as follows:

1 power connection (24V DC)
2 container ethernet in and out
3 reset for internal PC
4 toggle switch fuse
5 keyboard
6 VGA
7 mouse
8 ethernet for internal PC
9 hatch to access the flash memory card
10 temperature controller
11 glass fibre cable connectors
12 blinds for glass fibre cable connectors

Merely 1, 2 and 11 are used during measurement flights. The toggle switch fuse is certified for civil aviation and was obligable. All computer related adapters (3,5,6,7,8) provide external access to the measurement PC. During measurement flights, spectra are stored on the flash memory card. The data can either be transferred via the ethernet adapter of the internal PC (8) or the memory card can be removed through the hatch access (9) and be accessed with the card reader of any PC. The blinds (12) are mounted onto the glass fibre cable connectors (11) when the instrument is not on board. Even though the setup of the spectrograph box is designed to be air tight, the necessary insertion and removal of the glass fibre cables renders the box exposed to ambient moisture. It is very important to keep the spectrograph-detector units dry to prevent condensation of water vapor on optical components. Therefore, the blinds (12) are kept on the adapter pieces at all times (outside the aircraft) and a drying agent is put in the spectrograph box, which is routinely changed every four to six months. Judging by the additionally utilized humidity indicator and by the overall spectra quality, this time interval is sufficient.

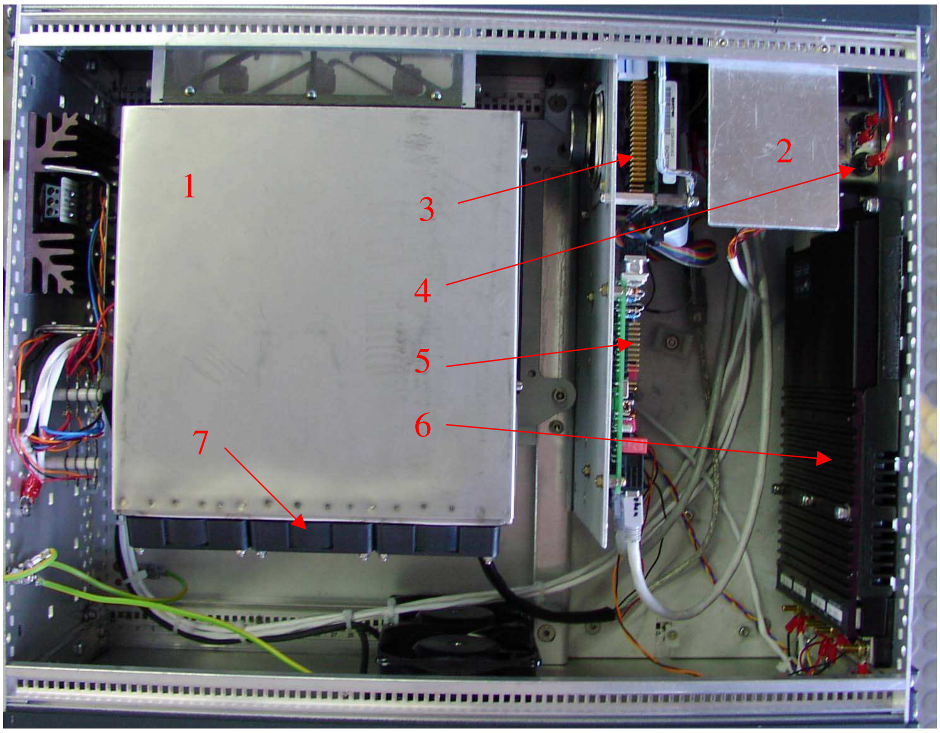

Figure 5.11: *Top view of the container instrument.*

Figure 5.12: *View inside the spectrograph box.*

The top view of the instrument, presented in Figure 5.11, shows the spectrograph box (1), the temperature controller underneath a metal hood (2), the embedded PC (3), the EMV filter (4), the RS232 ethernet converter (5), the DC/DC converter (6) and three fans (7) to sufficiently transport the waste heat caused by the Peltier elements. Figure 5.12 displays the opened spectrograph box. This picture is taken with the instrument turned upside down, because this box is only accessible from underneath. (1) denotes the three Ocean Optics USB2000 spectrograph-detector units that are mounted to a copper frame (2). Copper is chosen because of its particular heat conductivity. The copper frame surface, here underneath the spectrographs, constitutes the top of the spectrograph box, upon which three Peltier elements and a PT100 are adhered to, covered with a copper heat sink (see Appendix A.2 for construction plans) and a metal plate, seen in the top panel (1). The metal plate ensures heat transport to the back of the instrument where the fans are placed and an opening in the instrument housing is provided for heat release. The Ocean Optics USB2000 detectors offer no active cooling. Hence, the temperature stabilization is realized by cooling large areas of the USB2000 housing, placed in direct contact with the copper frame, which is intensified by thermal conductance paste. While this picture was taken, the USB cables (grey) were not connected to the spectrographs, but to the USB hub (3). Little packages of Silica gel as drying agent (4) can be seen inside the box as well as the humidity indicator (5). Upon closing, an adjusted Armaflex insulation (foam material with high insulation capacity and non-inflammable) is placed in the box to aid temperature stability.

5.2.3.1 The measurement program

During measurement flights, two programs are running: the actual measurement program, operating the spectrograph-detector units and a second program to establish communication with the master PC via the container ethernet. The latter receives and records periodically the UTC time sent by the master PC. Upon each first contact, the internal clock of the DOAS measurement PC is set to master UTC, thus ensuring time synchronization. The CARIBIC data protocol demands a time difference smaller than 10 s to master time, for all data shared among participants, or a specific data labeling otherwise. So far the DOAS measurements have always fulfilled the $\triangle$t < 10 s criterion.

Since the start of regular flights, there have been two different measurement programs in use, both in-house developments by *U. Frieß*. The first one, *OOIDOAS*, is a very basic program, performing the most important tasks of spectra recording (see below). The second software, *MiniMax*, is a much more sophisticated measurement software, designed to perform Multi-Axis DOAS measurements with a *Mini-DOAS* instrument, the latter being also an in-house development [*Hönninger* 2002]. In November 2005, OOIDOAS was succeeded by MiniMax, which, over course of time, has received several updates and necessary improvements. Important tasks of the utilized measurement programs as well as the improved features of the MiniMax program are listed below.

- The program initiates measurements and read-out of spectra. The recording of spectra is determined by an integration time and a number of scans N. The integration time denotes the exposure time of the detector. One scan is accomplished with data read out after one exposure time. In order to achieve an adequate signal to noise ratio, the saturation of each scan is kept within the target range of 70 to 90 % and adjusted, if necessary, based on the intensity of the previous scan. The total acquisition time t denotes the time needed for the recording of a spectrum consisting of several scans. The measured spectra are automatically stored on the hard disk of the computer.

- The program starts fully automated measurements upon power supply.

Additional tasks performed or being available by the MiniMax program:

- Oversaturated scans are discarded. If, e.g. the light intensity changes during one scan, which is likely to happen when flying over patches of scattered clouds, then this specific scan is discarded as it would otherwise introduce errors in the spectral fitting procedure.

- The number of pixels considered for the automatic adaption of saturation can be chosen freely. This is particularly important, because all utilized Ocean Optics USB2000 detectors exhibit so called hot pixel, i.e. pixel with a more than ten times higher background signal compared to the average (see below). In the past, these hot pixels ruined the desired suturation of spectra, because the criterion for saturation was not the average of the measured intensity, but the maximum value. Hence, the range for the automatic adaption of saturation has been adapted several times since the MiniMax program is in use.[7]

- The program records background spectra (offset and dark current, see below), once the measured intensity has dropped below a certain level. Since the measurement PC has no online access to the aircraft's position data, night time cannot be determined by local SZA calculations, as often done otherwise. Hence, night is defined by measured intensity values dropping below a certain level. Since the spectrographs exhibit different photon sensitivities, this level needs to be adapted individually.

- The program reboots the PC when no spectra are recorded within a certain time span, usually set to ten minutes. This is important, because the Ocean Optics software driver sometimes cause a system crash of the Windows based measurement program. Before the MinMax program had been conducted, a forced reboot about every hour prevented extensive data loss. Unfortunately, even the forced reboot command could not always resolve a full PC crash.

---

[7] Perhaps pixel get damaged due to higher cosmic radiation during measurement flights, since all CARIBIC DOAS Ocean Optics USB2000 exhibit completely damaged pixel over course of time, whereas this phenomenon has not been experienced with similar instruments during ground-based measurements.

5.2.3.2 The spectrograph-detector unit

The main components of an Ocean Optics USB2000 spectrograph-detector unit are sketched in Figure 5.13. The spectrograph type is a crossed Czerny-Turner, which reduces the required optical bench size. The linearly arranged glass fibre bundle (see 5.2.2) is aligned with the entrance slit (w = 50 μm, h = 1000 μm) of the Ocean Optics, which ensures the required spectral resolution. The entrance slit is mounted in the focal point of the collimating mirror (f = 42 mm). From there, parallel light is dispersed by a plane diffraction grating (Ocean Optics grating $\sharp$ 7, 2400 l/mm, holographic) and focused onto the detector by a second mirror (f = 68 mm). The detector consists of a linear CCD (charge-coupled device) array with 2048 pixel (SONY ILX511). Each of the 2048 pixels represents a potential well, which accumulates the energy dissipated on light exposure as electrical charge, the latter being proportional to the light intensity. Attached onto the CCD detector is a cylinder lens, which focuses the image of the entrance slit of 1000 μm height onto the detector of 200 μm height. Thermal stability of the whole unit is required to prevent misalignment of optical components. A preamplifier and a control logic unit as well as an A/D converter (12 bit data) complement the instrument. Recorded data is sent to the measurement PC via USB connection.

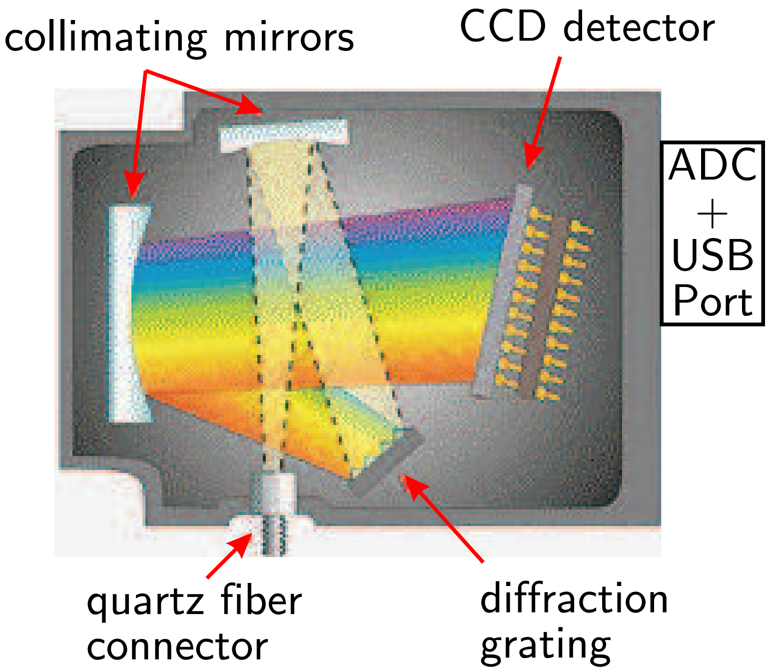

Figure 5.13: *Sketch of the Ocean Optics USB2000 spectrograph-detector unit.*

During course of time one spectrograph was exchanged due to degradation effects, indicated by a strong decrease in photon sensitivity, and another was traded in for a newer one, which adds up to a total of five utilized spectrograph-detector units. They all fit the above stated technical description. Overall, Ocean Optics USB2000 spectrographs exhibit very similar instrumental characteristics. Hence, the discussion in the following applies to all five spectrographs and provides representative examples.

Electronic offset and dark current

As mentioned in Section 3.1.3.1, spectra need to be corrected for electronic offset and dark current, before the DOAS fit can be applied. Both features are caused by the detector and electronics: Detector noise can produce negative analog signals, which cannot be interpreted by the A/D converter. Therefore, an artificial electronic offset signal is added to each measured scan. Before the analysis process starts, the electronic offset has to be subtracted from the measured spectra, weighted by the respective number of scans:

$$I_{corr}(n) = I(n) - \frac{N_{meas}}{N_{ofs}} \cdot I_{ofs}(n) \tag{5.2}$$

where $I_{corr}(n)$ is the intensity of pixel n after offset correction, N_{meas} the number of scans of the measured spectrum and N_{ofs} is the number of scans of the offset spectrum. $I(n)$ denotes the intensity of pixel n before the offset correction and $I_{ofs}(n)$ the respective offset intensity. Figure 5.14 shows a typical offset, recorded automatically at night during a measurement flight in November 2006. To determine the electronic offset, 10000 scans are taken at minimal integration time, which is 3 ms. The average offset signal is 153.65 counts per scan, which represents 3.7 % of the maximum number of counts per channel (4096) for the 12 bit A/D converter in the Ocean Optics spectrograph. In practice, the fraction of the electronic offset is slightly higher, because usually only 80 to 90 % of the maximum saturation degree are used to avoid saturation effects.

The electronic offset was found to be temperature dependent, caused by the cooling of the complete spectrograph-detector unit, which also affects the electronics. The offset signal exhibits an increase with decreasing temperature, which is an additional reason to keep the spectrograph-detector unit at a constant temperature.

The dark current signal is caused by thermal discharge of the CCD detector: Every single pixel can be regarded as a capacitor with a discharge proportional to the number of incoming photons. However, even under dark conditions, i.e. when the detector is not exposed to light, thermal excitation causes a dark current proportional to the Boltzmann factor: $I_{DC} \propto \exp(-\Delta E/kT)$. Hence, the dark current signal decreases exponentially with decreasing detector temperature. For the dark current correction, a dark spectrum is recorded by taking one scan with a high integration time (30000 ms). In Figure 5.15 a characteristic dark current spectrum is presented, taken from the same measurement flight as the offset spectrum above. Several detector pixels exhibit peak signals of more than 10 times the average DC signal. These high DC pixels (hot pixel) are probably caused by endowment defects of the silicon semiconductor material of the detector. With an average value of 3.4 counts per second and typical integration times

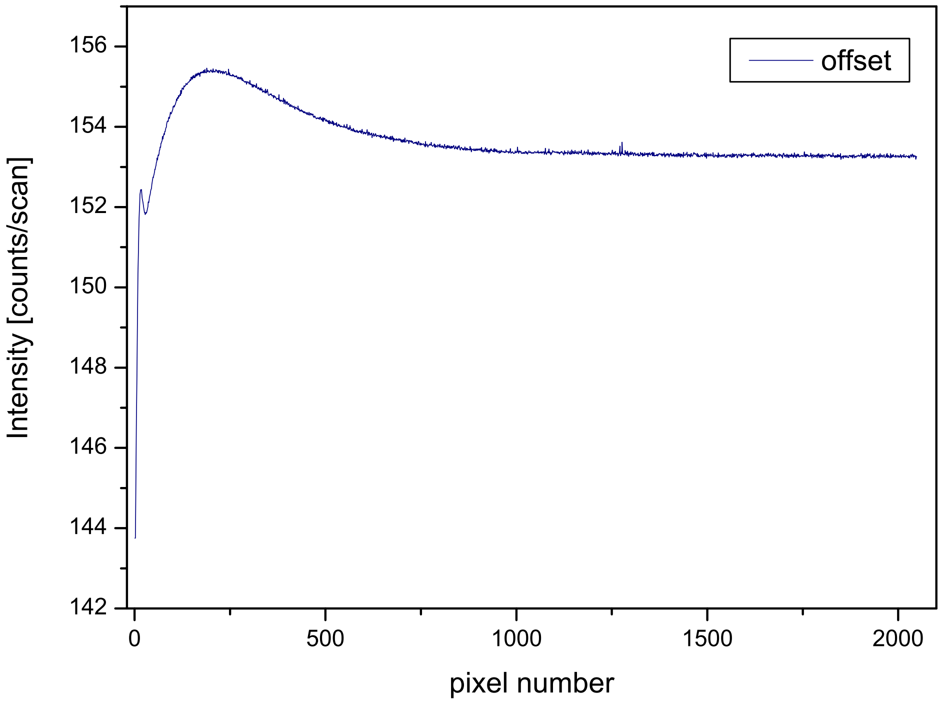

Figure 5.14: *Offset signal of the Ocean Optics USB2000 spectrograph-detector unit.*

< 1 second during daylight measurements, it is apparent, that the dark current needs to be offset corrected, which has been already performed for the displayed dark current spectrum. In analogue to the offset correction shown above, the dark current correction of spectra is done with an offset corrected dark current spectrum ($I_{dc-corr}(n)$), except that this correction is weighted by time instead of scans:

$$I_{corr}(n) = I(n) - \frac{t_{meas}}{t_{dc}} \cdot I_{dc-corr}(n) \tag{5.3}$$

To keep the dark current low, detectors are usually cooled to about -30° C. When utilizing Ocean Optics USB2000 spectrographs, the detector cannot be cooled separately, instead the whole unit needs to be cooled. It was found that the instrument function changes strongly with temperature, exhibiting an inferior resolution with lower temperatures (see next paragraph). Thus, the USB2000 are typically cooled to values between 5° and 15° C. The primary temperature of the CARIBIC DOAS instrument was set to 4° C. Yet it had to be changed after the first measurement flight in December 2004, because temperatures of the instrument container climbed unexpectedly to over 40°C, rendering the DOAS cooling in a futile trial to reach its set temperature. Since then, it is fixed to 18° C, which is, on average, reached within ten minutes after power supply (see also Section 5.2.4).

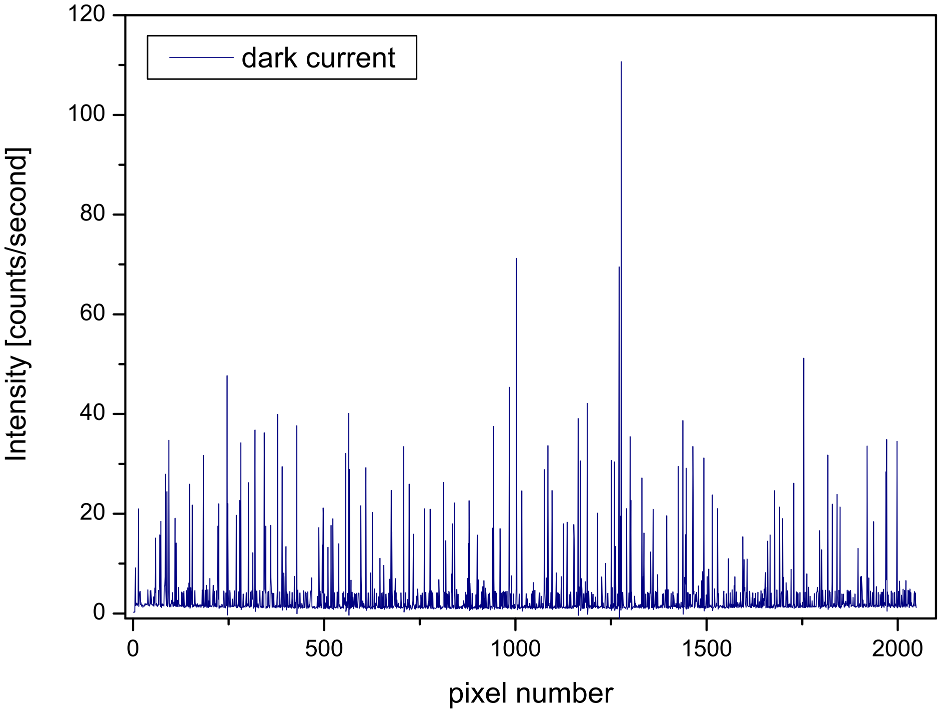

Figure 5.15: *Dark current signal of the Ocean Optics USB2000 spectrograph-detector unit.*

Wavelength calibration and resolution

The instrument should cover a suitable wavelength range with a sufficient spectral resolution to be able to detect the trace gases of interest. Since the original focus of the CARIBIC DOAS instrument was on the detection of BrO, which exhibits absorption lines in the UV, the wavelength range has been adapted accordingly (see also Section 5.4.2). It covers a range from either 290 to 440 nm or from 320 to 460 nm, depending on the individual spectrograph, with a spectral resolution of about 0.4 nm full width at half maximum (FWHM) or 8 to 10 detector pixel/FWHM, respectively. The utilized UG5 filter, integrated in the telescope units, leads to a strong intensity reduction at wavelengths greater than 400 nm as can be seen in Figure 5.16, whereas light intensities in the UV are naturally reduced by ozone absorptions. Hence, the wavelength range providing sufficient intensities and thus a suitable signal to noise ratio for the DOAS analysis, is between 320 and 400 nm, which renders the differences in wavelength range of the utilized spectrographs negligible.

The wavelength to pixel mapping of the spectrographs was determined by taking a spectrum of a mercury emission lamp. When attributing the known wavelength of the mercury emission peaks to the respective pixel number, then an interpolation performed on these points yields the wavelength to pixel mapping of the spectrograph. In case of the USB2000, this function is non-linear and is retrieved with a second order polynomial fit. Figure 5.17 shows the wavelength as a function of detector pixel number.

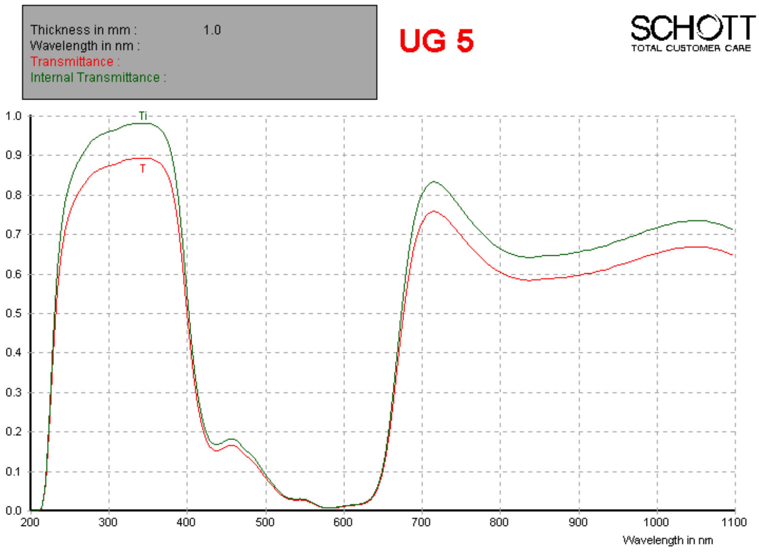

Figure 5.16: *Transmittance of the utilized UG5 filter.*

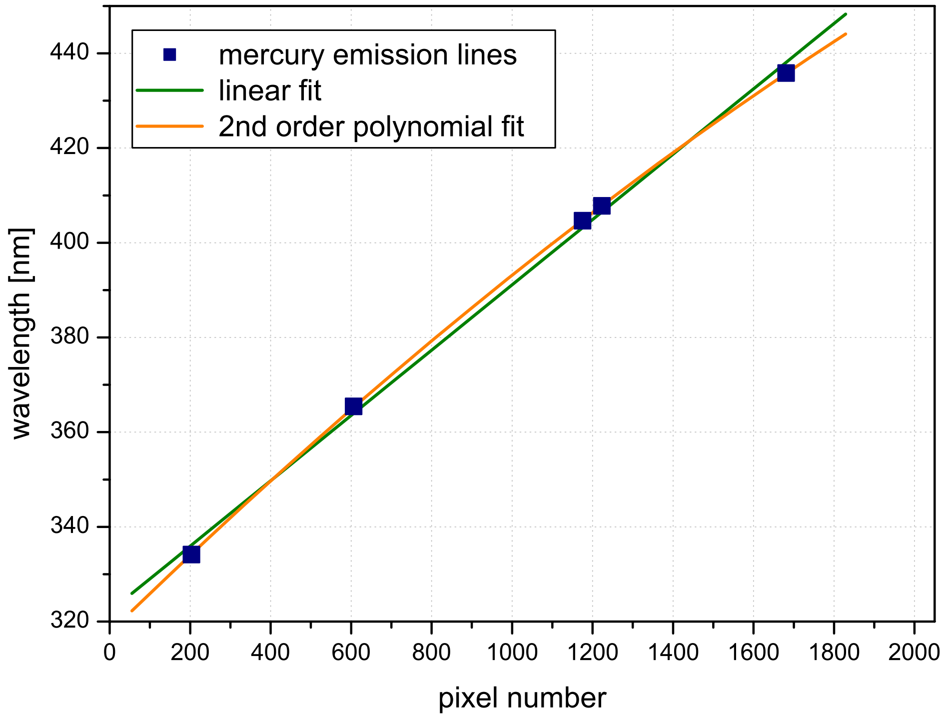

Figure 5.17: *Wavelength to pixel mapping of the USB2000 spectrograph.*

A mercury emission line has a line width of about 1 pm, which is much smaller than the resolution of the instrument. The mapping of these lines onto the detector therefore provides the instrument function H, which is required for the convolution of the highly resolved trace gas cross section references (see Section 3.1.3.3). In Figure 5.18 the mercury emission line at 334 nm is presented, recorded with the same

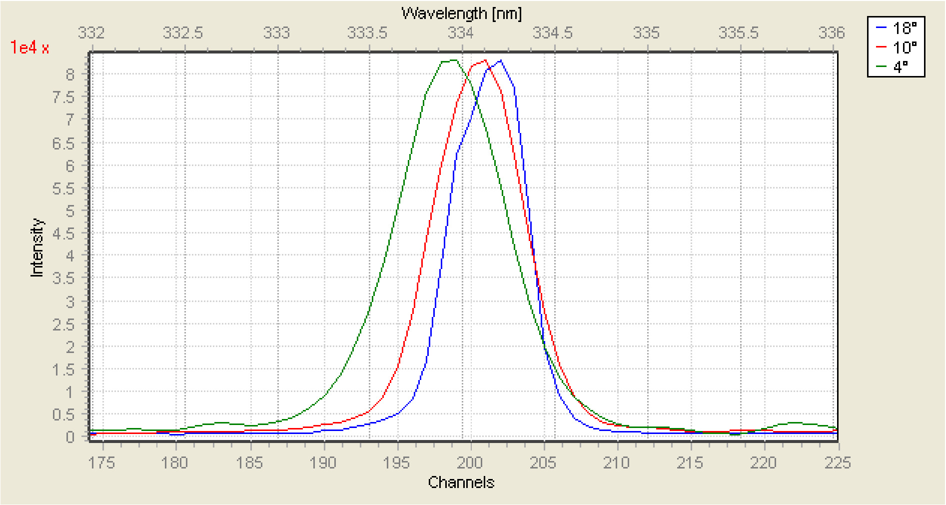

Figure 5.18: *Mercury emission lines recorded at different temperatures.*

spectrograph at three different temperatures, 4°, 10° and 18° C. The temperature dependency of the wavelength to pixel mapping as well as of the spectral resolution is apparent. The respective FWHM of the Hg-lines taken at 4°, 8° and 18° C are 10, 8 and 6 pixel, corresponding to 0.68, 0.55 and 0.4 nm. The temperature stability of the spectrograph-detector units is therefore highly important to avoid significant errors in the spectral fitting process.

The Ocean Optics USB2000 spectrographs are widely used and well documented. For further instrument characteristics refer to e.g. *Hönninger* [2002], *Weidner* [2005], *Weidner et al.* [2005].

5.2.4 Flight performance

Within the first year of measurements, several problems were encountered and subsequently solved, when possible. Numerous error sources could be sunsequently eliminated time by utilizing the MiniMax measurement program and its respective updates as described above in Section 5.2.3.1.

Other problems are related to temperature stability and a possible issue with the glass fibre cables or with the telescope unit, which are discussed below.

Temperature stability

The first measurement flight showed that the cooling capacity of the instrument container was not sufficient. Temperatures inside the container exceeded 40° C. This is why the initial DOAS cooling temperature of 4° C, as mentioned above, had to be raised to 18° C, to ensure a stable temperature within a time span of about ten minutes after measurement start. During cruise periods, at standard flight altitudes between 10 and

12 km, the temperature of the DOAS instrument is very stable as long as the container cooling is stable as well. Unfortunately, the latter is not always the case and respective spectra need to be sorted out (see Section 5.4.1). Since the container power supply is usually switched on shortly after take-off, spectra recorded during ascent periods exhibit strong shifts in their wavelength mapping, caused by the unstable instrument temperature and the above discussed temperature dependency of the spectrographs.

Upon landing, a similar problem occurs, because the air condition of the aircraft's cargo compartment, which is set to 5° C during measurement flight, needs to be switched off as otherwise the condensation of water vapor would set off the fire alarms. Accordingly, spectra recorded during descent periods exhibit also signs of temperature drift. However, as the descent of the aircraft proceeds usually slower than the ascent, the spectral shifts in the wavelength alignments can mostly be accounted for by the non-linear fitting procedure introduced in the DOAS anlysis (see Section 3.1.3.2).

Intensity losses by unknown cause

A severe problem that could not be solved up to now was encountered upon the second measurement flight in May 2005. While the first flight in December 2004 provided spectra with a similar quality for all viewing directions, subsequent flights exhibited a complete intensity loss for the 10° up viewing direction, very low intensity values for the 10° down viewing direction, and stable high quality measurements for the nadir viewing direction. Four flights in 2006, in May, July, August and September, however, surprisingly provided spectra of the 10° up and down viewing directions with increased or almost regular intensity levels, while subsequent flights reproduced the status of flights before May 2006. A period of minor intensity losses has also been observed for the nadir telescope between November 2006 and February 2007.

All tests that can be conducted without opening the inlet system have been performed: The coupling of the glass fibre cables with the spectrographs as well as the spectrographs themselves were examined and no abnormalities were detected. Two tests conducted inside the aircraft, in April 2006 and in August 2007, derived equal results: When illuminating the telescope units with a light source (e.g. a halogen lamp or UV LEDs), then the above described intensity losses are observed at the instrument end of the glass fibre cables. Hence, the problem is either caused by the glass fibre cable themselves or by the telescope unit. A shaking of the glass fibre cables does not influence the light transmittance. Furthermore, a broken glass fibre is completely "blind" as can be seen in the cable of the 10° down viewing direction, where one out of four glass fibres is broken since right after the installation of the inlet system. This fibre never conducts light. Explaining the encountered intensity losses by a "half broken" glass fibre that nevertheless would sometimes transmit light is a highly improbable theory. This view is shared by the company that manufactured these glass fibre cables.

Another possible cause could be freezing of the telescope "windows", i.e. of the prisms (see Section 5.2.1), either on the outside or even on the inside, in case the telescope unit fails to be vacuum tight. But since the intensity losses are also observed upon installation of the instrument container at the ground, even during summer, and particularly during the two testing phases described above, where the aircraft was inside a hall for more than a day, condensation or freezing of water is very unlikely. Additionally, the prisms are inspected and cleaned before each measurement flight. And after all, it remains unclear why this did not happen on those four flights in mid 2006.

The most likely cause is a mechanical problem, affecting either the connection of the glass fibre cables to the telescopes, or optical components inside the telescope unit have gotten loose. The respective components could "jump in and out of place" upon a severe abrasion of the aircraft, perhaps upon a bad landing. Unfortunately, further testing implies opening the inlet system, which is due to several reasons hardly possible. Any testing at the aircraft needs to be coordinated with grounding time of the aircraft and needs to be permitted by LH Technik. Furthermore, the inlet system is "built to last" and the first test of opening it in August 2007 failed due to the strong adhesive used during assembly. Further examinations might have to wait until a new inlet system is constructed. In consequence, almost only nadir spectra were available for the scientific studies of this work, which implies a great loss of spatial resolution.

5.3 Flight data and meteorological information

5.3.1 Arinc data

Arinc denotes a standard protocol for navigation data utilized by Airbus (and Boeing). During each measurement flight Arinc data is sent online to the CARIBIC master PC and available for CARIBIC participants after the flight. The Arinc data includes all navigation parameters measured in-situ by the aircraft, e.g. flight phase, longitude, latitude, pitch, roll, temperature, ground speed, angle of attack (wind), etc.

In order to derive solar zenith angles necessary for the interpretation of DOAS results, information on latitude, longitude and altitude is required, which is taken from Arinc data. The data file offers baro- and standard altitude values. Both are calculated from in-situ static pressure measurements and a ground reference. Baro-altitude utilizes the latest measured static pressure at ground level, while standard altitude calculations rely on a ground pressure of 1013.246 hPa. The difference between both depends on meteorological conditions. Maximum deviations of 100m were observed, causing a negligible error of the order of 10^{-4} in the SZA calculations. Hence, SZAs were consistently derived from Arinc standard altitude, latitude and longitude. Since the standard altitude is given in feet, it was converted in km by 1 foot = 0.0003048 km.

5.3.2 Meteorological data

All CARIBIC measurement flights are supplemented by meteorological information prepared by *Peter van Velthoven* (KNMI). The meteorological analysis is based on ECMWF (European Centre for Medium-range Weather Forecasts) data with a resolution of 1x1 degree on ECMWF model levels. Available are e.g. trajectories, surface maps, pressure level maps and vertical cross sections on cloud cover, cloud water and ice content, PV values, wind speed and wind direction or relative humidity. All data and plot descriptions are accessible at *www.knmi.nl/samenw/campaign_support/CARIBIC*. The following descriptions are adopted from the stated web page and refer directly to data utilized in the result chapter.

Vertical cross-sections: These profiles have been interpolated linearly in latitude, longitude and time to the aircraft location. The ECMWF data were available at 6 hour intervals and with a horizontal resolution of 1 degree in longitude and latitude for CARIBIC. A time step of 3 minutes between subsequent profiles (aircraft locations) is chosen. The reason not to have a higher time resolution is that only 360 profiles can be plotted with our current software. A typical CARIBIC flight lasts more than 10 hours.

PV: PV plots shows the potential vorticity (red contours) with values between 1 and 5 PVU shaded (from yellow to red). Isotachs (wind speed contours) are shown as blue dashed contours. (Dry) isentropes (potential temperature) are shown as quasi-horizontal blue dashed-dotted contours. Moist isentropes (equivalent potential temperature) are shown as quasi-horizontal light-green dashed-dotted contours. In the stratosphere (which moisture is almost absent) the moist isentropes and dry isentropes coincide. In the troposphere, in moist regions, moist isentropes can get strongly vertically inclined. Closed or buckled dry isentropes hardly ever occur as dry instability is very rare. However, closed or buckled moist isentropes, typical of moist instability do occur in the lower troposphere. These are regions where convection is likely. The 400 K isentrope is plotted in purple (not blue or green). This isentrope more or less coincides with the top of the lowermost stratosphere (middle world) and the tropical tropopause.

Cloud cover: Fraction of the area of the model grid cells covered by clouds (0 to 1). Also shown are potential temperature (quasi-horizontal blue dot-dashed), equivalent potential temperature (green dot-dashed) and selected PV-values typical of the tropopause (purple dotted). The 400 K isentrope (near the top of the plot at 100 hPa) is also purple.

Cloud water and cloud ice contents: Given in kg/m^3: Show the presence (and pronouncement) of clouds, Also shown are potential temperature (quasi-horizontal blue dot-dashed), equivalent potential temperature (green dot-dashed) and selected PV-values typical of the tropopause (purple dotted). The 400 K isentrope (near the top of the plot at 100 hPa) is also purple.

Vertical velocity: Vertical velocity dp/dt in 0.1 Pa/s (micro-bar/s). Green to blue shading indicates ever stronger downward motions. Yellow to red shading indicates ever stronger upward motions. In regions with strong upward motion cells clouds will in general be present. Also shown are potential temperature (quasi-horizontal blue dot-dashed), equivalent potential temperature (green dot-dashed) and selected PV-values typical of the tropopause (purple dotted). The 400 K isentrope (near the top of the plot at 100 hPa) is also purple.

5.4 Data analysis

The WinDOAS software [*Fayt and Van Roozendael* 2001] has been used for the DOAS analysis. In order to derive analysis settings that are optimized for the utilized instrumental setup, a large series of sensitivity studies has been performed. These studies included systematic variations of the spectral fitting window, of the polynomial order, of the number of simultaneously fitted trace gases, of the order of the additionally fitted intensity offset and of utilizing different Ring spectra. The most stable results were achieved for the settings described below. This description also includes exemplary discussions of the conducted sensitivity studies. But before the actual fitting process can be applied, the following general tasks need to be done first:

- An offset and dark current correction must be applied to all spectra (see Section 5.2.3.2). For this purpose an offset and dark current spectrum from the respective flight are chosen. For those flights where the measurement program did not yet include the automatic background spectra routine, an offset spectrum recorded in the laboratory close to flight time was chosen, whereas any spectrum of a measurement flight recorded during night could serve as dark current, since these spectra are recorded with only one scan and an exposure time of 30 s, which corresponds to the time resolution of the onboard measurements.

- All high resolution reference cross sections are convolved with the instrument function H that is gained from the mercury emission lamp measurements (see Section 5.2.3.2). Often these cross sections are convolved by choosing a single mercury emission line as convolution kernel, that lies within the spectral wavelength range of the analysis. Here, a software developed by *U. Frieß* is utilized, which convolves the trace gas references with an instrument function $H(\lambda)$ to account for the wavelength dependency of the instrument function. $H(\lambda)$ is derived by linear interpolation of two mercury lines (334 nm and 404 nm). During the convolution process, the references are interpolated on the wavelength grid of the respective spectrograph.

- A Fraunhofer reference spectrum (FRS) is chosen for each flight separately, since the instrument's stability is not sufficient to analyze several flights with one FRS without introducing systematic residual structures. FRS are chosen at high SZA to minimize stratospheric absorption structures. To avoid a polluted tropospheric background in the FRS (typically affecting NO_2 and HCHO measurements), spectra are chosen from an area near the Andes for South American flights and from over central Asia for the South-East Asian flight route. Even though the Ocean Optics USB2000 spectrographs exhibit similar instrumental characteristics, their actual spectral mapping characteristics are too different for cross evaluation of viewing directions.

- A Ring reference is calculated from the FRS utilizing the DOASIS software [*Kraus* 2006](see also Section 3.2.3) and is included in every fitting routine.

- The wavelength calibration performed on four to five mercury emission lines is based on very little information. When recording sunlight spectra, however, as done in this work, a more precise wavelength calibration is possible using the Fraunhofer structures. This approach is offered by the WinDOAS software and is briefly discussed here. For details see *Fayt and Van Roozendael* [2001]. The general idea is to calibrate the measurement spectrum by means of a high resolution solar spectrum with a very precise wavelength to pixel mapping. This high resolution spectrum is convolved with the instrument function $H(\lambda)$. In a fitting routine the FRS is adapted to the high resolution spectrum by applying second order shift and squeeze parameters, which yields a new function for the wavelength to pixel mapping of the respective spectrograph. This routine, however, works only well as long as the original wavelength calibration of the FRS is not too different from the calibration of the high resolution spectrum. This criterion is often not fulfilled by a wavelength to pixel calibration obtained from mercury emission lines, resulting in an output failure of the WinDOAS calibration tool. Hence, a manual calibration was often performed beforehand, similar as done with the known mercury emission lines, but using the known Fraunhofer lines instead. A somewhat exhausting task, but worthwhile as it usually results in a very stable WindDOAS wavelength calibration fit.

- A pre-logarithmic linear intensity offset was included in each fitting process to account for instrumental stray light (see Section 3.1.3.2).

  Shortcomings that are caused by specific project conditions or by the measurement program in its various development states lead to additional tasks that need to be performed before the DOAS fit can be applied and are introduced now.

5.4.1 Spectra preprocessing

The following tasks are project related and need to be performed prior to the DOAS fit can be applied.

- Before the MiniMax measurement program was applied in November 2006, oversaturated scans were not discarded, which results in very high systematic residual structures where applicable. Hence, a first DOAS fit process was performed to afterwards discard all spectra yielding unusually high RMS values.

- During this first evaluation process gaps were placed on those wavelength ranges that exhibit particularly strong hot pixel and which result in systematic residual structures. In the WinDOAS software a "gap" defines a wavelength range that is excluded from the fitting process. These "hot pixel" detector malfunctions typically affect one to three neighboring pixel.

- In order to increase the signal to noise ratio, spectra can be added before analysis. Once the oversaturated spectra are sorted out, 5, 10 and 15 spectra are added respectively, resulting in a new time resolution of 2.5, 5 and 7.5 minutes. As FRS, a spectrum consisting of either 10 or 15 added spectra is always chosen to reduce residual noise. Generally, results are presented in the original time resolution (30 s for nadir and either 30 s or 2 min for the other viewing directions), except where stated otherwise.

5.4.2 Trace gas cross sections

The trace gas cross sections utilized in this work for the spectral retrieval are listed in Table 5.2. To account for the temperature dependency of absorption cross sections, references recorded at different temperatures are used. All cross sections are interpolated on the instrument wavelength grid and convolved with the instrument function. The latter is omitted for O_4, due to its natural broad absorption structure. Additionally, cross sections of O_3 and NO_2 are I_0-corrected (see Section 3.2.2).

Table 5.2: *Trace gas references utilized in this work*

.

No.	Molecule	Reference
1	NO_2 (220 K)	[*Vandaele et al.* 1997]
2	NO_2 (294 K)	[*Vandaele et al.* 1997]
3	O_4 (298 K)	[*Hermans* 2002]
4	BrO (228 K)	[*Wilmouth et al.* 1999]
5	HCHO (298 K)	[*Meller and Moortgat* 2000]
6	HONO (294 K)	[*Stutz et al.* 2000]
7	O_3 (223 K)	[*Bogumil* 2003]
8	O_3 (243 K)	[*Bogumil* 2003]

Figure 5.19 provides an overview of the trace gases listed in Table 5.2. They are plotted after being adapted to the instrument resolution and wavelength grid. The wavelength ranges used for the spectral retrieval are each marked by a red box.

5.4.3 Spectral retrieval of NO_2 and O_4

NO_2 and O_4 are retrieved in a similar wavelength range. NO_2 is analyzed from 354 to 380 nm with a polynomial of order 3 to account for the broad band structures and O_4 from 350 to 356 nm with a second degree polynomial to avoid correlations with the broad absorption structures of O_4 itself. Trace gas references for both retrievals are (1),

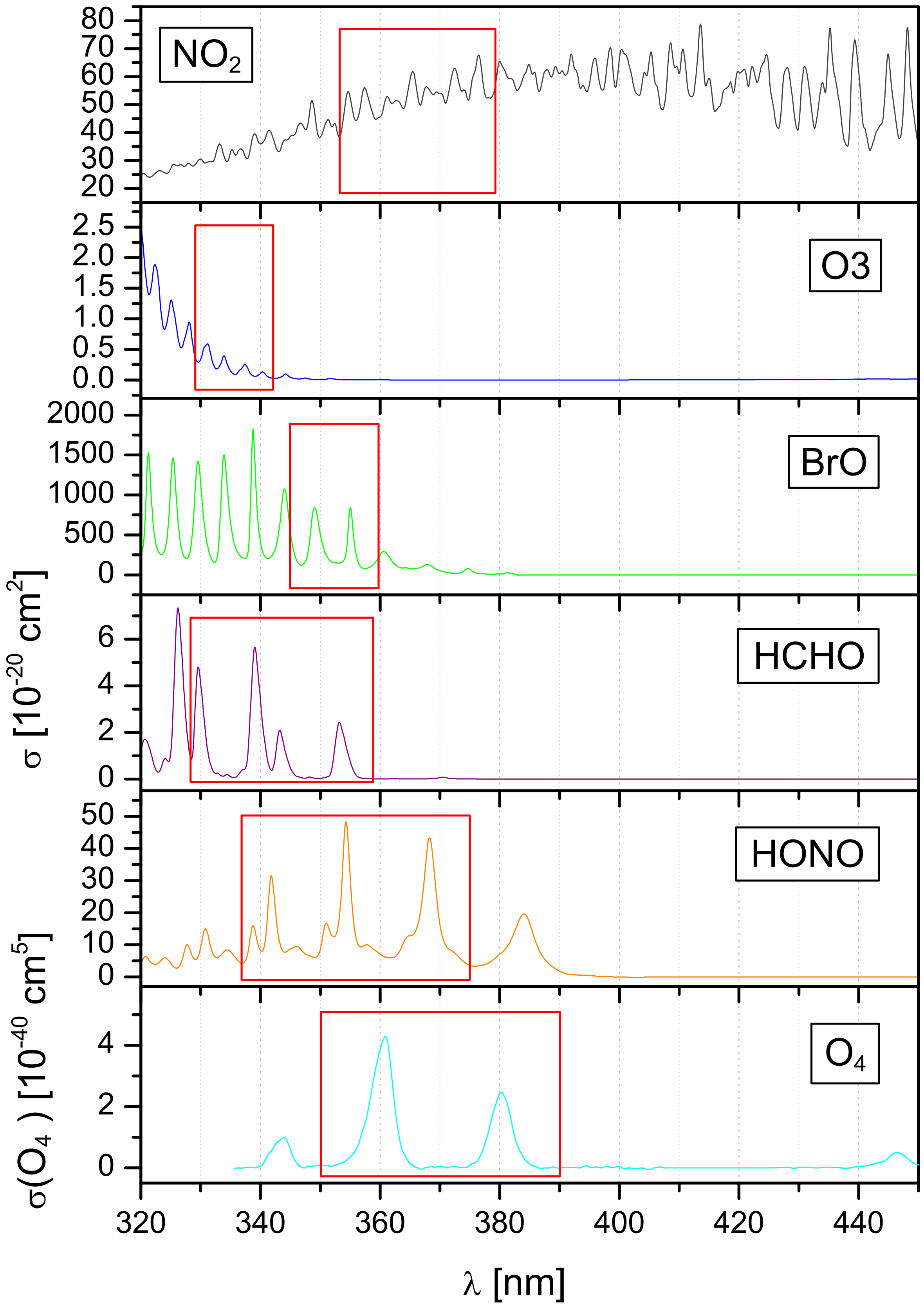

Figure 5.19: *Trace gas cross sections utilized in the DOAS fitting process. The cross sections are convolved with the instrument function $H(\lambda)$ and interpolated on the instrument wavelength grid.*

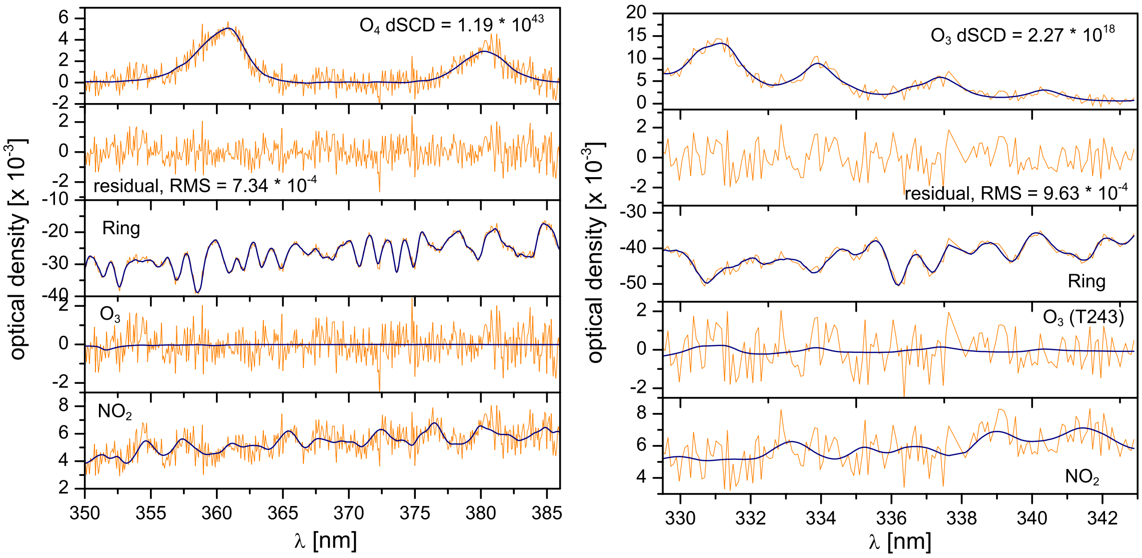

Figure 5.20: *Example for the spectral retrieval of* O_4 *(left panel) and* O_3 *(right panel). The analysis is performed with the same spectrum, recorded inside a deep convection cloud on flight LH158 (August 1, 2006) over central China at an altitude of 11.4 km and with a SZA of 15.6°. The FRS is taken from the same flight and altitude with a SZA of 17.6°.*

(3), (7) and (8) of Table 5.2, while for the NO_2 analysis of ascent and descent spectra additionally cross section (2) was applied to account for absorption structures caused by warmer NO_2 in the boundary layer. In this case, cross section (2) was orthogonalized to cross section (1). Thus the simultaneously fitted NO_2 references become linearly independent and correlation effects due to their very similar structures can be reduced.

In general, the spectral retrieval of NO_2 and O_4 proved to be quite stable. Both trace gases are retrieved in a wavelength range where the measured spectra exhibit maximum intensities. Therefore, these two species where the only trace gases that could sometimes be retrieved from spectra recorded by the 10° up or down viewing directions, which exhibit much lower intensities than the nadir viewing direction (or non at all, see Section 5.2.4). Examples of the spectral retrieval of NO_2 and O_4 are provided in Figures 5.20 and 5.21 respectively.

5.4.4 Spectral retrieval of O_3, HCHO and BrO

Ozone is analyzed in a wavelength range from 329.5 to 343 nm and using a polynomial of order 2. This spectral fitting window has proved to yield reasonable results for the simultaneously fitted NO_2, which caused strong correlation effects at higher wavelengths. Apart from NO_2, (3) and (8) were included in the fitting process, while cross section (8) was orthogonalized to (7). An example of the spectral retrieval of ozone is provided in Figure 5.20, where tropospheric ozone could be measured, because

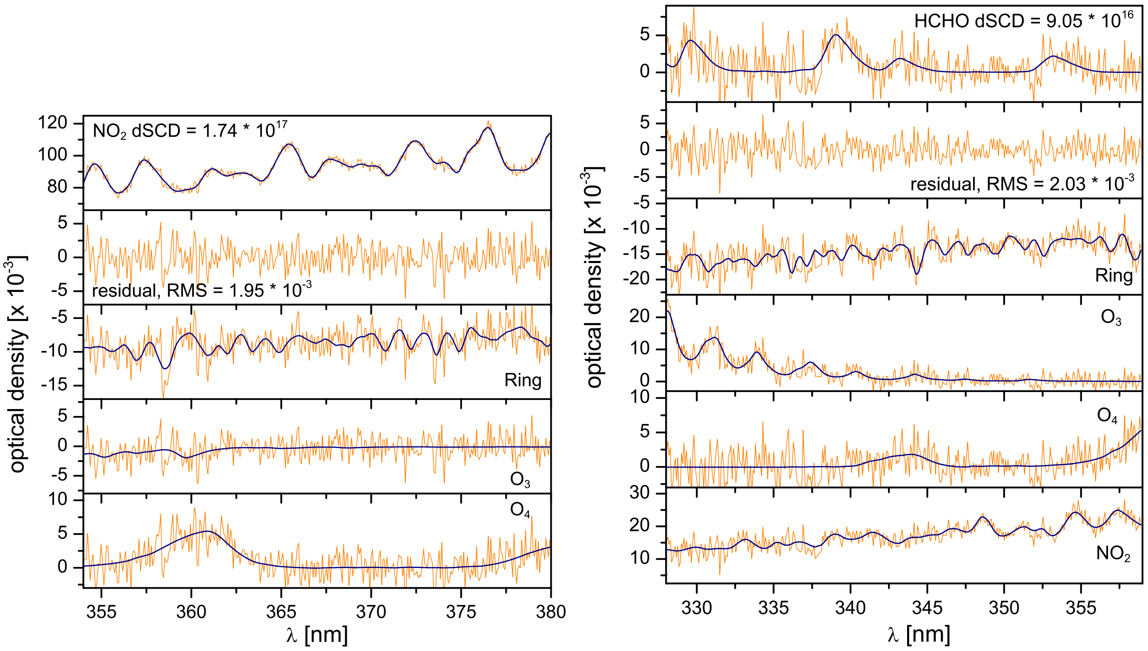

Figure 5.21: *Example for the spectral retrieval of NO_2 (left panel) and HCHO (right panel). The analysis is performed on spectra recorded within the boundary layer upon landing in Guangzhou/China on flight LH158 (August 1, 2006). The spectrum for the NO_2 analysis is recorded at an altitude of 1.3 km with a SZA of 34°, that for HCHO at 1.7 km and SZA = 33.8° respectively. The FRS is taken from the same flight at an altitude of 11.4 km with a SZA of 17.6°.*

its slant column was greatly enhanced by multiple scattering inside a cloud.

In general, the retrieval of ozone in the UV is very difficult due to the influence of strong ozone absorptions on the radiative transfer in this wavelength region (see Sections 3.1.3.3 and 4.3.1). As most ozone is located in the stratosphere, particularly large columns are measured at high solar zenith angles. Although the effects on radiative transfer could be accounted for by applying the modified DOAS approach as described in Section 4.3.1, the use of the Ocean Optics USB2000 spectrographs introduces an additional problem. An ozone fit of a spectrum recorded at a solar zenith angle of 83° can be seen in Figure 5.22, where an example of the spectral retrieval of BrO is presented. The result of the simultaneously fitted O_3 cross sections (the plotted ozone is the sum of the fit results of the ozone references (7) and (8)) reveals that the ozone absorption structure is not fitted accurately, causing a systematic structure in the residual at 351 nm.

The accuracy of the fitting process is a prerequisite for a quantitatively precise ozone retrieval. The observed discrepancies are caused by the non-linearity of the wavelength mapping and of the instrument function of the utilized USB2000 spectrographs. Hence, the convolved cross sections do not accurately match the measured absorption struc-

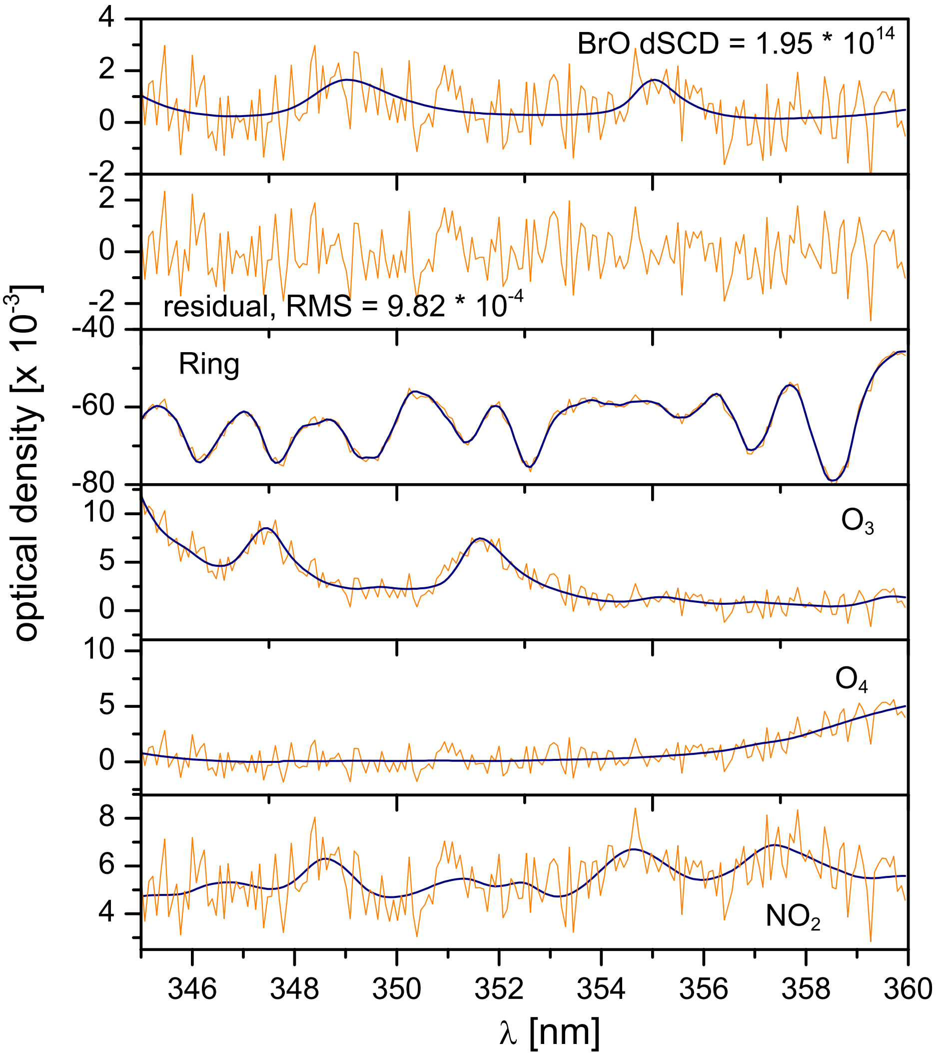

Figure 5.22: *Example for the spectral retrieval of BrO. The analysis is performed for a spectrum recorded over central Asia on flight LH158 (August 1, 2006) with an SZA of 84° at a flight altitude of 11.4 km and a time resolution of 7.5 minutes. The FRS is taken from the same flight and altitude with a SZA of 17.6°.*

tures. The problem worsens when moving the fitting window to shorter wavelengths. In consequence, O_3 columns derived at large solar zenith angles are inaccurate and are not discussed quantitatively in this work. The difficulties of the improper ozone fit also affect the BrO and HCHO retrieval, as both trace gases exhibit similar absorption structures in the same wavelength range as ozone (see Figure 5.19).

As proposed by *Aliwell et al.* [2002], BrO is analyzed in the spectral range from 345 to 360 nm. The polynomial is of order 2. Even though BrO exhibits stronger absorption structures in the UV wavelength range, the DOAS fit is constrained to start at 345 nm in order to avoid severe correlation effects with O_3. Nevertheless, the inaccuracy of the ozone analysis discussed above renders BrO values retrieved at high SZAs faulty. A more detailed discussion on the BrO retrieval is found in Section 6.2.4, where an upper limit of tropospheric BrO is derived from the measurements performed as part of this work. Simultaneously fitted cross section are (1), (3), (7) and (8). An example for a BrO fit is provided in Figure 5.22. In contrast to all other examples in this chapter, the analyzed spectrum consists of 15 consecutive spectra that were added, to achieve a better signal to noise ratio, as BrO is a very weak absorber.

A correlation plot for the retrieval of BrO in different fitting windows with respect to the above introduced settings is shown in Figure 5.23. While the fitting window starting at 340 nm corresponds still well with the original retrieval, the extension of the fitting window to 337 nm shows a bad correlation and large scattering, mostly caused by poorly fitted ozone structures.

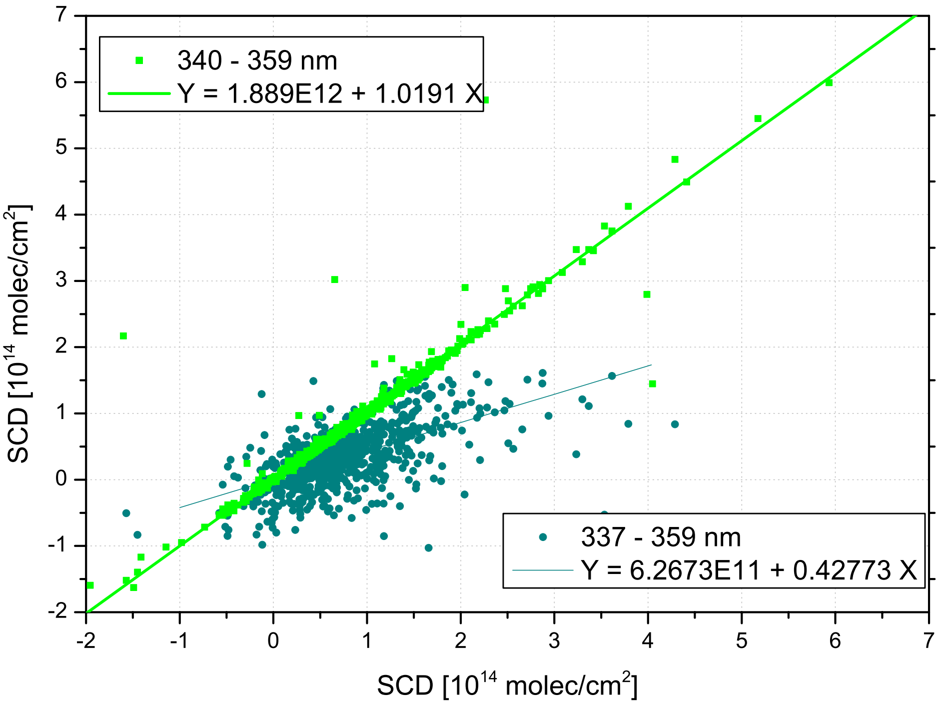

Figure 5.23: *BrO correlation for different fitting windows. Spectra are of flight LH154 to South East-Asia. The FRS is recorded over central Asia at an altitude of 11.4 km and with a SZA of 17.5°.*

Formaldehyde can either be retrieved from 337 to 359 nm, using three absorption bands, or the wavelength range of the spectral window can be extended further to the UV. The latter has been done, starting at 328 nm, with a 4th order polynomial, thus including four absorption bands, even though this range exhibits stronger correlation effects with O_3 and also with the Ring spectrum with rising SZA. On the other hand, when enhanced HCHO columns were encountered at lower SZAs (SZA $< 70°$), the larger fitting window provided a more stable HCHO fit. Since HCHO was mostly measured upon ascent and descent in the boundary layer as well as in tropospheric plumes at lower SZAs, the retrieval was kept starting at 328 nm, including cross sections (1), (3), (4), (7), (8) and (2) where necessary (see Section on NO_2 retrieval). HCHO slant columns retrieved at higher SZA $> 75°$ had to be sorted out due to the above discussed correlation effect, even when utilizing the fitting range starting at 337 nm (see also BrO correlation plot above). A HCHO fit example is presented in Figure 5.21. The analyzed spectrum was recorded during landing in the boundary layer of Guangzhou, China.

5.4.5 Spectral retrieval of HONO

Nitrous acid (HONO) is a weak absorber that has mostly been observed in the boundary layer. Only recently, HONO has also been measured in the free troposphere (see Section 2.4). Since HONO has been observed in the free troposphere on CARIBIC flights as well (see Section 6.2.1), yet with optical densities close to detection limit, the analysis of HONO has been performed particularly careful and thoroughly. An example of the spectral retrieval of HONO is provided in Figure 5.24. It is from a spectrum recorded on flight LH158 within a deep convection cloud. The absorption structure of HONO can be identified, even though its optical density is only slightly higher than the optical density of the residual noise. This analysis was performed in a spectral range from 337 to 375 nm and with a polynomial of order 4, which was also chosen as standard settings for the HONO analysis. Simultaneously fitted references are all of the above stated, except for (2).

The analyzed spectrum of Figure 5.24 is part of a data peak seen in all slant columns inside a deep convection cloud of flight LH158 (see Figure 6.2 in Section 6.2.1). To ensure that the observed data peak is real, different analysis settings have been tested, including a change of the polynomial order and of the spectral fitting range. No significant dependency on the polynomial degree (3-5) was observed. Exemplary results of HONO analyzes in different spectral ranges are shown in Figure 5.25. The observed deviations are within 10 % of the arithmetic mean of all plotted results.

On other occasions, the HONO analysis exhibited correlation effects with HCHO (see also below), for flight LH158 however, no such correlation was found in particular, as can also be seen in Figure 5.25. The HONO analysis for flight LH158 proved to be very robust and the clear systematic structure of this data peak renders this finding highly convincing. Furthermore, the HONO slant columns of other flights show mostly random noise, so that a systematic structure can be most probably attributed to a real HONO concentration.

On flight LH127, HONO was detected within a biomass burning plume. Here, however, the analysis exhibited a clear correlation with HCHO, which is shown in Figure 5.26. Compared to flight LH158, the HCHO slant column within the biomass burning plume is an order of magnitude higher ($\sim 2 \cdot 10^{17}$ molec/cm^2), which can

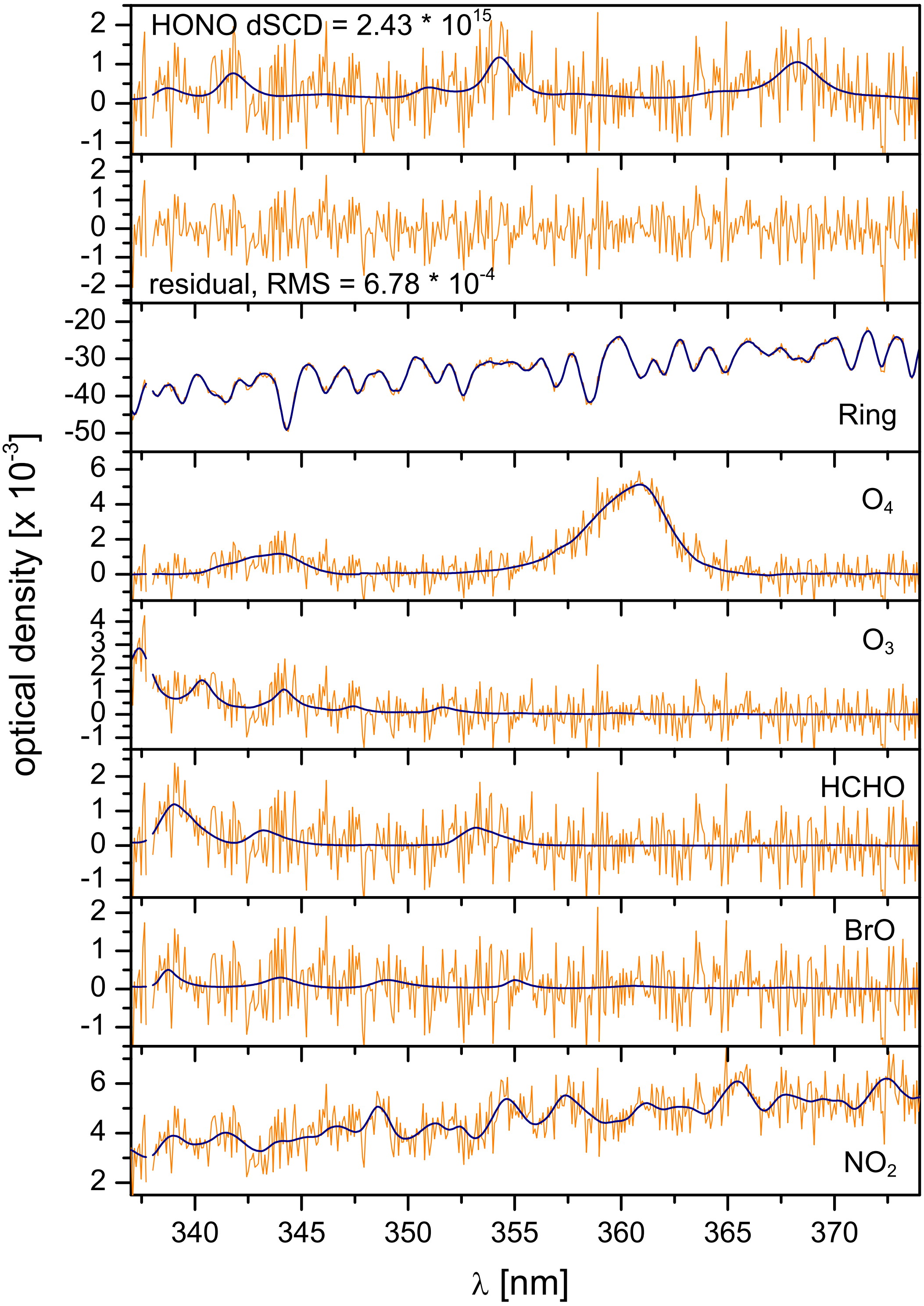

Figure 5.24: *Example of a spectral retrieval of HONO. The analysis is performed on a spectrum recorded inside a deep convection cloud on flight LH158 (August 1, 2006) over central China at an altitude of 11.4 km with a SZA of 15.6°. The FRS is taken from the same flight and altitude with a SZA of 17.6°.*

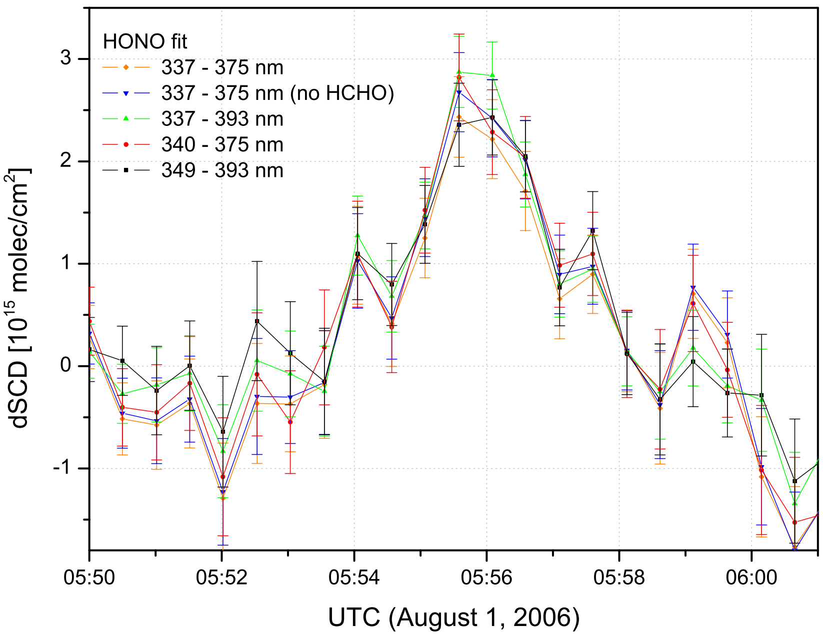

Figure 5.25: *Sensitivity study with different fitting windows for the retrieval of HONO. Observed deviations are within 10 % of the arithmetic mean of all plotted results.*

explain the observed strong correlation effect, as both trace gases exhibit very similar absorption structures.

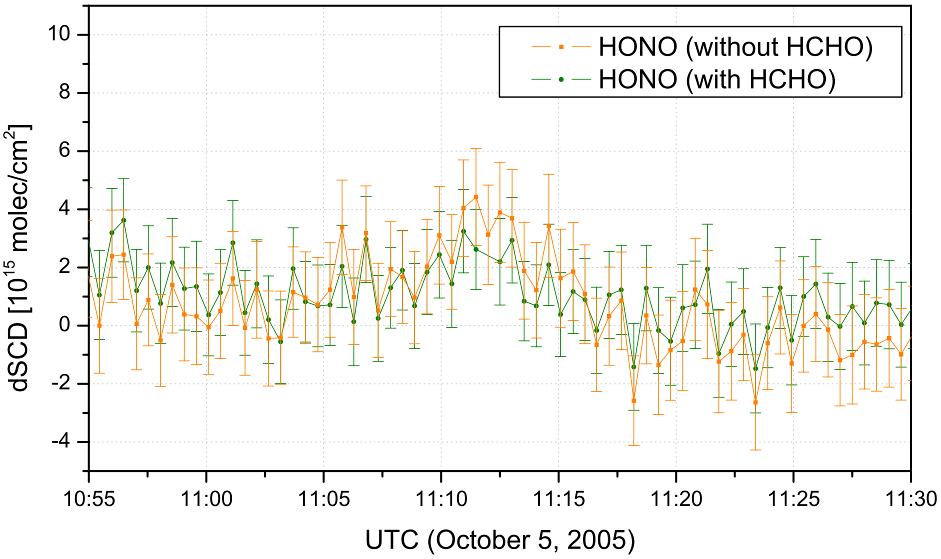

Figure 5.26: *HONO retrieval from a spectrum recorded in a biomass burning event on flight LH127, SZA 62°. The FRS is recorded with an SZA of 55°*

5.4.6 Error sources

The total noise contribution of a spectrum caused by photon and instrument noise is given by:

$$\sigma_{tot} = \sqrt{\sigma_{ph}^2 + \sigma_{dc}^2 + \sigma_{ofs}^2} \tag{5.4}$$

In a spectrum with a good saturation, the photon noise (σ_{ph}) determines the total noise as it contributes about 98 % to the total noise. Since the photon noise is proportional to $1/\sqrt{N}$, the signal to noise ratio can be increased by subsequently adding recorded spectra. The statistical error is directly retrieved by the WinDOAS software and plotted as fit errors of the slant column densities presented in this thesis. These numerical errors are calculated from the standard deviation of the linear and non-linear fit algorithms and weighted by the total RMS and the number of degrees of freedom [*Fayt and Van Roozendael* 2001]. The WinDOAS errors are in the same order as fit errors derived with the method proposed by *Stutz and Platt* [1996] [*Heue* 2005].

In general, errors are introduced by a combination of systematic and statistical sources (see also Section 3.1.3.3). The following systematic error sources can additionally affect the DOAS retrieval process:

- Errors caused by an improper wavelength calibration. This error is determined by the quality of the wavelength calibration performed with the WinDOAS software using a convolved high resolution solar spectrum as reference (see above). Each wavelength range for the spectral retrieval of different trace gases is calibrated separately. Usually deviations in this spectral alignment are below 0.1 channels, which corresponds to 0.007 nm. However, the largest error is introduced by the temperature dependency of the wavelength to pixel mapping of the USB2000 spectrographs. Since spectrograph temperatures are not always stable during flights, measured spectra exhibit an altered wavelength calibration compared to the FRS that cannot always be accounted for by the non-linear shift and squeeze parameters of the DOAS fit. In comparison, errors in the wavelength calibration of the utilized trace gas references can be neglected, since they have been measured with a much higher resolution.

- Trace gas reference cross sections typically exhibit a total error in the order of 5 %. Temperature dependencies of the observed trace gases cannot be completely accounted for and introduce an additional error.

- An important issue possibly leading to large systematical errors are correlations between the cross sections included in the fitting process. This effect is difficult to quantify as the residual structure can even become smaller when structures are improperly fitted by correlating cross sections. Several typical examples exist: Strong correlations exist between trace gases that exhibit similar absorption structures, e.g. O_3, BrO and HCHO, while O_4 typically correlates with the polynomial. An additionally fitted intensity offset to account for instrumental stray light often correlates with the Ring reference.

- Further instrumental error sources are detector non-linearities, instrumental stray light or different mapping characteristics of the spectrographs caused by a poor mechanical connection of the glass fibre cables to the instrument.

The quantitative determination of the systematical errors is far from being simple. The above mentioned sensitivity studies showed variations of slant column densities of up to 15 %. This, however, does not necessarily imply an error of each slant column in the same order. An overall error in the order of 10 % is most likely reasonable, probably smaller when the measured optical density is significantly higher than the respective RMS noise.

5.4.7 Quality assessment

Before slant columns are declared as "final products", several quality criteria need to be fulfilled:

- The photon sensitivity of the USB2000 allows in general no evaluation of spectra recorded with a solar zenith angle higher than 90°. Hence, all spectra with SZA $> 90°$ are sorted out. Since most evaluated spectra are recorded with the nadir viewing direction, the measured intensity is also strongly affected by ground albedo. On the South-Asian route, the sun always sets on the way to Manila over the South Chinese Sea. Since oceans usually exhibit lower albedo values than continents (except for sun glint situations), spectra recorded there yield intensities too low for a DOAS analysis at SZA *geq* 85°.

- The analysis of all spectra recorded during ascent and decent of the aircraft is checked manually for systematic structures in the residual. Typically these spectra exhibit large wavelength shifts of up to 0.3 pixel caused by the temperature drift of the spectrographs (see Section 5.2.4), whereas under stable conditions shift values are below 0.01 pixel. However, as long as the overall fitting results yields no indications of obvious errors, which would be apparent in systematic residual structures, then it is assumed, that the non-linear fitting routine has properly accounted for the spectral shifts caused by the temperature drift.

- Sometimes the container temperature changes during a flight for a certain period of time. Then analysis of the respective spectra yields high systematic RMS structures. Accordingly, these spectra are sorted out.

As mentioned in Section 5.2.4, almost only the nadir viewing direction provided spectra suitable for the DOAS analysis. Therefore it must be noted that *all plotted DOAS results are derived from the nadir viewing direction, except where stated otherwise.*

Chapter 6

Results

The general concept of this chapter is to explore the scientific potential of the CARIBIC DOAS data set. The following sections present selected results of the most interesting findings and provide exemplary discussions on the scientific yield of this data, such as studies on radiative transfer and chemical processes inside a deep convection cloud, observation of stratospheric trace gases in tropopause folds, or on the retrieval of boundary layer profiles. Often, supplementary data is utilized, which gives an impression on the information gained by a synergetic use of available CARIBIC data.

This chapter is divided in three main sections: in measurements of trace gases in the troposphere, in the stratosphere and in the boundary layer. However, many links exist between individual parts, which are pointed out and summarized in Section 7, along with ideas to follow up the topics discussed below. Concluding, suggestions on alternative systematic approaches to work with the available CARIBIC (DOAS) data set are provided in the outlook.

6.1 CARIBIC flights - an overview

From May 2005 to March 2006, the destination of measurement flights was South America, except for two flights. These two and subsequent flights were headed to South-East Asia. All flights are return flights from Frankfurt/Main, either to Santiago de Chile via São Paulo (Buenos Aires on the very first flight in December 2004) or to Manila via Guangzhou/China. In Figure 6.1 the respective flight routes are shown. Since the DOAS instrument utilizes scattered sunlight as radiation source, the measurements depend on available daylight. Unfortunately, it is Lufthansa policy to schedule their long-distance flights such that most of the flight time is spent during night. From 27 - 31 total airborne hours only about 40% are spent during daytime. Generally, flights start in the late evening at Frankfurt, mostly after sunset. On the South-American route the flight legs between São Paulo and Santiago de Chile are carried out during daytime. On the return flight to Frankfurt the sun rises at about 10° W. On the Asian route the sun rises when the airplane is at ca. 60° E and sets between Guangzhou and Manila, depending on season. There is no sufficient daylight on the return flight, merely twilight with light intensities being too low for spectra analysis. The day light stretches are marked with yellow bars in Figure 6.1 and the respective flight direction is indicated by arrows.

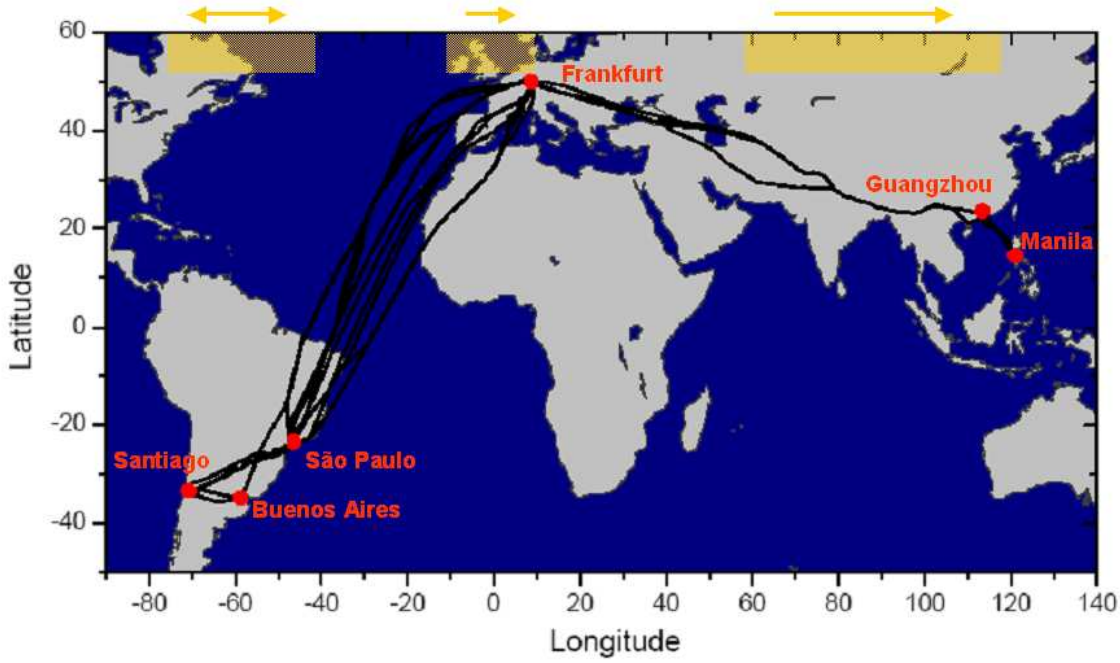

Figure 6.1: *CARIBIC flight routes from December 2004 to June 2007. All flights are 1-stop return flights from Frankfurt/Main. The yellow bars mark flight legs with daylight, while the arrows above indicate the flight direction of the sunlit part. Adapted from Brenninkmeijer et al. [2007].*

Considering the fact, that CARIBIC flights are on a regular monitoring basis, many flights proved to be particularly interesting: Biomass burning events were detected on several occasions, over South America and South-East Asia as well as over the Atlantic from African outflows. The route over the Andes was very often characterized by flying through stratospheric air, due to the specific atmospheric dynamics of this region. From a dynamical point of view, the flights to China are also very interesting, because often a highly structured tropopause was encountered, exhibiting (deep) tropopause folds, steep PV gradients and PV residues in the free troposphere. Furthermore deep convection of pollution plumes, mostly over China, could be detected. Since all flights start and end in big cities, pollution upon landing and take-off was always observed.

These events are not all reflected in the DOAS data as well, due to one of the following reasons: they were either encountered at night or the trace gases that can be measured by DOAS were below detection limit or not present at all. Furthermore, the life time of e.g. NO_2 and formaldehyde in the troposphere is much shorter than that of e.g. CO (days compared to months), which renders the latter a suitable tracer for tropospheric pollution events. Table 6.1 provides an overview of interesting events that could be detected by the DOAS instrument and names the trace gases associated with these events. The listed flight numbers are internal CARIBIC project numbers, starting with LH101, being the Lufthansa Technik test flight for the approval of the inlet system. Each flight leg gets a separate number, thus one complete measurement flight consists of four consecutive flight numbers. The destination abbreviations are official and utilized in international aviation: FRA = Frankfurt/Main, GRU = São Paulo/Brazil, SCL = Santiago de Chile/Chile, CAN = Guangzhou/China (formerly Canton).

Table 6.1: *Overview of events observed by the DOAS instrument.*

flight no. destination	**date**	**event**	**trace gases**
LH110 GRU SCL	May 20, 2005	deep convection lightning	HONO
LH123 GRU SCL	August 31, 2005	biomass burning flight in strat. air	NO_2, HCHO O_3, NO_2, BrO
LH124 SCL GRU	August 31, 2005	biomass burning flight in strat. air	HCHO O_3, NO_2, BrO
LH127 GRU SCL	October 05, 2005	biomass burning flight in strat. air	NO_2, HCHO, HONO, O_3 O_3, NO_2, BrO
LH128 SCL GRU	October 05, 2005	flight in strat. air	O_3, NO_2, BrO
LH158 FRA CAN	August 01, 2006	deep convection PV residues in the upper troposphere	NO_2, HCHO, HONO, O_3 NO_2

Enhanced NO_2 and HCHO values measured in the boundary layer upon landing or take-off are not listed in Table 6.1, because they occur regularly during all daylight arrivals and departures and are caused by local pollution. Selected events of Table 6.1 are presented and discussed in detail in the following sections, starting with the section on tropospheric measurements. Typical tropospheric trace gas plumes, encountered during CARIBIC flights, are either anthropogenic pollution plumes or biomass burning signals. Both are usually characterized by enhanced in-situ CO and NO/NO_y values as well as by a higher aerosol number concentration. Some of these plumes are also reflected in the DOAS data as elevated NO_2 and HCHO columns. Discussing such differences and similarities of DOAS and in-situ measurements allows to draw conclusions on chemistry and transport processes (e.g. estimates on the age of a plume).

The following interpretation of the DOAS results benefit from the information gained by the simultaneously measured in-situ data as can be seen in the subsequent sections on HONO measurements in the free troposphere (LH110/127/158) and on biomass burning events over South America (LH123/124 and LH127/128). The retrieval of an upper limit of tropospheric BrO in Section 6.2.4 concludes the section on the measurements of tropospheric trace gases. Observation of stratospheric trace gases (NO_2, O_3 and BrO), is the focus of Section 6.3. There, the influence of atmospheric dynamics, e.g. of tropopause folds on trace gas profiles is discussed and a total column comparison of CARIBIC NO_2 data with satellite measurements provides insight into the separation of stratospheric and tropospheric columns. This results chapter concludes with the retrieval of a boundary layer aerosol profile by means of O_4 measurements and a subsequent profile inversion of NO_2 and formaldehyde data, applying the optimal estimation method.

6.2 Discussion on trace gases measured in the free troposphere

6.2.1 HONO measurements over central Asia on flights LH110 and LH158

While measurement flights in the beginning of 2006 proved to be quite uneventful with respect to tropospheric trace gases, flight LH158, on August 1, 2006, from Frankfurt to Guangzhou, rewarded with a very interesting tropospheric plume over central China. Within this plume, enhanced levels of NO_2, HCHO and HONO could be detected. Particularly nitrous acid (HONO) is not expected to be found in the upper troposphere, which renders this finding even the more interesting.

Upon this detection, all previous measurement flights were reanalyzed to search for HONO absorption structures. Two other flights exhibited HONO signatures (LH110 to China and LH127 within a biomass burning event over South America), even though the optical densities of both signals range around detection limit. In the following, the available data of all three flights is presented first. Afterwards, in Section 6.2.3, flight LH158 is exemplary discussed with respect to the HONO measurement, as it provides the most convincing HONO signal (see also Section 5.4.5) and a multitude of supplementary data. In view of these findings the HONO measurements of flights LH110 and LH127 are subsequently discussed. Accordingly, the presentation of flight data also starts with flight LH158.

6.2.1.1 Flight LH158

On August 1, 2006, a trace gas plume was intercepted over central China, between 05:53 and 06:00 UTC (12:53/13:00 local time, SZA $\approx 15°$, longitude = 106.5°, latitude = 27.1°, altitude = 11.4 km). In Figure 6.2 the respective DOAS measurements are presented. The time period of plume contact is indicated by a red box. All trace gases exhibit enhanced slant columns inside the plume and peak values are found at 05:55 UTC, except for BrO. The FRS utilized for this analysis is recorded at 05:39 UTC, shortly before plume contact (but still outside a second, greater plume, seen in in-situ data presented below). The relative differences of all measured dSCDs plotted inside the red box of Figure 6.2 can therefore very likely be attributed to trace gas concentrations inside this plume.

The respective data peak starts at 05:53 UTC, while the highest slant columns are measured at 05:55/05:56 UTC in all species but BrO. HONO, HCHO and NO_2 show a very close positive correlation, while O_3 exhibits a slightly different distribution. The somewhat indicated structure of BrO at the same time can be attributed to correlation effects with ozone or HCHO during the analysis procedure (see Section 5.4.4). Enhanced O_4 columns at the same time indicate that multiple scattering occurred inside this plume (see 4.5), which greatly extended the light paths contributing to the measurement. Consequently, the respective AMFs became larger, resulting in a higher sensitivity of the DOAS instrument. A very pronounced Ring effect (see Figure 5.24 in Section 5.4.5) is another sign for very long light paths inside the plume. After 05:55/05:56 UTC, O_4 values drop rapidly until 05:58 UTC. The other trace gas columns follow this course. When looking at the noise levels of the trace gas dSCDs before and after plume contact, it becomes apparent that most probably the light path enhancement inside the plume caused the measured slant columns to be above the detection limit. HONO, HCHO and NO_2 values still seem to correlate between 05:58 and 06:00 UTC, even though values are not above background levels anymore. A single high data point of O_4 at 06:00 UTC has no response in other trace gases, thus indicating very likely the boundary of the plume. The question, whether similar trace gas concentrations were also present outside the encountered plume, but could not be detected due to smaller AMFs remains and is to be answered later.

Further information on the composition of this plume can be gained from the simultaneously measured in-situ data. Figure 6.3 provides data of in-situ CO, O_3, NO/NO_y, total and gaseous water and aerosol number concentration, plotted for the same period of time as the DOAS results in Figure 6.2, inclusive an identical position of the red box. It now becomes evident that the event, observed with the DOAS instrument, is embedded in a much bigger plume, starting at about 05:45 UTC and being characterized by enhanced levels of CO, NO/NO_y and aerosols. This extensive plume can be followed up until about 06:40 in CO and aerosol data (NO/NO_y data ends at 06:18 UTC). Outside the red box, CO, O_3 and NO/NO_y show a positive correlation, which can be explained as follows: In contrast to tropospheric CO and NO_x mixing ratios, which are dominated by primary emissions, tropospheric ozone exists mostly as a secondary compound, formed and destroyed in reactions involving VOCs, CO and NO_x (see Section 2.2.4). The compact correlation of O_3 and its precursor gases is a clear indication for a chemically processed air mass, with an age of about 3 to 4 days. This estimation is confirmed by a uniform distribution of different seized aerosol particles. Fresh air masses, in contrary, transported to the UTLS by deep convection, are usually distinguished by a higher number of ultra fine particles, because cloud-processed air is depleted of aerosol surface area, permitting thus the formation of new particles in the outflow region. The source of this pollution plume is very likely an-

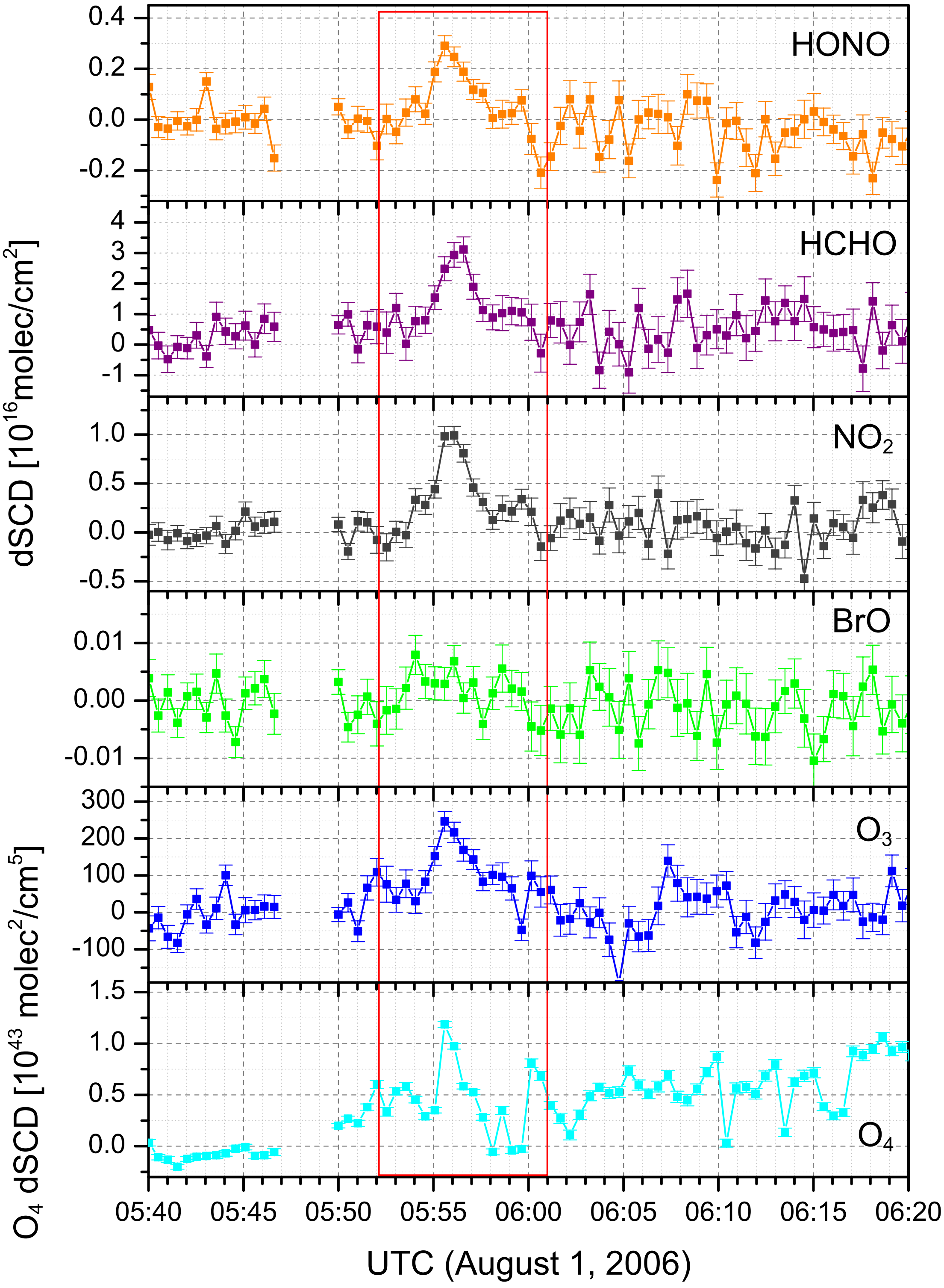

Figure 6.2: *DOAS results of measurements inside a tropospheric plume on flight LH158, August 1, 2006. The time period of plume interception is indicated by a red box. Inside the plume, all trace gases show enhanced dSCDs, except for BrO.*

thropogenic, concluded from an average Hg/CO ratio of 0.0073 ng/(m^3·ppb). Biomass burning would yield only about one fourth of this (*F. Slemr, personal communication*).

Inside the red box, however, in-situ values indicate quite a different scenario: the number concentration of ultra fine particles (4 - 12 nm) increases rapidly, coinciding with strong increases in NO/NO$_y$, thus suggesting a fresh air mass in accordance to the discussion above. From the simultaneously measured sharp drops in CO and O$_3$, it can be further concluded, that this air mass is not yet mixed with ambient air. Comparing DOAS and in-situ data shows, that the time period of the peak in HONO, HCHO, NO$_2$ and O$_3$ slant columns corresponds particularly well with in situ data between 05:55 and 05:58 UTC. During those three minutes, in-situ O$_3$ and CO show quite steady mixing ratios, whereas the course of NO/NO$_y$ values coincides with the total water measurement, both peaking at 05:56 UTC. The latter can be attributed to the presence of a large cloud, indicated by high total water values of over 1000 ppm. This cloud then is most probably the cause of the multiple scattering of light indicated by the O$_4$ columns. Data of the CARIBIC camera, mounted at the inlet system (see Section 5.1.2), supports this finding, showing that the aircraft is flying *inside* a huge cloud from 05:55 to 05:58 UTC, coinciding with the peak in the total water measurement.

Overall, these observations suggest that the aircraft is passing through a regime that has experienced a large entry of lower tropospheric air to the UTLS, characterized by high CO. 5-day backward trajectories compiled of ECMWF data (see 5.3.2) show that air masses, that were lifted up from 400 and 500 hPa levels to flight altitude, originate from the Red Basin. This area is a typical "pollution hot spot" in China, as can be seen, e.g. by satellite SO$_2$ retrievals [*Khokhar* 2006]. In Figure 6.4 24-h backward trajectories are provided, calculated with the HYSPLIT model.[1] Trajectories end point is set to 06:00 UTC at flight altitude. It is apparent, that these air masses originate from similar altitude levels, indicating no fresh entry of tropospheric pollutants, which is in accordance with the estimated age of the large pollution plume observed in in-situ data between 05:45 and 06:40 UTC.

The small intercepted plume (red box) is not resolved by the backward trajectories and is most likely a strong deep convection event, transporting a different air mass that is not yet diluted. Deep convection also explains the presence of the observed large cloud at this altitude. The diameter of this plume calculates to 46.5 km, with a plane velocity of 930 km/h and 3 minutes of interception time. This is in the order of a typical deep convective outflow regime. In Figure 6.5 three pictures are presented taken by the CARIBIC camera. Picture (1) shows the situation at the time when the FRS was recorded, in (2) the intercepted deep convection cloud can be seen, accentuated

---

[1] The HYSPLIT trajectory model (Hybrid Single-Particle Lagrangian Integrated Trajectory, see *www.arl.noaa.gov/ready/hysplit4.html*) is a freely available, PC compatible trajectory and dispersion model. It also offers online trajectory calculations, which was utilized for this work. Trajectories can be calculated on isentropic, isobaric and constant air density surfaces, or by using the modeled vertical motion given by the meteorological input data. The latter option is recommended by the authors and therefore applied within this thesis.

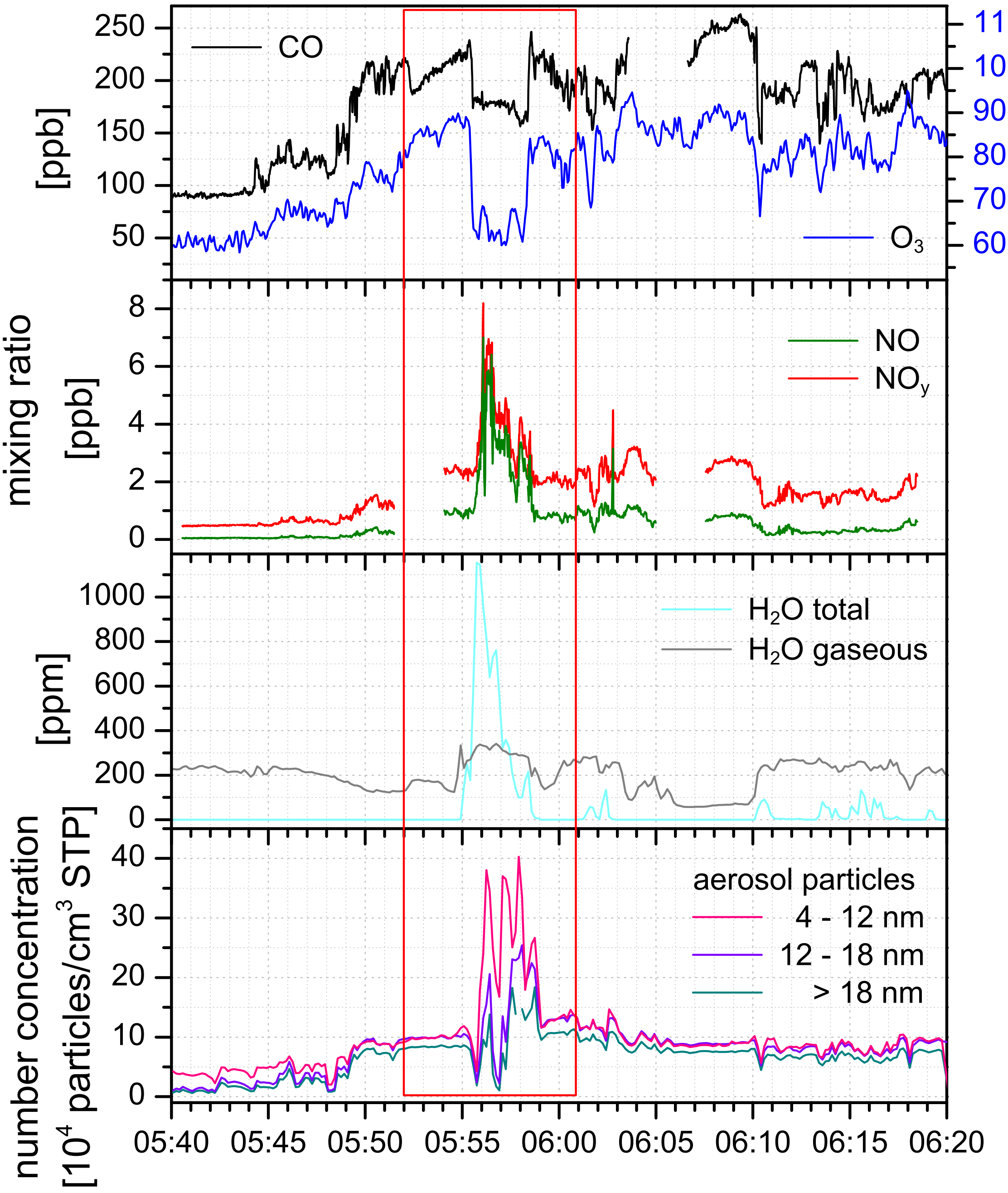

Figure 6.3: *In-situ results of measurements inside a tropospheric plume on flight LH158, August 1, 2006.*

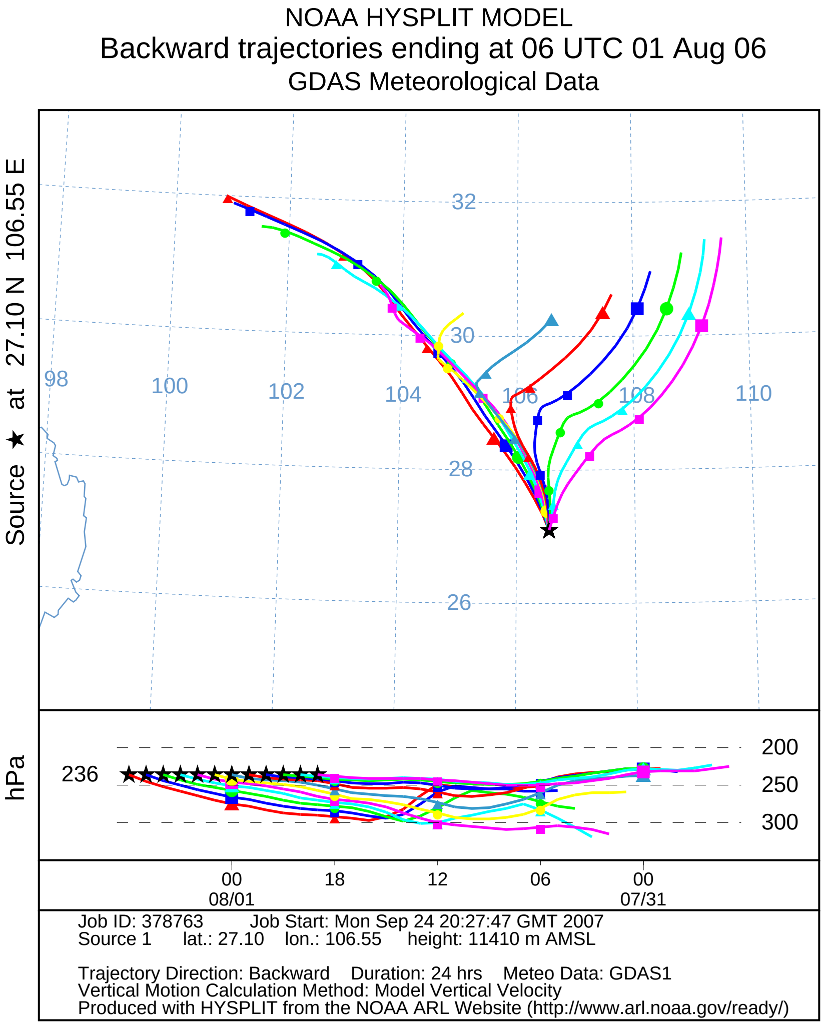

Figure 6.4: *24-h backward trajectories, ending at 06:00 UTC at the aircraft's position.*

by blue lines, and (3) is a snapshot from inside the cloud. Here, the visibility is barely good enough to still see the bottom of the aircraft, which corresponds to a high optical density of the cloud.

The findings on a deep convection event are supported by meteorological data: Figure 6.6 presents vertical wind velocities (top left panel) and total cloud cover (top right panel) for flight LH158 derived from ECMWF data. The deep convection episode between 05:55 and 05:58 UTC coincides with high vertical wind components (upward) indicated by a yellow to red shading. Such strong upward motion typically generates clouds as can be seen in the top right panel of Figure 6.6: The total cloud cover plot clearly shows the presence of clouds reaching all the way to the tropopause in altitude levels of around 120 hPa. These meteorological conditions suggest that the aircraft was very likely to pass through one deep convection cloud of possibly many others, (which is also supported by watching the complete CARIBIC camera movie).

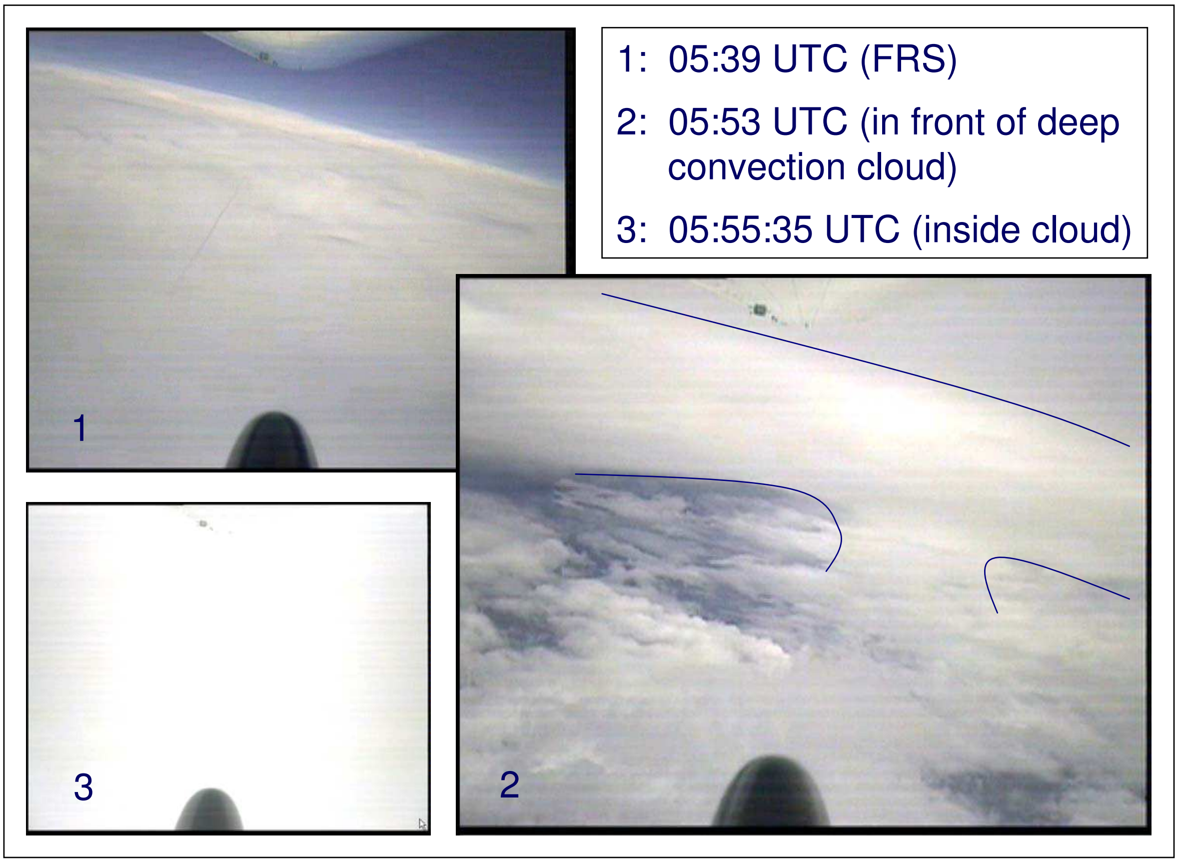

Figure 6.5: *CARIBIC camera photos taken at the time (1) when the FRS was recorded, (2) before intercepting the cloud and (3) inside the cloud at the moment yielding peak slant columns. The pictures also reveal the tip of the aerosol inlet tube (shroud) and the bottom of the aircraft.*

The Arinc data of the aircraft (see Section 5.3.1) provides another unique evidence for having passed through a deep convection event: The pitch and roll angle of the aircraft, recorded with a 1 s time resolution, reflect the impact of heavy turbulence within the respective three minutes length of time (pitch: ± 0.4°, regular ± 0.1°, roll: ± 5°, regular ± 0.5)°. Since turbulence experienced during flights is mostly caused by strong vertical winds, this is an additional indication for flying in an area experiencing strong deep convection.

Since aircrafts usually try to avoid flying through areas with strong convection, this observation provides a rare and unique opportunity to study the air inside a deep convection cell and in its outflow area respectively. In a first attempt, the observed trace gas values (red box), particularly those of NO_x and ultra fine aerosol particles, were tried to be explained by fresh aircraft emissions. Yet this approach was ruled out, because typical traces of other aircrafts occur on a much shorter time scale. As lightning very often goes along with deep convection, lightning NO_x could explain the

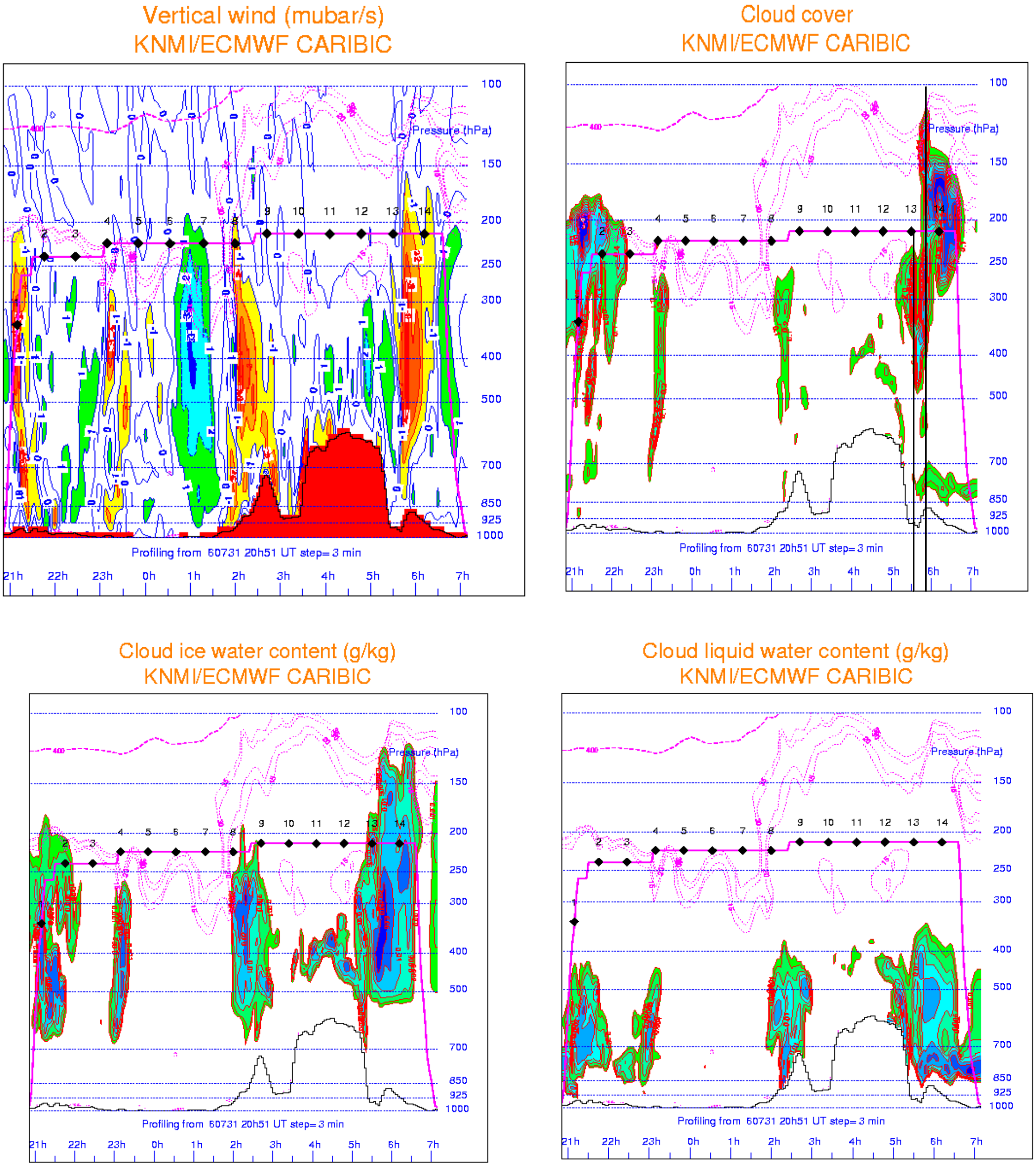

Vertical wind (mubar/s)
KNMI/ECMWF CARIBIC

Cloud cover
KNMI/ECMWF CARIBIC

Cloud ice water content (g/kg)
KNMI/ECMWF CARIBIC

Cloud liquid water content (g/kg)
KNMI/ECMWF CARIBIC

Figure 6.6: *Vertical wind velocity and cloud data derived from ECMWF data for flight LH158. Top left panel: Between 05:40 and 6:15 UTC, high upward wind velocities are seen, indicated by a yellow to red shading. Top right panel: The presence of clouds, reaching to the top of the tropopause, is associated with strong deep convection and is indicated by a green to dark blue shading in the total cloud cover plot. The black vertical lines show the time of the FRS being recorded and the time of cloud interception at 05:55 UTC. Bottom left panel: total ice water content, and bottom right panel: total liquid water content, both indicating the presence of clouds.*

observed NO/NO$_y$ values. Even though the total global contribution of lightning NO$_x$ is not entirely clear yet, lightning presents without a doubt a considerable NO$_x$ source (see e.g. overview on lightning NO$_x$ by *Schumann and Huntrieser* [2007]). Figure 6.7 shows data of the WWLLN network (World Wide Lightning Location Network, see *http://webflash.ess.washington.edu*) for flight LH158. The color scale denotes time in UTC. The interception of the deep convection plume at 05:55 UTC is marked by a pink dot and coincides directly with local lightning activity. Upon this finding the question is raised, whether the observed HONO columns are related to lithning NO$_x$, particularly as HONO is formed by OH and NO, both found in the vicinity of lightning activity. However, the chemistry on HONO is discussed later in Section 6.2.3.3 as following the measurements of flights LH110 and LH127 are presented.

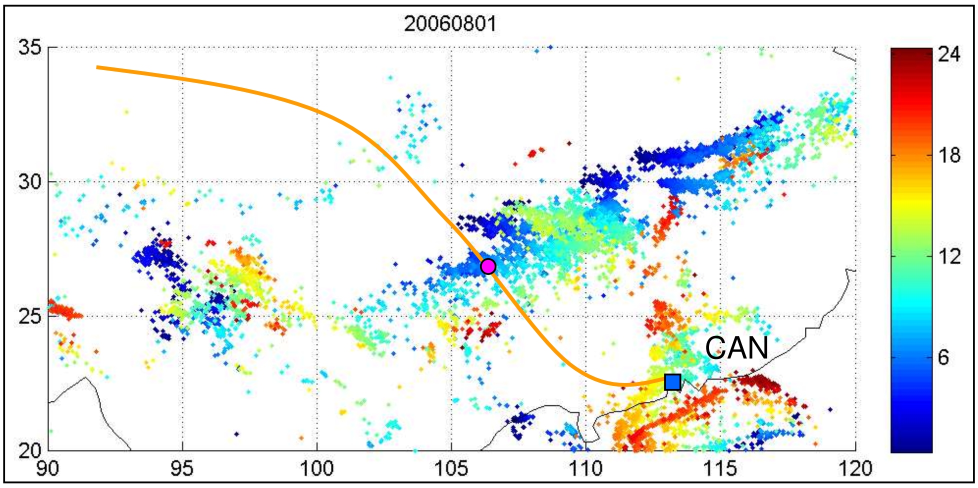

Figure 6.7: *WWLLN data of lightning activity during flight LH158. The flight track is indicated by an orange line and the pink dot marks the interception of the deep convection cloud at 05:55 UTC.*

6.2.1.2 Flight LH110

On flight LH110 to Guangzhou, on May 20, 2005, HONO was observed in the very same area as on flight LH158. Derived HONO slant columns are presented in Figure 6.8 along with NO$_2$ and O$_4$ results. These slant columns are retrieved from the 10° down viewing direction, which provided in that flight spectra of limited quality, yet exhibits a much higher sensitivity towards the free troposphere (nadir spectra are not available due to a computer problem). Since the evaluation of these spectra in wavelength ranges $<$ 345 nm is not possible, the HONO retrieval was performed between 349 and 390 nm, which is different from the standard range described in Section 5.4.5. Further limitations are that spectra of reasonable quality are only available for the time period shown in Figure 6.8.

A slight systematic structure in NO$_2$ and HONO columns can be seen, indicated

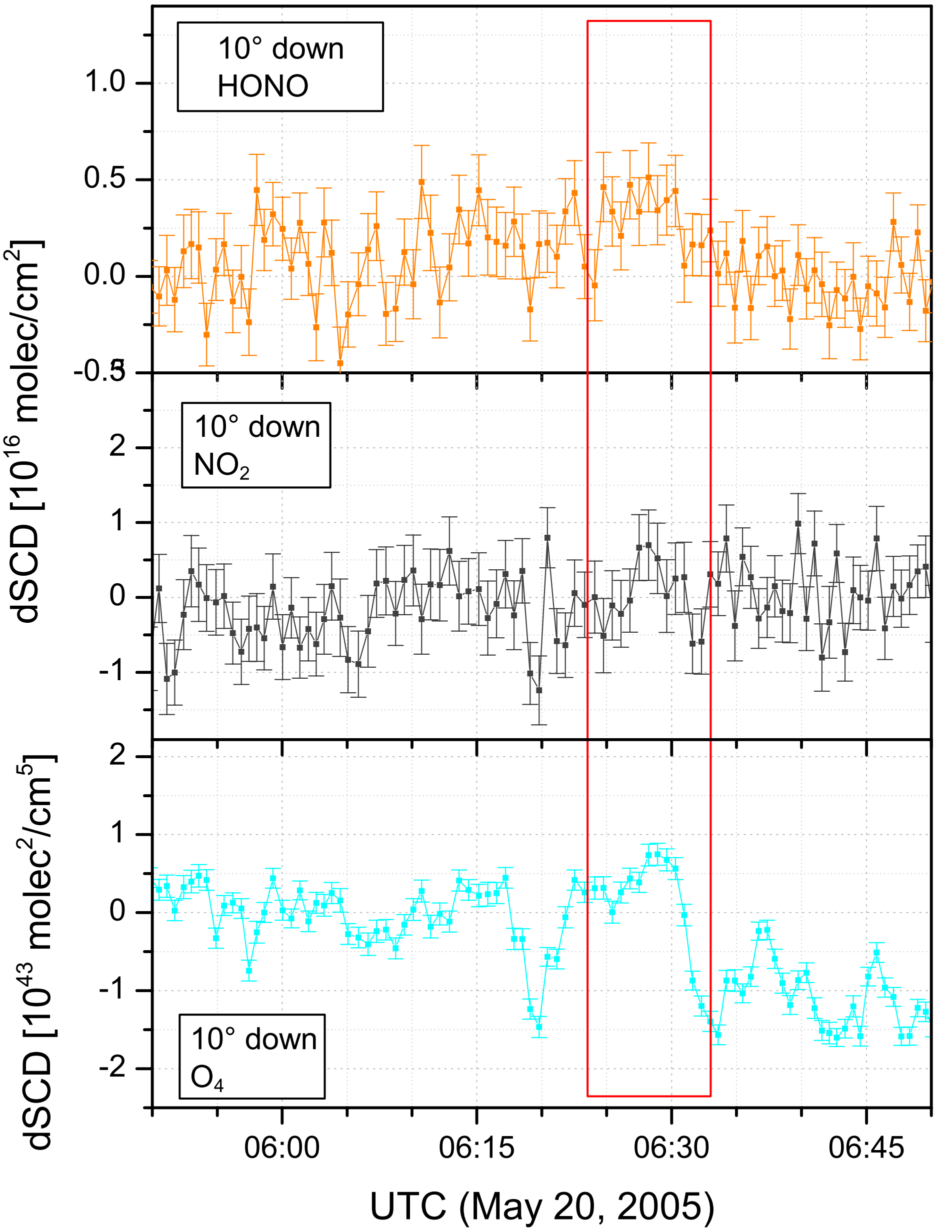

Figure 6.8: *HONO, NO_2 and O_4 dSCDs for flight LH110, for SZA = 6.9° - 33.1° (minimum: 3.6° at 05:33 UTC) and an altitude of 11.4 km. The FRS is recorded at 05:39 UTS with SZA = 5.3°.*

by a red box. One argument to support the reality of the HONO signal, is that other HONO analysis yield mostly no systematic structures, but pure noise columns around zero upon the absence of HONO, yet stand alone, these columns are not convincing. But when considering supplementary data, the similarities to the event of flight LH158 are striking: Figures 6.9 and 6.10 provide available in-situ data, WWLLN data and total cloud cover for flight LH110. During the time period marked with a red box, the slant column enhancements coincide with higher values of NO/NO_y and ultra fine aerosol particles, which is also marked with a red box. These trace gases and aerosols are measured in an area with lightning activity and within very high rising clouds, very likely deep convection clouds. Furthermore, ECMWF data of vertical wind components shows upward wind speeds in the free troposphere around 06:30. Even though data availability is limited and partly of inferior quality, the event encountered during this flight seems to be very similar to flight LH158.

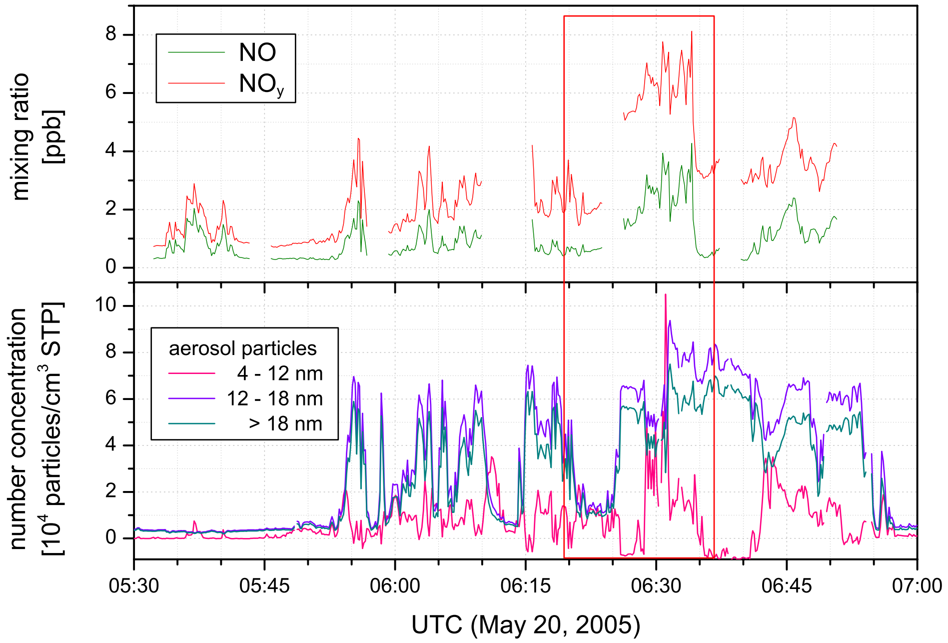

Figure 6.9: *In-situ data for flight LH110.*

In the following section, data measured in biomass burning events on flight LH123/124 and LH127/128 is presented. During flight LH127 HONO was detected as well within a tropospheric biomass burning plume. A further discussion on all HONO measurements is provided in Section 6.2.3.

6.2.2 Biomass burning events over South America

On two measurement flights in August and October 2005, biomass burning signatures were detected over South America. The plumes were each intercepted on the flight legs between São Paulo (GRU) and Santiago de Chile (SCL), shortly after leaving São Paulo. Figures 6.12 and 6.13 show DOAS results for flights LH123/124 on August 31, 2005 and LH127/128 on October 5, 2005 respectively, both taking the same route (GRU - SCL; SCL - GRU). Plotted are slant columns of NO_2, HCHO, O_3 and O_4 and the local SZA derived from Arinc data (see Section 5.3.1). For flights LH127/128 HONO dSCDs are plotted additionally. The time periods of biomass burning signatures in the DOAS data are marked with a red box. Figure 6.14 shows the corresponding in-situ measurements. Presented is data of CO, NO/NO_y (not available for LH123/124), O_3

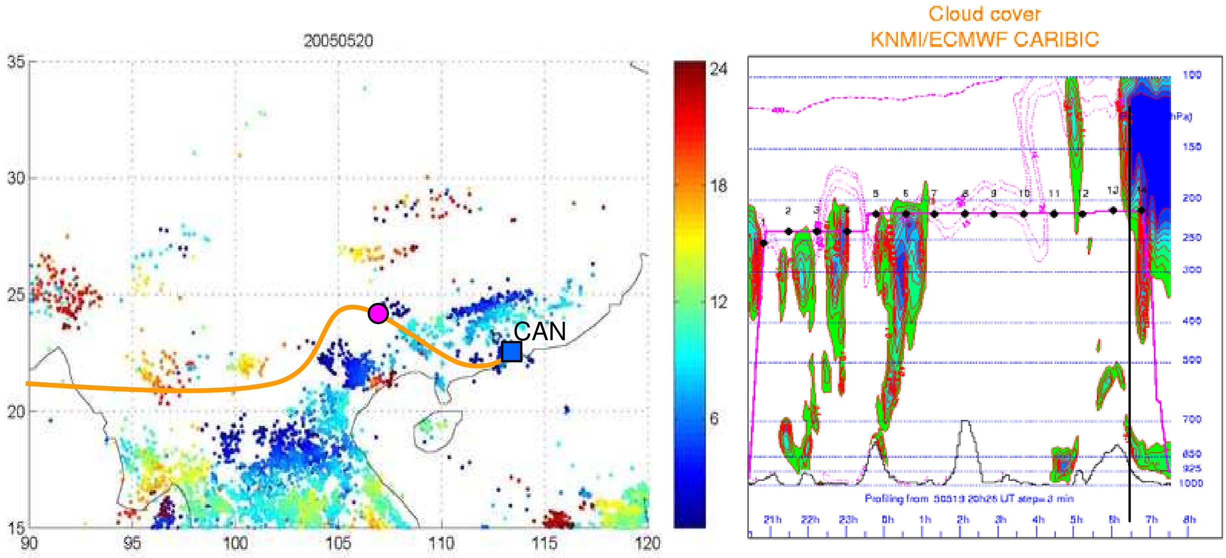

Figure 6.10: *Left panel: WWLLN data of lightning activity for flight LH110. The flight track is indicated by an orange line and the position of the aircraft at 06:30 UTC is marked with a pink dot. Right panel: ECMWF data of total cloud cover for flight LH110. The vertical black line indicates 06:30 UTC.*

and aerosol number concentrations. The red boxes (and also green boxes, see below) are placed in accordance with the DOAS data. Enhanced values of CO, NO_x and NO_y, HCHO and aerosols are a typical sign of polluted air masses. Indications for biomass burning being the source of these intercepted plumes are:

1) The flight dates at the end of August and in the beginning of October correspond with the biomass burning season over South America. 2) The ATSR World Fire Atlas of ESA (see *http : //earth.esa.int*), which provides monthly global fire maps, shows severe burning activity in central South America for August, September and October 2005. An example for August 2005 is given in Figure 6.11. The flight route is indicated by a yellow line. 3) The analyzes of air samples taken during the measurement flights exhibit substantial emissions of methyl chloride and methyl bromide, which are typically found in biomass burning plumes. Before the similarities and differences in the biomass burning signatures of DOAS and in-situ data are discussed, the DOAS measurements are introduced in more detail.

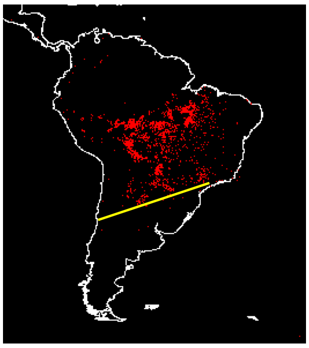

Figure 6.11: *ATSR monthly global fire map of South America for August 2005. The flight route is indicated by a yellow line.*

Outside the red boxes in Figures 6.12 and 6.13 high values of NO_2 and HCHO slant columns are found in the beginning and at the end of flights. These are caused by local pollution either in São Paulo or Santiago de Chile. When missing, e.g. at

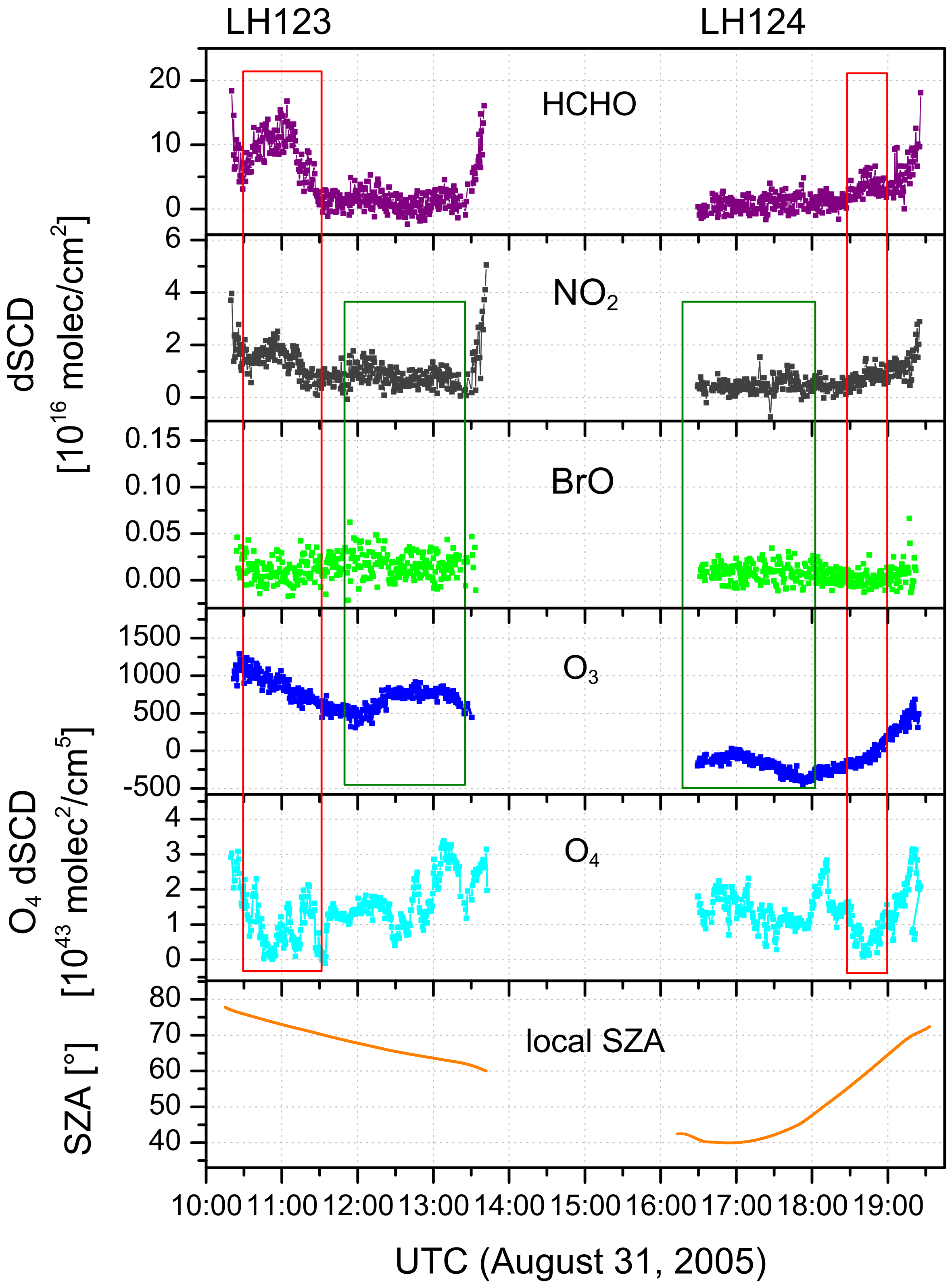

Figure 6.12: *DOAS results for flights LH123/124 between São Paulo and Santiago de Chile. Biomass burning signatures are marked with a red box, while flying in stratospheric air is indicated by a green box. The FRS is recorded at 17:11 UTC.*

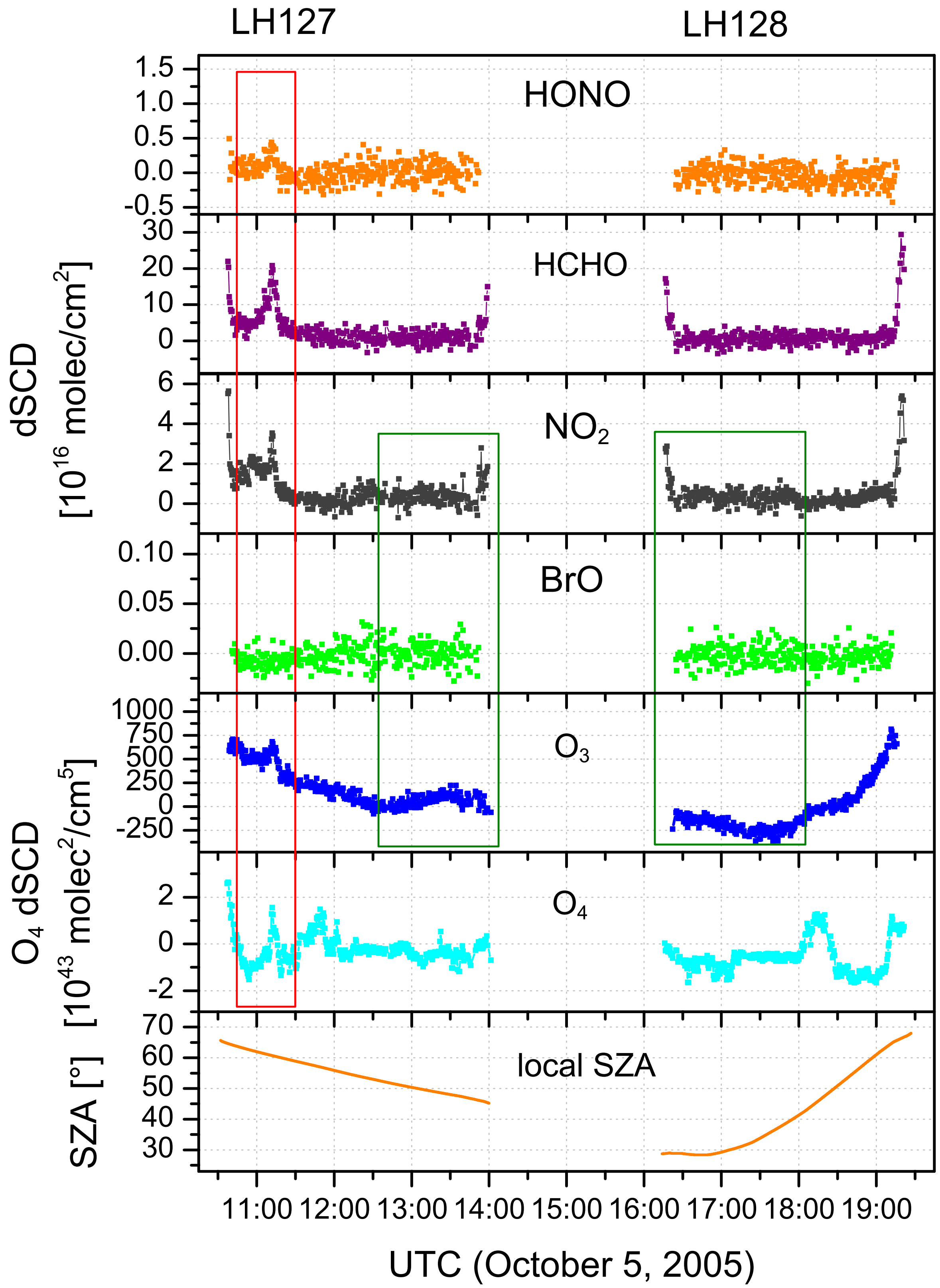

Figure 6.13: *DOAS results for flights LH127/128 between São Paulo and Santiago de Chile. Biomass burning signatures are marked with a red box, while flying in stratospheric air is indicated by a green box. The FRS is recorded at 12:33 UTC.*

the start of LH124, then this is because the respective spectra were sorted out after analysis due to poor quality (see 5.4.7). The data patterns of all four flights are quite similar: LH123 and LH127 show clearly high values of NO_2 and HCHO (inside the red box), while LH127 shows also enhanced O_3 and HONO. There are no corresponding signals on the return flights over the same area except for LH124 exhibiting slightly enhanced HCHO (second red box). All four flights are additionally characterized by passing through stratospheric air, marked with green boxes, between 12:00 and 17:45 UTC for LH123/124 and between 12:45 and 17:45 UTC for LH127/128, represented by much higher ozone dSCDs and slightly higher NO_2 for these time periods. This effect is attributed to a lower tropopause height, leading to a change in vertical trace gas profiles and thus to higher air mass factors for ozone and NO_2. Ozone values measured in-situ (green boxes in Figure 6.14) exhibit the effect of flying through stratospheric air very clearly, as mixing ratios exceed 150 ppb on all four flights. Ozone mixing ratios $>$ 150 ppb usually characterize stratospheric air. A further discussion on this effect is given in Section 6.3.1.1, where stratospheric measurements are discussed. Two blue boxes in Figure 6.14 indicate air masses that exhibit a very clear positive correlation of in-situ O_3, CO and NO_y. As described in Section 6.2.1, such a correlation denotes an aged air mass, presumably about 2 - 4 days old.

The comparison of DOAS and in-situ data yields similarities on flights LH123 and LH127 to SCL, with corresponding CO, NO/NO_y, NO_2 and HCHO measurements, yet upon flying back to GRU, the DOAS data shows no such signs, except for slightly enhanced HCHO columns on flight LH124. The differences in DOAS and in-situ can either be explained by local concentrations or by radiative transfer effects, i.e. the light path lengths inside the respective trace gas layer are not long enough to raise the absorption signal above detection limit. In practice, it is very likely a combination of both effects. With respect to local concentrations, the following needs to be considered: A closer look on the correlation of CO and O_3 reveals, that several air masses of different age are intercepted along the flight track. This finding is confirmed by 5-day backwards trajectories compiled of ECMWF data: trajectories of air coming from the lower troposphere originate at different locations within northern South-America, which holds true for all four flights. Furthermore, the material being burned, e.g. grass or wood, has an influence on the the amount of emitted HCHO. Local meteorological conditions, e.g. pressure and temperature, the presences of clouds or SZA determine life times of e.g. NO_2 and formaldehyde.

In regard to radiative transfer the following aspects need to be considered: All flights tracks lead through very clouded areas, while the aircraft changes occasionally its flight altitude. Both affects the air mass factors of the measured slant column. Particularly an insufficient knowledge on cloud properties leads to problems in quantifying these effects. A detailed study on all the mentioned parameters could reveal more information on origin and chemical processes inside various biomass burning plumes. This, however, is beyond the scope of this work and might be done elsewhere.

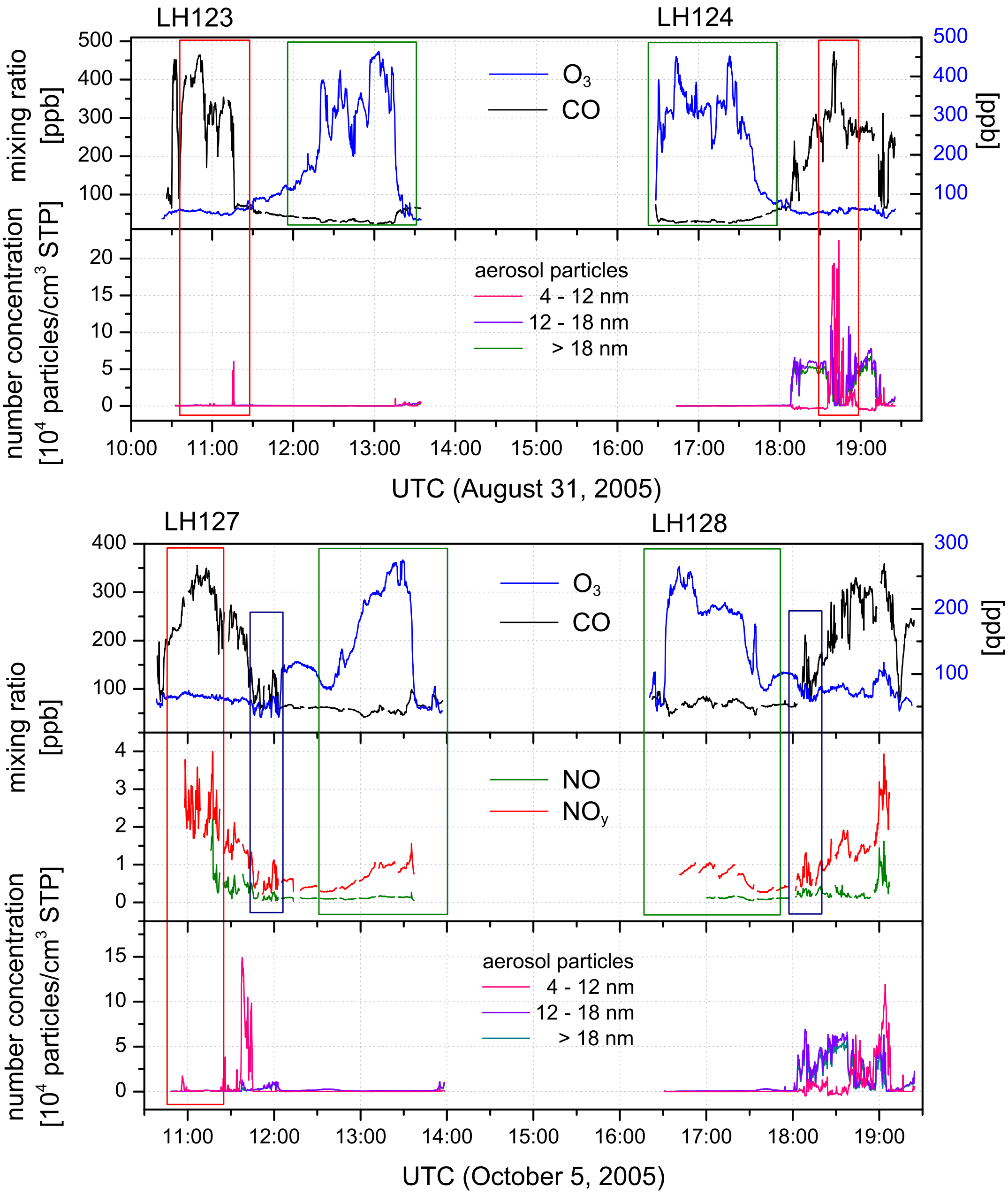

Figure 6.14: *In-situ results for flights LH123/124 and LH127/128 between São Paulo and Santiago de Chile. The time periods corresponding to enhanced DOAS NO_2 and HCHO columns are marked with a red box, while flying in stratospheric air is indicated by a green box.*

In light of the HONO measurements during flights LH110 and LH158, the slant column peak of flight LH127 at 11:12 UTC is a very striking feature. All slant columns peak at the same time and the enhancement of the O_4 column indicates the effect of multiple scattering. A single high NO peak at 11:16 UTC is also found. Unfortunately, there is no NO data available at 11:12 UTC, but in view of the measured NO_y values, NO for 11:12 UTC might be in the same order of magnitude as at 11:16 UTC, around 2 - 3 ppb. Figure 6.15 reveals lightning activity in this area, retrieved from NASA's lightning imaging sensor (LIS, see *http://thunder.msfc.nasa.gov*). The total cloud cover plot for flight LH127 is shown in the same Figure. The black line marks 11:12 UTC. It is apparent that the aircraft is flying through a huge high reaching cloud cover. ECMWF data of vertical wind components exhibit strong upward wind speeds, which is indicative for deep convection. Overall, the atmospheric conditions are almost identical to those encountered on flight LH158 and similar to flight LH110. The findings on HONO measurements of all three flights are discussed in the following section.

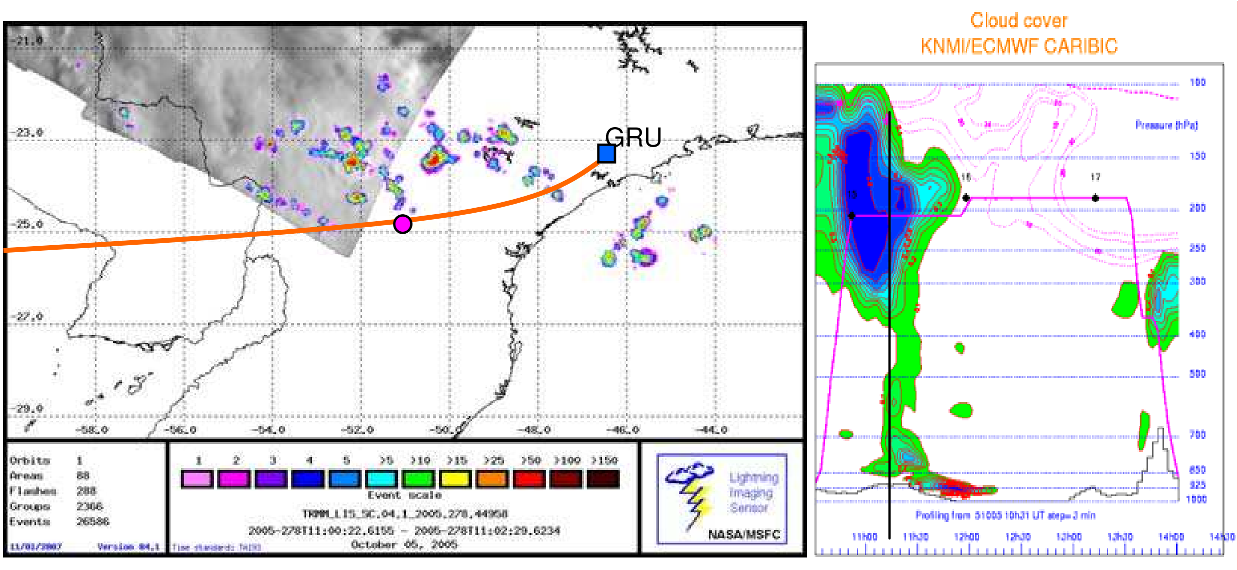

Figure 6.15: *Left panel: LIS data of lightning activity for flight LH127. The flight track is indicated by an orange line and the position of the aircraft at 11:12 UTC is marked with a pink dot. Right panel: ECMWF data of total cloud cover for flight LH127. The vertical black line indicates 11:12 UTC.*

6.2.3 Discussion on HONO measurements

Flight LH158 provides the most convincing HONO absorption signal and plenty of supplementary data. Therefore, the following discussions are primarily on flight LH158. HONO measurements of flights LH110 and LH127 are included later.

When wanting to utilize all available data on flight LH158 to further investigate the observed HONO slant columns and to quantify chemical processes, then it becomes necessary to convert slant columns, derived by the DOAS instrument, into concentrations (or mixing ratios) that are comparable to the data measured in-situ. The interception of the deep convection cell during flight LH158 coincides mostly, but not entirely with passing through a large cloud. Since the DOAS measurements yield only slant columns above detection limit when flying inside the cloud, most likely due to the effect of multiple scattering, the following discussions will only refer to data measured inside the cloud. To derive concentrations from differential slant column densities (dSCDs) requires the calculation of air mass factors. To do so in this case, several difficulties are faced: First, an insufficient knowledge on the optical properties of the intercepted cloud introduces larger errors to the AMF calculations. However, information on the cloud optical density as well as on cloud base and cloud top height can be gained from meteorological data and in particular from the DOAS O_4 measurements, which will be discussed below. Secondly, the retrieved DOAS concentrations are only comparable with in-situ data, if the following assumptions can be reasonably made:

1. The dSCDs to be converted in concentrations contain absorption structures only caused by trace gases inside the intercepted cloud.

2. The air mass observed by the DOAS instrument is comparable to the air measured in-situ at flight level.

Ad 1: The correlation of DOAS and in-situ measurements for this event is surprisingly well (see Figures 6.2 and 6.3). The highest O_4 data point at 05:55:35 UTC, recorded from 05:55:20 to 05:55:50 UTC, coincides with flying inside the observed cloud, indicated by the total water data and by the camera. From the sudden rise in the O_4 dSCD it can be concluded, that this single measurement is dominated by photons that have experienced multiple scattering *inside* the cloud, thus allowing the assumption that all slant columns measured at this specific point in time contain absorptions caused by trace gases inside the cloud.

Figure 6.16 shows a sketch of the measurement process inside this cloud. All measured photons traversed the stratosphere before reaching the cloud, leading to stratospheric absorption signals of NO_2, O_3 and BrO. This contribution is canceled out by the (same) absorptions contained in the FRS, recorded closely before plume contact at 05:39 UTC. Between 05:39 and 06:00 UTC, the solar zenith angle θ changes from 13.5° to 16.9°. The respective stratospheric air mass factors for e.g. NO_2 are 1.125 and 1.138, yielding a difference of 0.013, which can be neglected. The analogue holds true for stratospheric O_3 and BrO AMFs. Typical tropospheric background values of O_3 and BrO, (for O_3 below 100 ppb, for BrO around 1 - 3 ppt, for the latter see also Section 6.2.4) are well below detection limit for the nadir viewing direction[2] as long as no extensive light path enhancements occur. Accordingly, the tropospheric columns contained in the FRS, which has not been exposed to multiple scattering effects, is also negligible. In fact, the FRS has been recorded over a closed layer of clouds. In a situation like this, most light obtained by the detector is reflected from the upper part of the cloud cover, thus shielding tropospheric columns below the clouds. The measurements inside the cloud, in contrast, are strongly determined by multiple scattering, increasing highly the sensitivity of the DOAS measurements. A slight bias introduced by a tropospheric NO_2 background column cannot be excluded. But in conclusion, it

---

[2] In case of ozone, the detection limit is determined on how accurate the stratospheric contribution is canceled out. Since about 90 % of ozone is located in the stratosphere, the error caused by subtracting a stratospheric reference is mostly larger than the respective tropospheric absorption signal.

can be reasonably assumed that the absorption structures of the dSCDs at 05:55 UTC are largely caused by the trace gas concentrations c(z) found inside the cloud.

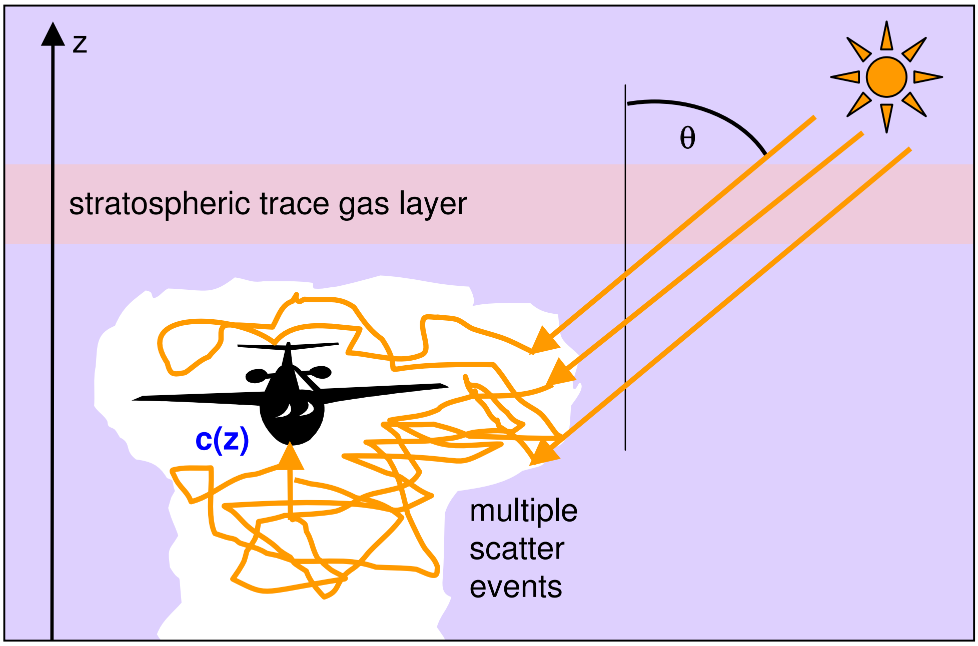

Figure 6.16: *Sketch of multiple scattering inside a cloud. The stratospheric absorption structures are canceled out by the FRS recorded shortly before plume contact.*

Ad 2: To compare DOAS data with in-situ data measured at flight level (11.4 km), it must either be assumed that the photon path distribution of the respective measurement at 05:55 UTC has a maximum located around the aircraft and within an area that exhibits no strong concentration gradients. To validate this assumption, the radiative transfer inside this cloud needs to be studied, to yield information on the light path distribution.

Accordingly, model studies on the radiative transfer inside an optically thick cloud were performed, serving two purposes: First, the optical properties of the intercepted cloud need to be constrained by means of utilizing the measured O_4, to derive a model scenario that adequately represent the intercepted cloud. Secondly, once the optical properties are sufficiently constrained, the light path distribution can be studied, to see whether assumption 2 is valid. If it is valid, the AMFs derived from the constrained cloud scenario can be used to convert the measured slant columns into concentrations.

6.2.3.1 Model studies on the radiative transfer inside a deep convection cloud

The general idea of this model approach is to vary cloud scenarios as long until the O_4 dSCD that was actually measured inside the cloud at 05:55 UTC can be reproduced.

However, when wanting to compare modeled O_4 columns, S(mod), with slant columns S(meas) derived from measurements, then the absorption contained in the FRS, S(ref) must be obtained first in order to derive S(meas) = dS(meas) + S(ref). Usually, S(ref) is retrieved from a Langley Plot (see Section 4.3.2), but this leads only to suitable results when the observed O_4 concentration is constant throughout the time period of measurements and when the measured slant columns, dS(meas) are not influenced by additional scattering or absorption caused by e.g. clouds or aerosols. For CARIBIC flights, this is never fulfilled, due to the following reasons: It is apparent that in practice a long-distance flight will never completely pass over areas that exhibit neither clouds nor (background) aerosols. However, a cloud and (almost) aerosol free atmosphere can be assumed for parts of a flight, which is done below. A constant O_4 profile is not encountered, mainly because the flight track leads over uneven terrain. During flight LH158 to China, ground level heights ranged between 0 and more than 4000 m above seal level (flying over the Tibetan plateau), hence exhibiting highly varying O_4 concentration profiles along the flight track. A second cause, but of minor effect, is the fact that during a long-distance flight from Frankfurt to China a wide range of different local pressure and temperature is encountered, which affect additionally the concentration profile of O_4.

Hence, a different approach needed to be chosen to derive S(ref): AMFs were modeled for a number of selected spectra that should serve as new FRS for the data analysis and which were recorded under conditions that can be well simulated by the radiative transfer model: The criteria for the selection were as follows: the spectra must be recorded over a cloud free sky, which was checked with CARIBIC camera data. Secondly, during the retrieval time of 30 seconds, the ground levels being passed over should remain at constant height. Since these selected spectra shall specifically yield a reliable S(meas) of the spectrum recorded at 05:55 UTC inside the cloud, a third criterion was introduced: the new FRS should be recorded as closely as possible in time to cloud interception, to find similar atmospheric conditions. Subsequently, two spectra were chosen to serve as new FRS and their O_4 columns (S(ref)) were modeled accordingly. The corresponding ground level heights were taken from google earth (*http://earth.google.de*) and the O_4 concentration profile, utilized in the radiative transfer model, was adapted to pressure and temperature measured in-situ by the aircraft and interpolated to the ground (see also Excursion in Section 4.5). These FRS were then used to analyze spectra recorded inside the deep convection cloud. The results are summarized in the Table below.

The fact that for the measurements inside the deep convection cloud only the nadir viewing direction is available (time resolution and spectra quality of both other viewing directions are not good enough to resolve this event), presents a further difficulty, since the nadir telescope is particularly sensitive to lower atmospheric layers, where O_4 is most abundant. Errors when modeling S(ref) are introduced by an unknown aerosol profile and especially by the varying ground level height. In view of this, the agreement in the derived S(meas) at 05:55 UTC for all modeled S(ref) is particularly well, yielding results within the estimated error range of +/- $1 \cdot 10^{42}$ molec^2/cm^5 of the model results,

Table 6.2: *Modeled O_4 columns for selected FRS and respective S(meas).*

time [UTC]	height [m]	SZA [°]	S(ref) [$molec^2/cm^5$]	dS(meas) [$molec^2/cm^5$]	S(meas) [$molec^2/cm^5$]
03:26	900	41.3°	$1.92 \cdot 10^{43}$	$0.43 \cdot 10^{43}$	$2.45 \cdot 10^{43}$
03:40	3500	37.1°	$1.01 \cdot 10^{43}$	$1.37 \cdot 10^{43}$	$2.38 \cdot 10^{43}$
05:39	1000	28.9°	$1.3 \cdot 10^{43}$	$1.18 \cdot 10^{43}$	$2.48 \cdot 10^{43}$

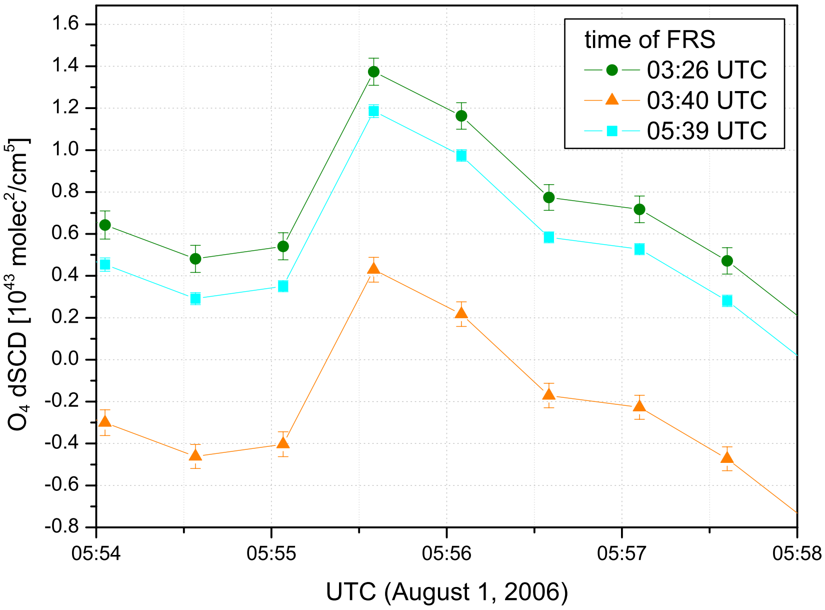

Figure 6.17: *O_4 dSCDs for different FRS for flight LH158.*

based mostly on an improper knowledge on background aerosols - S(ref) were modeled for a pure Rayleigh atmosphere. The third result, retrieved for the originally utilized FRS at 05:39 UTC will be discussed later.

In Figure 6.17 dS(meas) are shown, retrieved with the above introduced FRS in order to see whether the relative O_4 enhancement presumably caused by multiple scattering inside the cloud is reproduced consistently. Each result exhibits a relative O_4 column rise of about $0.8 \cdot 10^{43}$ molec^2/cm^5 between 05:55:04 and 05:55:35 UTC, which yields the difference of being outside and inside the cloud. In a next step, O_4 SCDs for different cloud scenarios are modeled in order to constrain a cloud scenario that yields total columns in the order of $2.4 \cdot 10^{43}$ molec^2/cm^5 (see S(meas) in Table 6.2).

The input parameters needed for this specific radiative transfer modeling are the spatial extent of the cloud, its optical density and single scattering albedo as well as an adequate value for the asymmetry coefficient g (see 4.2.3). The latter two are defined by standard values, being suitable for most cloud scenarios: g is set to 0.85 and the single scattering albedo is given by SSA = 0.99999. The spatial extent and optical den-

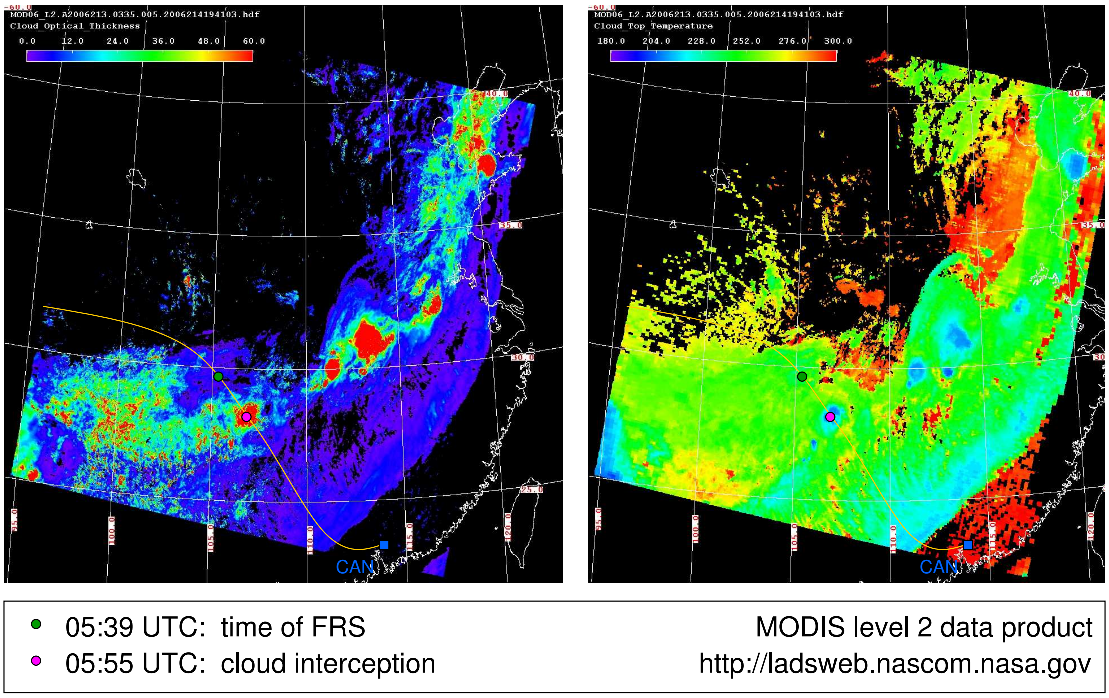

Figure 6.18: *MODIS satellite images of cloud OD and cloud top temperature. The flight track is indicated by an orange line.*

sity of the intercepted cloud can be constrained by supplementary meteorological and satellite data. Figure 6.18 shows images of cloud optical thickness and cloud top temperatures, retrieved by the NASA terra satellite (see *http://ladsweb.nascom.nasa.gov*). The CARIBIC flight track is indicated by a yellow line, the time at which the original FRS was recorded (used for the analysis of the dSCDs shown in Figure 6.2) is marked green and the point in time of cloud interception has a pink label. The latter coincides with a very high cloud optical density and a low cloud top temperature, consistent with the observations discussed in Section 6.2.1 above. Both pictures reveal that the encountered deep convection cloud is part of a huge frontal system, extending over China, which also explains the extensive lightning activity in this area and also why the aircraft could not avoid passing through on its way to Guangzhou.

An optical density of 60, derived from the satellite image, has been chosen as starting point for the radiative transfer modeling. According to *King et al.* [1997], the retrieval algorithm of Modis cloud optical thickness data is mainly intended for plane-parallel liquid water clouds. To retrieve the cloud optical thickness, a radiative transfer model is used to compute the reflected intensity field. Therefore, a cloud optical density of 60 can only serve as an orientation point for the radiative transfer studies conducted here. Temperatures for cloud top height range between 180° and 220° K, which corresponds to a cloud top height from 12 km to the top of the tropopause. The cloud data plots of Figure 6.6 contain PV values, showing the height and course of the tropopause in purple dashed lines. Shortly before 06:00 UTC, the tropopause exhibits a strong upward curving structure, allowing clouds to extend up to pressure levels of about 120 hPa (ca. 15 km). Cloud ice content, presented in the bottom left panel of the same Figure, propagates slightly lower up, to about 140 hPa at 05:55 UTC. Cloud top heights in the radiative transfer model were therefore tested between 12 and 15 km. Defining a suitable cloud base height is more difficult. The total cloud cover plot shows scattered values of smaller cloud cover fractions (green) below 500 hPa, yet the cloud water content plot, shown in the bottom right panel of Figure 6.6, exhibits a troposphere characterized by a high relative humidity. Hence, cloud base heights were modeled between 2 and 8 km. Further input parameters for the radiative transport model are temperature and air density profiles, which were adapted to the temperature and pressure measured by the aircraft ($p = 212$ hPa, $T = 228^\circ$ K) in flight altitude and interpolated to the ground.

The O_4 SCDs derived from these model runs are presented in Figure 6.19.

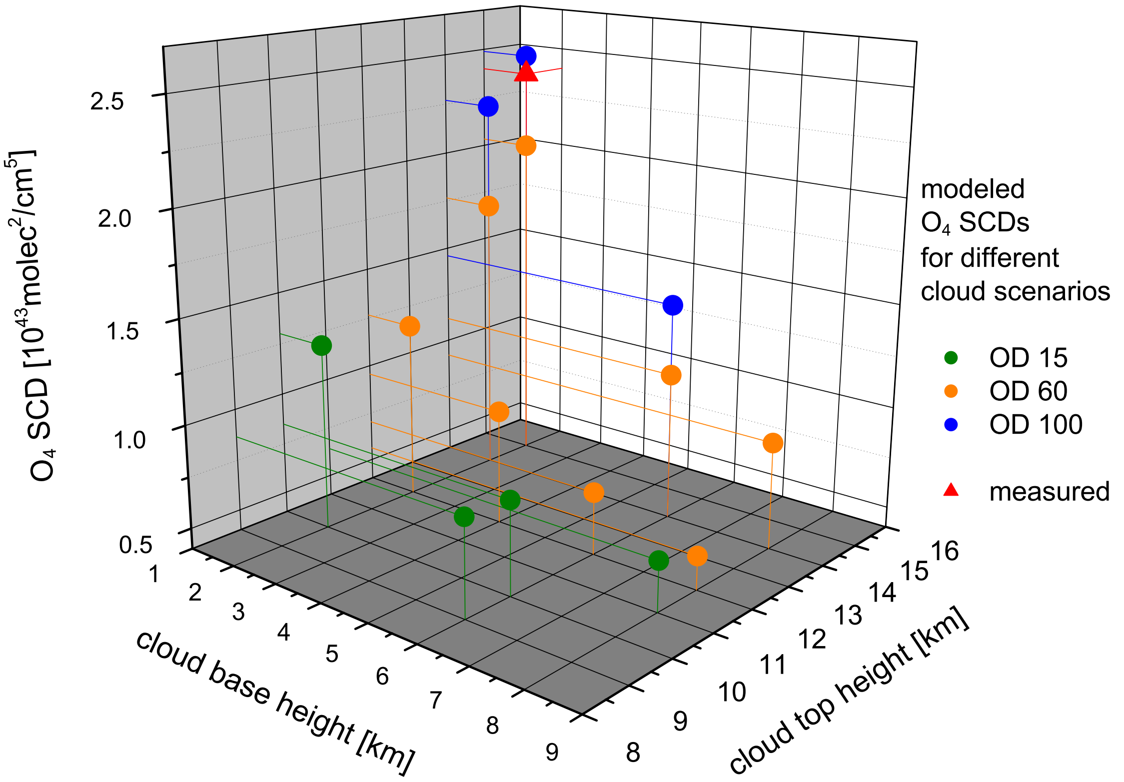

Figure 6.19: *Modeled O_4 SCDs for different cloud scenarios.*

These results clearly constrain cloud scenarios that yield an O_4 SCD of $2.4 \cdot 10^{43}$ molec^2/cm^5 to a large cloud, extending from about 2 km to 15 km with an optical density of about 60 - 100. Model values of lower clouds with an optical density of 15 were included to represent the cloud cover the aircraft was passing over at 05:39 UTC, when the original FRS was recorded. It becomes apparent that this kind of cloud cover cannot cause such a great enhancement of O_4 slant columns as observed at 05:55 UTC, which is an additional argument that slant columns measured at 05:55 UTC represent the air masses inside the intercepted deep convection cloud. The S(ref) found in the third row of Table 6.2, is derived "backwards": When taking S(meas) for 05:55 UTC derived from the two other FRS, then the column S(ref) that needs to be contained in the original FRS at 05:39 UTC must be in the order of $1.3 \cdot 10^{43}$ molec^2/cm^5 to acquire the same S(meas) at 05:55 UTS as by using the other two FRS. This is the case for a cloud from 2 - 10 km with an optical density of 15. Cloud base height 15 minutes before the interception of the deep convection cloud is in the same order of magnitude as at 05:55 UTC, which can probably be attributed to the extensive band of clouds seen in the above shown satellite images. In the subsequent section, concentrations are derived from slant clomuns by means of AMFs modeled for the above constrained cloud scenario.

6.2.3.2 Retrieval of trace gas concentrations from slant column densities

In Figure 6.20, Box-AMFs for three cloud scenarios are presented, which all exhibit O_4 slant columns around $2.4 \cdot 10^{43}$ molec^2/cm^5. The best fit of modeled and measured O_4 values is achieved for clouds with an optical density of 100, reaching from 2 km up to between 14 and 15 km altitude.

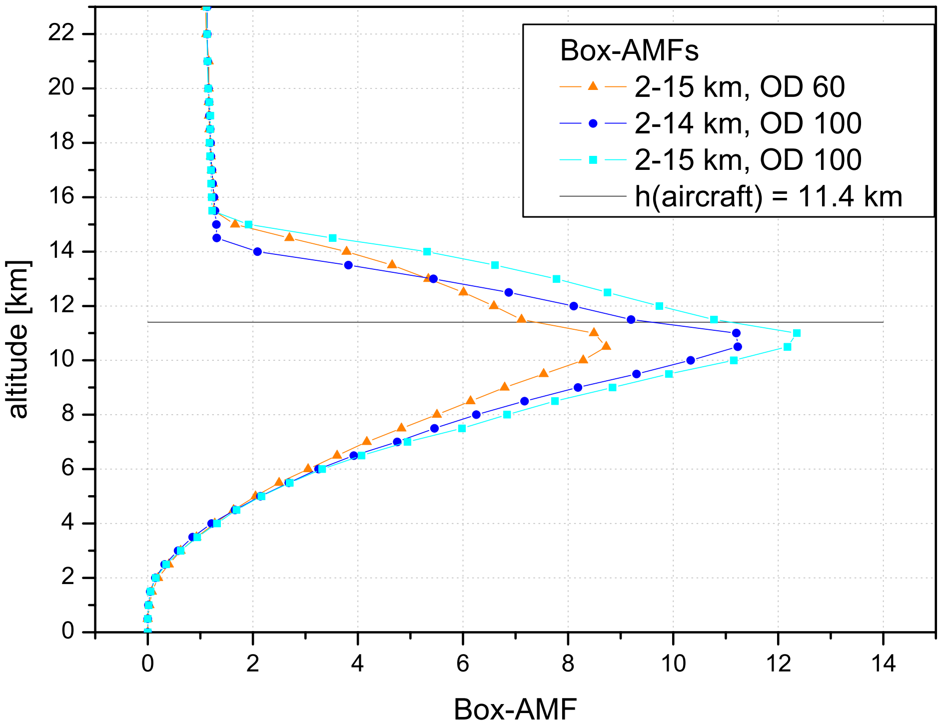

Figure 6.20: *Modeled BOX-AMFs for most likely cloud scenarios encountered at 05:55 UTC.*

It is apparent that the measurements inside the deep convection cloud exhibit the highest sensitivities for air masses near the aircraft, with a FWHM of the Box-AMFs in the order of 5 - 7 km. In deep convection clouds, vertical wind speeds can reach values of 10 m/s, which implies a rising of air within 6 km around the airplane in 10 minutes. Since in-situ ozone levels drop sharply from around 90 to 65 ppb upon entering the deep convection cloud, it can be assumed, that air from the lower troposphere has been transported to flight altitude (11.4 km). The same applies to CO, which exhibits also a very sharp drop from values around 230 ppb to 180 ppb. Even though the air within the deep convection cloud is subject of chemical processes, a depletion of 50 ppb CO within hours is extremely improbable. Therefore, the measured mixing ratios are assumed to be the result of transport and it is thus further assumed that the air within the deep convection cloud is well mixed, exhibiting homogenous trace gas distributions for HONO, NO_2, HCHO and O_3 between 6 and 14 km of altitude.

The calculation of AMFs using equation (4.29), introduced in Section 4.4.1, by means of the Box-AMFs derived for both clouds of optical density 100, for an altitude range between 6 and 13 km yields AMFs of 7.63 and 8.59 respectively. The calculation omits cloud top and cloud bottom, where concentrations are very likely diluted by ambient air. When comparing the Box-AMFs for the cloud reaching to either 14 or 15 km of altitude, then it becomes apparent, that for air masses above the aircraft, the Box-AMFs differ more than for air masses below the aircraft. An error in cloud top height exerts thus also a greater effect on the AMFs. Converting the O_3 slant column measured by the DOAS instrument, $2 \cdot 10^{18}$ molec/cm^2, into a vertical column by the above retrieved AMFs, and assuming a constant O_3 concentration within these 7 km, yields a concentration of $3.7 \cdot 10^{11}$ molec/cm^3 and $3.3 \cdot 10^{11}$ molec/cm^3 respectively. Converting the O_3 mixing ratio of 65 ppb, measured in-situ, into a concentration at flight altitude, with N[3] = $6.73 \cdot 10^{18}$, derives at $4.37 \cdot 10^{11}$ molec/cm^3, which is in the same order of magnitude as the concentration gained from the DOAS measurements. Assuming a constant concentration profile of O_3, when converting slant columns into concentrations, most certainly introduces an error, because O_3 profiles can exhibit strong concentration variations and the effect of mixing by deep convection cannot be further constrained. In lack of further profile information and since the AMF of 7.63 yields a result closer to the in-situ measurement, concentrations are derived with an AMF of 7.63 and for constant trace gas profiles in an altitude range from 6 to 13 km.

An overview on in-situ and DOAS measurements inside the intercepted deep convection cloud is provided in Table 6.3. All listed data is measured at 05:55 UTC. It must be noted, that DOAS data averages over 30 seconds, while the time resolution of the in-situ data is in the order of 1 - 10 s (see also Appendix A.1). Assumption number 2, discussed in Section 6.2.3 with respect to comparing DOAS and in-situ data is valid, but based on the above introduced assumptions and their underlying limitations.

It further needs to be considered that the comparison of modeled and measured O_4 columns introduced an error by neglecting the pressure and temperature dependency

---

[3] The number density N is derived from Arinc data with p = 212 hPa and T = 228° K.

of the O_4 cross section. Yet data analysis and model calculations are consistent, as for both the same O_4 cross has been used. A detailed study on this effect should be done, when following up these studies. Considerations need also be given to the fact that the calculated AMFs are 1-D AMFs. While in general, the path of photons through the atmosphere can be described as a long random walk, photon paths through optically thick media, e.g. clouds with high optical densities, can be described as classical diffusion processes. This is possible, because the random motion of a photon due to anisotropic Mie-scattering can be expressed as isotropic diffusion [*Scholl* 2006]. Therefore the modeled 1-D Box-AMFs can be assumed to also be representative for a 3-D environment. The overall uncertainty of the AMFs is estimated to be around 20 - 30%, which applies to the derived concentrations in accordance.

Table 6.3: *Trace gases measured inside the intercepted deep convection cloud*

trace gas	**method**	**SCD** [molec/cm^2]	**mixing ratio**	**concentration h = 11.4 km** [molec/cm^3]
HONO	DOAS	$2.5 \cdot 10^{15}$	69.5 ppt	$4.68 \cdot 10^{8}$
NO_2	DOAS	$1 \cdot 10^{16}$	0.28 ppb	$1.87 \cdot 10^{9}$
HCHO	DOAS	$2 \cdot 10^{16}$	0.55 ppb	$3.74 \cdot 10^{9}$
O_3	DOAS	$2 \cdot 10^{18}$	55.6 ppb	$3.7 \cdot 10^{11}$
O_3	in-situ		65 ppb	$4.37 \cdot 10^{11}$
NO	in-situ		3 ppb	$2 \cdot 10^{10}$
NO_y	in-situ		4 ppb	$2.7 \cdot 10^{10}$
CO	in-situ		180 ppb	$1.2 \cdot 10^{12}$
H_2O (gas.)	in-situ		320 ppm	$2.15 \cdot 10^{15}$

The next section presents a discussion on possible chemical processes inside the intercepted deep convection cloud to explain the observed concentrations of the species listed in the Table above.

6.2.3.3 Chemistry inside a deep convection cloud

The underlying aim of this section is to explain the presence of HONO within the intercepted cloud and to understand its observed abundance. The formation of HONO is connected to NO_x chemistry (see Section 2.4). When having O_3 and NO_x data available, it is therefore a suitable first step to calculate the Leighton ratio (see Section 2.2.1), to see whether NO_x and O_3 are in steady state conditions:

$$\frac{[\mathrm{NO}] \cdot [\mathrm{O_3}] \cdot k}{[\mathrm{NO_2}]} = J(\mathrm{NO_2}) \tag{6.1}$$

Inserting the values provided in Table 6.3 (taking in-situ ozone) and with k(228K) $= 4.16 \cdot 10^{-15}$ cm^{3}molec^{-1}s^{-1} [*Sander et al.* 2006], J(NO_2) yields $= 1.94 \cdot 10^{-2}$ s^{-1}. A typical value of the NO_2 photolysis frequency in the (cloud free) upper troposphere is $1 \cdot 10^{-2}$ s^{-1} [*Finlayson-Pitts and Pitts, Jr.* 2000], but particularly inside the upper part of clouds, photolysis frequencies can be larger, caused by a higher actinic flux, which can lead to increases by a factor of 2 - 3, depending on the specific cloud [*Madronich* 1987]. Accordingly, the observed J(NO_2) could still indicate steady state conditions. Additional information on conditions inside this cloud is provided by the ratio of NO_x and HNO_3. According to *Bertram et al.* [2007], wet scavenging of nitric acid in deep convection clouds and additional lightning NO_x makes the NO_x to HNO_3 ratio in the upper troposphere an effective indicator of convective influence. The authors have conducted aircraft measurements in convective outflow regimes and find NO_x /HNO_3 $\gg$ 1 to be indicative for recent convective outflow. Here, HNO_3 measurements are not available, but a similar information is provided by the ratio of NO_x and (NO_y - NO_x), since HNO_3 is included in NO_y. If this ratio is $\gg$ 1, than the respective yield of NO_x /HNO_3 would be even higher. With NO_x = NO + NO_2 = 3.28 ppb and NO_y - NO_x = 0.72 ppb, the ratio of NO_x and (NO_y - NO_x) calculates to = 4.56 $\gg$ 1. This is in accordance to values observed by *Bertram et al.* [2007], who present NO_x /HNO_3 ratios between 2 and 12 for convective outflow regimes. From this, the findings on encountering a deep convection cloud and on the presence of lightning NO_x are further supported.

Lightning activity is also associated with OH production, even though the exact amounts are unclear. Accordingly, HONO can be formed by OH and NO. Assuming steady state conditions, the HONO concentration is derived by:

$$[\mathrm{HONO}] = \frac{[\mathrm{NO}] \cdot [\mathrm{OH}] \cdot k}{J(\mathrm{HONO})} \tag{6.2}$$

Inserting k(228K) = $5.2 \cdot 10^{-12}$ cm^{3}molec^{-1}s^{-1} [*Sander et al.* 2006], J(HONO) = $2.5 \cdot 10^{-3}$ s^{-1} (*R. Volkamer, personal communication* with an estimated uncertainty of 40%) and assuming an OH concentration of $1 \cdot 10^7$ molec/cm^3 leads to:

$$[\mathrm{HONO}] = \frac{2 \cdot 10^{10} \cdot 1 \cdot 10^{7} \cdot 5.2 \cdot 10^{-12}}{2.5 \cdot 10^{-3}} = 4.16 \cdot 10^{8} [molec/cm^3] \tag{6.3}$$

This HONO concentration corresponds to a mixing ratio of 61.8 ppt at flight altitude, which is very close to the observed 69.5 ppt, particularly in light of the assumed error of the HONO concentration. However, there are several underlying uncertainties: During the 30 s recording time of the DOAS spectra at 05:55 UTC, NO values vary between 1 and 4 ppb (3 ppb being an average), which leads to possible HONO mixing ratios between 20 and 83 ppt. An error of 40% in J(HONO) leads to possible mixing ratios between 44 and 100 ppt. $1 \cdot 10^6$ OH molec/cm^3 would lead to only 6 ppt of HONO while $5 \cdot 10^6$ molec/cm^3 yields 30.9 ppt. The strongest constrain on the HONO formation is therefore given by OH concentration, which is discussed below.

At this point, the measured HONO mixing ratio of 69.5 ppt could very well be observed under steady state conditions. Within this system, the HONO concentration at any given time can by derived by:

$$\frac{d[\mathrm{HONO}]}{dt} = -J[\mathrm{HONO}] + [\mathrm{NO}] \cdot [\mathrm{OH}] \cdot k \tag{6.4}$$

A solution for this equation is provided by:

$$[\mathrm{HONO}] = a \cdot exp(\frac{-t}{\tau}) + b = a \cdot exp(-J(\mathrm{HONO}) \cdot t) + b \tag{6.5}$$

with

$$b = \frac{[\mathrm{NO}] \cdot [\mathrm{OH}] \cdot k}{J(\mathrm{HONO})} = HONO_{steadystate} \tag{6.6}$$

After 400 s the HONO concentration has reached 1/e of its steady state concentration. Steady state is reached within 1 % after half an hour. These time scales are consistent with time scales of a deep convection event. To present knowledge [*Schumann and Huntrieser* 2007], only one publication by [*Bhetanabhotla et al.* 1985] has presented estimates on the lightning induced HONO production based on model simulations. The authors deduce a HONO to NO_x ratio of about 0.006, 100 s after flash activity. Inserting 100 s in equation (6.5), results in a ratio of 0.004 for the measurements on flight LH158, while the observed ratio 05:55 UTC is about 0.02. The derived value of 0.004 is based on the assumption that the observed NO_x concentrations remained constant between 100 s after flash activity and the time of measurement, as the lightning production yield of NO is about two orders of magnitude higher than that of HONO. This assumption is not completely valid. However, in view of all underlying uncertainties, the overall picture yields nevertheless very consistently a system in steady state.

As mentioned above, the limiting factor of the observed HONO concentration is dominated by OH concentration. The photolysis of HONO itself yields already about $1.2 \cdot 10^6$ molec cm^{-3} s^{-1}. An increased photolysis of ozone inside the cloud, caused by a higher actinic flux, yields more $O(^1D)$, which by reaction with H_2O produces OH. 320 ppm of gaseous water are measured inside the cloud, however, most $O(^1D)$ reacts with N_2 and O_2. A rough estimate on the OH yield by reaction of $O(^1D)$ with H_2O is in the order of $4 \cdot 10^5$ molec cm^{-3} s^{-1}, when assuming 1 molec/cm^3 of $O(^1D)$ available for this reaction.

Yet OH does not only react with NO, but also with CO, NO_2 and CH_4, leading to a life time of OH at this altitude of about 4.5 s. The reaction with CH_4 leads to the formation of HCHO, which could explain the observed HCHO concentration. Among these reactions, the reaction of OH with NO is the fastest, with k (NO)

$= 5.2 \cdot 10^{-12}$cm^{3}molec^{-1}s^{-1}, whereas k(CO) $= 1.95 \cdot 10^{-13}$cm^{3}molec^{-1}s^{-1}, k(CH_4) $=$ $1.02 \cdot 10^{-15}$cm^{3}molec^{-1}s^{-1} and k(NO_2) 0 $6.29 \cdot 10^{-12}$cm^{3}molec^{-1}s^{-1}. The reaction of OH with NO_2 is also very fast, but is only of minor importance as there was not much NO_2 observed.

Mixing ratios of trace gases measured on flight LH127 could also be derived by applying a similar method as described in Section 6.2.3.2. On this flight HONO was presumably also observed within a deep convection cloud, coinciding with a biomass burning plume (see Figure 6.13, red box, in Section 6.2.2). The mixing ratios for this event are as follows: NO_2 : 0.55 ppb, HCHO: 3.2 ppb, HONO: 60 ppt. NO_2 and HCHO are higher as on flight LH158, but this is not unusual within a biomass burning plume. However, this event raises the question on the importance of lightning NO_x for the HONO formation, as the biomass burning plume is also a considerable NO_x source. In either case, sufficient OH concentrations are needed. NO is not available for 11:12 UTC, but as mention in Section 6.2.2, it is very likely in the order of 2 - 3 ppb. Based on this assumption, also on flight LH127 steady state conditions of HONO, NO and OH would have been observed. For flight LH110 no concentrations could be derived, but the coincidence of enhanced NO, clouds, lightning activity and HONO is striking.

These findings can be summarized as follows:

- The HONO observed on all three flights was most likely formed by lightning induced OH and NO. The contribution of biomass burning NO_x is uncertain.
- The observed photochemical system on flight LH158 seems to be in steady state, which is reached within 1% 30 minutes after flash activity.
- Increased photolysis frequencies inside the deep convection cloud can yield a higher production of OH by O_3 photolysis and furthermore an increased J(NO_2) reduces the OH sink given by reaction with NO_2.

The following issues need further consideration:

- The steady state conditions are largely based on an assumed OH concentration of $1 \cdot 10^7$ molec/cm^3, which needs to be further verified.
- So far HONO formation by heterogeneous reactions has been neglected. HONO formation by reaction of NO_2 with water could play a role (see Section 2.4).
- The impact of chemistry versus transport should be further studied.
- The uncertainties in J(HONO) need to be further constrained as well as the increase of photolysis frequencies inside clouds.
- An uncertainty is also introduced by the conversion of slant columns in concentrations and comparing those to in-situ measurements.

A next suitable step would certainly be to conduct sensitivity studies with a chemical model to further constrain the conditions of HONO production inside deep convection clouds.

Incidently, the observation during flight LH158 at 05:55 UTC, which started the discussion on HONO, proves to be fortunate in many ways: not only because civil aircrafts usually evade areas with lightning activity, but particulary since the gap in the DOAS data between 05:46 and 05:50 UTC is caused by a routine computer reboot, which came none too soon!

6.2.4 An upper limit of tropospheric BrO

Bromine oxide plays an important role in global ozone chemistry, amongst other things, as described in Section 2.3. While the stratospheric BrO abundance is quite well quantified, there are still open questions on the BrO distribution in the troposphere. In recent years, observations have shown that reactive halogen species are present in many parts of the troposphere. Apart from the high amounts of BrO found during tropospheric ozone depletion events in polar regions, BrO was detected in mid latitudes and in the tropics (see also Section 2.3), exhibiting mixing ratios up to 3 ppt. The CARIBIC long-distance flights provide a good opportunity for the observation of BrO in the free troposphere between mid latitudes and the tropics. Except for BrO observed in residues of stratospheric air (see Section 6.3.1.2), no tropospheric BrO above detection limit was measured up to now on CARIBIC flights. It must be noted, however, that suitable measurement results were so far only obtained from the nadir viewing direction.

6.2.4.1 Detection limit of the BrO retrieval

The retrieval of an upper limit depends on the detection limit of the instrument. According to the definition of *Stutz and Platt* [1996], the detection limit of the BrO SCD S_{limit} is given by:

$$S_{limit} = 2 \cdot \frac{\chi}{\sqrt{\sum_k (\sigma(\lambda_k) - \overline{\sigma})^2}} \tag{6.7}$$

The sum covers the fit region and $\overline{\sigma}$ is the average of the cross section. For a RMS residual of $\chi = 6.2 \cdot 10^{-4}$, a detection limit of $S_{limit} = 1.8 \cdot 10^{13}$ molec/cm^2 is derived. To find out whether this value is a suitable detection limit for the utilized instrument, in Figure 6.21 measured BrO dSCDs of flight LH154 to South-East Asia are provided. Slant columns are plotted for different time resolutions, which are achieved by adding consecutive spectra. As expected, the overall scattering of the dSCDs decreases with a decreasing time resolution, because adding of spectra leads to an improved signal to noise ratio. The above utilized RMS residual of $\chi = 4.2 \cdot 10^{-4}$ is taken from analyzing spectra of a 7.5 minutes time resolution. The RMS residuals for 5, 2.5 minutes and 30 seconds are $7.1 \cdot 10^{-4}$, $7.8 \cdot 10^{-4}$ and $2.3 \cdot 10^{-3}$ molec/cm^2 respectively. The bottom panel of Figure 6.21 shows a zoomed sector of the graph in the upper panel, presenting

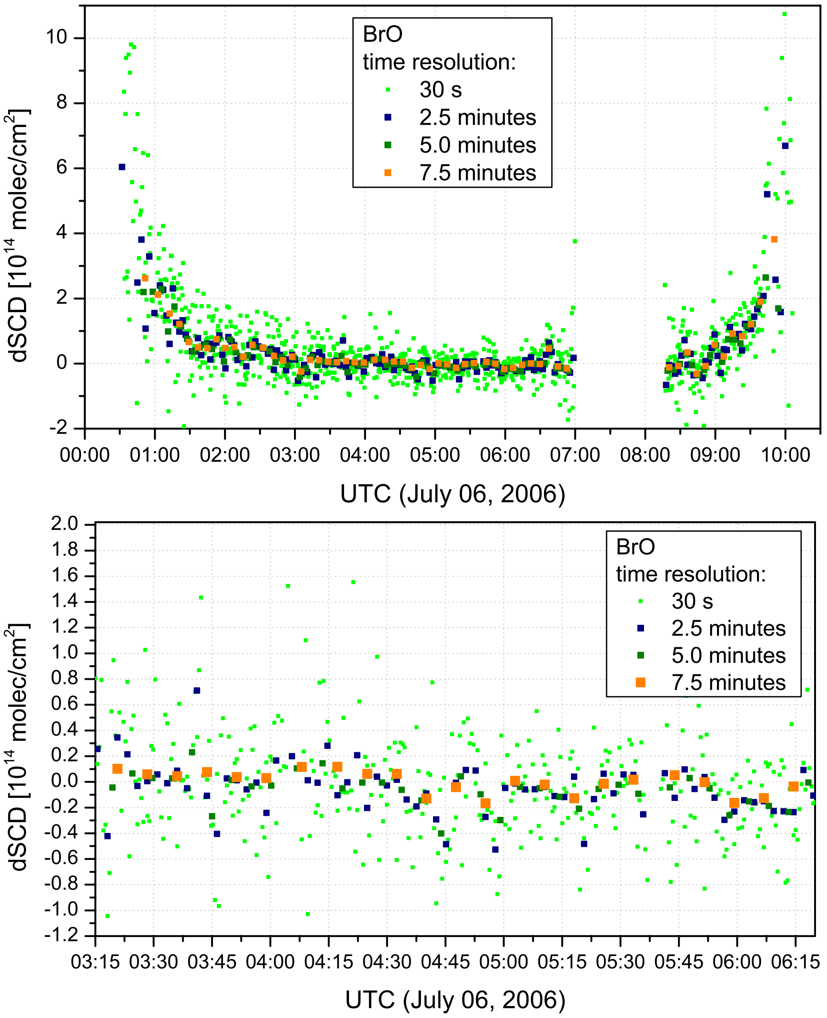

Figure 6.21: *BrO dSCDs for different time resolutions. Top panel: Results of flight LH154/155 to Guangzhou/Manila, covering almost a complete daily cycle from SZA = 90° to SZA = 84°. The respective FRS is taken from the same flight, recorded at 04:29 UTC, SZA = 17.5°. Bottom panel: Zoomed sector of the graph above.*

a time period from SZA = 43° - 20°. The FRS is recorded at 04:29 UTC with a SZA of 17.5°. dSCDs measured within an hour before and after 04:29 UTC can therefore be regarded to be around 0, particularly as no systematic structure in the dSCDs can be identified. The overall scattering of the 7.5 minutes time resolution (orange) is in the order of $3 \cdot 10^{13}$ molec/cm^2, which is higher as the above derived detection limit, but more suitable for the DOAS analysis of spectra recorded with the current instrumental setup.

6.2.4.2 Deriving an upper limit for tropospheric BrO

Since currently a pure stratospheric FRS is not available, the observation of tropospheric BrO relies on differences measured in tropospheric columns. These differences could either be caused by sufficiently strong tropospheric concentration gradients along the flight track or by different AMFs, e.g. due to ascent and descent of the aircraft or by a change in SZA. Accordingly, the yield of maximum differences of measured slant columns is analyzed for different tropospheric BrO profiles.

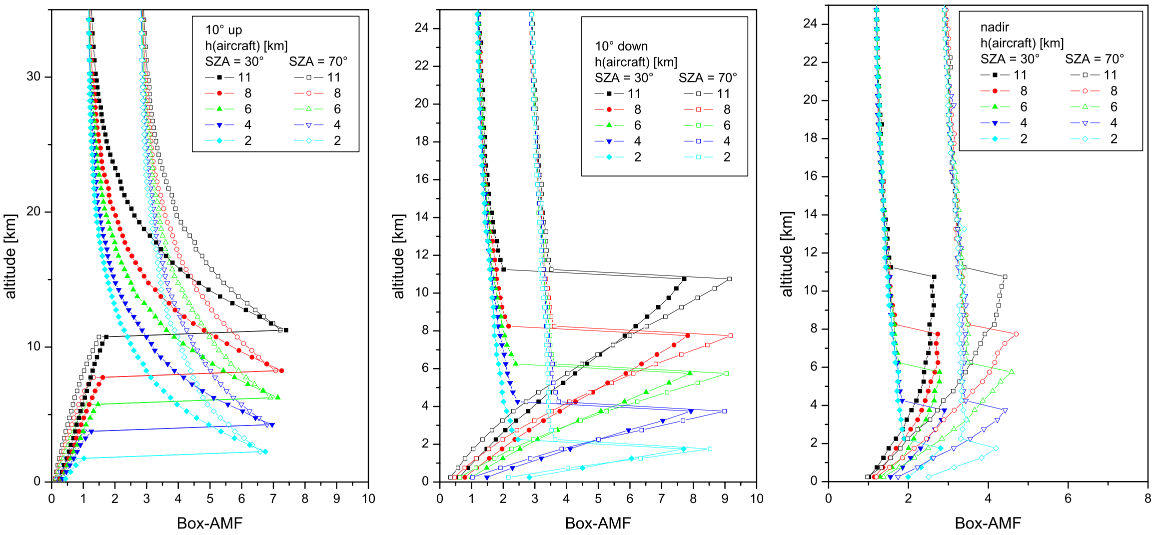

Figure 6.22: *Box-AMFs for all viewing directions, derived for different detector heights and for SZA = 30° and 70°.*

In Figure 6.22, Box-AMFs are presented for all three viewing directions. They are plotted for five different aircraft heights and for two different SZAs, 30° and 70°. These solar zenith angles are chosen, as they allow a proper BrO analysis with the current instrumental setup (see Section 5.4.4). Note the different altitude scales! The Box-AMFs were retrieved for a pure Rayleigh atmosphere, with a height grid of 500 m and at 355 nm, which is within the wavelength range of the BrO analysis. From studying the Box-AMFs, several aspects become apparent: Even though the 10° up viewing direction would yield the highest dSCD differences e.g. upon descent, as it subsequently enters new layers of an assumed tropospheric BrO profile, it cannot be used to derive a precise BrO limit, because the stratospheric Box-AMFs depend on the altitude of the aircraft. The strength of this effect depends on SZA. For small SZAs, a FRS recorded et e.g. 5 or 6 km altitude and for a sufficiently strong tropospheric signal, this effect can be neglected, like when measuring NO_2 in polluted boundary layers (see Section 6.4). Here, however, the BrO signal is dominated by the stratospheric absorptions, which would not be accurately canceled out by any FRS when analyzing spectra recorded at different altitudes. For both other viewing directions, this effect is negligible. Comparing the 10° down and nadir viewing direction makes clear, that the 10° down viewing direction exhibits the highest sensitivity towards the troposphere. Accordingly, the sensitivity of the 10° down viewing direction towards different tropospheric BrO profiles is tested.

Recent ground based zenith-sky observation by *Hendrick et al.* [2007] retrieved inversion profiles at 60° N that show a rather homogenous tropospheric BrO concentration profile in the order of 1 - $2{\cdot}10^7$ molec/cm^3, which corresponds to vertical columns in the order of 1 - $1.52{\cdot}10^{13}$ molec/cm^2 or 0.6 - 1 pptv respectively, when BrO is assumed to be mixed uniformly in the troposphere. According to the authors, these column values are consistent with previous estimates made from balloon, satellite, and other ground-based observations. The retrieved concentration profiles by *Theys et al.* [2007], by inversion technique from MAX-DOAS measurements in the tropics (Reunion island), yield tropospheric BrO vertical columns in the same order of magnitude, $1.1{\cdot}10^{13}$ molec/cm^2, but the authors also indicate a BrO maximum in the tropical free troposphere around 6 km altitude. The first tropospheric BrO profiles were obtained by balloon-borne measurements in Kiruna, Sweden, by *Fitzenberger et al.* [2000]. These profiles also exhibited pronounced maxima between 4 and 6 km altitude. In view of these observations, the profiles shown in Figure 6.23 (top panel) are utilized to analyze slant columns that would be measured, if the aircraft was flying in an area exhibiting such a profile.

The SCDs shown in Figure 6.23 (bottom panel) were retrieved by solving the following equation:

$$\overrightarrow{S_i} = \mathbf{A}_{ij} \cdot \overrightarrow{V_i} \tag{6.8}$$

The Box-AMF Matrix $\mathbf{A}_{ij}$ contains a Box-AMF for each box i and for each detector (aircraft) height j, while $\overrightarrow{V_i}$ contains one of the profiles shown in the top panel of Figure 6.23. Thus, a tropospheric SCD is derived for each detector altitude. When assuming that the stratospheric column is accurately canceled out by the FRS (on that topic see also Section 6.4.2.1), then the maximum dSCDs that can be measured are given by the difference of the SCD measured at any height and the tropospheric column contained in the FRS: dS = S(meas) - S(ref). It is apparent that two occasions would yield the highest differences: (1) The tropospheric BrO concentration appears suddenly, more like a "BrO plume", then the FRS would contain no tropospheric column and any measured dSCD would yield the total slant column shown in Figure 6.23. In light of the present knowledge on tropospheric BrO this is very unlikely. (2) Taking a FRS from the lowermost box would yield the highest differences. However, in practice, CARIBIC flight destination exhibit always a polluted boundary layer. Unknown aerosol profiles and also the strong effect of ground albedo in this layer would introduce several errors to the Box-AMFs calculations. Therefore, a FRS recorded at a higher detector altitude needs to be chosen and furthermore, any dSCD measured within the lowermost boxes cannot be properly converted to VCDs owed to the same cause.

When taking a FRS recorded at an altitude of 11 km, then the following maximum dSCDs (= S(meas) - S(ref)) in molec/cm^2 could be measured (omitting the boxes from 0 - 2 km): blue profile: $3.2 \cdot 10^{13}$, green profile: $1.5 \cdot 10^{13}$, red profile: $2.6 \cdot 10^{13}$, orange profile: $5.9 \cdot 10^{13}$. Merely dSCDs retrieved with the blue and orange profiles

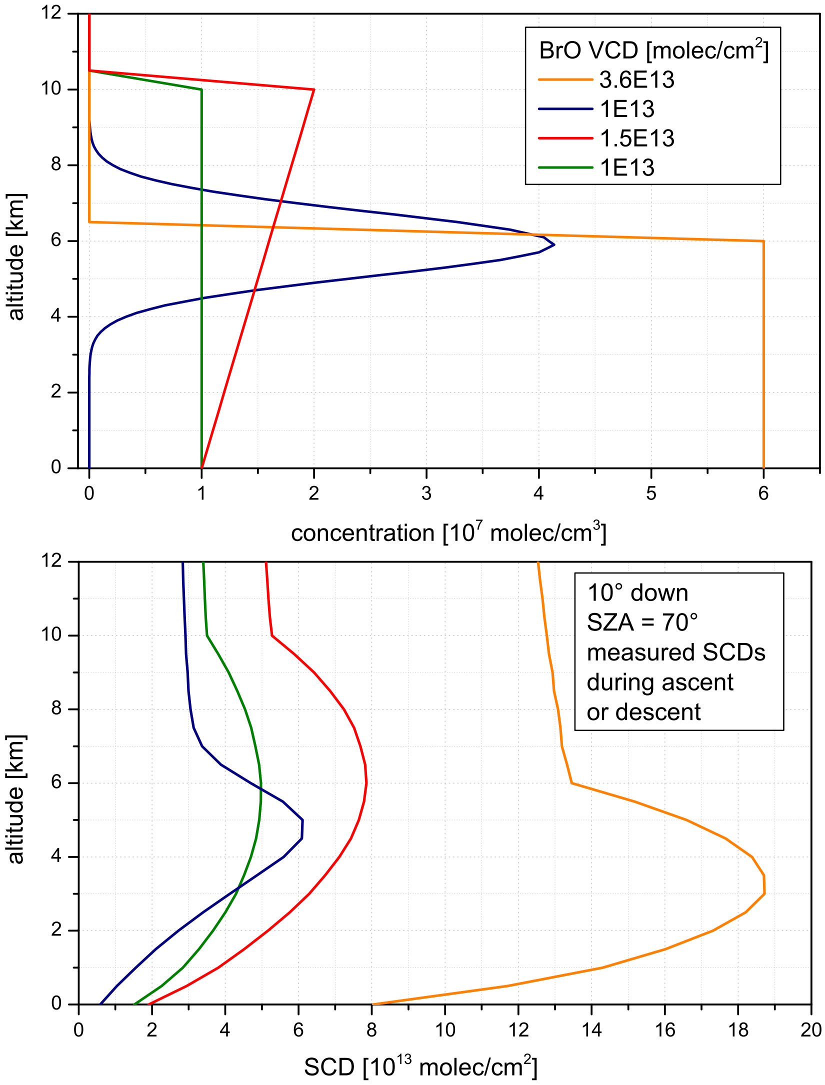

Figure 6.23: *Top panel: Tropospheric BrO profiles. Bottom panel: Retrieved SCDs for the 10° down viewing direction with SZA = 70°.*

are above the instrumental detection limit of $3 \cdot 10^{13}$ molec/cm^2. The blue profile corresponds to the measurements in Kiruna, exhibiting 3 ppt at maximum. On average, the orange profile contains 3 ppt from 0 - 5 km. Accordingly, the detection limit of the 10° down viewing direction for tropospheric BrO is in the order of 3 ppt, while that of the nadir viewing direction is about a factor 2 higher, based on the Box-AMFs shown in Figure 6.23.

Judging from recent publications, the green and red profiles characterize best the tropospheric columns found in mid-latitudes and sub-tropics, where CARIBIC flight destinations are located. Even when assuming that the 10° down viewing direction will function well soon, then the derived detection limit of 3 ppt is likely too high to properly delimit tropospheric BrO columns. The current instrumental status allows merely the determination of an upper limit of tropospheric BrO in the order of 6 ppt.

6.3 Discussion on trace gases measured in stratospheric air

CARIBIC DOAS measurements are also sensitive for stratospheric trace gases, such as NO_2, O_3 and BrO. Particularly during mornings and evenings, the AMFs of stratospheric absorbers become very large, due to very long light paths through the stratosphere. As explained in Section 5.4.4, an accurate quantitative analysis of O_3 and BrO is not possible with the current instrumental setup, whereas the NO_2 analysis works very well. In the following, measurements of stratospheric trace gases in areas with tropopause folds are presented, while a comparison of stratospheric NO_2 with satellite measurements is shown in Section 6.3.2, which includes the separation of the total vertical column in a stratospheric and tropospheric column.

6.3.1 Measurements of NO_2, O_3 and BrO in areas with tropopause folds

Tropopause folds play an important role in the exchange of air between the troposphere and the stratosphere (see also Section 2.1.2.3), which renders the measurement of trace gases inside tropopause folds highly interesting. The stratospheric air encountered over the Andes on flights LH123/124 and LH127/128 can be attributed to tropopause folding. On the flight route to Asia, several steep tropopause folds have been intercepted. Unfortunately, the nadir viewing direction was not sensitive enough to detect a difference in slant columns caused by the intrusion of stratospheric air below the aircraft. Flight LH158 to China marks an exception, as for this flight spectra of the 10° down viewing direction were of reasonably quality. While flying over the Tibetan plateau, an area in the upper troposphere was encountered that exhibited enhanced PV values. These can most likely be attributed to a recent exchange of air masses between the troposphere and the stratosphere, caused by tropopause folding.

6.3.1.1 Dynamical tropopause folding over the Andes

The measurements of stratospheric trace gases on flights LH123/124 and LH127/128 are presented in Section 6.2.2 and marked with green boxes in Figures 6.12, 6.13 and 6.14 respectively. These findings can be explained by a dynamical tropopause that on these occasions "folded down" into the flight track. The strongest folding event can be seen on flight LH127. The respective PV values are shown in Figure 6.24.

Compared to the much more pronounced tropopause folds seen on the Asian route, see e.g Figure 2.2 in Section 2.1.2.3, the folding over the Andes is rather weak. However, it must be noted that flights over the Andes are much shorter, which causes folds to be less apparent in the PV plots for these flights. The strongest impact is seen in O_3 data, in both, DOAS and in-situ measurements. A slight effect is indicated in NO_2 columns, but not strong enough to be quantified. Further studies on this area could perhaps reveal to what extent a mixing of air masses between troposphere and

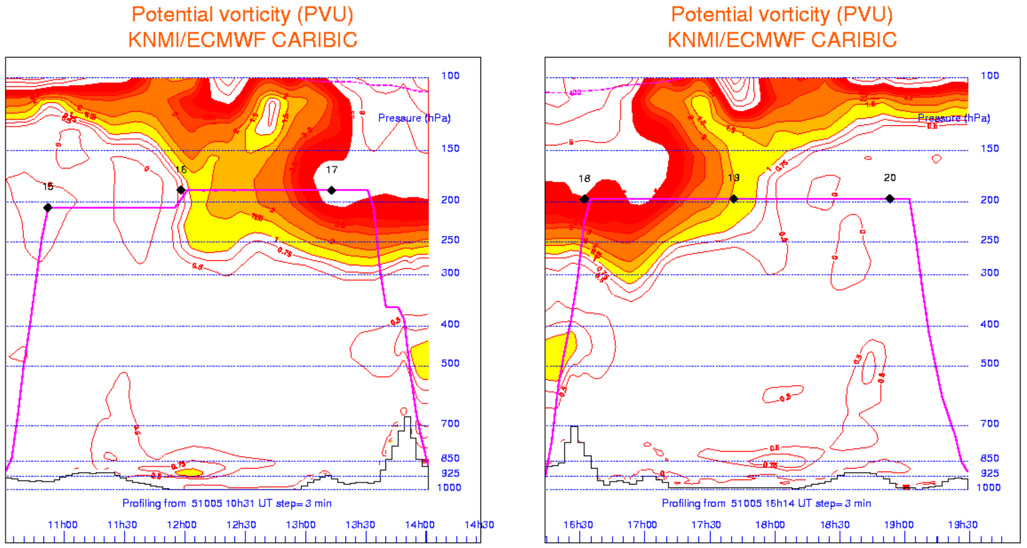

Figure 6.24: *PV values derived from ECMWF data for flights LH127/128 over the Andes.*

stratosphere has taken place. Utilizing information of in-situ O_3 for the calculation of air mass factors could yield information on the influence of the tropopause folding on the ozone profile. At this point, both tasks are left for future work.

6.3.1.2 NO_2 and BrO measurements in an area of PV residues

Before the deep convection plume on flight LH158 was encountered, the flight track incidently passed over an area characterized by enhanced PV values, which are very likely the residues of a dissolved tropopause fold. Figures 6.25 and 6.26 show slant columns of NO_2 and BrO derived from the 10° down viewing direction and respective PV values. Slant columns are plotted for different time resolutions, as adding spectra leads to a better signal to noise ratio. The incident is labeled with a blue box. Even though the quality of the analysis of the 10° down spectra is limited, the enhancement in slant columns of both trace gases is clearly visible. Apparently, the PV residues are constrained over the Tibetan plateau by the deep convection area starting at about 05:30 UTC, after the aircraft has passed the plateau.

An estimate on the total column contained in this area can be derived by calculation of AMFs using equation (4.29), introduced in Section 4.4.1. Under the assumption that the total column is contained in an area between 8 and 11 km of altitude, indicated by the PV plot, the AMF is calculated by means of the Box-AMFs for these altitude layers and calculates to 6.7. The SZA for the AMF calculation was set to 30°, which correspond to 04:00 UTC. The FRS is recorded at 04:48 UTC with an SZA of 15.8°. The yield of the slant column enhancement in the area of PV residues is determined by averaging data with a 20 min time resolution over a period of thirty minutes around

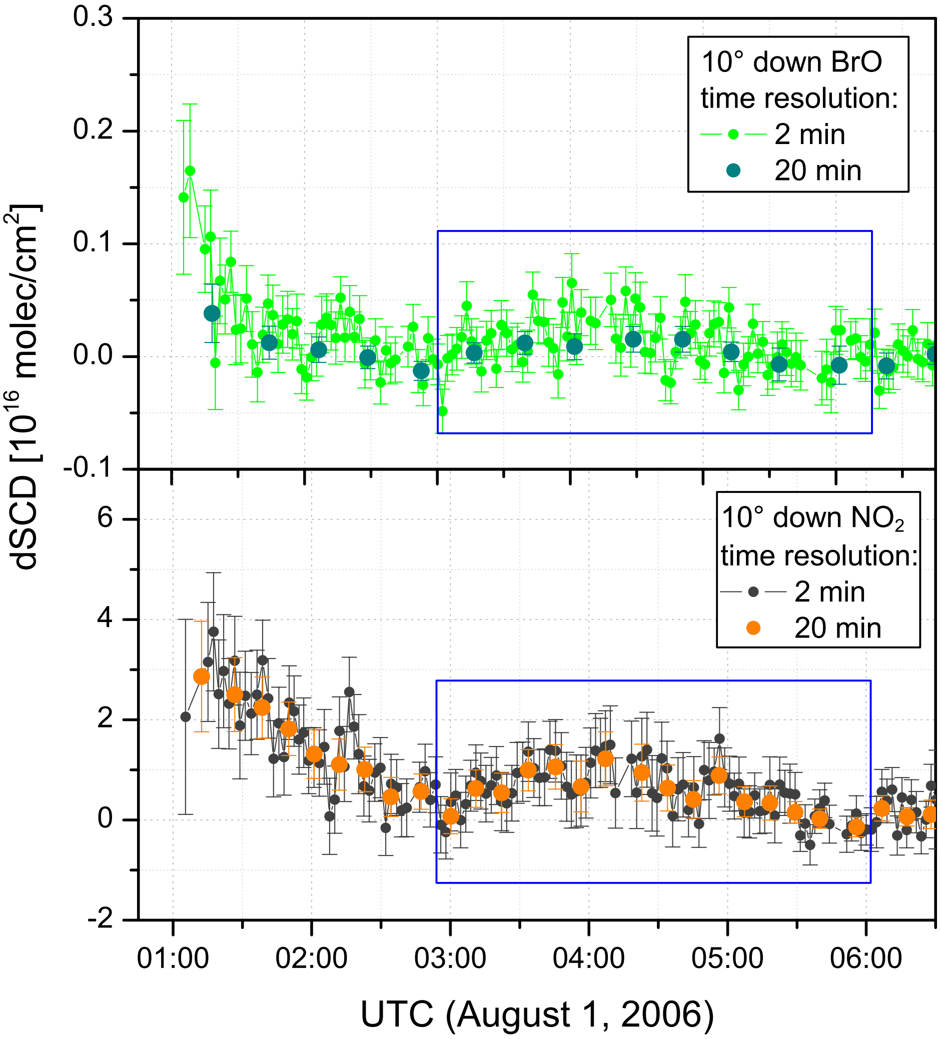

Figure 6.25: *BrO and NO_2 dSCDs of the 10° viewing direction for flight LH158. The FRS is recorded at 04:48 UTC with a SZA of 15.8°.*

04:00 UTC. Assuming that stratospheric columns are canceled out by the column contained in the FRS (see also Section 6.4.2.1), leads to tropospheric slant columns of about $1.2 \cdot 10^{14}$ molec/cm^2 for BrO and $1 \cdot 10^{16}$ molec/cm^2 for NO_2, which corresponds to tropospheric vertical columns of about $1.8 \cdot 10^{13}$ molec/cm^2 for BrO and $1.5 \cdot 10^{15}$ molec/cm^2 for NO_2. When further assuming that these columns are homogenously distributed over 3 km, between 8 and 11 km of altitude, then with $N \approx 9 \cdot 10^{18}$, mixing ratios of 6.6 ppt for BrO and 0.55 ppb for NO_2 are derived.

These values are based on several assumptions and are derived of spectra with inferior quality. Therefore, the retrieved information should be regarded with sufficient care. The vertical tropospheric columns are in the order of typical tropospheric background columns (see Section 6.2.4.2 and below). Even though the CARIBIC camera shows only a few scattered clouds for the respective time period, multiple scattering

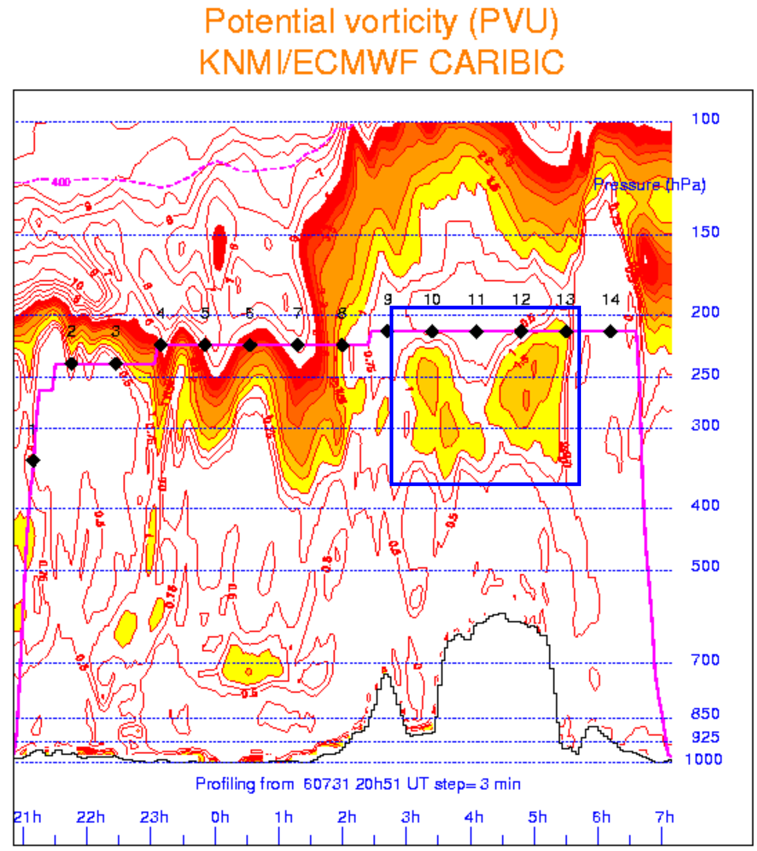

Figure 6.26: *PV values derived from ECMWF data for flight LH158.*

effects, also possibly on aerosols, cannot be excluded, causing an increased sensitivity of the measurements towards tropospheric columns. However, the coincidence of enhanced tropospheric columns and PV residues in the troposphere is striking. In case this viewing direction will function properly again one time, chances are high, that similar observations can be achieved, particularly also measurements directly inside tropopause folds. These observations could provide valuable insights to troposphere-stratosphere exchange processes.

6.3.2 NO_2 total column comparison with satellite data

To get an estimate on the quality of CARIBIC DOAS measurements with respect to the quantitative accuracy of measured trace gas columns, a total column comparison with satellite data is suitable. As described in Section 5.4.3, the analysis of spectra at high SZA, where absorption structures of stratospheric trace gases are large, is with sufficient quality only possible for NO_2. Accordingly, the following presents a total column comparison of CARIBIC DOAS vertical NO_2 columns with vertical columns retrieved by the OMI satellite (see *www.temis.nl*).

Figure 6.27 (top panel) shows NO_2 dSCDs measured on flight LH166/167 from

Frankfurt to Guangzhou/China and Manila, on October 20, 2006. The stop-over in China exhibits enhanced NO_2 columns caused by local pollution, marked by a red box in Figure 6.27. These data points are omitted for the retrieval of the total NO_2 column. Data is plotted for a full day (stretched over several time zones), from SZA 91.2° - 90.8° and with a time resolution of 2.5 minutes. The sun sets before Manila is reached. The FRS is recorded at 04:47 UTC with a SZA of 43°. The minimum SZA encountered on that flight was 41.3°. The FRS is recorded over the Tibetan plateau, which is assumed to exhibit a rather clean troposphere. Some small data variations are seen during the time period marked by a blue box in Figure 6.27 (top panel), which will be discussed below.

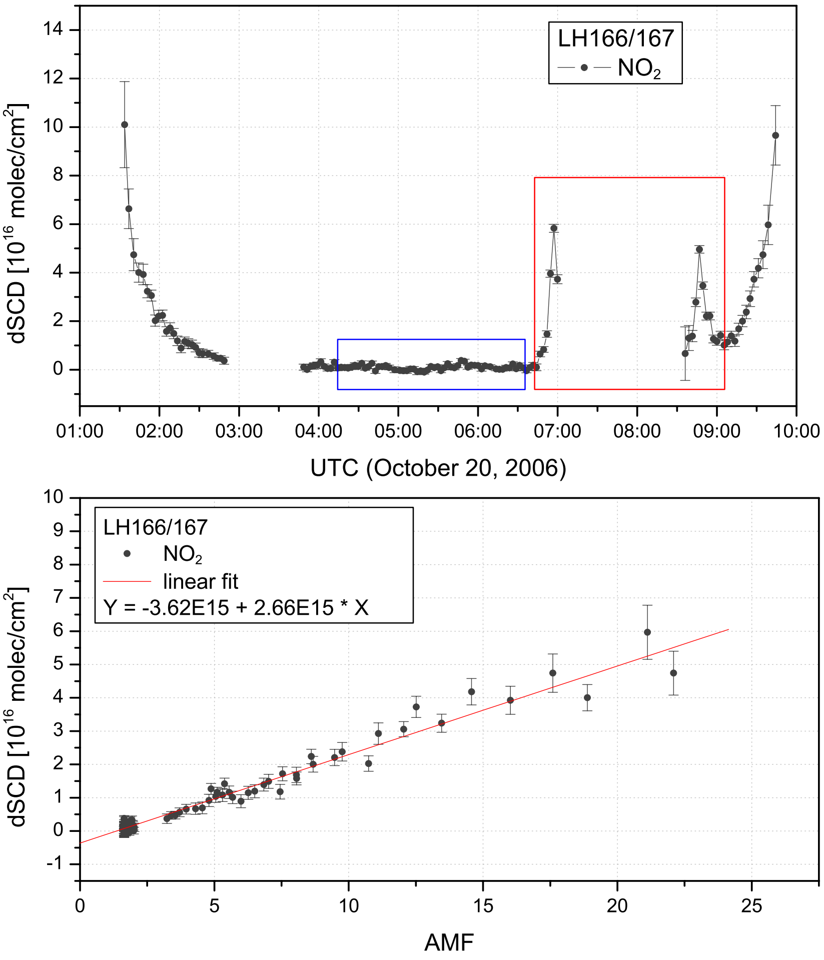

Figure 6.27: *NO_2 dSCDs (top panel) and respective Langley plot (bottom panel) of flight LH166/167. The FRS is recorded 04:47 UTC with SZA = 43°.*

As described in Section 4.3.2, the column contained in the FRS can be derived with a Langley plot. The Langley plot for flight LH166/167 is shown in the bottom panel of Figure 6.27, revealing a slant column contained in the FRS of $3.62 \cdot 10^{15}$ molec/cm^2 and an average vertical column density of $2.66 \cdot 10^{15}$ molec/cm^2. Since the NO_2 concentration increases throughout the day (see Section 2.2), retrieved vertical column densities need to be analyzed for morning an evening separately. In Figure 6.28, the respective vertical columns are plotted. They are derived by adding the slant column contained in the FRS to the measured dSCDs and by dividing the total slant columns with the respective stratospheric AMFs.

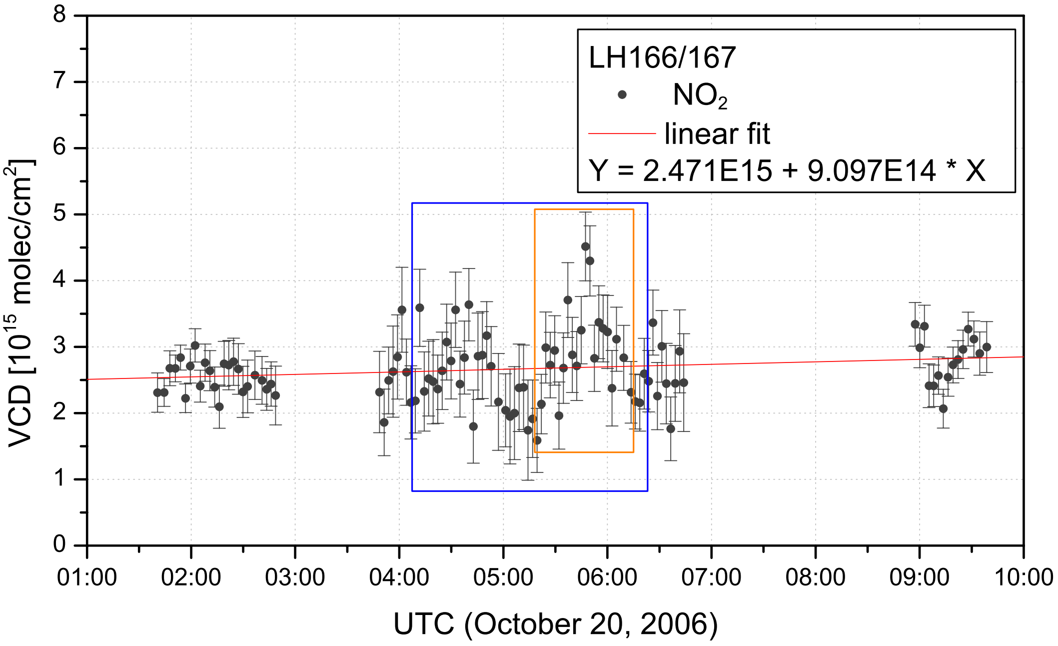

Figure 6.28: *NO_2 VCDs of flight LH166/167.*

The data plot reveals a VCD of $2.54 \cdot 10^{15}$ molec/cm^2 in the morning and as expected a larger VCD of $2.82 \cdot 10^{15}$ molec/cm^2 in the evening. A bias is introduced by averaging over latitudes (from 48° to 18°), where the real stratospheric NO_2 profile is not constant as assumed for the AMF calculations. Another effect on the VCD retrieval is clearly visible, marked with a blue and orange box respectively. The blue box corresponds to the blue box in Figure 6.27. The variations in the vertical column data are very likely caused by tropospheric columns that are not considered in the AMF calculations. Figure 6.29 presents total and tropospheric vertical columns retrieved from the OMI satellite instrument. The flight track of flight LH166 as well as the respective blue and orange box are included. A comparison of total columns derived by CARIBIC DOAS and satellite instrument, shows that vertical columns, which are mainly determined by stratospheric NO_2, are in the same order of magnitude, around 2 - $3 \cdot 10^{15}$ molec/cm^2. NO_2 total columns retrieved by the Sciamachy satellite instrument reveal similar columns (*S. Beirle, personal communication*). A more detailed comparison would require a sufficient knowledge on the retrieval procedures of the satellite and particularly a better adaption of the NO_2 profiles used for the AMF calculations to local conditions along the flight track. However, based on the present findings it can be assumed, that CARIBIC DOAS NO_2 measurements yield quantitatively reliable results.

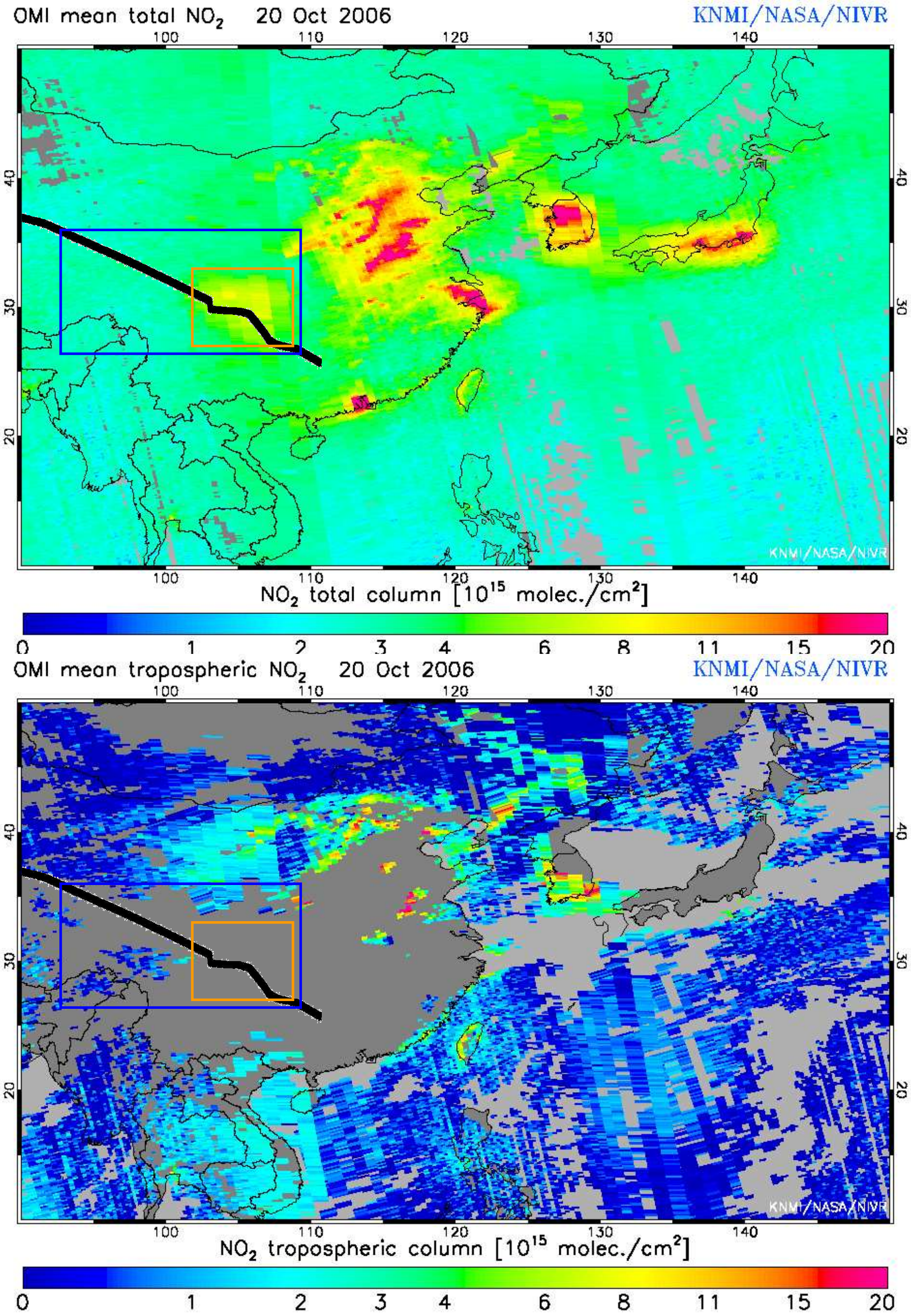

Figure 6.29: *Total (top panel) and tropospheric (bottom panel)* NO_2 *columns retrieved by the OMI satellite instrument for October 20, 2006.*

More interesting, however, is the potential of the CARIBIC DOAS measurements to reveal tropospheric columns. The area marked with the orange box coincides with flying over the Red Basin, which is often characterized by a highly polluted troposphere (see e.g [*Beirle* 2004]). An increase of the total NO_2 columns to about 4 - $6 \cdot 10^{15}$ molec/cm^2 in this area is seen in both instruments. The OMI retrieval of tropospheric columns shows no data for the time period marked by the orange box. This implies that cloud fractions were too high for a reliable retrieval of tropospheric columns. The effects of clouds on nadir measurements performed above clouds, are quite complex and are determined e.g. by cloud top height, optical density and by total cloud cover fractions. Unfortunately, for flight LH166 there is no camera data available. In future studies on CARIBIC NO_2 data, the retrieval of tropospheric columns with a high temporal and spatial resolution along the flight track is possible. These studies could provide valuable information on local NO_x sources and transport processes.

6.4 Discussion on measurements in the boundary layer

CARIBIC flight destinations are very large cities that usually exhibit high levels of NO_2 and formaldehyde, caused by local pollution. During ascent and descent of the aircraft, spectra are obtained at different altitude levels, within and above the boundary layer. These spectra yield information on the vertical distribution of trace gases. However, most ascent spectra cannot be considered, because of instable instrument temperatures (see Section 5.2.4). In the following section boundary layer profiles of NO_2 and HCHO are obtained from spectra recorded during descent and the information content of these measurements is discussed.

6.4.1 Direct retrieval of boundary layer heights

A simple approach to retrieve a good estimate on the height of the boundary is to make use of the specific sensitivity of the 10° up viewing direction. As shown in Figure 6.22 (Section 6.2.4.2), this viewing direction exhibits very high Box-AMFs for atmospheric layers above the aircraft, whereas Box-AMFs for air masses below are rather small. Qualitatively, this sensitivity pattern does not change upon a variation in the aircraft's altitude (see same Figure). Therefore, once the aircraft has entered the boundary layer, the 10° up viewing direction starts to "see" NO_2 and HCHO concentrations within, indicated by higher slant columns. In Figure 6.30, a schematic drawing of this method is provided.

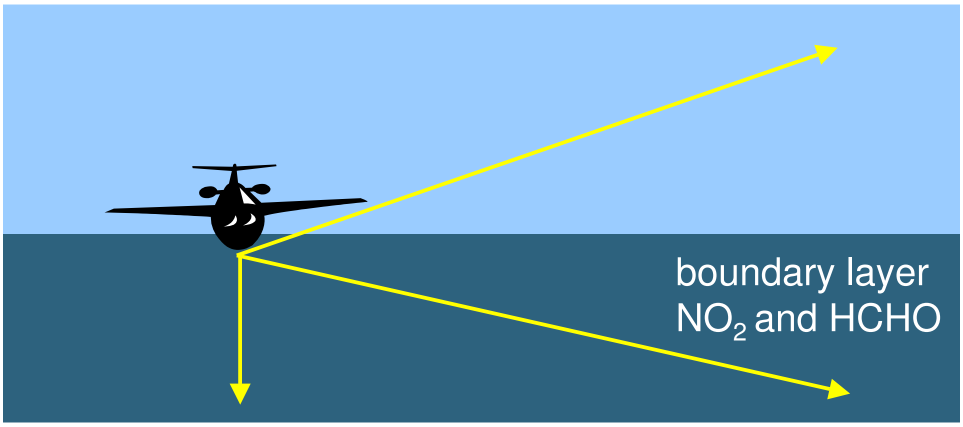

Figure 6.30: *Sketch of the aircraft entering the boundary layer.*

This approach works well, as long as the trace gas concentrations at the top of the boundary layer are sufficiently large to induce a clear signal in the 10° up dSCDs. With a time resolution of 30 s, corresponding roughly to a 100 to 200 m height resolution, the boundary layer top height can be determined within an accuracy in the same order of magnitude. Figure 6.31 presents an example of NO_2 measurements upon landing in

Santiago de Chile from flight LH102 (around 11:00 local time). This flight in December 2004 was the only flight where the 10° up and down viewing directions worked properly (see also Section 5.2.4).

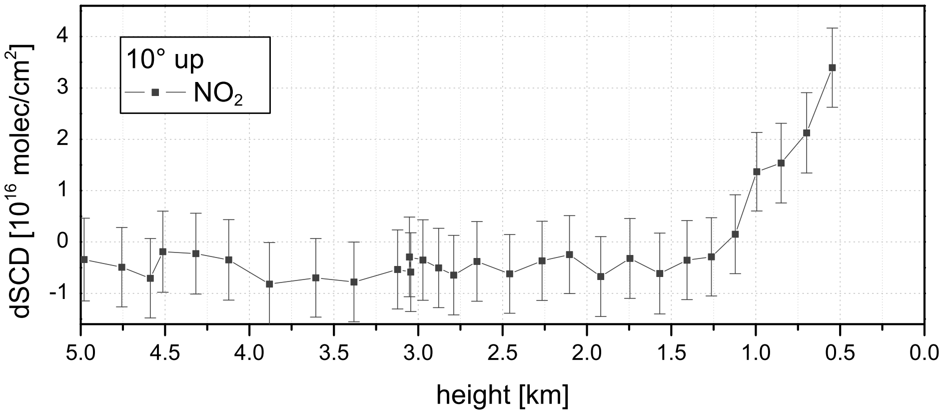

Figure 6.31: *NO_2 dSCDs measured during descent on flight LH102.*

Here, the top of the boundary layer can be confined to 1.2 km ± 100 m. A limitation of this approach is given by the dependency of the stratospheric AMF on the altitude of the aircraft (see respective Box-AMFs in Figure 6.22). This effect becomes more important with increasing SZA, yet only for trace gases with a stratospheric profile such as NO_2. Alternatively, HCHO columns can be observed, because the stratospheric formaldehyde column is below the detection limit of the deployed instrumental setup.

Supplementary data is provided by the CARIBIC camera. Occasionally, the entry into the boundary layer is visible, depending on the aerosol load. Figure 6.32 shows a camera photo taken upon landing in Guangzhou/China (flight LH158, August 1, 2006) at an altitude of about 2.5 km. A seemingly very leveled, rather dark aerosol layer can be seen. Upon entering this layer, the visibility was extremely reduced, which usually is a sign of high aerosol load, exhibiting large extinction coefficients. However, a visible aerosol load on camera pictures does not necessarily imply the top of the boundary layer (see below).

6.4.2 Retrieval of NO_2 and HCHO boundary layer profiles

The retrieval of trace gas profiles from DOAS measurements makes use of the vertical information contained in a set of slant column measurements. The latter is derived, e.g. as a function of detector altitude or of solar zenith angle. The vertical information content of these slant columns is described by the respective Box-AMFs (see Section 4.4.1). During descent measurements, the measured slant columns are a function of detector height (h), detector elevation angle (α), solar zenith angle (θ) and solar azimuth angle (φ). For each measured SCD(h, α, θ, φ) a set of Box-AMFs is derived by radiative transfer modeling, describing the sensitivity of the measurement to the atmospheric state, i.e. here, the trace gas profile. When combining the Box-AMFs of all

Figure 6.32: *CARIBIC camera picture taken upon landing in Guangzhou/China on flight LH158.*

descent measurements in a matrix **A**, in analogue to the Box-AMF matrix introduced in Section 6.2.4.2, then the SCDs measured during descent can be described as:

$$\overrightarrow{S} = \mathbf{A} \cdot \overrightarrow{V} \tag{6.9}$$

where $\overrightarrow{S}$ is a vector that contains all measured SCD values and $\overrightarrow{V}$ a vector containing the desired vertical column densities. From these, the concentration of each altitude layer c_i can be inferred by dividing V_i by the respective layer height h_i: $c_i = V_i/h_i$. The layer height is determined by the height grid utilized for the radiative transfer calculations. However, the height resolution that actually can be inferred from measurements is mainly determined by the observation geometry.

To infer the vertical column densities, the Box-AMF matrix needs to be inverted:

$$\overrightarrow{V} = \mathbf{A}^{-1} \cdot \overrightarrow{S} \tag{6.10}$$

This represents an inversion problem, which can be solved by the widely used *optimal estimation method* as described by *Rodgers* [2000]. Here, $\overrightarrow{S}$ can contain up to three measurements for one height (derived from three different viewing directions) or no entry at all for some heights, therefore **A** is not a square matrix and equation (6.10) cannot be solved by simple matrix inversion. Furthermore, the measurements do not contain sufficient information on *all* altitude layers of $\overrightarrow{V}$, so that an a priori profile is needed as additional input for the profile retrieval by optimal estimation technique.

Before this technique can be applied, the measured dSCDs need to be converted to total slant columns to derive $\overrightarrow{S}$, and secondly, for the calculation of accurate Box-AMFs the atmospheric conditions during the time of measurement must be reproduced properly. In a polluted boundary layer, the AMFs are mainly determined by multiple scattering and absorption caused by aerosols. Therefore, the local aerosol profile is determined by means of O_4 measurements. Both tasks are described in the following sections.

6.4.2.1 Deriving tropospheric SCDs from dSCDs

The conversion of dSCDs into SCDs usually requires the knowledge on the slant column contained in the Fraunhofer reference spectrum (S(ref)), which can be derived with the Langley plot method (see Section 4.3.2). This method, however, is only suitable for a trace gas profile being constant during the period of measurements. Yet the slant columns retrieved from measurements in the boundary layer are particularly caused by differences in the tropospheric trace gas column, compared to flying over remote regions before. This difference can be utilized to derive total tropospheric slant columns from dSCDs. Therefore, a FRS recorded over an area that exhibits presumably no tropospheric column of the desired trace gases, here of NO_2 and HCHO, is chosen. When the SZA of the FRS is small and does not differ much from the SZAs of the spectra recorded in the boundary layer, then the respective stratospheric AMFs can be assumed to be equal and the stratospheric columns $S(ref)_{strat}$ and S_{strat} cancel out. Accordingly, the measured dSCDs yield total tropospheric slant columns:

$$\begin{aligned} dS &= S - S(ref) \qquad (6.11)\\ &= (S_{trop} + S_{strat}) - (S(ref)_{trop} + S(ref)_{strat}) \\ &\equiv S_{trop} - S(ref)_{trop} \\ &\equiv S_{trop} - 0 = S_{trop} \end{aligned}$$

6.4.2.2 Aerosol profile retrieval using O_4 measurements

The retrieval of the local aerosol profile is more difficult as it implies an iterative model approach: Similar to the model studies performed for a large cloud in Section 6.2.3.1, total O_4 SCDs are modeled for different aerosol scenarios and compared with O_4 measurements. Again, the measured O_4 dSCDs need to be converted in SCDs first. For a discussion on the general underlying difficulties of this, refer also to Section 6.2.3.1. Incidently, these boundary layer studies are performed for spectra of the same flight exhibiting the HONO detection discussed in Section 6.2.1 (for selection criteria, see below). Since there, measured and modeled O_4 SCDs are compared as well, an identical

FRS for the nadir O_4 analysis of descent spectra was utilized, recorded at 03:40 UTC, over a cloud free sky and with a ground elevation of 3500 m. The respective column contained in the FRS is taken from Table 6.2 of Section 6.2.3.1. FRS recorded at the same time and the same model environment were then used to derive total O_4 columns of the other two viewing directions as well.

A prerequisite for a proper retrieval of the aerosol profile from O_4 measurements is that the O_4 AMFs are mainly determined by the aerosol profile itself. This holds only true for a cloud free atmosphere. Accordingly, a flight had to be chosen that fulfills this criterion, which was checked with camera data. As three viewing directions contain more vertical information as merely the nadir viewing direction, a second criterion was also to have suitable measurements from all three telescopes (see also Section 5.2.4). These considerations lead to choosing flight LH158 to Guangzhou, on August 1, 2006. Touch down was at 14:08 local time, with an SZA of 36°. The camera picture shown in Figure 6.32 is taken from this flight. When watching the camera movie of the complete descent of the aircraft, it can be seen that the aircraft is flying through one of those few scattered clouds seen at the horizon in Figure 6.32 directly upon entering the aerosol layer. So far, this was the most "cloud free" descent available of all measurement flights.

The model environment for the retrieval of the aerosol profile was adapted to local temperature and pressure, as measured by the aircraft. At mid day, the boundary layer can be assumed to be well mixed. Therefore an aerosol box profile with a constant extinction coefficient was used as a first guess for the O_4 model calculations. The height of this box profile was set to 1.8 km, which is the altitude at which the aircraft entered the aerosol layer seen in the camera picture. Also needed is information on the aerosol optical density, the single scattering albedo and on the asymmetry coefficient g. The latter was set to 0.68, which is a typical value for urban aerosol. The single scattering albedo at 360 nm was set to 0.75. This value is based on information provided by AERONET (AErosol RObotic NETwork, see *http://aeronet.gsfc.nasa.gov*), as well as on observations by *Bergstrom et al.* [2004].

According to AERONET, the local aerosol optical density can vary strongly from day to day. In Guangzhou, optical densities at 360 nm can reach values as high as 5, whereas average values are between 1 and 2. To get a rough first estimate on the aerosol optical density on that specific day - for which no AERONET data was available - the camera data was used again: Upon entering the aerosol layer seen in the photo, the visibility was strongly reduced. At an aircraft altitude of 1.6 km the ground was visible again. This corresponds to a visibility of 7.1 km, with a camera viewing angle of 13° down. When treating the camera like a human eye, then the extinction coefficient at 360 nm calculates to 0.84 km^{-1}, according to the equations introduced in Section 4.2.4. Accordingly, the total aerosol optical density for a box of 1.8 km height is 1.5. Hence, aerosol box profiles were modeled for optical densities of 1, 1.5 and 2. Additionally, an aerosol profile decreasing exponentially with altitude was included. The resulting modeled O_4 SCDs are presented in Figures 6.33 and 6.34, along with measured O_4 columns.

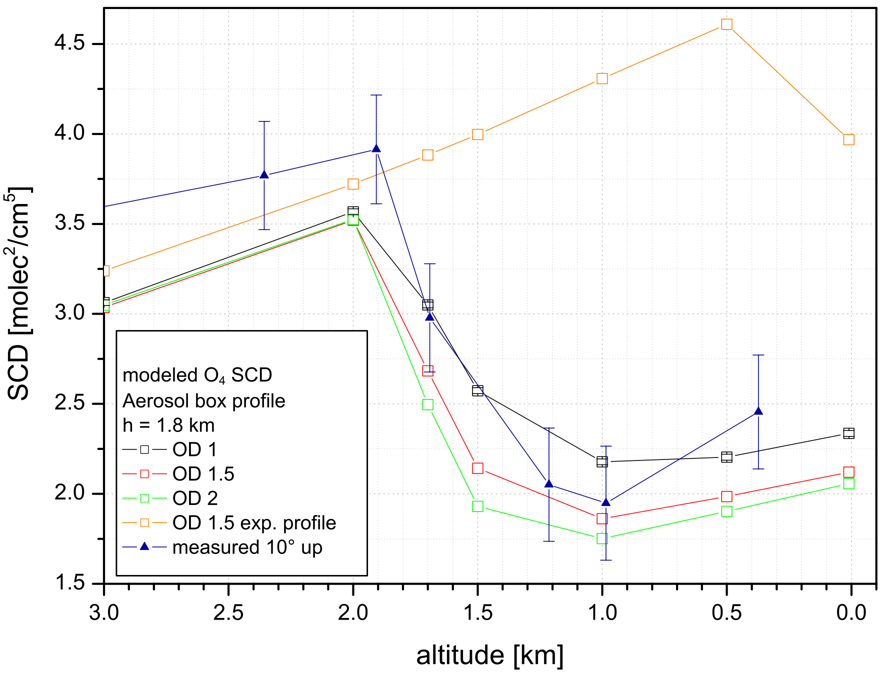

Figure 6.33: *Modeled O_4 SCDs for different aerosol profiles.*

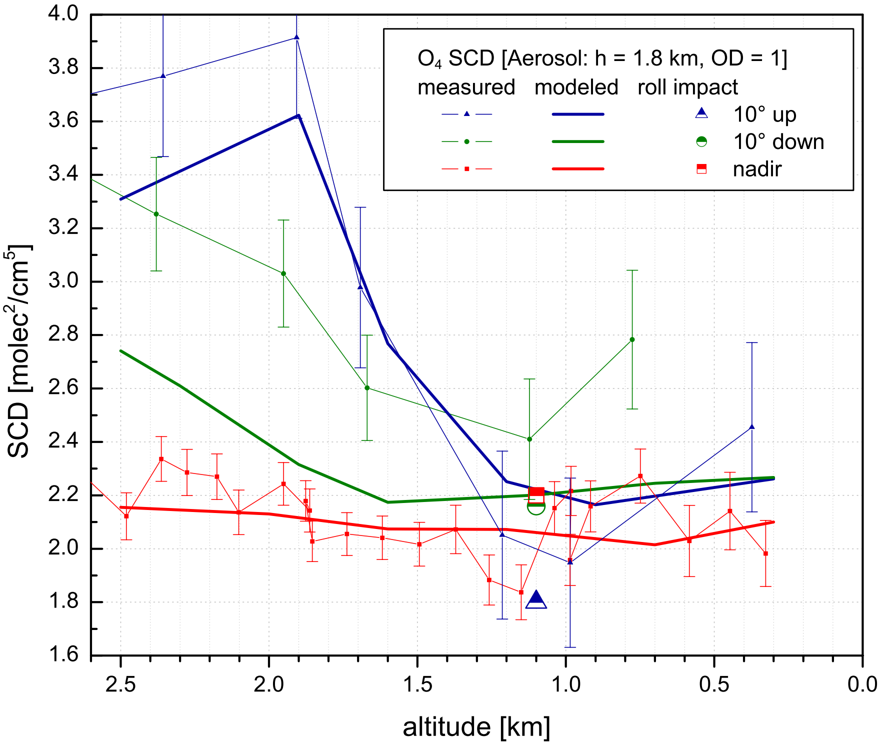

Figure 6.34: *Comparison of modeled and measured O_4 SCDs.*

In Figure 6.33, merely the O_4 column of the 10° up viewing direction is plotted as it exhibits the strongest sensitivity towards changes caused by aerosol in the boundary layer. In an aerosol free boundary layer, the total O_4 column would rise steadily during descent, similar to the NO_2 measurements of Figure 6.31 shown above. Here, the O_4 measurements clearly exhibit the effect of aerosol extinction, leading to shorter light paths compared to a pure Rayleigh atmosphere and to smaller measured slant columns accordingly. The impact of the aerosol extinction can be located in the measured columns between an altitude of 1.9 and 1.7 km. The comparison of modeled and measured O_4 columns shown in Figure 6.33 indicates that an aerosol box profile with a height of 1.8 km and an optical density between 1 and 1.5 is a reasonable estimate.

In Figure 6.34, all measured O_4 SCDs are plotted along with model results for a box profile with an optical density of 1. It is apparent that the agreement is quite good for the 10° up and for the nadir viewing direction, whereas the measured O_4 columns of the 10° down viewing direction are systematically too high compared to the modeled values. A possible explanation is that the column contained in the FRS has been retrieved improperly. Since the AMF of the 10° down viewing direction for the above introduced FRS is 1.56, compared to 0.58 and 0.92 for the 10° up and nadir viewing direction, respectively, the 10° down viewing direction is most sensitive for an error introduced by a faulty FRS column. Further error sources are the rather poor spectra quality of both the 10° up and down viewing directions, as well as the aircraft's turns during measurements, which lead to a change in the telescope elevation angles.

The roll angle of the aircraft, plotted in Figure 6.35, indicates two turns within the aerosol layer, one directly upon entering the layer, and the second turn at an altitude of about 1.2 km. The influence of the second turn was modeled with its maximum value of 14.7°, and the results are added to Figure 6.34. Note that the measurement period of two minutes of the 10° up and down viewing directions as well as the time resolution of 30 s of the nadir viewing directions leads to an averaging over the aircraft movements during measurements. These uncertainties need to be kept in mind and are again discussed below. For the subsequent profile inversion, an aerosol box profile with a height of 1.8 km and an optical density of 1 was used.

In Figure 6.35 also tropospheric SCDs of NO_2 and HCHO are presented, derived as explained above. The FRS for the NO_2 and HCHO analysis was recorded at 13:44 local time with an SZA of 30° at an altitude of 6.6 km, in a distance of about 100 km from Guangzhou. The SZA at touch-down was 36°, hence it can be assumed that the stratospheric columns of the descent spectra are canceled out by the respective column of the FRS. The HCHO analysis was only possible for nadir spectra, as it is retrieved at shorter wavelength than NO_2 and O_4, where the signal to noise ratio of the other viewing directions is too poor for a proper analysis. At an altitude of 2.5. km, the down looking telescopes start to "see" elevated NO_2 and HCHO levels. At 1.8 km, the nadir viewing direction shows a rise in both species, indicated by the red box on the right in Figure 6.35, which might be caused by a small cloud that has been intercepted at this point and which was the only cloud encountered during descent, judging by the camera

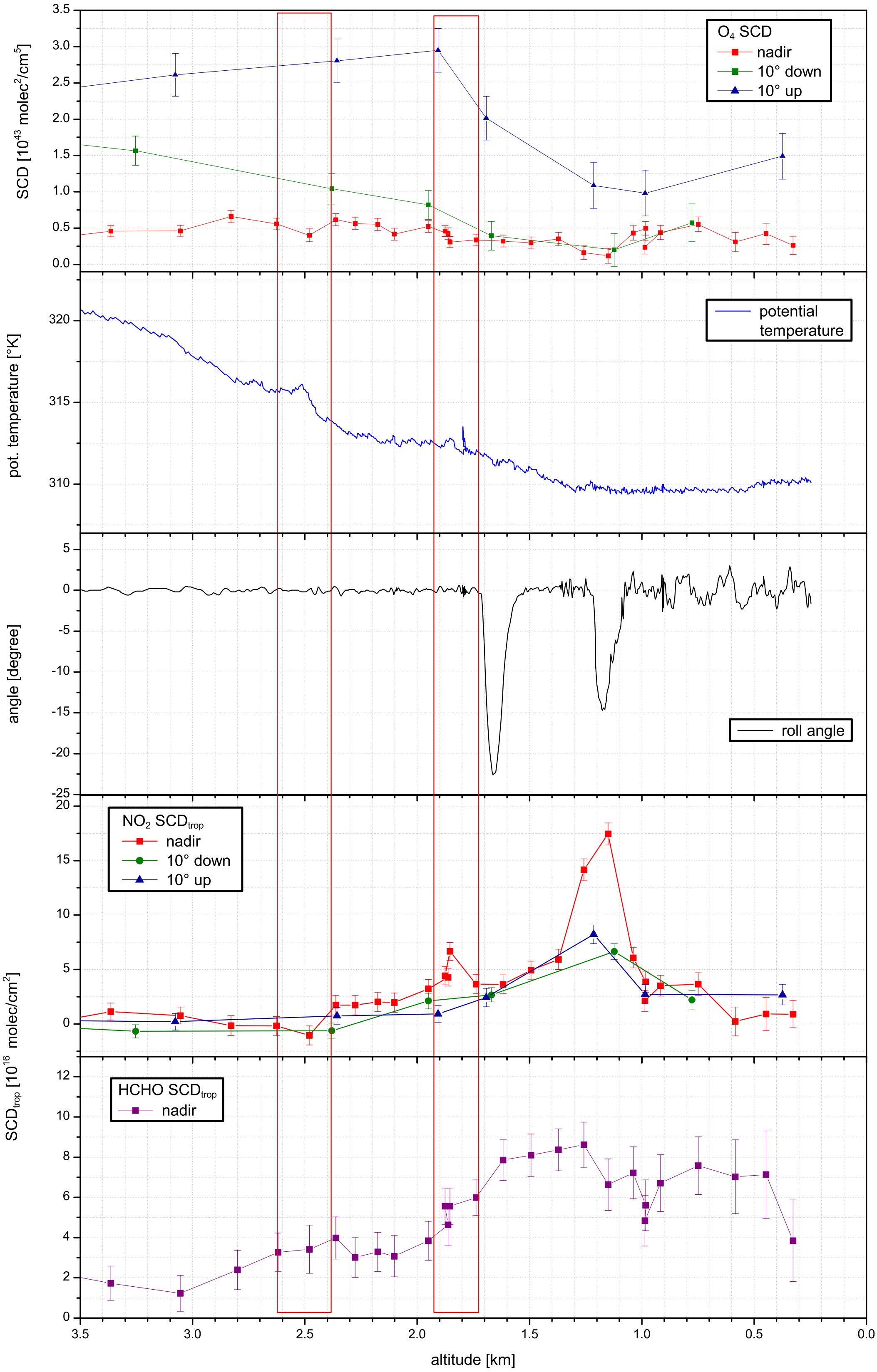

Figure 6.35: *NO_2, O_4 and Arinc data of descent measurements in Guangzhou on flight LH158.*

data. The first roll of the aircraft seems to have no apparent influence on the measured columns. However, the second roll coincides with a rise in NO_2 columns in all viewing directions, whereas an analogue rise cannot be observed in the HCHO columns. A change of 14° in the nadir viewing direction was modeled for a homogenous NO_2 layer with $VCD_{trop} = 2 \cdot 10^{16}$ molec/cm^2 and the above retrieved aerosol box profile. The retrieved change in the modeled tropospheric NO_2 column was smaller than the errors of the measurement. It is therefore very likely that the aircraft encountered a NO_x cloud. At this point in time the plane was already very close to the airport and was approaching with head wind (retrieved from Arinc data) - as planes usually do - and most probably followed the same route as previous aircrafts had taken only minutes before. Since modern aircrafts hardly emit any hydrocarbons, but definitely present a NO_x source, this peak in NO_2 columns can most likely be attributed to aircraft exhausts.

Figure 6.35 also provides a plot of potential temperature (see Section 2.1.2.3), derived from Arinc data[4]. The potential temperature usually increases with height. At an altitude of 2.5 km, marked by the red box on the left in Figure 6.35, the potential temperature exhibits a slight "bump", which could indicate the top of a local inversion layer. Turbulence in the boundary layer is usually convectively driven, which is why the vertical extent of the boundary layer increases during the course of a day. An inversion at the top restrains the domain of turbulence. Accordingly, clouds would be confined at the top of the inversion layer. When looking at the camera picture in Figure 6.32, it is apparent, that the few scattered clouds seen at the horizon, reach slightly further up than the aerosol layer at 1.8 km, perhaps to a height of 2.5 km. This, however, cannot be conceived from this Figure or further camera data. In view of this finding, boundary layer trace gas profiles are expected to reach above 1.8 km.

6.4.2.3 NO_2 and HCHO profile retrieval by inversion technique

For the profile retrieval, the *McArtim* radiative transfer and retrieval algorithm was used, which is the successor of Tracy-II, developed by the same authors (see Section 4.4.1). McArtim provides an integrated algorithm for the retrieval of profiles based on the above introduced optical estimation method. The program version used for the following profile retrievals is an in-house release, which is still in its testing phase. All configuration files utilized in Tracy-II can be adopted, thus allowing a consistency in the radiative transfer modeling.

Input files for the profile retrieval include the measured SCD_{trop} and an a priori profile. In both files an estimated error for each entry needs to be included. Additionally, the aerosol box profile defined above is used for the radiative transfer calculations to derive the Box-AMF matrix. The altitude resolution of the model grid is 0.5 km. A measure for the quality and information content of the profile retrieval is provided by the averaging kernel matrix, which is an important output of the optimal estimation

---

[4] The potential temperature θ is calculated by means of temperature T and pressure p derived from Arinc data.

method. The averaging kernel matrix is determined by the Box-AMF matrix and by the covariance matrix of the measured slant columns and a priori profile. The covariance matrix is defined as a diagonal matrix containing the squared errors of the measured slant columns and a priori profile respectively. Results of the inversion of NO_2 and HCHO measurements are presented in Figures 6.36 and 6.37.

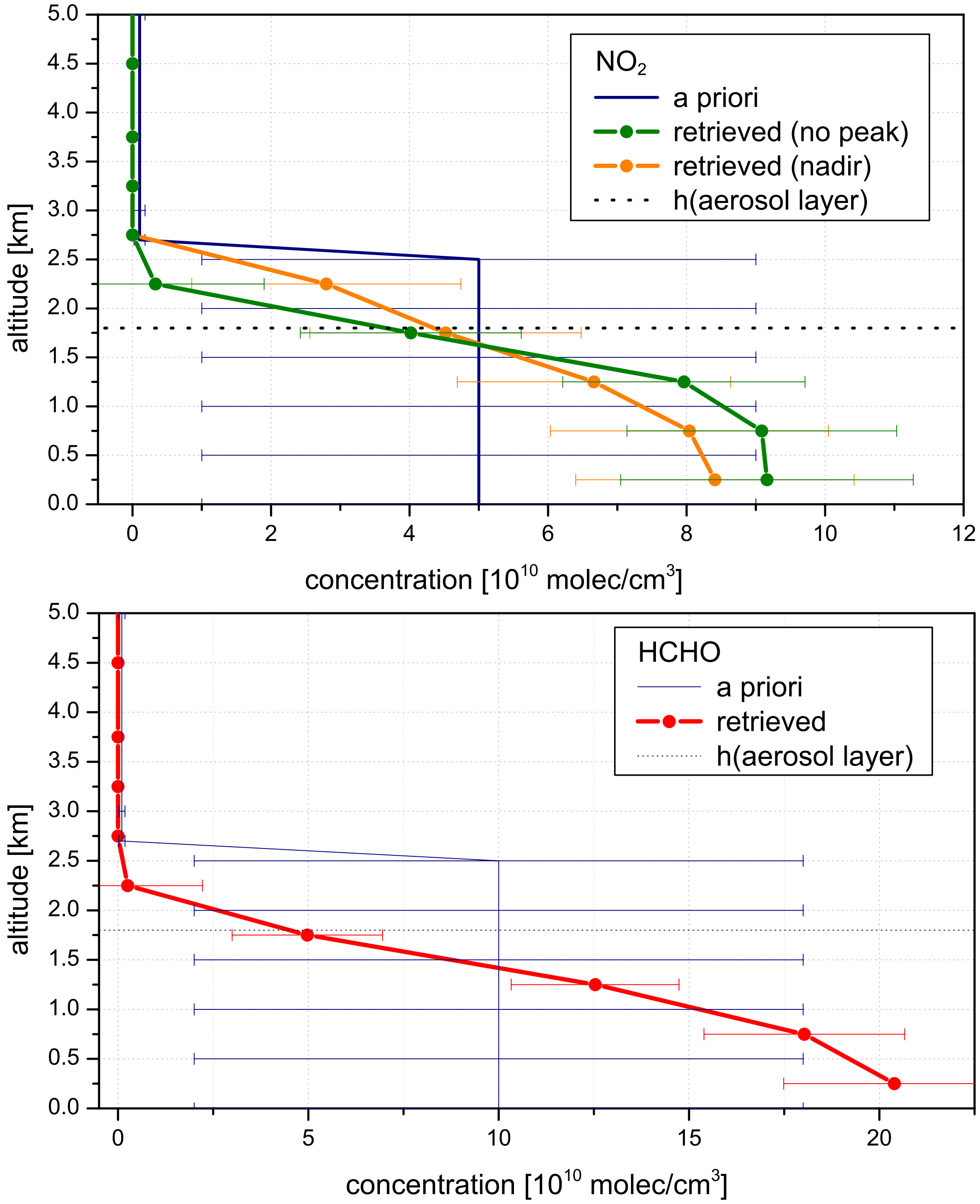

Figure 6.36: *Retrieved NO_2 and HCHO profiles. Also plotted are the a priori profiles and the height of the aerosol box profile.*

As expected, the boundary layer trace gas profiles exceed the above retrieved aerosol layer in height and reach values of around zero in the box between 2.5 and 3.0 km, which coincides with the height of the above assumed inversion layer at about 2.7 km. The NO_2 plot shows two profiles: green denotes the result utilizing the SCDs of all viewing directions and orange is a profile retrieved from nadir measurements only. In both profiles, the peak SCD values at an altitude of about 1.2 km discussed above, had to be omitted, because otherwise the retrieval failed. It is apparent that when utilizing merely measurements of the nadir viewing direction, the profile shape is less pronounced, caused by the reduction in altitude information. The fact that this profile exhibits a much higher NO_2 concentration in the altitude layer between 2.0 and 2.5 km might also be caused by the above discussed NO_x plume. Since the nadir viewing direction has a time resolution of 30 s, compared to 2 minutes of the other two viewing directions, the nadir telescope is more sensitive to local inhomogeneities in the concentration profile, which most likely introduces an error to the profile retrieval.

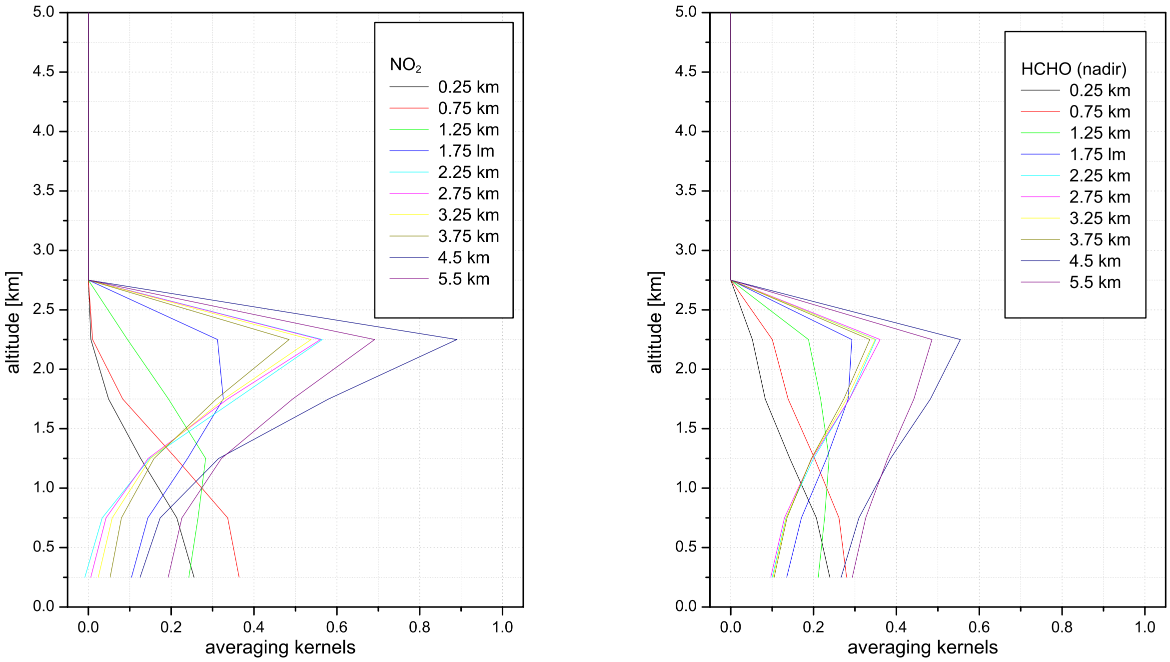

Figure 6.37: *Averaging kernels of the NO_2 and HCHO profile retrieval.*

In Figure 6.37, the averaging kernels for the profile retrieval are presented. The averaging kernels describe the height resolution that can be retrieved from the measurements. Not surprising, the NO_2 profile retrieval utilizing all viewing direction, yields overall a higher sensitivity. The trace of the averaging kernel matrix gives the number of independent points in the retrieved profile, which is 1.8 for the NO_2 profile 1.35 for the HCHO profile. It is thus apparent that the available set of viewing directions cannot further resolve the boundary layer.

To further explore the true information content of these measurements and also to further test the McArtim program, sensitivity studies need to be conducted to test the influence of the a priori profile on the retrieved results. Modeled profiles could be inverted to fully explore the limitations and capabilities of profile inversion with the specific CARIBIC DOAS viewing directions. Furthermore, sensitivity studies on the influence of the aerosol profile on the radiative transfer need to be conducted as well as on the impact of the turns of the aircraft. Perhaps also an inversion of the aerosol profile by means of O_4 measurements could be tested.

Overall, a stable profile retrieval utilizing merely the nadir viewing direction is quite a success. Retrieved mixing ratios for the lowermost kilometer are 4.1 ppb ± 0.9 ppb for NO_2 and 8.2 ppb ± 1.2 ppb for HCHO respectively. The vertical column of the complete boundary layer profiles are VCD(NO_2) $= 1.53 \cdot 10^{16}$ molec/cm^2 and VCD(HCHO) $= 2.8 \cdot 10^{16}$ molec/cm^2. The derived concentrations and vertical columns are in the order of what can be expected in a large city such as Gunagzhou. Tropospheric NO_2 columns retrieved by the OMI satellite instrument for the same day, show columns for Guangzhou in the order of 1.5 to $2 \cdot 10^{16}$ molec/cm^2 and a tropospheric NO_2 column of about $0.3 \cdot 10^{16}$ for the area where the FRS was recorded (see *www.temis.nl*). When adding this column, which is assumedly still contained in the FRS, then the total tropospheric NO_2 column of the DOAS measurements is derived as $1.83 \cdot 10^{16}$ molec/cm^2. Thus, these DOAS measurements exhibit a good agreement with satellite observations.

6.4.3 Information content of measurements during descent

The CARIBIC DOAS measurements apparently yield very reliable information on the boundary layer height and on the vertical trace gas columns within the boundary layer. The height resolution, however, is limited and is in the order of 0.5 to 1 km at best. Sensitivity studies need to be conducted to further constrain the specific sensitivity of the profile retrieval from CARIBIC DOAS slant columns. Apart from these sensitivity studies, the following aspects can affect the profile retrieval and need to be considered:

- The descent of the aircraft does not only provide a vertical resolution, but also a horizontal resolution. While descending the last 3 km before touch-down, the aircraft covered a distance of roughly 60 km. On this specific day, the flight route was downwind of the city, which most likely led to enhanced trace gas columns of NO_2 and HCHO also outside city limits. Thus the complete descent period leads to an averaging of the measurements over different tropospheric trace gas columns.

- The boundary layer within city limits exhibits most likely also inhomogeneous NO_2 concentrations. Measurements conducted with a mobile Mini-Max DOAS instrument by *Volkamer et al.* [2006] in Guangzhou one months before showed a high variability in local tropospheric NO_2 columns. Observed values, downtown and close to the airport, ranged from $2 \cdot 10^{16}$ to $4 \cdot 10^{16}$ molec/cm^2, with a maximum of $1.2 \cdot 10^{17}$molec/cm^2.

- The time assigned to each measured spectrum is the time when one half of the complete acquisition time is reached. The respective height values are attributed to these times. In reality, however, the aircraft descends mostly continuously, which in consequence leads also to an averaging over height during the recording of each spectrum.

6.5 Summary

The results derived in the previous sections can be summarized as follows and are further discussed in Chapter 7:

- A HONO mixing ratio of 69.5 ppt was observed in a deep convection cloud on flight LH158. Mixing ratios of HONO, HCHO, NO_2 and O_3 slant column measurements of flight LH158 were derived by means of O_4 measurements and radiative transfer calculations. A HONO mixing ratio of about 60 ppt was observed on flight LH127, presumably also inside a deep convection cloud. HONO slant columns could be measured on flight LH110 as well, and again very likely inside a deep convection cloud. HONO formation is believed to proceed by reaction of NO with OH, initiated by lightning activity, yielding NO_x and OH. The observed HONO concentrations of flights LH158 and LH127 seem to be in steady state with NO that was measured in-situ and OH, when assuming an OH concentration of $1 \cdot 10^7$ molec/cm^3. A contribution of biomass burning NO_x emissions to the HONO formation observed on flight LH127 is possible.

- An upper limit for tropospheric BrO in mid-latitudes and sub-tropics is derived for both the nadir and the 10° down viewing direction. Respective detection limits are about 6 ppt for the nadir viewing direction and 3 ppt for the 10° down viewing directions. Since recent observations suggest a tropospheric BrO background in the order of 1 - 2 ppt, the CARIBIC DOAS detection limit is not suitable to sufficiently constrain tropospheric BrO levels.

- BrO, NO_2 and ozone were measured in areas with tropopause fold activity, on flights LH123/124, LH127/128 and LH158. On flight LH158 vertical columns of about $1.8 \cdot 10^{13}$ molec/cm^2 for BrO and $1.5 \cdot 10^{15}$ molec/cm^2 for NO_2 were observed in the upper troposphere in an area characterized by higher PV values, most likely caused by a previously dissolved tropopause fold. Similar measurements in the future could give insight on the influence of tropopause folds on troposphere-stratosphere exchange processes.

- A total column comparison of NO_2 measurements on flight LH166/167 yields a VCD of $2.54 \cdot 10^{15}$ molec/cm^2 in the morning and a VCD of $2.82 \cdot 10^{15}$ molec/cm^2 in the evening. These values are in good agreement with the total columns measured by the OMI and Sciamachy satellite instruments. CARIBIC DOAS NO_2 measurements are also sensitive to tropospheric columns, observing enhanced values over the Red Basin Area in China, which is also in agreement with satellite observations.

- Boundary layer profiles of NO_2 and HCHO were retrieved for flight LH158 to Guangzhou/China on August 1, 2006. Derived mixing ratios for the lowermost kilometer are 4.1 ppb ± 0.9 ppb for NO_2 and 8.2 ppb ± 1.2 ppb for HCHO.

Chapter 7

Conclusions and Outlook

CARIBIC DOAS: potentials and limitations

This work's scope was to explore the information content of the CARIBIC data set and to give an overview of the scientific yield of these measurements. The outcome provides a great variety of scientific aspects, most of which are worth to be studied further. In the following, these aspects are summarized and recommendations for a continuous work with the CARIBIC DOAS data are given. The next section starts with technical considerations, followed by scientific considerations.

7.1 Technical considerations

Tn regard to instrument performance, the largest concern is the still unexplained low intensity yield of the 10° up and down viewing directions. Plenty tests and thorough discussions on this subject delimit this problem with a very high probability to loose parts inside the telescope units. Currently, there seems to be the possibility to exchange the telescope and the glass fibre cables in January 2008, which up to now has been no option. So far, the best odds are to built a new telescope block and use a different adhesive for the optical parts that is better suited for the extreme temperature changes the inlet system needs to endure daily. At least, upon opening the inlet system in January, the cause of the problem should finally become apparent and be resolved at some time.

The following aspects are worthwhile considering with respect to an optimized performance of the instrument:

- The mechanical coupling of the glass fibre cables and spectrographs demands a rather delicate handling as the stainless steel end pieces tend to get stuck when not properly inserted. To ensure a more precise mechanical reproduction of the glass fibre cable positions and thus of the mapping characteristics of the spectrographs, an improved coupling mechanism is advisable.
- A more efficient cooling capability would help to make better use of the spectra

recorded during ascent and descent of the aircraft. Furthermore, the instrument would be less affected by ambient temperature changes. An improvement might already be achieved by applying a better insulation to the spectrograph box. The overall stability of the Ocean Optics USB2000 spectrograph-detector units is mainly determined by a stable temperature. Accordingly, a more stable temperature would perhaps allow the analysis of several flights using the same FRS, which, for the same flight routes, could yield a climatology of trace gases. At present, spectra can only be analyzed with a FRS taken from the same flight in order to yield a suitable signal to noise ratio.

- In order to obtain a better detection limit, particularly for the measurement of weak absorbers in the troposphere, such as BrO or HONO, or for HCHO measurements in the stratosphere, spectrographs and detectors of higher quality are needed. However, assuming all viewing directions will function properly after January 2008, and in view of the still unexplored potentials of the current data set, exchanging the spectrograph-detector units is not a necessity.

- A definite improvement for the measurements of tropospheric absorbers would be to have a(n) (almost) pure stratospheric FRS available. The 10° up viewing direction could provide such a reference on the condition that spectra recorded from other viewing directions can be properly analyzed with this FRS. With the current instrumental setup this is not possible due to the different mapping characteristics of the spectrographs. To change this implies introducing moving parts to be able to map spectra of different viewing directions onto the same detector. At the same time, this would also improve the above discussed detection limit.

- A more general aspect of measurements on long-distance flights is the amount of available daylight, which, of course, is subject of flight plans and disposition by the respective airline. Accordingly, it is rather a scientific wish than a technical improvement to ask for daylight stretches across the equator and over tropical oceans, while the latter would be particularly interesting with respect to tropospheric BrO (see next section). It is, however, to be kept in mind, in case any influence on flight destinations can be exerted.

7.2 Scientific considerations

Below, ideas are developed to follow up the topics discussed in the results chapter.

- Probably the most interesting finding is the observation of HONO in deep convection clouds. Even though the overall picture seems quite plausible, the present data suffers from measured slant columns that are around or merely slightly above detection limit. This could be changed by utilizing a better spectrograph-detector system. However, possible further HONO measurements depend also on luck, since deep convection clouds are typically avoided during flights. To further pursue the specific questions raised in Section 6.2.3, a different measurement platform should be used that can be directly brought into deep convection clouds, e.g. balloons or research aircrafts.

- The measurements of biomass burning events provide a multitude on further studies, as has already been mentioned in the respective Section. Particularly the synergetic use of all CARIBIC data enables detailed studies on origin, age and chemistry of different air masses. Global biomass burning, which very often is of anthropogenic cause, affects tropospheric ozone concentrations and cloud structures. CARIBIC DOAS O_4 measurements could yield information on aerosols, which can be combined with measurements of aerosol number concentrations and optical properties, conducted by two other CARIBIC instruments. Furthermore, South America is a CARIBIC destination and chances of encountering biomass burning signals on future flights are rather high. Concluding, studies on biomass burning events are definitively worthwhile to be followed up.

- As shown in Section 6.2.4.2, CARIBIC DOAS measurements are not well suited for the observation of tropospheric BrO. Nevertheless, if a change in the instrumental setup leads to an improved detection limit, this topic could be followed up again.

- With respect to atmospheric dynamics, CARIBIC DOAS measurements yield definitively interesting possibilities, particularly when assuming, that all three viewing directions will function properly soon, which would imply a great increase in spatial resolution. On the route to South-East Asia, a highly dynamical tropopause often is encountered, exhibiting steep up and downward folds. As shown in Section 5.2.4, the 10° down viewing direction is quite sensitive towards changes in trace gas profiles caused by these effects, whereas the sensitivity of the nadir viewing direction was not sufficient to resolve such an event. Assuming all viewing directions are available, then estimates on the contribution of tropopause folds to the global troposphere-stratosphere exchange could be made. In addition, the seasonal dependency of convection over the Tibetan Plateau could be studied, which could also be done on a statistical basis.

- The separation of tropospheric and stratospheric columns to analyze e.g tropospheric NO_2 sources, is an interesting topic for the comparison with satellite data. A comparison could also be performed on retrieved aerosol optical densities from O_4 measurement. The CARIBIC DOAS measurements could provide a higher spatial resolution, however only one-dimensional along the flight track. The question of how much knowledge would be gained from this approach in view of constantly improving satellite instruments, remains to be answered.

- The retrieval of boundary layer profiles at its present state is just in its beginnings. Possible next steps have already been discussed in Section 6.4. The yield of ascent and descent measurement would greatly benefit from an improved instrumental setup and from the availability of all three viewing directions. While the first point could be addressed any time, the second issue is hopefully resolved soon, as indicated above.

7.3 Outlook

While the section above was specifically aimed in following up the topics presented in the results chapter, the following develops ideas on different systematic approaches to work with the CARIBIC (DOAS) data. A lot of these ideas are based on a more statistical approach, which requires a consistent data set of suitable quality. In order to achieve this the current instrumental setup should be more stable, to ensure a similar spectra quality of all flights. However, when existing limitations are considered, a lot of these ideas could also be followed up with the current data set.

- The synergetic use of all available data provides a huge potential for studies on various topics, e.g. on tropospheric pollutants or on troposphere-stratosphere exchange. Many topics of this work have benefited greatly form supplementary data. This approach is certainly worth to be continued in order to gain the full infirmation content of the CARIBIC DOAS measurements.
- The total CARIBIC project time is 10 years. Such a long time span provides the possibility to retrieve new information by means of statistical methods.
- Within the scope of this work e.g. the question of comparing DOAS with in-situ data was raised. A systematic discussion on this topic could yield potentials and limitations of the information gained by the respective method. Similar studies could be conducted on the following topics: effects of radiative transfer versus chemistry, stratospheric versus tropospheric measurements, vertical versus horizontal resolution

After all, perhaps the greatest potential of the CARIBIC DOAS measurements is that each flight offers the possibility of surprising new findings.

Appendix

A.1 CARIBIC instrumentation

Species	In-situ or Laboratory	Principle	Time Resolution	Institute
O_3	In-situ	UV absorption	8 s	IMK
		Chemiluminescence	0.2 s	
CO	In-situ	VUV fluorescence	2 s	MPI
Aerosol concentration	In-situ	CPC>4 nm	2 s	IFT
		CPC>12 nm	2 s	
		CPC>18 nm	2 s	
H_2O total	In-situ	Laser photoacoustic	10–90 s	IMK
H_2O gaseous	In-situ	Dew point	10–90 s	IMK
		Laser photoacoustic	10–90 s	
NO	In-situ	Chemiluminescence	10 s	DLR
NO_y	In-situ	Chemiluminescence with Au converter	10 s	DLR
CO_2	In-situ	NDIR	15 s	LSCE
O_2 with high resolution	In-situ	Electrochemical cells	15 s	University of Bern
OVOCs	In-situ	PTR-MS	20–60 s	IMK
Halogen oxides, NO_2, O_3	Remote	DOAS	30 s	University of Heidelberg
Hg	In-situ	Enrichment and atomic fluorescence	15 min	GKSS
Aerosol size distribution 150–5000 nm	In-situ	Optical particle counter	20 s	IFT
Clouds	In-situ	Video camera	0.5 s	IFT
Aerosol elemental analyses	Laboratory	Impactor, PIXE analyses	16 samples	University of Lund
Particle morphology	Laboratory	Impactor, electron microscope	16 samples	University of Lund
CO_2, CH_4, N_2O, SF_6	Laboratory	Glass canisters, GC-FID-ECD	28 samples	MPI
NMHCs	Laboratory	Glass canisters, GC-FID	28 samples	MPI
VOCs	Laboratory	Adsorption, GC-MS	16 samples	MPI
Halocarbons	Laboratory	Glass canisters, GC-MS	28 samples	University of East Anglia

DLR: Deutsches Zentrum für Luft- und Raumfahrt, Institut für Physik der Atmosphäre, Wessling, Germany

GKSS: GKSS-Research Centre, Institute for Coastal Research, Geesthacht, Germany

IFT: Leibniz-Institut für Troposphärenforschung, Leipzig, Germany

IMK: Institut für Meteorologie und Klimaforschung, Forschungszentrum Karlsruhe, Karlsruhe, Germany

LSCE: Laboratoire des Sciences du Climat et de l'Environnement, Gif sur Yvette Cedex, France

MPI: Max-Planck-Institut für Chemie, Mainz, Germany

A.2 Construction plans

The following Figures show construction plans of the spectrograph-detector box inside the container instrument and of the telescope unit.

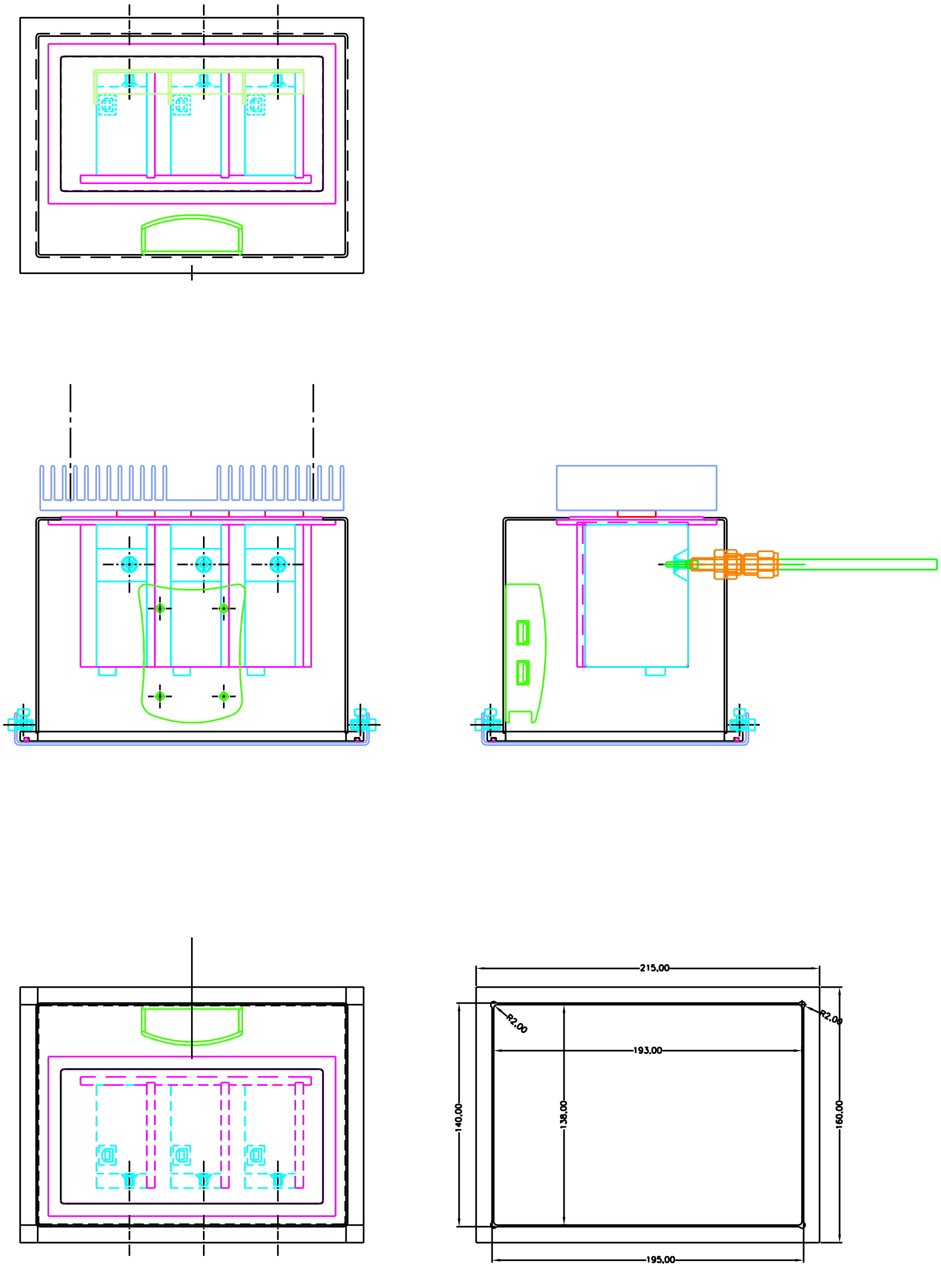
215,00
R2,00
R2,00
193,00
140,00
138,00
160,00
195,00

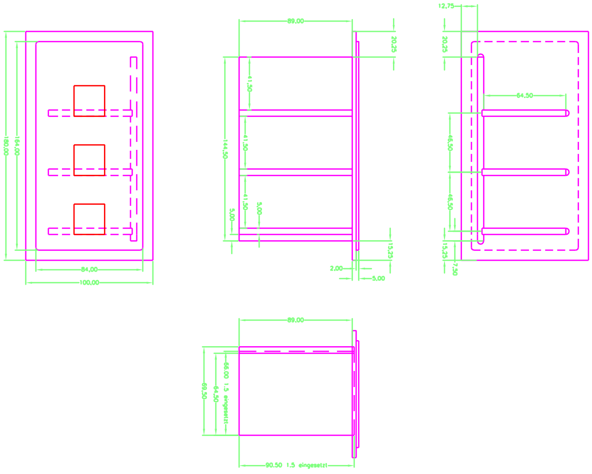
180,00
164,00
84,00
100,00
89,00
20,25
41,50
41,50
41,50
144,50
5,00
5,00
15,25
2,00
5,00
12,75
20,25
64,50
46,50
46,50
15,25
7,50
89,00
66,00 1.5 eingesetzt
64,50
69,50
90,50 1.5 eingesetzt

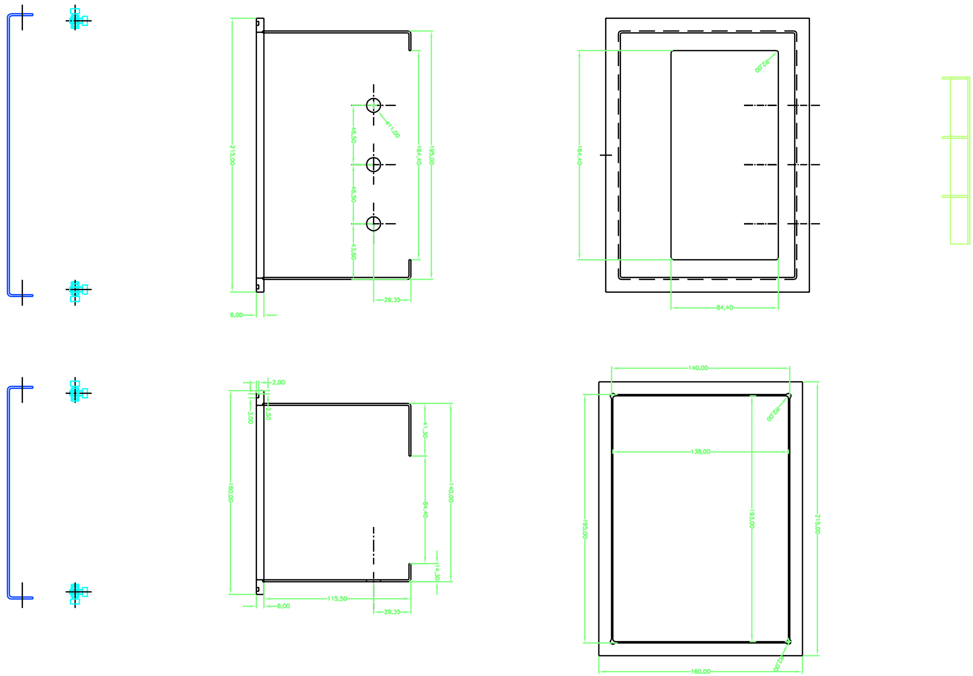
215,00
6,00
46,50
46,50
43,60
Ø11,00
164,40
195,00
29,35
R2,00
164,40
84,40
2,00
3,00
2,50
160,00
41,30
84,40
14,30
140,00
115,50
6,00
29,35
140,00
R2,00
138,00
195,00
193,00
215,00
160,00
R2,00

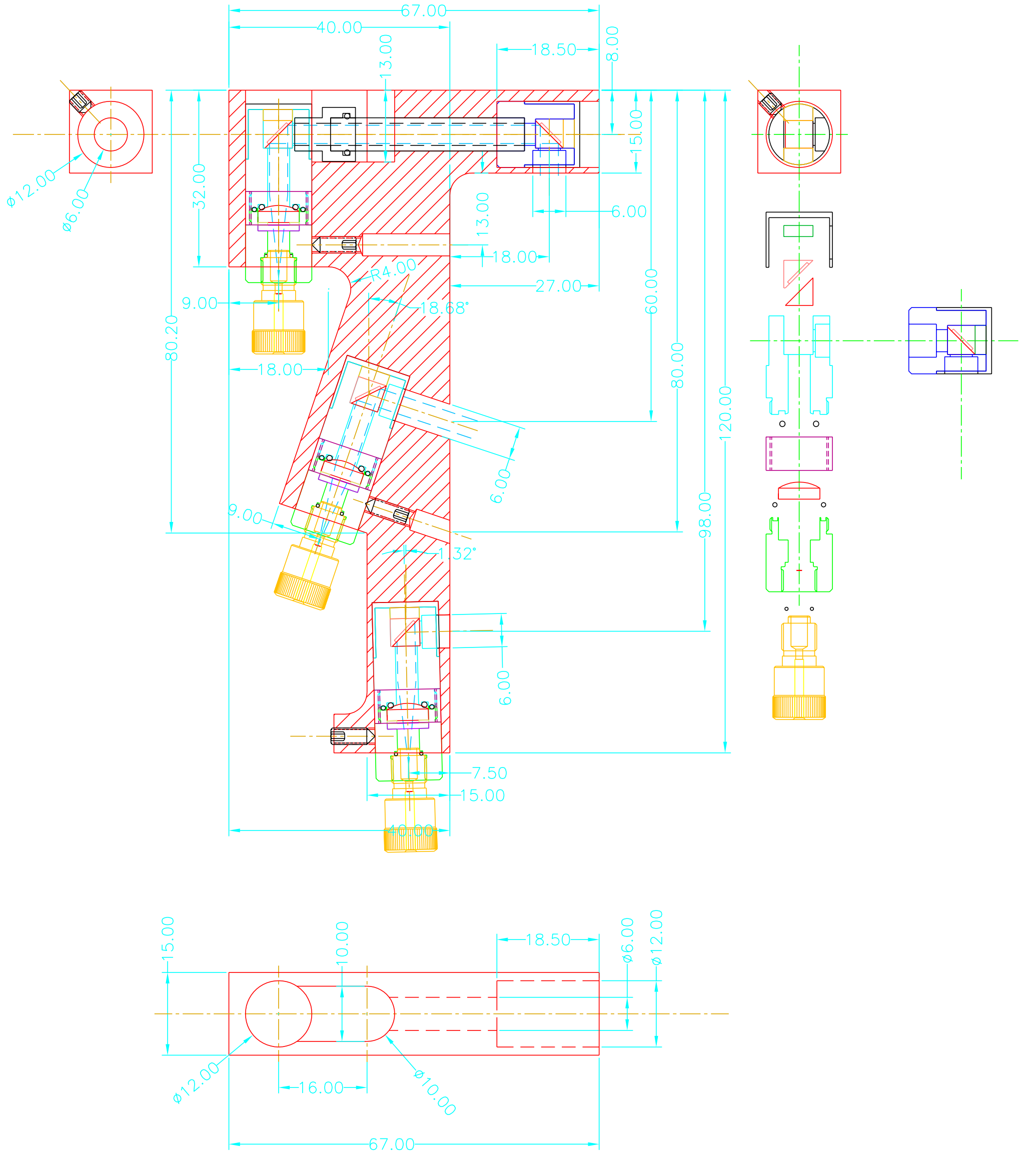

Name: Udo Frieß	Masstab: 1:1	Material: Aluminium
Datum: 07.11.02	Bezeichnung: CARIBIC Teleskop	
Änderung: 30.01.03 Fletterer		
Blatt: von:		

A.3 Flight overview

CARIBIC - DOAS overview

analysis

n.a.: not available

🟩 good anaysis

🟪 limited analysis

Flight-No.	Date of take-off	NO2/O4	BrO/O3/ HCHO/HONO	NO2/O4	BrO/O3/ HCHO/HONO	NO2/O4	BrO/O3/ HCHO/HONO
		nadir		**10°down**		**10°up**	
EZE 102	13.12.2004	🟪	🟪	🟪	🟪	🟪	🟪
103	14.12.2004	🟪	🟪	🟪	🟪	🟪	🟪
104	14.12.2004	🟪	🟪	🟪	🟪	🟪	🟪
105	14.12.2004	n.a.	n.a.	n.a.	n.a.	n.a.	n.a.
GRU 106	18.02.2005	n.a.	n.a.	n.a.	n.a.	n.a.	n.a.
107	19.02.2005	n.a.	n.a.	n.a.	n.a.	n.a.	n.a.
108	19.02.2005	n.a.	n.a.	n.a.	n.a.	n.a.	n.a.
109	19.02.2005	n.a.	n.a.	n.a.	n.a.	n.a.	n.a.
CAN 110	19.05.2005	n.a.	n.a.	🟪	🟪	n.a.	n.a.
111	20.05.2005	n.a.	n.a.	🟪	🟪	n.a.	n.a.
112	20.05.2005	🟦	🟦	🟦	🟦	🟦	🟦
113	20.05.2005	🟦	🟦	🟦	🟦	🟦	🟦
GRU 114	20.06.2005	🟦	🟦	🟦	🟦	🟦	🟦
115	21.06.2005	🟩	🟩	🟪	🟪	n.a.	n.a.
116	21.06.2005	🟩	🟩	🟪	🟪	n.a.	n.a.
117	21.06.2005	🟦	🟦	🟦	🟦	🟦	🟦
GRU 118	27.07.2005	🟦	🟦	🟦	🟦	🟦	🟦
119	28.07.2005	n.a.	n.a.	🟪	n.a.	n.a.	n.a.
120	28.07.2005	n.a.	n.a.	🟪	n.a.	n.a.	n.a.
121	28.07.2005	n.a.	n.a.	n.a.	n.a.	n.a.	n.a.
GRU 122	30.08.2005	🟦	🟦	🟦	🟦	🟦	🟦
123	31.08.2005	🟩	🟩	🟪	n.a.	n.a.	n.a.
124	31.08.2005	🟩	🟩	🟪	n.a.	n.a.	n.a.
125	31.08.2005	n.a.	n.a.	n.a.	n.a.	n.a.	n.a.
GRU 126	04.10.2005	🟦	🟦	🟦	🟦	🟦	🟦
127	05.10.2005	🟩	🟩	🟪	n.a.	🟪	n.a.
128	05.10.2005	🟩	🟩	🟪	n.a.	🟪	n.a.
129	05.10.2005	🟩	🟩	🟪	n.a.	🟪	n.a.
CAN 130	14.11.2005	🟩	🟩	n.a.	n.a.	n.a.	n.a.
131	15.11.2005	🟦	🟦	🟦	🟦	🟦	🟦
132	15.11.2005	🟦	🟦	🟦	🟦	🟦	🟦
133	15.11.2005	🟦	🟦	🟦	🟦	🟦	🟦
GRU 134	14.12.2005	n.a	n.a.	n.a.	n.a	n.a.	n.a.
135	15.12.2005	🟩	🟩	🟪	n.a.	🟪	n.a.
136	15.12.2005	🟩	🟩	n.a.	n.a.	🟪	n.a.
137	15.12.2005	n.a.	n.a.	n.a.	n.a.	n.a.	n.a.
GRU 138	20.02.2006	🟦	🟦	🟦	🟦	🟦	🟦
139	21.02.2006	🟩	🟩	🟪	n.a.	n.a.	n.a.
140	21.02.2006	🟩	🟩	🟪	n.a.	n.a.	n.a.
141	21.02.2006	🟩	🟩	🟪	n.a.	n.a.	n.a.
GRU 142	20.03.2006	🟦	🟦	🟦	🟦	🟦	🟦
143	21.03.2006	🟩	🟩	🟪	n.a.	n.a.	n.a.
144	21.03.2006	🟩	🟩	🟪	n.a.	n.a.	n.a.
145	21.03.2006	🟩	🟩	🟪	n.a.	n.a.	n.a.
CAN 146	27.04.2006	🟩	🟩	🟪	🟪	n.a.	n.a.

147	28.04.2006	🟩	🟩	🟪	🟪	n.a.	n.a.
148	28.04.2006	🟦	🟦	🟦	🟦	🟦	🟦
149	28.04.2006	🟦	🟦	🟦	🟦	🟦	🟦
CAN 150	29.05.2006	🟩	🟩	🟪	🟪	🟪	n.a.
151	30.05.2006	🟩	🟩	🟪	🟪	🟪	n.a.
152	30.05.2006	🟦	🟦	🟦	🟦	🟦	🟦
153	30.05.2006	🟦	🟦	🟦	🟦	🟦	🟦
CAN 154	05.07.2006	🟩	🟩	🟪	🟪	🟪	🟪
155	06.07.2006	🟩	🟩	🟪	🟪	🟪	🟪
156	06.07.2006	🟦	🟦	🟦	🟦	🟦	🟦
157	06.07.2006	🟦	🟦	🟦	🟦	🟦	🟦
CAN 158	31.07.2006	🟩	🟩	🟪	🟪	🟪	🟪
159	01.08.2006	🟩	🟩	🟪	🟪	🟪	🟪
160	01.08.2006	🟦	🟦	🟦	🟦	🟦	🟦
161	01.08.2006	🟦	🟦	🟦	🟦	🟦	🟦
CAN 162	07.09.2006	🟩	🟩	🟪	🟪	🟪	🟪
163	08.09.2006	🟩	🟩	🟪	🟪	🟪	🟪
164	08.09.2006	🟦	🟦	🟦	🟦	🟦	🟦
165	08.09.2006	🟦	🟦	🟦	🟦	🟦	🟦
CAN 166	19.10.2006	🟩	🟩	🟪	n.a.	n.a.	n.a.
167	20.10.2006	🟩	🟩	🟪	n.a.	n.a.	n.a.
168	20.10.2006	🟦	🟦	🟦	🟦	🟦	🟦
169	20.10.2006	🟦	🟦	🟦	🟦	🟦	🟦
CAN 170	14.11.2006	🟩	🟩	🟪	n.a.	n.a.	n.a.
171	15.11.2006	🟩	🟩	🟪	n.a.	n.a.	n.a.
172	15.11.2006	🟦	🟦	🟦	🟦	🟦	🟦
173	15.11.2006	🟦	🟦	🟦	🟦	🟦	🟦
CAN 174	13.12.2006	🟩	🟩	🟪	n.a.	n.a.	n.a.
175	14.12.2006	🟦	🟦	🟦	🟦	🟦	🟦
176	14.12.2006	🟦	🟦	🟦	🟦	🟦	🟦
177	14.12.2006	🟦	🟦	🟦	🟦	🟦	🟦
CAN 178	05.02.2007	🟩	🟪	🟪	n.a.	n.a.	n.a.
179	06.02.2007	🟩	🟪	🟪	n.a.	n.a.	n.a.
180	06.02.2007	🟦	🟦	🟦	🟦	🟦	🟦
181	06.02.2007	🟦	🟦	🟦	🟦	🟦	🟦
CAN 182	06.03.2007	🟩	🟪	🟪	n.a.	n.a.	n.a.
183	07.03.2007	🟩	🟪	🟪	n.a.	n.a.	n.a.
184	07.03.2007	🟦	🟦	🟦	🟦	🟦	🟦
185	07.03.2007	🟦	🟦	🟦	🟦	🟦	🟦
CAN 186	18.04.2007	n.a.	n.a.	🟪	n.a.	n.a.	n.a.
187	19.04.2007	n.a.	n.a.	🟪	n.a.	n.a.	n.a.
188	19.04.2007	🟦	🟦	🟦	🟦	🟦	🟦
189	19.04.2007	🟦	🟦	🟦	🟦	🟦	🟦
CAN 190	22.05.2007	🟪	n.a.	🟪	n.a.	n.a.	n.a.
191	23.05.2007	🟪	n.a.	🟪	n.a.	n.a.	n.a.
192	23.05.2007	🟦	🟦	🟦	🟦	🟦	🟦
193	23.05.2007	🟦	🟦	🟦	🟦	🟦	🟦
CAN 194	21.06.2007	🟩	🟪	🟪	n.a.	n.a.	n.a.
195	22.06.2007	🟩	🟪	🟪	n.a.	n.a.	n.a.
196	22.06.2007	🟦	🟦	🟦	🟦	🟦	🟦
197	22.06.2007	🟪	n.a.	n.a.	n.a.	🟦	🟦

A.4 Data

The following Figures provide "final product" data.

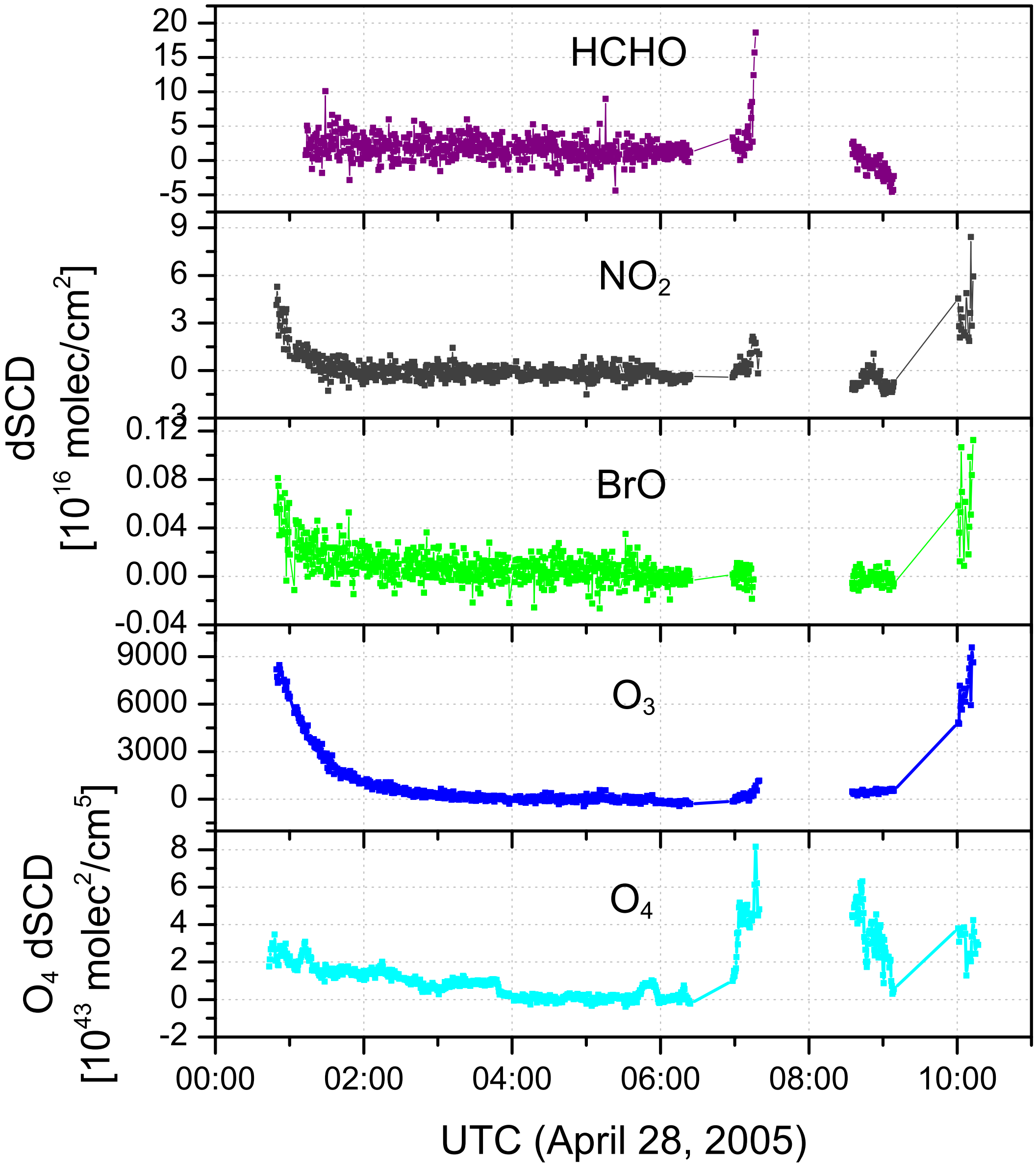

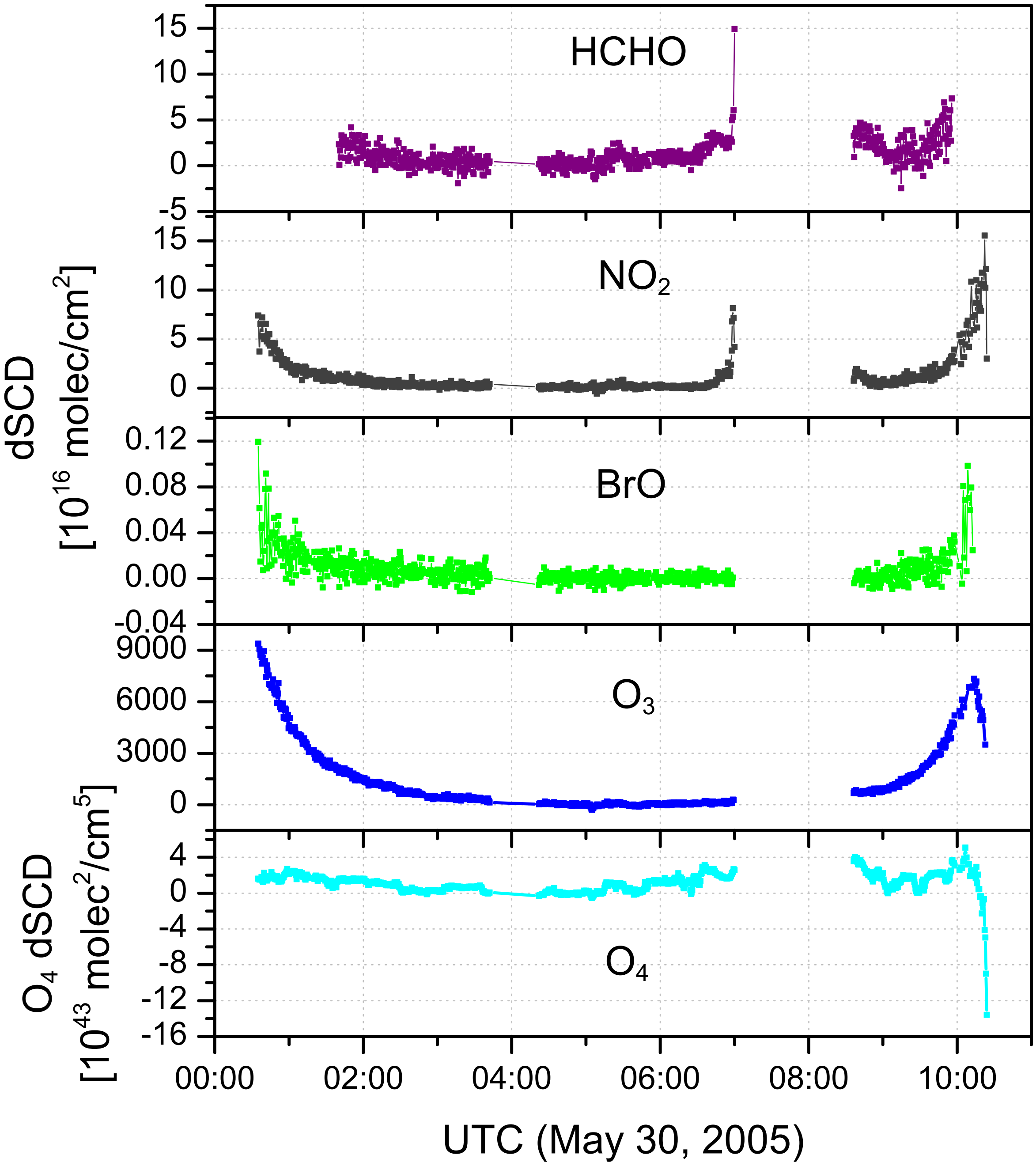
HCHO
NO$_2$
BrO
O$_3$
O$_4$
dSCD [10^{16} molec/cm^2]
O$_4$ dSCD [10^{43} molec^2/cm^5]
15
10
5
0
-5
0.12
0.08
0.04
0.00
-0.04
9000
6000
3000
4
-4
-8
-12
-16
00:00
02:00
04:00
06:00
08:00
10:00
UTC (May 30, 2005)

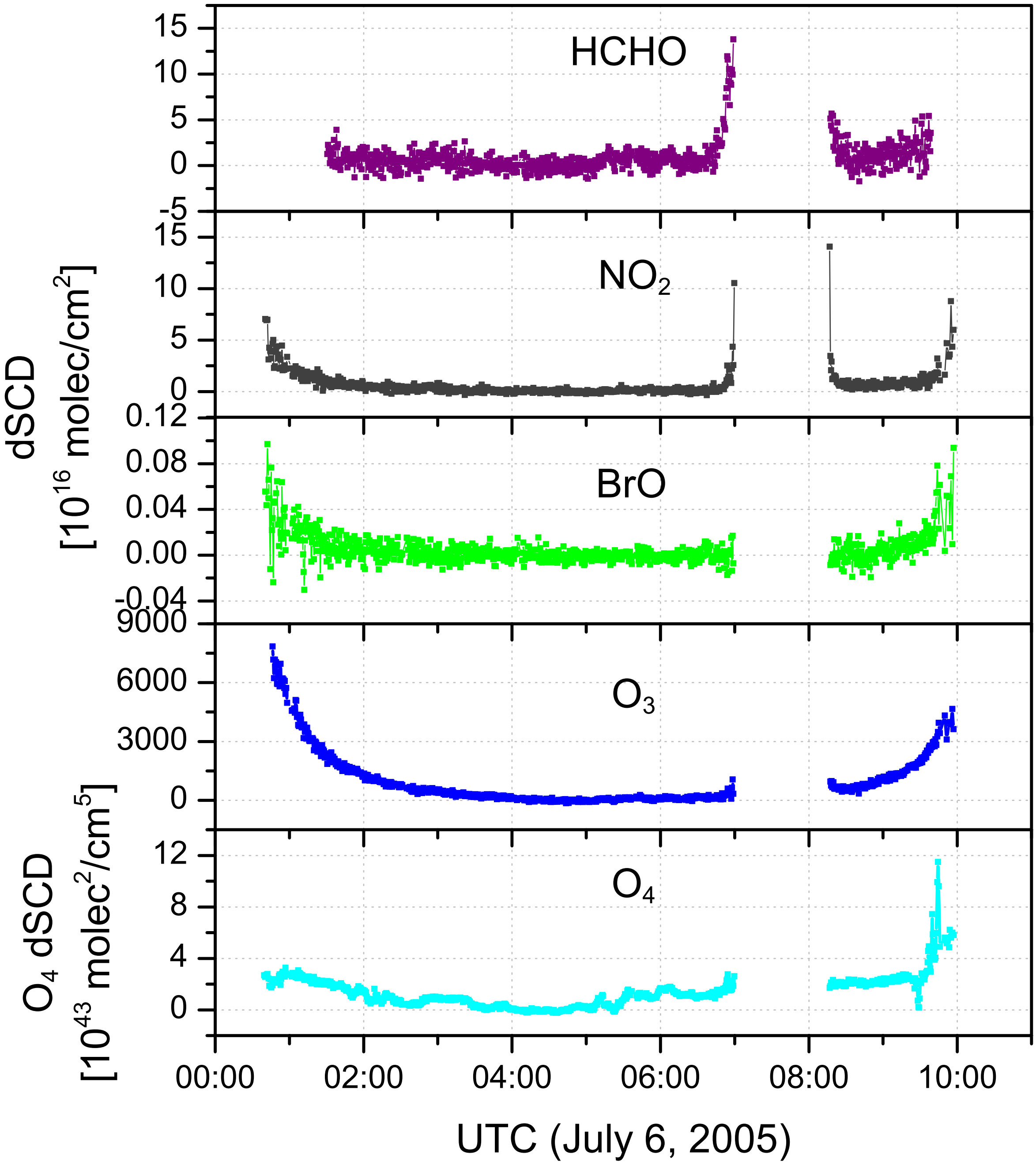
HCHO
NO$_2$
BrO
O$_3$
O$_4$
dSCD [10^{16} molec/cm^2]
O$_4$ dSCD [10^{43} molec^2/cm^5]
15
10
5
0
-5
15
10
5
0
0.12
0.08
0.04
0.00
-0.04
9000
6000
3000
0
12
8
4
0
00:00
02:00
04:00
06:00
08:00
10:00
UTC (July 6, 2005)

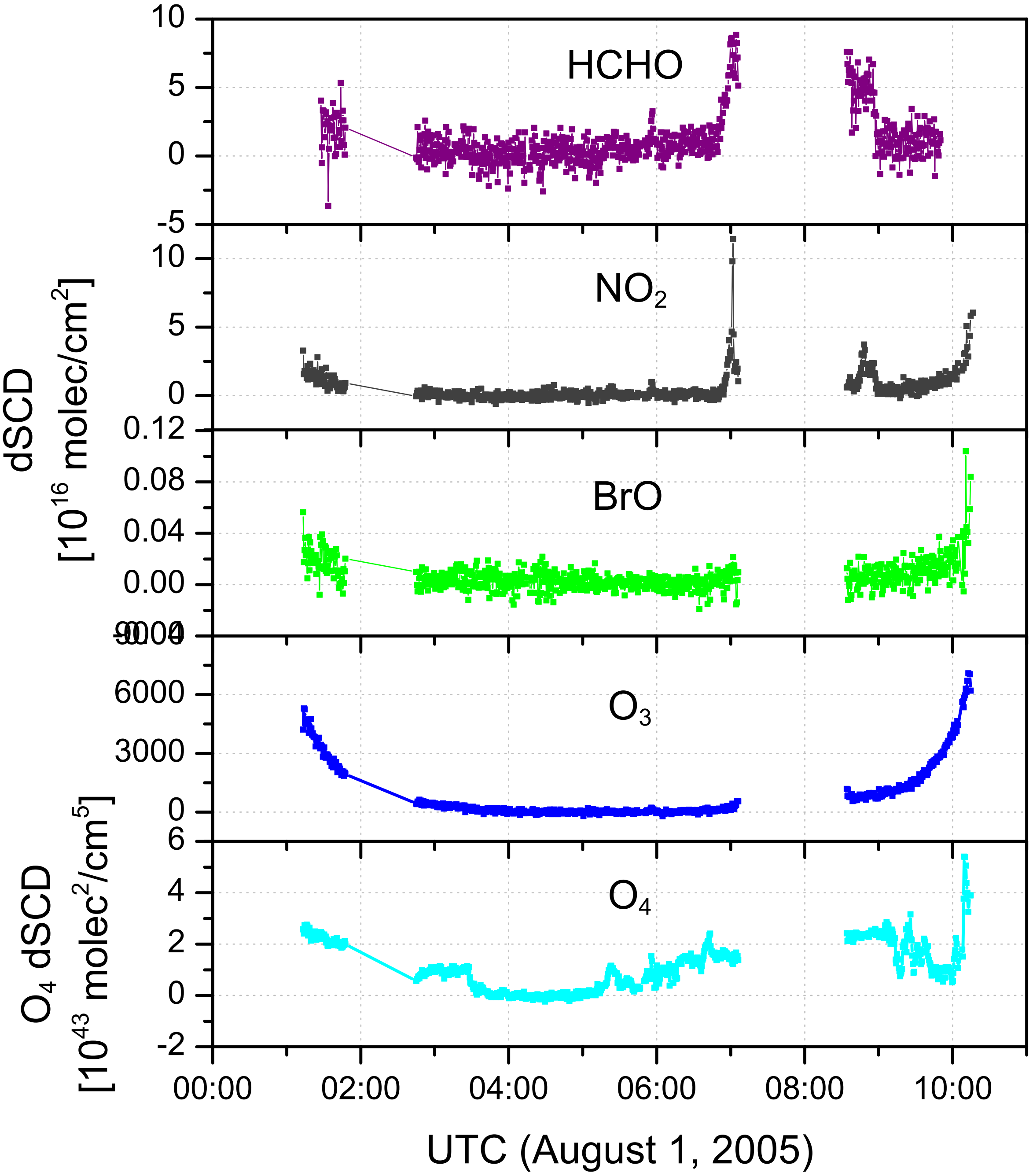
HCHO
NO$_2$
BrO
O$_3$
O$_4$
dSCD
[10^{16} molec/cm^2]
O$_4$ dSCD
[10^{43} molec^2/cm^5]
10
5
0
-5
10
5
0
0.12
0.08
0.04
0.00
-0.04
9000
6000
3000
0
6
4
2
0
-2
00:00
02:00
04:00
06:00
08:00
10:00
UTC (August 1, 2005)

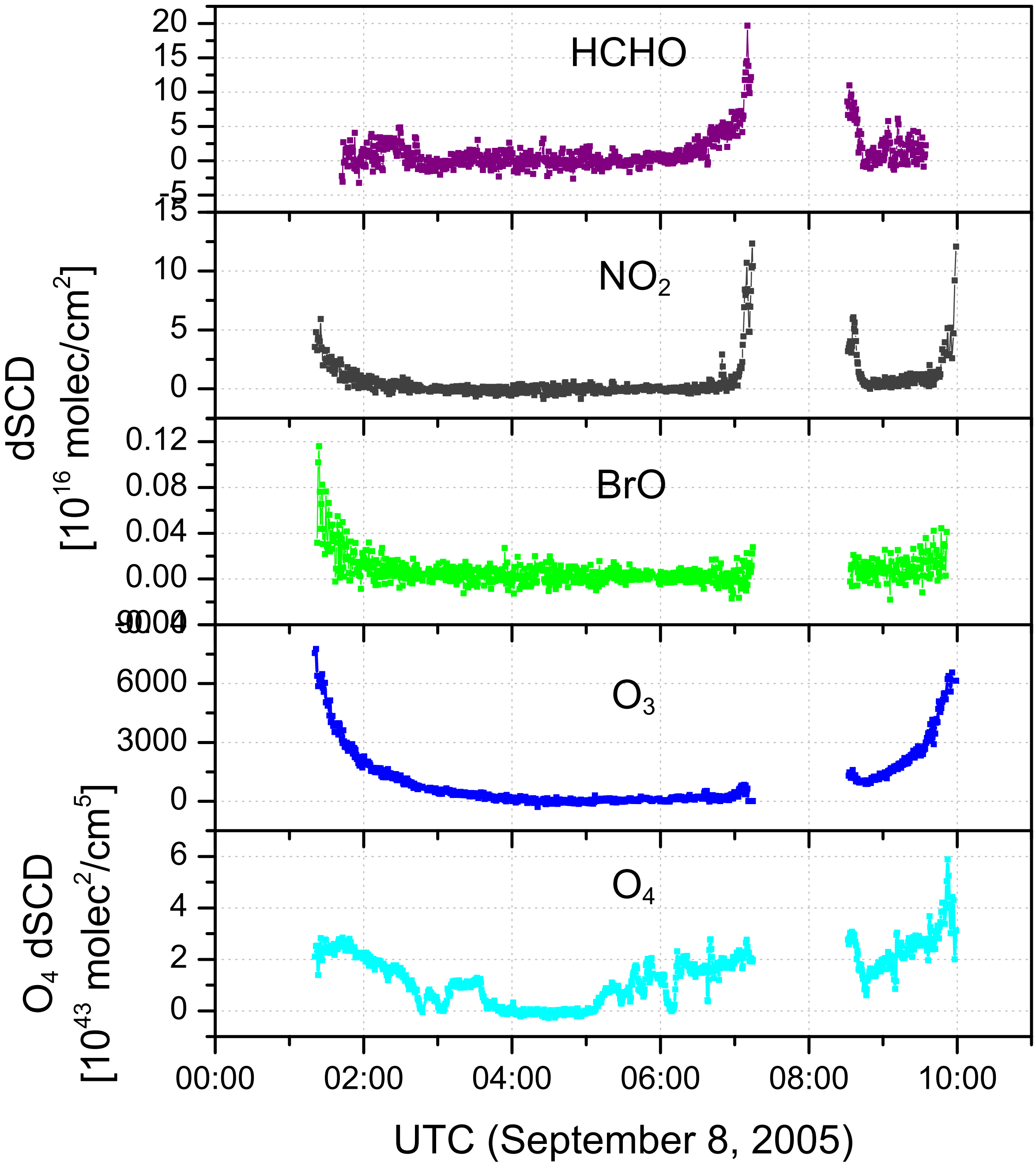
HCHO
NO$_2$
BrO
O$_3$
O$_4$
dSCD [10^{16} molec/cm^2]
O$_4$ dSCD [10^{43} molec^2/cm^5]
20
15
10
5
0
-5
15
10
5
0
0.12
0.08
0.04
0.00
-0.04
9000
6000
3000
0
6
4
2
0
00:00
02:00
04:00
06:00
08:00
10:00
UTC (September 8, 2005)

List of Figures

List of Tables

References

(2003). *Scientific Assessment of Ozone depletion.* WMO Global Ozone Research and Monitoring Project, Report 47.

Aben, I., D. M. Stam, and F. Helderman (2001). The Ring effect in skylight polarisation. *Geophys. Res. Lett.,* Vol. 28, 519–522.

Acker, K., D. Möller, W. Wieprecht, F. Meixner, B. Bohn, S. Gilge, C. Plass-Dülmer, and H. Berresheim (2006). Strong daytime production of OH from HNO_2 at a rural mountain site. *Geophys. Res. Lett.,* Vol. 33, L02809.

Albritton, D. L., A. L. Schmeltekopf, and R. N. Zare (1976). An Introduction to the Least-Squares Fitting of Spectroscopic Data. In R. K. Narahari and M. W. Weldon (Eds.), *Molecular Spectroscopy: Modern Research.* Orlando, Florida, USA: Academic Press.

Alicke, B., A. Geyer, A. Hofzumahaus, F. Holland, S. Konrad, H.-W. Pätz, J. Schäfer, J. Stutz, A. Volz-Thomas, and U. Platt (2003). OH formation by HONO photolysis during the BERLIOZ experiment. *J. Geophys. Res.,* Vol. 108 (D4), 8247.

Alicke, B., K. Hebestreit, J. Stutz, and U. Platt (1999). Iodine oxide in the marine boundary layer. *Nature,* Vol. 397, 572–573.

Aliwell, S., M. V. Roozendael, P. Johnston, A. Richter, T.Wagner, D. Arlander, J. Burrows, D. Fish, R. Jones, K. Tornkvist, J.-C. Lambert, K. Pfeisticker, and I. Pundt (2002). Analysis for BrO in zenith-sky spectra: An intercomparison exercise for analysis improvement. *J. Geophys. Res.,* Vol. 107 (D14).

Ammann, M., M. Kalberer, D. T. Jost, L. Tobler, E. Rössler, D. Piguet, H. W. Gäggeler, and U. Baltensperger (1998). Heterogeneous production of nitrous acid on soot in polluted air masses. *Nature,* Vol. 395, 157 – 160.

Barrie, L., J. Bottenheim, R. Schnell, P. Crutzen, and R. Rasmussen (1988). Ozone destruction and photochemical reactions at polar sunrise in the lower Arctic atmosphere. *Nature,* Vol. 334, 138–141.

Bates, D. R. and M. Nicolet (1950). Atmospheric hydrogen. *Publ. Astron. Soc. Pac.,* Vol. 62, 106–110.

Beirle, S. (2004). *Estimation source strengths and lifetime of Nitrogen Oxides from satellite data.* Dissertation, Institute of Environmetal Physics, University of Heidelberg, Germany.

Bergstrom, R. W., P. Pilewskie, J. Pommier, R. M, P. B.Russell, B. Schmid, J. Redemann, A. Higurashi, T. Nakajima, and P. Quinn (2004). Spectral absorption of solar radiation by aerosols during ACE-Asia. *J. Geophys. Res.,* Vol. 109.

Bertram, T. H., A. E. Perring, P. J. Wooldridge, J. D. Crounse, A. J. Kwan, P. O. Wennberg, E. Scheuer, J. Dibba, M. Avery, G. Sachse, S. A. Vay, J. H. Crawford, C. S. McNaughton, A. Clarke, K. E. Pickering, H. Fuelberg, G. Huey, D. R. Blake, H. B. Singh, S. R. Hall, R. E. Shetter, A. Fried, B. G. Heikes, and R. C. Cohen. (2007). Direct Measurements of the Convective Recycling of the Upper Troposphere. *Science,* Vol. 315, 816 – 820.

Bevington, P. (1969). *Data Reduction and Error Analysis for the Physical Sciences.* New York: McGraw-Hill.

Bhetanabhotla, M., B. Crowell, A. Coucouvinos, R. Hill, and R. Rinker (1985). Simulation of trace species production by lightning and corona discharge in moist air. *Atmos. Environ.,* Vol. 19, 1391 – 1397.

Bobrowski, N. (2005). *Volcanic Gas Studies by Multi Axis Differential Optical Absorption Spectroscopy.* Dissertation, Institute of Environmental Physics, University of Heidelberg, Germany.

Bobrowski, N., G. Hönninger, B. Galle, and U. Platt (2003). Detection of bromine monoxide in a volcanic plume. *Nature,* Vol. 423, No. 6937, 273–276.

Bogumil, K., e. a. (2003). Measurements of molecular absorption spectra with the SCIAMACHY pre-flight model: Instrument characterization and reference data for atmospheric remote-sensing in the 230 2380 nm region. *J. Photochem. Photobiol. A: Chem.,* Vol. 157, 167 – 184.

Brasseur, G. and S. Solomon (1986). *Aeronomy of the middle atmosphere.* Dordrecht, Boston, Lancaster, Tokyo: D. Reidel Publ.

Brenninkmeijer, C. A. M., P. Crutzen, F. B. T. Dauer, B. Dix, R. Ebinghaus, D. Filippi, H. Fischer, H. Franke, U. Frieß, J. Heintzenberg, F. Helleis, M. Hermann, H. H. Kock, C. Koeppel, J. Lelieveld, M. Leuenberger, B. G. Martinsson, S. Miemczyk, H. P. Moret, H. N. Nguyen, P. Nyfeler, D. Oram, D. O'Sullivan, S. Penkett, U. Platt, M. Pupek, M. Ramonet, B. Randa, M. Reichelt, T. S. Rhee, J. Rohwer, K. Rosenfeld, D. Scharffe, H. Schlager, U. Schumann, F. Slemr, D. Sprung, P. Stock, R. Thaler, F. Valentino, P. van Velthoven, A. Waibel, A. Wandel, K. Waschitschek, A. Wiedensohler, I. Xueref-Remy, A. Zahn, U. Zech, and H. Ziereis (2007). Civil aircraft for the regular investigation of the atmosphere based on an instrumented container: the new CARIBIC system. *Atm. Chem. and Phys.,* Vol. 7, 4953–4976.

Brenninkmeijer, C. A. M., P. J. Crutzen, H. Fische, H. Güsten, W. Hans, G. Heinrich, J. Heintzenberg, M. Hermann, T. Immelmann, D. Kersting, M. Maiss, M. Nolle, A. Pitscheider, H. Pohlkamp, D. Scharffe, K. Specht, and A. Wiedensohler (1999). CARIBIC: civil aircraft for global measurement of trace gases and aerosols in the tropopause region. *J. Atmos. Ocean. Tech.,* Vol. 16, 1373 – 1383.

Brinkmann, R. T. (1968). Rotational Raman scattering in planetary atmospheres. *Astrophys. J.,* Vol. 154, 1087–1093.

Bussemer, M. (1993). *Der Ring-Effekt: Ursachen und Einflußauf die spektroskopische Messung stratosphärischer Spurenstoffe.* Diploma thesis, Institut für Umweltphysik, Universität Heidelberg.

Chance, K., P. I. Palmer, R. J. D. Spurr, R. V. Martin, T. P. Kurosu, and D. J. Jacob (2000). Satellite observations of formaldehyde over North America from GOME. *Geophys. Res. Lett.,* Vol. 27 (21), 3461–3464.

Chance, K. and R. J. D. Spurr (1997). Ring effect studies; Rayleigh scattering, including molecular parameters for rotational Raman scattering and the Fraunhofer spectrum. *Appl. Opt.,* Vol. 36, 5224–5230.

Chapman, S. (1930). On ozone and atomic oxygen in the upper atmosphere. *Philos. Mag.,* Vol. 10, 369–383.

Crutzen, P. J. (1970). The influence of nitrogen oxide on the atmospheric ozone content. *Q.J.R. Meteorol. Soc.,* Vol. 96, 320–327.

Deutschmann, T. and T. Wagner (2006). TRACY-II Users manual. University of Heidelberg.

Diebel, D., J. Burrows, R. de Beek, R. Munro, B. Kerridge, L. Marquard, U. Platt, and H. Frank (1995). Detailed analysis of the retrieval algorithms selected for the level 1-2 processing of GOME data (Tracegas study). Technical report, ESA contract 10728/94/NL/CM, prepared by SERCO Europe Ltd., Southall, U.K.

Dobson, G. M. B. and D. N. Harrison (1926). Measurements of the amount of ozone in the Earth's Atmosphere and its Relation to other Geophysical Conditions. *Proc. R. Soc. London,* Vol. 110, 660–693.

Dorf, M. (2005). *Investigation of Inorganic Stratospheric Bromine using Balloon-Borne DOAS Measurements and Model Simulations.* Ph.D. thesis, Combined Faculties for the Natural Sciences and for Mathematics, Universität Heidelberg.

Eskes, H. J. and K. F. Boersma (2003). Averaging kernels for DOAS total-column satellite retrievals. *Atm. Chem. and Phys.,* Vol. 3, 1285 – 1291.

Etzkorn, T. (1998). *Untersuchungen atmosphärisch relevanter Reaktionssysteme mittels Differentieller Optischer Absorptionsspektroskopie.* Ph.D. thesis, Institut für Umweltphysik, Universität Heidelberg.

Farman, J. C., B. G. Gardiner, and J. D. Shanklin (1985). Large losses of total ozone in Antarctica reveal seasonal ClO_x/NO_x interaction. *Nature,* Vol. 315, 207–210.

Fayt, C. and M. Van Roozendael (2001). WinDOAS. ISAB/BIRA Belgium, http://www.oma.be/BIRA-IASB.

Finlayson-Pitts, B. and J. N. Pitts, Jr. (2000). *Chemistry of the Upper and Lower Atmosphere* (First ed.). San Diego: Academic Press.

Fishman, J. and P. Crutzen (1978). The origin of ozone in the troposphere. *Nature,* Vol. 274, 855–858.

Fitzenberger, R., H. Bösch, C. Camy-Peyret, M. Chipperfield, H. Harder, U. Platt, B.-M. Sinnhuber, T. Wagner, and K. Pfeilsticker (2000). First profile measurement of tropospheric BrO. *Geophys. Res. Lett.,* Vol. 27, 2921–2924.

Frankenberg, C., U. Platt, and T. Wagner (2005). Iterative maximum a posteriori (IMAP)-DOAS for retrieval of strongly absorbing trace gases: Model studies for CH_4 and CO_2 retrieval from near infrared spectra of SCIAMACHY onboard ENVISAT. *Atm. Chem. and Phys.,* Vol. 5, 9–22.

Frieß, U. (2001). *Spectroscopic Measurements of Atmospheric Trace Gases at Neumayer-Station, Antarctica.* Ph.D.thesis, Institut für Umweltphysik, Universität Heidelberg.

Frieß, U., J. Hollwedel, G. König-Langlo, T. Wagner, and U. Platt (2004). Dynamics and chemistry of tropospheric bromine explosion events in the Antarctic coastal region. *J. Geophys. Res.,* Vol. 109, D06305, doi: 10.1029/2003JD004133.

Frieß, U., P. S. Monks, J. J. Remedios, A. Rozanov, R. Sinreich, T. Wagner, and U. Platt (2006). MAX-DOAS O_4 measurements: A new technique to derive information on atmospheric aerosols: 2. Modeling studies. *J. Geophys. Res.,* Vol. 111, D14203, doi:10.1029/2005JD006618.

Geyer, A., K. Bächmann, A. Hofzumahaus, F. Holland, S. Konrad, T. Klüpfel, H. Pätz, D. Perner, D. Mihelcic, H. Schäfer, A. Volz-Thomas, and U. Platt (2003). Nighttime formation of peroxy and hydroxyl radicals during BERLIOZ – Observations and modeling studies. *J. Geophys. Res.,* Vol. 108 (D4), 8249.

Gomer, T., T. Brauers, F. Heintz, J. Stutz, and U. Platt (1993). *MFC User Manual, Vers. 1.98.* Institut für Umweltphysik, Universität Heidelberg.

Grainger, J. and J. Ring (1962). Anomalous Fraunhofer line profiles. *Nature,* Vol. 193, 762.

Greenblatt, G. D., J. J. Orlando, J. B. Burkholder, and A. R. Ravishankara (1990). Absorption Measurements of Oxygen between 330 and 1140 nm. *J. Geophys. Res.,* Vol. 95, 18577–18582.

Hak, C. (2006). *Variability of formaldehyde in the polluted planetary boundary layer - measurements in the Milano metropolitan area, Italy (Po basin).* Ph. D. thesis, Institute of Environmetal Physics, University of Heidelberg, Germany.

Haug, H. (1996). *Raman-Streuung von Sonnenlicht in der Erdatmosphäre.* Master's thesis, Institut für Umweltphysik, Ruprecht-Karls-Universität Heidelberg.

Hausmann, M., U. Brandenburger, T. Brauers, and H.-P. Dorn (1997). Detection of tropospheric OH radicals by long-path differential-optical-absorption spectroscopy: Experimental setup, accuracy, and precision. *J. Geophys. Res.,* Vol. 102, 16011–16022.

Hausmann, M., U. Brandenburger, T. Brauers, and H.-P. Dorn (1999). Simple Monte Carlo methods to estimate the spectra evaluation error in differential-optical-absorption spectroscopy. *Appl. Opt.,* Vol. 38, No. 3, 462–475.

Hausmann, M. and U. Platt (1994). Spectroscopic measurement of bromine oxide and ozone in the high Arctic during Polar Sunrise Experiment 1992. *J. Geophys. Res.,* Vol. 99 (D12), 25399–25413, 10.1029/94JD01314.

Hebestreit, K., J. Stutz, D. Rosen, V. Matveev, M. Peleg, M. Luria, and U. Platt (1999). DOAS measurements of tropospheric bromine oxide in mid-latitudes. *Science,* Vol. 283, 55–57.

Hegels, E., P. J. Crutzen, T. Klüpfel, D. Perner, and P. J. Burrows (1998). Global distribution of atmospheric bromine monoxide from GOME on earth-observing satellite ERS 2. *Geophys. Res. Lett.,* Vol. 25, 3127–3130.

Hendrick, F., M. V. Roozendael, M. P. Chipperfield, M. Dorf, F. Goutail, X. Yang, C. Fayt, C. Hermans, K. Pfeilsticker, J.-P. Pommereau, J. A. Pyle, N. Theys, and M. D. Maziere (2007). Retrieval of stratospheric and tropospheric BrO profiles and columns using ground-based zenith-sky DOAS observations at Harestua, 60° N. *Atm. Chem. and Phys.,* Vol. 7, 4869 – 4885.

Henyey, L. and J. Greenstein (1941). Diffuse radiation in the Galaxy. *Astrophys. J.,* Vol. 93, 70 – 83.

Hermans, C. (2002). personal communication. For details see: http://www.oma.be/BIRAIASB/Scientific/Topics/lower/LaboBase/acvd/O4Info.html.

Heue, K.-P. (2005). *Airborne Multi AXis DOAS instrument and measurements of two-dimensional tropospheric trace gas distributions.* Ph.D. thesis, Combined Faculties for the Natural Sciences and for Mathematics, Universität Heidelberg.

Hollwedel, J., M. Wenig, S. Beirle, S. Kraus, S. Kühl, W. Wilms-Grabe, U. Platt, and T. Wagner (2004). Year-to-Year Variability of Polar Tropospheric BrO as seen by GOME. *Adv. Space Res.,* Vol. 34, 804–808.

Holton, J. R., P. H. Haynes, M. E. McIntyre, A. R. Douglass, R. B. Rood, and L. Pfister (1995). Stratosphere-Troposphere Exchange. *Rev. Geophysics,* Vol. 33, 403 – 439.

Hönninger, G. (2002). *Halogen Oxide Studies in the Boundary Layer by Multi Axis Differential Optical Absorption Spectroscopy and Active Longpath-DOAS.* Ph.D. thesis, Institut für Umweltphysik, Universität Heidelberg.

Hönninger, G., N. Bobrowski, E. Palenque, R. Torrez, and U. Platt (2004). Reactive bromine and sulfur emissions at Salar de Uyuni, Bolivia. *Geophys. Res. Lett.,* Vol. 31, No. 4.

Hönninger, G., H. Leser, O. Sebastián, and U. Platt (2004). Ground-based measurements of halogen oxides at the Hudson Bay by active longpath DOAS and passive MAX-DOAS. *Geophys. Res. Lett.,* Vol. 31, No. 4.

Hönninger, G., C. von Friedeburg, and U. Platt (2004). Multi axis differential optical absorption spectroscopy (MAX-DOAS). *Atm. Chem. and Phys.,* Vol. 4, 231–254.

Johnston, H. S. (1971). Reduction of stratospheric ozone by nitrogen oxide catalysts from supersonic transport exhaust. *Science,* Vol. 173, 517–522.

Johnston, P. (1996). Making UV/Vis cross sections, reference fraunhofer and synthetic spectra. unpublished manuscript.

Junge, C. E. (1963). *Air chemistry and radioactivity*, Volume 4 of *Internat. Geophys. Ser.* New York, London: Academic Press.

Kessler, C. and U. Platt (1984). Nitrous acid in polluted air masses – Sources and formation pathways. In *Physiochemical behaviour of atmosperic pollutants.* Edited by B. Versino and G. Angeletti, D. Reidel, Varese, Italia.

Khokhar, M. F. (2006). *Retrieval and Interpretation of Tropospheric SO_2 from UV/VIS Satellites Instruments.* Ph. D. thesis, Universität Leipzig, Germany.

King, M. D., S. Tsy, S. Platnik, M. Wang, and K. Liou (1997). Cloud Retrieval Algorithms for MODIS: Optical Thickness, Effective Particle Radius, and Thermodynamic Phase. In *MODIS Algorithm Theoretical Basis Document No. ATBD-MOD-05.* MODIS Web, NASA.

Kleffmann, J., K. Becker, and P. Wiesen (1998). Heterogeneous NO_2 conversion processes on acid surfaces: possible atmospheric implications. *Atmos. Environ.,* Vol. 32, 2721–2729.

Kraus, S. (2006). *DOASIS. A framework Design for DOAS. Dissertation Universität Mannheim.* Shake Verlag, Aachen.

Kreher, K., P. V. Johnston, S. W. Wood, B. Nardi, and U. Platt (1997). Ground-based measurements of tropospheric and stratospheric BrO at Arrival Heights, Antarctica. *Geophys. Res. Lett.,* Vol. 24, 3021 – 3024.

Leser, H., G. Hönninger, and U. Platt (2003). MAX-DOAS measurements of BrO and NO_2 in the marine boundary layer. *Geophys. Res. Lett.,* Vol. 30, No. 10.

Levenberg, K. (1944). A Method for the Solution of Certain Non-Linear problems in Least Squares. *Quart. Appl. Math.,* Vol. 2, 164–168.

Lindberg, S., S. Brooks, and C.-J. Lin (2001). Formation of reactive gaseous mercury in the Arctic: Evidence of oxidation of Hg^0 to gas-phase Hg-II compounds after Arctic sunrise. *Water Air and Soil Pollution,.*

Logan, J. A., M. J. Prather, S. C. Wofsy, and M. B. McElroy (1981). Tropospheric chemistry: A global perspective. *J. Geophys. Res.,* Vol. 86 (C8), 7210–7254.

London, J. (1980). Proceedings of the NATO Advanced Institute on the Atmospheric Ozone (Portugal). Faa - washington, d.c., usa, U.S. Dept. of Transportation.

Madronich, S. (1987). Photodissociation in the Atmosphere .1. Actinic Flux and the Effects of Ground Reflections and Clouds. *J. Geophys. Res.,* Vol. 92, 9740 – 9752.

Marbach, T., S. Beirle, C. Frankenberg, U. Platt, and T. Wagner (2007). Identification of tropospheric trace gas sources: synergistic use of HCHO and other satellite observations. In *Proceedings to the ENVISAT Symposium 2007.*

Marchuk, G., G. Mikhailov, M. Nazaraliev, R. Darbinjan, B. Kargin, and B. Elepov (1980). *The Monte Carlo Methods in Atmospheric Optics.* Berlin, New York: Spinger.

Marquard, L., T. Wagner, and U. Platt (2000). Improved Air Mass Factor Concepts for Scattered Radiation Differential Optical Absorption Spectroscopy of Atmospheric Species. *J. Geophys. Res.,* Vol. 105, 1315–1327.

Marquardt, D. W. (1963). An Algorithm for Least Squares Estimation of Non-Linear Parameters. *Soc. Indust. Appl. Math,* Vol. 11, 431–441.

McElroy, C., C. McLinden, and J. McConnell (1999). Evidence for bromine monoxide in the free troposphere during the Arctic polar sunrise. *Nature,* Vol. 397, 338–341.

McElroy, M. B., R. J. Salawitch, C. S. Wofsy, and J. A. Logan (1986). Reductions of Antarctic ozone due to synergistic interactions of chlorine and bromine. *Nature,* Vol. 321, 759–762.

Meller, R. and G. K. Moortgat (2000). Temperature dependance of the absorption cross sections of HCHO between 223 and 323K in the wavelength range 225 - 375 nm. *J. Geophys. Res.,* Vol. 105, 7089–7102.

Miller, H. L., A. Weaver, R. W. Sanders, K. Arpag, and S. Solomon (1997). Measurements of artic sunrise surface ozone depletion events at Kangerlussuaq, Greenland (67°N, 51°W). *Tellus,* Vol. 49B, 496–509.

Molina, L. and F. Rowland (1974). Stratospheric sink for chloroflurомethanes: chlorine atom catalyzed destruction of ozone. *Nature,* Vol. 249, 820–822.

Molina, L. T. and M. J. Molina (1987). Production of Cl_2O_2 from the self reaction of the ClO radical. *J. Phys. Chem.,* Vol. 91, 433.

Noxon, J. F. (1975). Nitrogen Dioxide in the Stratosphere and Troposphere measured by Ground-based Absorption Spectroscopy. *Science,* Vol. 189, 547–549.

Penndorf, R. (1957). Tables of the refractive index for standard air and the rayleigh scattering coefficient for the spectral region between 0.2 and 200 μ and their application to atmospheric optics. *J.Opt. Soc. Am.,* Vol. 47, No. 2, 176–182.

Perliski, L. M. and S. Solomon (1993). On the evaluation of air mass factors for atmospheric near-ultraviolet and visible absorption spectroscopy. *J. Geophys. Res.,* Vol. 98, 10,363–10,374.

Perner, D., D. H. Ehhalt, H. W. Paetz, U. Platt, E. P. Roeth, and A. Volz (1976). OH Radicals in the lower Troposphere. *Geophys. Res. Lett.,* Vol. 3, 466–468.

Perner, D. and U. Platt (1979). Detection of Nitrous Acid in the Atmosphere by Differential Optical Absorption. *Geophys. Res. Lett.,* Vol. 6, 917–920.

Peters, C., S. Pechtl, J. Stutz, K. Hebestreit, G. Hönninger, K. G. Heumann, A. Schwarz, W. J., and U. Platt (2005). Reactive and organic halogen species in three different European coastal environments. *Atm. Chem. and Phys.,* Vol. 5, 3357–3375.

Pfeilsticker, K., W. T. Sturges, H. Bösch, C. Camy-Peyret, M. P. Chipperfield, A. Engel, R. Fitzenberger, M. Müller, S. Payan, and B.-M. Sinnhuber (2000). Lower stratospheric organic and inorganic bromine budget for the arctic winter 1998/99. *Geophys. Res. Lett.,* Vol. 27, 3305 – 3308.

Pitts, J., E. Sanhueza, R. Atkinson, W. Carter, A. Winer, G. Harris, and C. Plum (1984). An investigation of the dark formation of nitrous acid in environmental chambers. *Int. J. Chem. Kinet.,* Vol. XVI, 919–939.

Platt, U. (1978). Dry Deposition of SO_2. *Atmos. Env.,* Vol. 12, 363–367.

Platt, U. (1986). *The origin of nitrous and nitric acid in the atmosphere*, pp. 299–319. W. Jaeschke, Springer Verlag.

Platt, U. (1994). Differential Optical Absorption Spectroscopy (DOAS). In M. W. Sigrist (Ed.), *Monitoring by Spectroscopic Techniques.* New York: John Wiley & Sons, Inc.

Platt, U. and G. Hönninger (2003). The role of halogen species in the troposphere. *Chemosphere,* Vol. 52, No. 2, 325–338.

Platt, U., L. Marquard, T. Wagner, and D. Perner (1997). Corrections for Zenith Scattered Light DOAS. *Geophys. Res. Letters,* Vol. 24, No. 14, 1759–1762.

Platt, U. and D. Perner (1980). Direct Measurements of Atmospheric CH_2O, HNO_2, O_3, NO_2 and SO_2 by Differential Optical Absorption in the Near UV. *J. Geophys. Res.,* Vol. 85, 7453–7458.

Platt, U., D. Perner, G. Harris, A. Winer, and J. Pitts (1980). Observations of nitrous acid in an urban atmosphere by differential optical absorption. *Nature,* Vol. 285, 312 – 314.

Platt, U., D. Perner, G. W. Harris, A. M. Winer, and J. N. Pitts, Jr. (1980). Detection of NO_3 in the Polluted Troposphere by Differential Optical Absorption. *Geophys. Res. Lett.,* Vol. 7, 89–92.

Platt, U., D. Perner, and H. W. Pätz (1979). Simultaneous Measurement of Atmospheric CH_2O, O_3 and NO_2 by Differential Optical Absorption. *J. Geophys. Res.,* Vol. 84, 6329–6335.

Platt, U. and J. Stutz (2008). *Differential Optical absorption Spectroscopy. Principles and Applications.* Springer-Verlag.

Richter, A. (1997). *Absorptionsspektroskopische Messungen stratosphärischer Spurengase über Bremen. 53°N.* Ph. D. thesis, University of Bremen, Bremen, Germany.

Richter, A., F. Wittrock, and J. Burrows (1998). GOME measurements of tropospheric BrO in northern hemispheric spring. *Ann. Geophys. Suppl. II,* Vol. 16, C721.

Rinsland, C. P., M. R. Gunson, R. J. Salawitch, M. J. Newchurch, R. Zander, M. M. Abbas, M. C. Abrams, G. L. Manney, H. A. Michelsen, A. Y. Chang, and A. Goldman (1996). ATMOS measurements of $H_2O + 2\,CH_4$ and total reactive nitrogen in the November 1994 Antarctic stratosphere: Dehydration and denitrification in the vortex. *Geophys. Res. Lett.,* Vol. 23, 2397–2400.

Rodgers, C. D. (1976). Retrieval of Atmospheric Temperature and Composition From Remote Measurements of Thermal Radiation. *Rev. Geophys.,* Vol. 14, No. 4, 609–624.

Rodgers, C. D. (2000). *Inverse Methods for Atmospheric Sounding.* London: Worls Scientific.

Roedel, W. (2000). *Physik unserer Umwelt - Die Atmosphäre* (3. ed.). Berlin Heidelberg New York: Springer-Verlag.

Röth, E.-P. (1994). *Ozonloch – Ozonsmog: Grundlagen der Ozonchemie.* Mannheim: Bibliographisches Institut.

Saiz-Lopez, A. and J. M. C. Plane (2004). Recent applications of differential optical absorption spectroscopy: Halogen chemistry in the lower troposphere. *J. Phys. IV France,* Vol. 121, 223 –238.

Saliba, N., M. Mochida, and B. Finlayson-Pitts (2000). Laboratory studies of sources ofHONO in polluted urban atmospheres. *Geophys. Res. Lett.,* Vol. 27 (19), 3229–3232.

Sander, S. P., A. R. Ravishankara, D. M. Golden, C. E. Kolb, M. J. Kurylo, M. J. Molina, G. K. Moortgat, H. Keller-Rudek, B. J. Finlayson-Pitts, P. H. Wine, R. E. Huie, and V. L. Orkin (2006). Chemical Kinetics and Photochemical Data for Use in Atmospheric Studies-Evaluation Number 15. Technical Report JPL Publication 06-2, Jet Propulsion Laboratory, Pasadena, CA.

Sanders, R. W., S. Solomon, M. A. Carroll, and A. L. Schmeltekopf (1988). Ground based Measurements of O_3, NO_2, OClO and BrO during the Antarctic Ozone Depletion Event. In R. D. Bjokov and P. Fabian (Eds.), *Ozone in the Atmosphere, Quadrennial Ozone Symposium 1988*, pp. 65–70. Hampton, Va.: Deepak Publishing.

Sanders, R. W., S. Solomon, J. P. Smith, L. Perliski, H. L. Miller, G. H. Mount, J. G. Keys, and A. L. Schmeltekopf (1993). Visible and Near-Ultraviolet Spectroscopy at McMurdo Station Antarctica, 9. Obeservations of OClO from April to October 1991. *J. Geophys. Res.,* Vol. 98, 7219–7228.

Sanghavi, S. (2003). *An effcient Mie theory implementation to investigate the influence of aerosols on radiative transfer.* Diploma thesis, University of Heidelberg.

Scholl, T. (2006). *Photon Path Lengths Distributions for Cloudy Skies. Their first and second-order moments inferred from high resolution oxygen A-Band spectroscopy.* Ph.D. thesis, Combined Faculties for the Natural Sciences and for Mathematics, Universität Heidelberg.

Schumann, U. and H. Huntrieser (2007). The global lightning-induced nitrogen oxides source. *Atm. Chem. and Phys.,* Vol. 7, 3823 – 3907.

Schurath, U. (2003). Lecture on Atmospheric Chemistry, Summer school Heidelberg.

Seinfeld, J. and S. Pandis (1997). *Atmospheric Chemsity and Physics.* Hoboken, N.J.: John Wiley.

Sheperd, T. G. (2003). Large-Scale Atmospheric Dynamics for Atmospheric Chemists. *Chem. Rev.,* Vol. 103, 4509 – 4531.

Simpson, W. R., L. A.-A. T. A. D. M. S. and F. Domine (2005). Halogens in the coastal snow pack near Barrow, Alaska: Evodence for active bromine in air-snow chemistry during springtime. *Geophys. Res. Lett.,* Vol. 32, L04811.

Sinreich, R., U. Frieß, T. Wagner, and U. Platt (2005). Multi axis differential optical absorption spectroscopy (MAX-DOAS) of gas and aerosol distributions. *Faraday Discuss.,* Vol. 130, 153–164.

Sioris, C. E. and W. F. J. Evans (1999). Filling in of Fraunhofer and gas-absorption lines in sky spectra as caused by rotational Raman scattering. *Appl. Opt.,* Vol. 38, No. 12, 2706–2713.

Solomon, S., A. L. Schmeltekopf, and R. W. Sanders (1987). On the interpretation of zenith sky absorption measurements. *J. Geophys. Res.,* Vol. 92, 8311–8319.

Steck, T., N. Glatthor, T. von Clarmann, H. Fischer, J. M. Flaud, B. Funke, U. Grabowski, M. Höpfner, S. Kellmann, A. Linden, A. Perrin, and G. P. Stiller (2007). Retrieval of global upper tropospheric and stratospheric formaldehyde (H_2CO) distributions from high-resolution MIPAS-Envisat spectra. *Atmos. Chem. Phys. Discuss.,* Vol. 7, 13627 – 13652.

Stutz, J. (1996). *Messung der Konzentration troposhärischer Spurenstoffe mittels Differentieller Optischer Absorptions Spektroskopie: Eine neue Generation von Geräten und Algorithmen.* Ph. D. thesis, Institut für Umweltphysik, Universität Heidelberg.

Stutz, J., R. Ackermann, J. D. Fast, and L. Barrie (2002). Atmospheric Reactive Chlorine and Bromine at the Great Salt Lake, Utah. *Geophys. Res. Lett.,* Vol. 29, doi: 10.1029/2002GL014812.

Stutz, J., E. Kim, U. Platt, P. Bruno, C. Perrino, and A. Febo (2000). UV-visible absorption cross section of nitrous acid. *J. Geophys. Res.,* Vol. 105 (D11), 14858–14592.

Stutz, J. and U. Platt (1996). Numerical Analysis and Estimation of the Statistical Error of Differential Optical Absorption Spectroscopy Measurements with Least-Squares methods. *Appl. Opt.,* Vol. 35, No. 30, 6041–6053.

Stutz, J. and U. Platt (1997). Improving longpath differential optical absorption spectroscopy with a quartz-fiber mode mixer. *Applied Optics,* Vol. 36, No. 6, 1105–1115.

Svensson, R., E. Ljungström, and O. Lindqvist (1987). Kinetics of the reaction between nitrogen dioxide and water vapour. *Atmos. Environ.,* Vol. 21, 1529–1539.

Theys, N., M. V. Roozendael, F. Hendrick, C. Fayt, C. Hermans, J.-L. Baray, F. Goutail, J.-P. Pommereau, and M. D. Maziere (2007). Retrieval of stratospheric and tropospheric BrO columns from multi-axis DOAS measurements at Reunion Island (21° S, 56° E). *Atm. Chem. and Phys.,* Vol. 7, 4733 – 4749.

Trick, S. (2004). *Formation of Nitrous Acid on Urban Surfaces – A physical-chemical perspective.* Dissertation, University of Heidelberg.

Van de Hulst, H. (1981). *Light scattering by small particles.* New York: Dover publication.

Van Roozendael, M., D. W. Arlander, J. Burrows, M. Chipperfield, C. Fayt, F. Hendrick, C. Hermans, P. Johnston, R. Jones, K. Kreher, J.-C. Lambert, N. Tahrin, D. Newnham, K. Pfeilsticker, U. Platt, J.-P. Pommereau, I. Pundt, A. Richter, B. Sinnhuber, A. South, K. Tørnkvist, and T. Wagner (2000). Lessons learned from 2 years of coordinated multi-platform UV-visible observations of atmospheric bromine monoxide. *Proceedings of the Quadrennial Ozone Symposium, Hokkaido University, Sapporo, Japan,,* 157–158.

Van Roozendael, M., C. Fayt, P. Post, C. Hermans, and J.-C. Lambert (2003). *Retrieval of BrO and NO_2 from UV-Visible Observations, in: Sounding the troposphere from space: a new era for atmospheric chemistry, edited by: Borell, P., Borrell, P. M., Burrows, J. P., and Platt, U.,.* Springer-Verlag.

Van Roozendael, M., T. Wagner, A. Richter, I. Pundt, D. W. Arlander, J. P. Burrows, M. Chipperfield, C. Fayt, P. V. Johnston, J.-C. Lambert, K. Kreher, K. Pfeilsticker,

U. Platt, J.-P. Pommereau, B.-M. Sinnhuber, K. K. Tørnkvist, and F. Wittrock (2002). Intercomparision of BrO measurements from ERS-2 GOME, ground-based and balloon platforms. *Adv. Space Res.,* Vol. 29, 1661 – 1666.

Vandaele, A. C., C. Hermans, P. C. Simon, M. Carleer, R. Colin, S. Fally, M.-F. Merienne, A. Jenouvrier, and B. Coquart (1997). Measurements of the NO_2 absorption cross-section from 42000 cm-1 to 10000 cm-1 (238 to 1000 nm) at 220 K and 294 K. *J. Quant. Spectrosc. Radiat. Transfer,* Vol. 59.

Volkamer, R., T. Kurosu, K. Chance, Z. Li, Y. Zhang, T. Brauers, and A. Wahner (2006, December). Spatial Variability of Glyoxal and Formaldehyde during PRD-2006: Comparison of mobile Mini-MAX-DOAS and OMI satellite data in the Pearl River Delta, China. *AGU Fall Meeting Abstracts,*, B897+.

Volkamer, R., L. T. Molina, M. J. Molina, T. Shirley, and W. H. Brune (2005). DOAS measurement of glyoxal as an indicator for fast VOC chemistry in urban air. *Geophys. Res. Lett.,* Vol. 32, L08806.

Volkamer, R., P.Sheehy, L. Molina, and M. Molina (2007). Oxidative Capacity of the Mexico City Atmosphere. Part 1: A Radical Source Perspective. *Atmos. Chem. Phys. Discuss.,* Vol. 7, 5365 – 5412.

Volkamer, R., P. Spietz, J. P. Burrows, and U. Platt (2005). High-resolution absorption cross-sections of glyoxal in the UV-vis and IR spectral ranges. *J. Photochem. Photobiol. A: Chem.,* Vol. 172, 35–36.

von Friedeburg, C. (2003). *Derivation of Trace Gas Information combining Differential Optical Absorption Spectroscopy with Radiative Transfer Modelling.* Ph.D. thesis, Combined Faculties for the Natural Sciences and for Mathematics, Universität Heidelberg.

von Glasow, R. and P. J. Crutzen (2003). Tropospheric halogen chemistry. In O. Elsevier-Pergamon (Ed.), *The Atmosphere (ed. R. F. Keeling), Vol. 4 Treatise on Geochemistry (eds. H. D. Holland and K. K. Turekian)*, pp. 21–64. Elsevier-Pergamon, Oxford.

Wagner, T. (1999). *Satellite observations of atmospheric halogen oxides.* Ph. D. thesis, University of Heidelberg, Heidelberg, Germany.

Wagner, T., J. P. Burrows, T. Deutschmann, B. Dix, C. von Friedeburg, U. Frieß, F. Hendrick, K.-P. Heue, H. Irie, H. Iwabuchi, Y. Kanaya, J. Keller, C. A. McLinden, H. Oetjen, E. Palazzi, A. Petritoli, U. Platt, O. Postylyakov, J. Pukite, A. Richter, M. van Roozendael, A. Rozanov, V. Rozanov, R. Sinreich, S. Sanghavi, and F. Wittrock (2007). Comparison of box-air-mass-factors and radiances for Multiple-Axis Differential Optical Absorption Spectroscopy (MAX-DOAS) geometries calculated from different UV/visible radiative transfer models. *Atm. Chem. and Phys.,* Vol. 7, 1809 – 1833.

Wagner, T., B. Dix, C. von Friedeburg, U. Frieß, S. Sanghavi, R. Sinreich, and U. Platt (2004). MAX-DOAS O_4 measurements: A new technique to derive information on atmospheric aerosols. Principles and information content. *J. Geophys. Res.,* Vol. 109, doi:10.1029/2004JD004904.

Wagner, T., C. Leue, M. Wenig, K. Pfeilsticker, and U. Platt (2001). Spatial and temporal distribution of enhanced boundary layer BrO concentrations measured by the GOME instrumnet aboard ERS-2. *J. Geophys. Res.,* Vol. 106, 24225 – 24235.

Wagner, T. and U. Platt (1998). Satellite mapping of enhanced *BrO* concentrations in the troposphere. *Nature,* Vol. 395, 486–490.

Weidner, F. (2005). *Development and Application of a Versatile Balloon-Borne DOAS Spectrometer for Skylight Radiance and Atmospheric Trace Gas Profile Measurements.* Ph.D. thesis, Combined Faculties for the Natural Sciences and for Mathematics, Universität Heidelberg.

Weidner, F., H. Bösch, H. Bovensmann, J. P. Burrows, A. Butz, C. Camy-Peyret, M. Dorf, K. Gerilowski, W. Gurlit, U. Platt, C. von Friedeburg, T. Wagner, and K. Pfeilsticker (2005). Balloon-borne limb profiling of UV/vis skylight radiances, O_3, NO_2, and BrO: technical set-up and validation of the method. *Atm. Chem. and Phys.,* Vol. 5, 1409 – 1422.

Wilmouth, D. M., T. F. Hanisco, N. M. Donahue, and J. G. Anderson (1999). Fourier transform ultraviolet spectroscopy of the $A^2\Pi_{3/2} \leftarrow X^2\Pi_{3/2}$ transition of BrO. *J. Phys. Chem.,* Vol. 103, 8935–8945.

Winer, A. and H. Biermann (1994). Long Pathlength Differential Optical Absorption Spectroscopy (DOAS) Measurements of Gaseous HONO, NO_2 and HCHO in the California South Coast Air Basin. *Research On Chemical Intermediates,* Vol. 20 (3-5), 423–445.

Wiscombe, W. J. (1980). Improved Mie scattering algorithms. *Appl. Opt.,* Vol. 19, 1505–1509.

Wittrock, F., H. Oetjen, A. Richter, S. Fietkau, T. Medeke, A. Rozanov, and J. P. Burrows (2004). MAX-DOAS measurements of atmospheric trace gases in Ny- ° Alesund - Radiative transfer studies and their application. *Atm. Chem. and Phys.,* Vol. 4, 955 – 966.

Woyde, M. (2007). *Erprobung einer InGaAs-Photodiodenzeile zur Detektion von Methan im NIR-Bereich.* Diploma thesis, University of Heidelberg.

Yienger, J. and H. L. II (1995). Empirical model of global soil-biogenic NO_x emissions. *J. Geophys. Res.,* Vol. 100, 11447–11464.

Zeldovich, Y. and Y. Raizer (1967). Rates of relexation processes in gases (8/9). *Physics of Shock Waves and High-Temperature Hydrodynamic Phenomena,* Vol. 1, 374–382.

Acknowledgements

Ein herzliches Dankeschön...

an Herrn Prof. Platt für die Ermöglichung dieser spannenden Arbeit, für viele interessante Anregungen und Impulse, sowohl während des Gerätebaus auch als bei der Interpretation der Daten.

an das ganze CARIBIC Team! Insbesondere ein Danke an Carl, Dieter, Franz, Claus, Andreas und Markus. Danke für Eure Unterstützung in allen Projektphasen, für Eure Mühen, u.a. mit der Madenschraube, dem Kupferrohr und den Glasfasern, letzteres sowohl beim Einbau als auch bei jedem Messflug. Ohne Euch wäre das CARIBIC DOAS nicht so hoch geflogen!

an Udo für den Bau des CARIBIC DOAS Teleskops, für die Messprogramme und für all die vielen anderen Beiträge zum CARIBIC DOAS Instrument. Vor allem aber ein großes Danke für die gute Betreuung und Begleitung auf dem ganzen Weg!

an Thomas, für die gute Betreuung, für die vielen guten Ratschläge, Tipps und Anregungen und vor allem für ein offenes Ohr in allen "DOAS Lebenslagen"!

an all die Menschen am Institut die mich zu unterschiedlichen Zeiten und auf unterschiedlichen Wegen begleitet und voran gebracht haben, bei der Arbeit und auch privat: Roman, Nicole, Günther, Tina, Steffen, Thierry, Ossama, Tim, Klaus-Peter, Oli, Rainer und Roland.

an Lena und vor allem an Klaus für die "last minute" Betreuung.

an meine Büro Kollegen, Thomas, Jens und Thomas, für die gute Atmosphäre, für die "Sekretariatsdienste" während meiner "home office" Zeit und ein extra Danke an Thomas fürs Korrekturlesen.

an die Werkstatt. Ohne die schnelle Bearbeitung der "gaaanz dringenden Aufträge" hätte das CARIBIC DOAS Instrument nicht so schnell abheben können!

an Sekretariat und Verwaltung für eine stets freundliche und unkomplizierte Zusammenarbeit.

an die Mitarbeiter von LH Technik, die ich bei allen Arbeiten am Flugzeug stets hilfsbereit, interessiert und freundlich erlebt habe.

Dankeschön auch an alle bei diesem Projekt beteiligten Firmen:
Lufthansa , Lufthansa Technik, Enviscope GmbH, Garner CAD Technik GmbH, Heggemann Aerospace AG, Kolt Engineering GmbH